DATA RECONCILIATION BASED SCHEME FOR SENSOR FAULT DETECTION

by

VIDYA SAGAR YELLAPU

ENGG01201104006

BHABHA ATOMIC RESEARCH CENTRE, MUMBAI

A thesis submitted to the

Board of Studies in Engineering Sciences

In partial fulfilment of requirements

for the degree of

DOCTOR OF PHILOSOPHY

of

HOMI BHABHA NATIONAL INSTITUTE

September, 2016

Homi Bhabha National Institute

Recommendations of the Viva Voce Committee

As members of the Viva Voce Committee, we certify that we have read the dissertation prepared by **Vidya Sagar Yellapu** entitled **"Data Reconciliation based Scheme for Sensor Fault Detection"** and recommend that it may be accepted as fulfilling the thesis requirement for the award of Degree of Doctor of Philosophy.

Chairman – Dr. (Smt.) Archana Sharma	Archana	**Date:** 29-9-16
Guide / Convener - Dr. A. P. Tiwari		**Date:** 29.9.16
Co-Guide - Dr. S. B. Degweker		**Date:** 29.9.2016
Examiner - Dr. Ketan Detroja		**Date:** 29/9/2016
Member 1- Dr. Biswaranjan Dikshit	B Dikshit	**Date:** 29/9/16
Member 2- Dr. (Smt.) Gopika Vinod		**Date:** 29.9.2016
Member 3- Dr. V. H. Patankar	V.H. Patankar	**Date:** 29.09.16

Final approval and acceptance of this thesis is contingent upon the candidate's submission of the final copies of the thesis to HBNI.

We hereby certify that we have read this thesis prepared under our direction and recommend that it may be accepted as fulfilling the thesis requirement.

Date: 07/10/2016
Place: Mumbai

07/10/2016

Dr. S. B. Degweker
(Co-Guide)

Dr. A. P. Tiwari
(Guide)

STATEMENT BY AUTHOR

This dissertation has been submitted in partial fulfillment of requirements for an advanced degree at Homi Bhabha National Institute (HBNI) and is deposited in the Library to be made available to borrowers under rules of the HBNI.

Brief quotations from this dissertation are allowable without special permission, provided that accurate acknowledgement of source is made. Requests for permission for extended quotation from or reproduction of this manuscript in whole or in part may be granted by the Competent Authority of HBNI when, in his or her judgement, the proposed use of the material is in the interests of scholarship. In all other instances, however, permission must be obtained from the author.

VIDYA SAGAR YELLAPU

DECLARATION

I, hereby declare that the investigation presented in the thesis has been carried out by me. The work is original and has not been submitted earlier as a whole or in part for a degree/diploma at this or any other Institution/University.

Y. Vidyasagar

VIDYA SAGAR YELLAPU

List of Publications based on this thesis

Journal Publications

1. Y. V. Sagar, A. P. Tiwari, and S. B. Degweker, "Application of data reconciliation and fault detection and isolation of ion chambers in advanced heavy water reactor," *Annals of Nuclear Energy,* Vol. 85, pages 1210-1225, 2015.

2. Y. V. Sagar, A. K. Mishra, A. P. Tiwari, and S. B. Degweker, "On-line Fault Detection and Diagnosis of In-core Neutron Detectors using Generalized Likelihood Ratio method," *IEEE Transactions on Nuclear Science,* Vol. 62 (6), pages 3311-3323, 2015.

Conference Publications

1. Y. V. Sagar, A. P. Tiwari, S. R. Shimjith, M. Naskar, and S. B. Degweker, "Space-time kinetics modeling for the determination of neutron detector signals in advanced heavy water reactor," In *2013 IEEE International Conference on Control Applications (CCA)*, Hyderabad, India, pages 1224-1229, 2013.

2. Y. V. Sagar, A. P. Tiwari, and S. B. Degweker, "Application of data reconciliation and fault detection and isolation of SPNDs in AHWR," In *3rd National Symposium on Advances in Control & Instrumentation (SACI),* Mumbai, India, pages 542-551, 2014.

3. Y. V. Sagar, A. P. Tiwari, and S. B. Degweker, "An Iterative Principal Component Test for Fault Detection and Isolation," In *2015 IEEE International Conference on Control Applications (CCA)*, Sydney, Australia, pages 972-977, 2015.

Dedicated to my family

ACKNOWLEDGEMENTS

I would like to express my sincere gratitude to my guide Dr. A. P. Tiwari for formulating this research topic and for the guidance and encouragement to work to the best of my abilities. His knowledge, insightfulness and consistent care for the best output have been great assets without which this research would not have been possible. I would also like to thank my co-guide Dr. S. B. Degweker for the constant encouragement.

I am indebted to the chairman and other members of the doctoral committee for their valuable comments and suggestions during the review presentations, oral general comprehensive examination and pre-synopsis viva-voce. I specially thank Dr. Kallol Roy, former chairman of the doctoral committee, for this.

It gives me great pleasure in acknowledging the help and support of Dr. S. R. Shimjith in Reactor Control Systems Design Section (RCSDS), BARC, regarding the mathematical modeling of the reactors and for careful proof-reading of the manuscripts. Special thanks to Shri A. K. Mishra, RCSDS, for the valuable discussions and suggestions. I also wish to thank the other members of RCSDS for their help and support.

I am indebted to Homi Bhabha National Institute (HBNI) for creating this opportunity of pursuing research in real-time applications. I wish to thank the people at Bhabha Atomic Research Centre (BARC) who either directly or indirectly helped me completing my doctoral studies. I also wish to thank my fellow research scholars at HBNI for making my stay pleasant.

Last but not least, I want to express my heartful thanks to my family. I am grateful to my brother Shri Siva Prasad for encouraging me to pursue the doctoral studies at BARC. I express my deep gratitude and admiration to my parents Smt. Vara Lakshmi and Shri Paidiyya Yellapu for the unconditional love and for letting me go for higher studies. Their sacrifices are invaluable to me.

VIDYA SAGAR YELLAPU

Contents

SYNOPSIS

In controlled systems, errors are always inevitable during the measurement though the measuring instruments are precisely calibrated to represent the true values. The errors may broadly be classified as random errors and gross errors or 'faults'. Random errors, as the name suggests, are random in nature as neither the sign nor the magnitude can be estimated with certainty. They cannot be completely eliminated but their effects can be reduced considerably with the use of filtering techniques and also with their statistical properties. On the other hand, faults are unpermitted deviations that occasionally arise in one or more of the characteristic properties of the components from the acceptable, usual and standard conditions [34]. Faults, being either incipient or abrupt changes in the parameters of the components, can appear due to either external or internal causes. Faults in system or process components including sensors, if not detected and diagnosed, endanger the system reliability, reduce safety margins, activate safety systems, cause operational upsets and establish the need for maintenance activities. They can also cause off-specification production, increased operating costs, unnecessary line shut-downs, and detrimental environmental impacts. Nevertheless, faults can be detected from their reflections in the signals associated with the system. They should be detected 'early' before they result into serious consequences.

Nuclear reactors are the best example for safety-critical systems and hence they have stringent requirements for safety and economy. They use a large number of neutron detectors placed both inside and outside the core for providing measurement signals to the independent control and protection systems. For the efficient performances from these systems, a scheme which can reduce the effects of random errors while eliminating the faults is of utmost importance. Methods based on analytical redundancy can be implemented to meet this need. Considering the complexity and inaccuracy involved in the model-based and signal-based Fault Detection and Isolation (FDI) schemes [50, 79], measurement data-based FDI schemes are promising.

The neutron detector signals are corrupted by random noise because of the probabilistic nature of the neutron flux hitting the emitter material of the detectors and other factors related to operation of detectors [115]. Apart from random errors, the detectors might also develop failures. Failures in detectors can be broadly classified as hard failures (complete loss of signal, *e.g.*, sheath failure) and soft failures or faults (signal changes gradually or suddenly by a relatively small amount). Hard failures in detectors can be easily identified and those detectors can be replaced. However, soft faults are difficult to detect since they produce degraded signals over a period of time, because of changes in the parameters resulting in changes in the sensitivity; improper calibration; and systematic biases. These factors reflect as faults in their output signals.

Data Reconciliation (DR) technique, posed first in [45], exploits the spatial relationships among the variables as constraints to obtain estimates for the true values of the measurements, which are more accurate than the original measurements. For the cases in which the process is almost steady and the linear relationships are not violated, a linear steady-state DR is sufficient for random error reduction. The linear steady-state DR problem can be formulated as follows:

In the presence of random errors, at a time instant k, the measurement vector $\boldsymbol{y}(k)$ of variables is the summation of their true values $\boldsymbol{x}(k)$ and the corresponding random errors $\boldsymbol{\varepsilon}(k)$, given by

$$\boldsymbol{y}(k) = \boldsymbol{x}(k) + \boldsymbol{\varepsilon}(k),\ \boldsymbol{y}(k) \in \mathbb{R}^n,\ \boldsymbol{x}(k) \in \mathbb{R}^n,\ \boldsymbol{\varepsilon}(k) \in \mathbb{R}^n,$$

where it is assumed that $\boldsymbol{x}(k)$ and $\boldsymbol{\varepsilon}(k)$ are considered to be independent of each other and there exists sufficient signal to noise ratio. According to steady-state DR, when all the signals are fault-free, the estimates of the signals at a time instant k are obtained by minimizing the function

$$\min_{\boldsymbol{x}(k)} (\boldsymbol{y}(k) - \boldsymbol{x}(k))^T \boldsymbol{\Sigma}_{\varepsilon}^{-1} (\boldsymbol{y}(k) - \boldsymbol{x}(k)),$$

s.t.

$$\boldsymbol{A}\boldsymbol{x}(k) = \boldsymbol{0},$$

where $\boldsymbol{A}$ represents the algebraic relationships among the variables, whose variance is represented by the matrix $\boldsymbol{\Sigma}_{\varepsilon}$. The reconciled estimates of the true values of the signals obtained from the above optimization problem are given by [65]

$$\hat{\boldsymbol{x}}(k) = \boldsymbol{y}(k) - \boldsymbol{\Sigma}_{\varepsilon}\boldsymbol{A}^T(\boldsymbol{A}\boldsymbol{\Sigma}_{\varepsilon}\boldsymbol{A}^T)^{-1}\boldsymbol{A}\boldsymbol{y}(k).$$

The reconciled estimates $\hat{\boldsymbol{x}}(k)$ are accurate as long as there are no faulty variables in $\boldsymbol{y}(k)$. When faults are present, they should be detected and the faulty variables should be eliminated for accurate DR.

An FDI system can be designed to monitor the mean value of either the adjustment vector $\boldsymbol{a}(k) = \boldsymbol{y}(k) - \hat{\boldsymbol{x}}(k)$ or the constraint residual vector $\boldsymbol{r}(k) = \boldsymbol{A}\boldsymbol{y}(k)$ to take a binary decision about the presence of fault(s). DR technique can be reformulated to solve also for the faulty variables, if any, in $\boldsymbol{y}(k)$ [12]. The projection matrix concept presented in [12] essentially separates the healthy and faulty variables in $\boldsymbol{y}(k)$ from the above optimization problem and gives separate solutions. This DR based FDI is efficient for sensor fault detection as it needs only the algebraic relationships (in the form of constraint model $\boldsymbol{A}$) among the sensors.

For ex-core detector applications, ion chambers are used in major reactors because of their insensitivity to applied voltage, proportionality to the energy deposited and less vulnerability to gas deterioration. Coming to in-core detector applications, Self Powered Neutron Detectors (SPNDs) is more prevalent because of their small size, requirement of simple electronics. Considering the complexity and the probable inaccuracy in the model of the reactor, FDI of the neutron detectors of the reactors can be attempted with the help of a DR scheme powered by the constraint model $\boldsymbol{A}$.

The objective of this thesis is to establish the effectiveness of the DR-based FDI of neutron detectors of Advanced Heavy Water Reactor (AHWR) [103], which is a vertical, pressure tube type, heavy water moderated and boiling light water cooled natural circulation reactor, designed to generate 920 MW (thermal). Automatic regulation of total reactor power as well as spatial control of power distribution in the AHWR are carried out by the Reactor Regulating System (RRS) with the help of Regulating Rods (RRs). There are two more independent systems for the protection of the reactor labelled as primary shut down system (SDS-1) and secondary shut down system (SDS-2). RRS relies on ex-core ion chambers for the measurement of total reactor power in both log and linear ranges and in-core Vanadium Self Powered Neutron Detectors (VSPNDs) in linear range for measurement of zonal powers. Ion chambers can reflect the variations in the reactor flux in a prompt manner. Hence the DR and FDI are straight forward. On the other hand, VSPNDs have inherent dynamics, which delay their response significantly. However, the delayed nature can be compensated with the use of a dynamic compensator, which uses the dynamic model of the VSPNDs. Apart from bulk power control, functions such as monitoring spatial flux transients, flow changes in coolant channels, reactivity device movements and ensuring peaking factors are within analyzed safety limits are also required for large reactors like AHWR. These functions are performed from the information about axial, azimuthal and radial flux distribution obtained through an in-core VSPND based flux mapping and flux tilt control systems. Hence, the neutron flux detector signals should be reliable, free from random errors and any faults in these detectors should be timely identified.

As shown in Fig. 1, 9 ion chambers are placed in vault water around the calandria vessel [103], in lattice tubes placed close to calandria. Hence, each ion chamber gives a current signal proportional to the core leakage flux at its location, which is representative

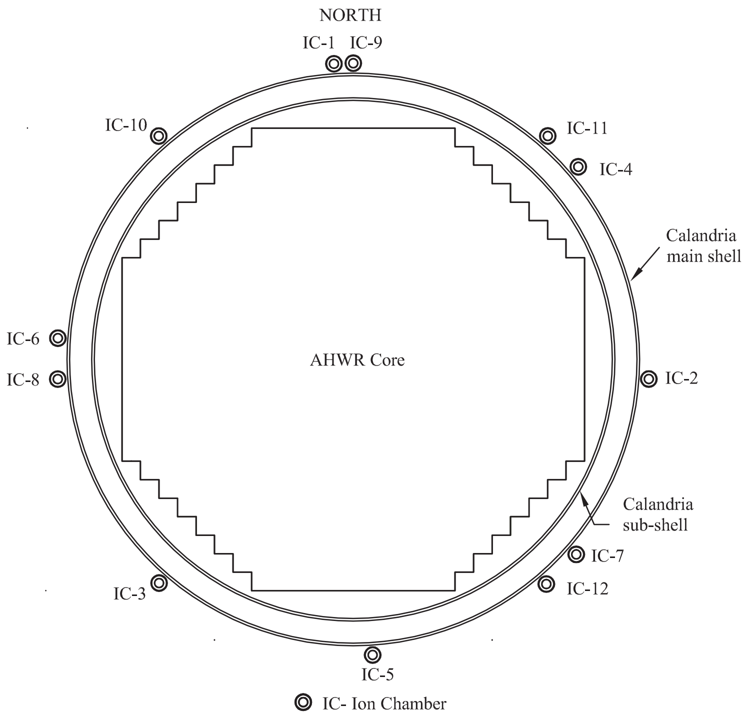

Figure 1: Schematic layout of ex-core ion chambers in AHWR.

of the core average flux. Ion chambers 1, 2 and 3 are for RRS; ion chambers 4, 5 and 6 are for SDS-1; ion chambers 7, 8 and 9 are for SDS-2; ion chambers 10, 11 and 12 are the spare detectors respectively for RRS, SDS-1 and SDS-2.

VSPNDs are 200 in number, distributed in different layers in 32 In-Core Detector Housings (ICDHs) at inter-lattice locations. Locations of ICDHs are shown in Fig. 2(a). Each ICDH can accommodate up to 7 VSPNDs at $Z1$, $Z2$, $Z3$, $Z4$, $Z5$, $Z6$ and $Z7$ positions as indicated in Fig. 2(b). Only eight ICDHs, *i.e.*, ICDHs numbered as 5, 8, 13, 14, 19, 20, 25 and 28 contain 7 VSPNDs each while the remaining 24 ICDHs contain 6 VSPNDs each.

When the reactor is in steady-state operation, a DR scheme supplied by the steady-state algebraic relations (constraint model $\boldsymbol{A}$) among the signals of ion chambers and VSPNDs can be implemented for the minimization of random errors and elimination of faults. This scheme can handle both the incipient and abrupt faults in the ion chambers and VSPNDs. The static linear model $\boldsymbol{A}$ can be obtained through the data driven mod-

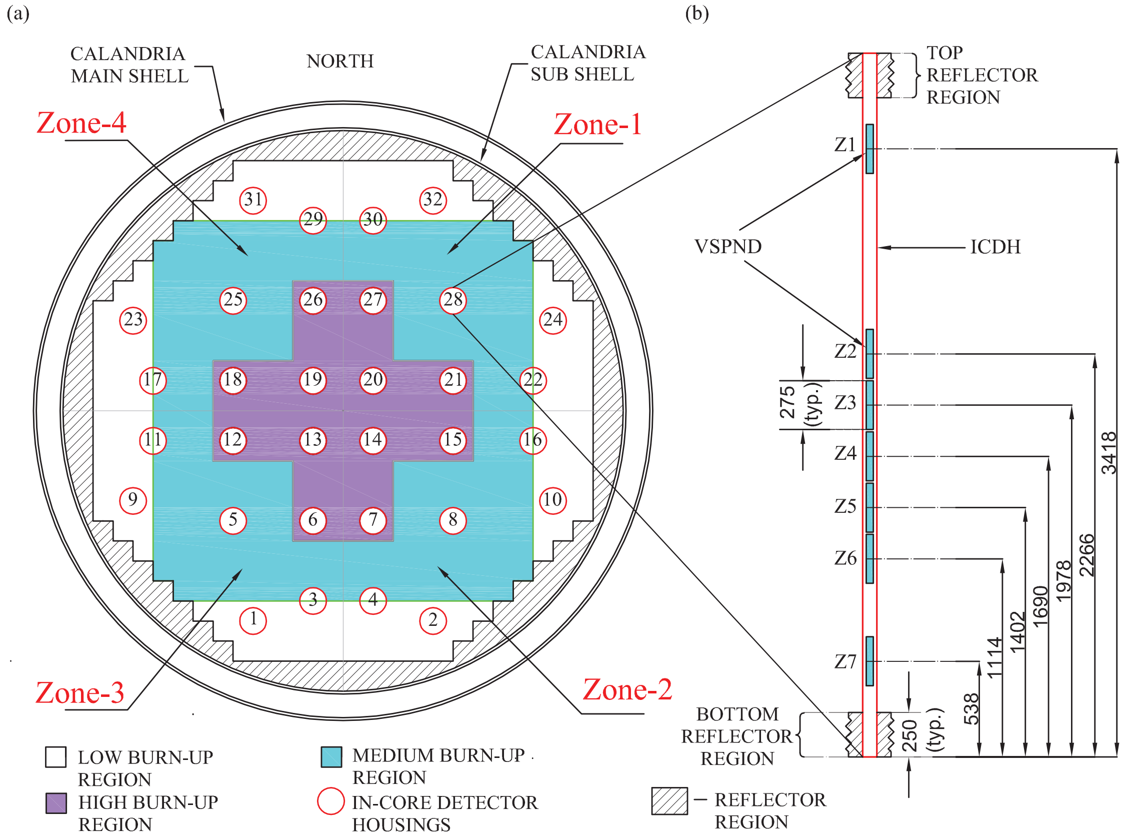

Figure 2: (a) Cross-section of the AHWR core, showing the location of ICDHs (schematic) (b) Placement of 7 VSPNDs along an ICDH in AHWR (all the dimensions are in mm).

eling methods, *e.g.*, Principal Component Analysis (PCA) [32] and Iterative Principal Component Analysis (IPCA) [66]. PCA is used for dimensionality reduction such that prominent variability in the data is captured with a lesser number of latent variables. This method aims at splitting the multidimensional space of the multivariate data into two subspaces namely the principal component subspace and the residual subspace that respectively hold maximum and minimum variability in the data. The residual subspace helps in identifying the process constraint model $\boldsymbol{A}$, which is required for estimating the covariances of the measurement errors of the variables and for DR and FDI analyses. However, the order of the residual subspace, called as model order, is not known exactly from the PCA. As an immediate consequence of this, FDI could become erroneous. IPCA, an improved version of PCA, simultaneously estimates the constraint model $\boldsymbol{A}_I$

with exact order of residual subspace and covariance matrix of measurement errors $\mathbf{\Sigma}_{\varepsilon}$. To perform these functions, IPCA relies upon the concept of scaling of the data. However, the constraint model developed from either of these methods is expected to work successfully for any data holding the same correlations among the variables as exhibited by the training data.

For a well maintained process, faults more than one in number are very rare. However, the tests to detect the faults should be capable of detecting multiple faults. For detecting the faults, threshold tests like $k-$sigma and sequential probability ratio tests [128] are more popular due to their simplicity and ease of implementation. The outcomes of these threshold tests are fault occurrence time and fault identification and localization but they do not give any information regarding the magnitude of the fault. Therefore, these tests are not utilized in the applications where on-line fault correction is essential. Tests for single fault detection such as Global Test (GT) [85] and Measurement Test [3]; and Nodal Test [55] were proposed in the early years of development of FDI. A Generalized Likelihood Ratio (GLR) approach to the detection and estimation of jumps in linear systems was developed by Willsky and Jones [127]. Narasimhan and Mah developed GLR method for steady-state systems [63], which can identify multiple faults. Following these developments, Tong and Crowe illustrated the efficacy of Principal Component test in fault detection in their work [113]. In this thesis, an Iterative Principal Component Test (IPCT), which applies PCA on the measurement adjustments, has been proposed. In this thesis, FDI tests such as GLR method, Iterative Measurement Test (IMT) and IPCT have been considered alongwith DR scheme. Performance indices such as detection and identification rates are computed when each of these methods are used in combination with the steady-state DR. Indices such as average error reduction, average adjustments made to the variables as a result of DR are also computed. These indices are used not only for making a decision about the best suitable FDI scheme but also for finding the effectiveness of the entire DR based FDI.

Though the data-based models are very efficient for FDI, they are very sensitive to the operating mode of the plant [123]. For example, although the ion chambers are expected to give signals proportional to the core average flux, the signals of the 9 ion chambers for RRS and SDSs are seldom equal. Their outputs differ from each other due to differences in leakage flux at their respective locations, caused due to control rod shadowing effects. Also, the core power distribution could be unsymmetrical due to refuelling or xenon-induced spatial variations. Such regularly occurring variations are, of course, not to be treated as faults in ion chambers. Accordingly, the DR and FDI analysis should be made robust to such effects by proper tuning of PCA and IPCA algorithms. It is highly desirable to test the applicability of DR based FDI to different operating modes or transients of the reactor. The operating modes can be obtained either from real-time reactor or from a simulated process. The simulated process gives the wide-degree of flexibility in obtaining different operating transients representing the reactor behaviour. Based on this, effectiveness of the DR based FDI of ion chambers and VSPNDs of the AHWR can be carried out with their signal data simulated under various operating transients of the reactor. However, the simulation requires a dynamic model of the reactor obtained either through the first principles or through empirical modeling.

AHWR, being a large reactor, necessitates a space-time kinetics modeling for accurate determination of the space-dependent flux behaviour. Some of the modeling methods are finite difference methods, coarse mesh methods, nodal methods, space-time factorization methods, modal and synthesis methods, transverse integrated nodal methods and time integration methods [19]. Out of them nodal methods are promising with respect to their formulations in terms of differential equations and computation time, when they are used for control system studies. In this work, a nodal method aiming at finding a model of reasonable order, has been adopted for AHWR so as to represent the neutronic sensor signals as a function of local neutron flux [19].

The large reactor spatial domain is partitioned into a large number of meshes. The nodal fluxes are reconstructed [27] so that they represent the flux values in the representative meshes. The fluxes at the VSPNDs are then simulated using the diffusion coefficient weighted homogenization [23] of fluxes of the surrounding fictitious mesh boxes. As the ion chambers sense the leakage flux from the nearby nodes, simulation of their signals is carried out using a formulation based on the albedo boundary condition [19]. The simulated flux values at the ion chambers and VSPNDs are compared with those obtained from the quasi-static modeling of the static finite difference method to validate the nodal model.

Simulations based on space-time kinetics modeling, in four representative situations of reactor operation are considered. In one of the cases, the reactor power is assumed to be unregulated while the signal to RRs is varied from the steady-state value, in a preprogrammed manner. The other three cases correspond to typical operational situations in which the reactor power is regulated by means of the RRS, but either the demand power is changed or one coolant channel is being refuelled on-power, or the closed loop system is experiencing xenon-induced spatial instability. In all these cases, signals of all the 9 ion chambers belonging to regulating and protection systems are generated and in order to represent realistic behaviour, a noise having Gaussian distribution and standard deviation of 0.2933 mA has been added to the computed values. The added noise is equivalent to 2% random fluctuations around the full power steady-state. Some of these data are used in the PCA and IPCA algorithms to obtain the constraint model and standard deviation of measurement errors, while the remaining data are used for evaluation of the performance of the proposed DR and FDI schemes. However, IPCA, owing to its mathematical advancements, is preferred over PCA in the control of the reactor. Faults (some deviations) are sequentially introduced in the signals of some of the ion chambers and the effectiveness of the DR based FDI is established. Among different FDI techniques considered, IPCT is proven to be efficient in terms of the chosen performance indices, hence it is recommended to be used with the DR. The constraint model developed under one transient is proven effective to be used for the data of other transients provided the steady-state relationships are not violated. The implementation of the proposed IPCA based scheme for DR and FDI in the control of the reactor has been elaborated.

For the case of VSPNDs, same levels of noise as considered for the case of ion chambers are considered. VSPND data is generated during some of the above four representative situations. Generally, in a plant with many detectors, the constraint model developed on all the detectors is not consistent as a result of varying correlation patterns among the detector signals in the course of a transient. This situation leads to infeasible performances from DR and FDI schemes reflected in their indices. The control systems deployed in nuclear reactors can keep the global power at the desired set poin, however it and might fail to maintain the desired flux shape within the core. This leads to inconsistent algebraic relationships among the VSPND signals, which are strong functions of the local core flux. This prohibits the use of steady-state DR coupled with FDI for VSPNDs. However, even during the transients, significant performances can be extracted from the DR and FDI schemes, when applied on the set of VSPNDs with consistent correlation structures.

Clustering is the task of grouping the most similar objects or variables into a group or cluster such that intra-cluster variables are more similar to each other than to those in other clusters. Hence, the VSPNDs may be grouped into different clusters based on their correlations. DR and FDI analyses performed on each cluster are expected to be effective. The $k-$means algorithm [53] in non-hierarchical or centroid-based clustering is the mostly used method by the practising engineers [81]. In applications like FDI, it is the variables, rather than the items that must be grouped. In this thesis, the $k-$means algorithm is used for clustering the VSPNDs. DR and FDI analyses are performed on one of the clusters with its own constraint model, when faults are introduced in some of the VSPNDs. When the signals possess similar algebraic relationships under the action of spatial control, the constraint model of the cluster remains the same and can be used for DR and FDI of other data sets.

When the reactor is in transient state, since the steady-state relations are no longer trusted for FDI, dynamic models of the ion chambers and VSPNDs can be used for the detection of at least abrupt jumps (additive biases) in the signals arising from faults. Model based FDI techniques possess inherent capability of fault detection, even during transients, though their performance would be strongly dependent on the accuracy of the model [50]. To overcome the limitations of threshold testing based FDI schemes, a GLR based FDI scheme relying on the temporal redundancy in the data is proposed in [127, 128]. This scheme gives all the information regarding the fault, *i.e.*, fault occurrence time, fault location and magnitude of the fault, but at the cost of increased computational effort. Therefore, it is further modified [64] to reduce its computational burden so that it can be used for on-line FDI and fault compensation and correction efficiently. The on-line implementation of GLR based FDI scheme requires prior knowledge of probable fault modes (state jump, state step, sensor jump, sensor step, hard-over actuator or sensor, increased actuator or sensor noise, dynamic shift *etc.*) and associated fault signature matrices of the system for which it is designed [64, 127, 128]. A Kalman filter based dynamic compensation for the VSPNDs with unknown input has been evolved such that it also performs FDI using GLR method. In other words, a hybrid scheme can be developed which can dynamically compensate the VSPND signal for promptness; minimize the random errors through Kalman filter; and perform detection and diagnosis of the faults with GLR method. The efficacy of the method has been validated from simulations.

Some important contributions of the thesis are as follows:

1. The space-time kinetics model of the AHWR has been extended to include the determination of the signals from the ion chambers and VSPNDs whose responses are the functions of the neutron fluxes at their respective locations.

2. The effectiveness of the DR based scheme for FDI has been established under various simulated operating transients, which the reactors generally undergo. It was revealed that the constraints model developed during one transient has successfully worked for other transients, provided the reactor is in steady-state. This kind of procedure for knowing the accuracy characteristics of the neutron flux detectors is the first attempt in the field.

3. The IPCT, which is a modified version of the conventional principal component test, has been proposed in this work. This test proved to be efficient among its counterparts.

4. The GLR based scheme that simultaneously compensates for the slow response of the VSPNDs and performs FDI is also proposed in this work.

The conclusions from the work are:

- The effectiveness of the DR based scheme for the FDI of ion chambers and VSPNDs of AHWR has been established. Constraint models developed from time-series data of the detectors during an operating mode of the reactor have been used for other operating modes involving similar correlation pattern among the signals. The scheme exhibited desired performances in all cases, when the constraint relations among the signals do not vary.

- For VSPNDs, clustering-based DR and FDI has been found to be efficient.

- The IPCT, which is the outcome of this thesis, also proved to be efficient. It can be used for the FDI of the real-time systems.

- The model based FDI based on the Kalman filter also performed well. The scheme was found to compensate the slow response of the VSPNDs, while successfully aiding in the FDI. This unique feature of the scheme may be of future use in the field of control systems.

Possible future extensions of the work would be:

- An Augmented State Kalman Filter, which uses the spatial relationships alongwith the dynamic models of the VSPNDs, can also be developed for FDI.

- Based on the dynamic model of the AHWR, a Dynamic Data Reconciliation scheme for the FDI of the detectors can also be implemented in future.

List of Figures

List of Tables

Acronyms

AA	Average Adjustments
AER	Average Error Reduction
AHWR	Advanced Heavy Water Reactor
CVA	Canonical Variate Analysis
DR	Data Reconciliation
FCT	Fault Confirmation Test
FDD	Fault Detection and Diagnosis
FDI	Fault Detection and Isolation
FDT	Fault Detection Test
FDM	Finite Difference Method
FRM	Flux Reconstruction Method
FP	Full Power
GLR	Generalized Likelihood Ratio
GT	Global Test
ICDH	In-core Detector Housing
IMT	Iterative Measurement Test
IPCA	Iterative Principal Component Analysis
IPCT	Iterative Principal Component Test
LTI	Linear Time Invariant
ODR	Overall Detection Rate
OP	Overall Power
PCA	Principal Component Analysis
PHWR	Pressurized Heavy Water Reactor
PLS	Partial Least Squares
pu	Per unit
RR	Regulating Rod
RRS	Reactor Regulating System
SDS	Shut-Down System
SPND	Self-Powered Neutron Detector
VSPND	Vanadium Self-Powered Neutron Detector
WT	Whiteness Test

Nomenclature

$\widetilde{a}$	Hypothetical extrapolated distance
$\boldsymbol{a}$	Vector of measurement adjustments
A_{hk}	Area of interface between nodes h and k
$\boldsymbol{A}$	Constraint matrix of all variables
$\boldsymbol{A}^{(i)}$	System matrix in continuous domain for a VSPND i
$\boldsymbol{A}_1$	Columns of $\boldsymbol{A}$ corresponding to measured variables
$\boldsymbol{A}_2$	Columns of $\boldsymbol{A}$ corresponding to unmeasured variables
$\boldsymbol{A}_I$	Constraint model obtained from IPCA
$\boldsymbol{A}_P$	Constraint model obtained from PCA
b	Magnitude of additive bias
$\boldsymbol{c}^{(i)}$	Measurement matrix for a VSPND i
C	Set of all faulty measurements
C_i	Concentration of delayed neutron precursors in group-i
$\boldsymbol{C}$	Output matrix in state-space formulation
$\boldsymbol{d}$	Vector of IMT test statistics
D_g	Diffusion coefficient for energy group-g
$\boldsymbol{e}_i$	Unit vector with a 1 at position i
f_p	Prompt fraction of output signal of VSPND

f_q	Delayed fraction of output signal of VSPND
g	Number of faulty detectors
G_{IC}	Product of ion chamber sensitivity and its amplifier gain
G_{RR}	A constant for RR drive
G_V	Product of VSPND sensitivity and its amplifier gain
$\boldsymbol{G}_{k,\theta}$	Fault signature matrix at instant k for a bias at θ
$\boldsymbol{G}_x$	Reduced constraint matrix
H_0	Null hypothesis
H_1	Alternative hypothesis
i_{IC}	Current of linear amplifier of an ion chamber
i_V	Current of linear amplifier of a VSPND
I	Iodine concentration
$I^{(i)}$	Output signal of a VSPND i
$\boldsymbol{I}$	Identity matrix
J_u	Neutron current density in the direction-u
$\boldsymbol{J}_{k,\theta}$	Matrix giving the relation between state corrections and bias at instant k for a bias at θ
k	Discrete time instant
K_h	Multiplication factor in node-h
$\boldsymbol{K}$	Kalman gain
l	Prompt neutron life-time
L	Diffusion length
$\boldsymbol{L}$	The Cholesky factor of $\boldsymbol{\Sigma}_\varepsilon$
$\bar{m}$	Number of states in state-space formulation
m	Number of constraint equations or model order

m_d	Total number of precursors groups
$\boldsymbol{M}$	Diagonal matrix of ordered set of singular values
n	Total number of measured variables
n_h	Number of measurements in T
N	Total number of observations
N_{RR}	Number of RRs available for control
N_f	Number of observations in the time window for fault confirmation
N_g	Number of observations during a fault scenario
N_w	Number of observations in the window for whiteness test
$\bar{N}_h$	Number of all the neighbouring nodes to node-h
p	Number of healthy signals treated as measured variables
$\bar{p}$	Number of inputs in state-space formulation
$\boldsymbol{p}_i$	Eigenvector i
P_l	%-in position of the l^{th} RR
$\boldsymbol{P}$	Projection matrix
q	Number of faulty signals treated as unmeasured variables
$\boldsymbol{Q}$	Q in $Q-R$ factorization of unmeasured signals
r_u	Rank of $\boldsymbol{A}_2$
$\boldsymbol{r}$	Vector of residuals
R	Number of nodes in reflector region
$\boldsymbol{R}$	R in $Q-R$ factorization of unmeasured signals
$s_{k-\theta}$	Step function for all integers $k \geq \theta$
S	Set of all healthy measurements
$\boldsymbol{S_v}$	Sensitivity of VSPND

t	Time variable
T	Set of all measurements in reduced DR problem
$\bar{\boldsymbol{u}}$	Input vector in state-space formulation
$\boldsymbol{u}$	Vector of faulty measurements
$\boldsymbol{U}$	Matrix of ordered set of eigenvectors
$\boldsymbol{U}_1$	Eigenvectors of principal component subspace
$\boldsymbol{U}_2$	Eigenvectors of residual subspace
V_i	VSPND with number i, $i = 1, ..., 200$
$\bar{V}$	Volume
$\boldsymbol{V}$	Matrix of right singular vectors in singular value decomposition
$\boldsymbol{w}$	Process noise vector
$\bar{\boldsymbol{x}}$	State vector
$\bar{\boldsymbol{x}}^{(i)}$	State vector for a VSPND i
$\boldsymbol{x}$	Vector of true values of measured variables
$\dot{\bar{\boldsymbol{x}}}$	Time derivative of $\bar{\boldsymbol{x}}$
$\hat{\boldsymbol{x}}$	Estimated value of $\boldsymbol{x}$
X	Xenon concentration
y	Scalar measurement
$\boldsymbol{y}$	Measurement vector
$\boldsymbol{Y}$	Measurement data matrix
$\boldsymbol{Y}_s$	Measurement data matrix scaled in IPCA algorithm
Z	Number of nodes in core region
Z_i	Layer i in an ICDH
$\bar{Z}_i$	Principal component i

α	Level of significance for false alarms, which is 0.05
$\bar{\beta}$	Modified level of significance for IMT
β	Effective fraction of delayed neutrons
β_i	Fraction of delayed neutrons of i^{th} group precursors
$\delta_{k,l}$	Kronecker delta which turns unity when $k = l$
η	State variable in in state-space formulation of VSPND
γ	Fractional yield
$\mathbf{\Gamma}$	Input matrix in discrete domain
λ_i	Decay constant of i^{th} group precursors
μ_i	Eigenvalue i
ν	Mean number of fission neutrons
ω	Coupling coefficient between nodes
ϕ	One-group neutron flux
ϕ_C	Per-unit value of the neutron flux
ϕ_{IC}	Per-unit value of the neutron flux at the ion chamber location
ϕ_V	Per-unit value of the neutron flux at the VSPND location
ϕ_g	Neutron flux in energy group-g
ψ	FCT statistic
$\mathbf{\Phi}$	State transition matrix
$\mathbf{\Pi}$	Permutation matrix
ρ_h	Reactivity in node-h
$\boldsymbol{\sigma}$	Vector of standard deviations
σ	Microscopic cross section
σ_0	Variance of measurement adjustments from DR

σ_j	Auto-covariance of measurement adjustments with lag index j from DR
Σ	Macroscopic cross section
Σ_{12}	Scattering cross section from group-1 to group-2
Σ_{21}	Scattering cross section from group-2 to group-1
Σ_{ag}	Absorption cross section for energy group-g
Σ_{fg}	Fission cross section for energy group-g
$\boldsymbol{\Sigma}$	Covariance matrix
$\hat{\theta}$	Estimated instant of bias occurrence
τ	Time constant of ${}^{52}_{23}V$
θ	Instant of bias occurrence
$\boldsymbol{\varepsilon}$	Vector of random measurement errors
υ	Mean velocity of neutrons
υ_g	Mean velocity of neutrons in energy group-g
φ	FDT statistic
ϑ_l	Control signal applied to the l^{th} RR drive
$\bar{\boldsymbol{\xi}}$	Set of innovations in a time window of N_f samples
$\boldsymbol{\xi}$	Innovation vector
ζ	State variable in Kalman filter

Operations

$\boldsymbol{A}^{-1}$	Inverse of A
$\boldsymbol{A}^T$	Transpose of A

Superscripts

0	Initial value
-1	Inverse Operator

(c)	Corrected value
(f)	Component corresponding to fault condition
(i)	Corresponding to VSPND $V_i,\ i = 1, ..., 200$
(h)	Component corresponding to healthy condition
pu	per-unit value
T	Transpose Operator
κ	Iteration index

Subscripts

1	Fast group
2	Slow group
a	Absorption
$\boldsymbol{a}$	Measurement adjustments
C	Core average value
$\boldsymbol{d}$	Statistics with maximal power in IMT
f	Fission
g	Energy group
$i\|j$	Conditional estimate at instant i, when measurements up to instant j are available
I	Iodine
IC	Ion chamber
k	Sampling instant k in discrete domain
p	Healthy measurements
$\boldsymbol{p}$	Error in the state estimate
r_u	Rank of unmeasured signals
$\boldsymbol{r}$	Constraint residuals

u Unmeasured variables

u_1 Independent unmeasured signals

u_2 Dependent unmeasured signals

x True values

X Xenon

y Measured values

$\boldsymbol{\varepsilon}$ Measurement errors

$\boldsymbol{\xi}$ Innovations

Other Notations

$\mathrm{cov}[a, b]$ Covariance of variables a and b

$\exp\{.\}$ Exponential function

$\mathrm{E}[.]$ Expected value

$f(.)$ Probability density function

$\mathcal{N}(.)$ Normal or Gaussian distribution

$\mathrm{Pr}\{.\}$ Probability

$\mathbb{R}$ Real space

$\mathrm{svd}(.)$ Singular value decomposition

sup Supremum value

$\lambda(.)$ Generalized likelihood ratio

Chapter 1

Introduction

A system is a meaningful interconnection of many subsystems or components. For improving the performance and reliability of controlled systems, a set of measurement signals of potential interest are used for feedback control, monitoring, protection and estimation. However, in general, a measurement represents the true value to certain limited precision. In the process of approximation, errors are always inevitable though the measuring instruments are precisely calibrated to represent the true values.

The signals might always contain high frequency components called random errors, contributed by slight variations in operating conditions of the components and other probabilistic phenomenon. As the name suggests they are random in nature as neither the sign nor the magnitude can be estimated with certainty. Random errors cannot be completely eliminated but their effects can be reduced considerably with the use of filtering techniques and also with the use of their statistical properties as each outcome of the random error has a certain probability of occurrence. On the other hand, unpermitted deviations may also occasionally arise in one or more of the characteristic properties of the components from the acceptable, usual and standard conditions. These deviations are termed as 'faults' [34]. Faults, being either incipient or abrupt changes in the parameters of the components, can appear due to either external or internal causes. External causes can be environmental influences on the components. Internal causes may include miscalibration, wear and tear, overheating, leaks, ageing and poor maintenance *etc.* Faults in system or process components including sensors, if not detected and diagnosed, reduce safety margins, establish the need for maintenance activities, endanger the system reliability, activate safety systems and cause operational upsets. They can also cause off-specification production, increased operating costs, unnecessary line shut-downs, and detrimental environmental impacts. Usually faults can be detected from their reflections in the signals associated with the system. However, they should be detected early before serious consequences.

The total error which is the difference between the true and the measurement values is contributed by both random errors and faults. In case of safety-critical control systems, apart from random error filtering, there is an intense need for timely detecting and locating the faults. Three Mile Island and Chernobyl accidents are the best examples demonstrating this need. Human operator should be timely provided with the information regarding the faults and there should not be any operator error in taking the safety actions. However, taking random errors and faults into consideration, it can be said that a reliable system that automatically takes care of operators' duties is of utmost importance. Some data processing techniques may be used in such a system for achieving this objective. In the early ages, analog and digital filters were designed for dealing with random errors. Faults were dealt by limit checking in which the measured data and their rate of change are checked to know whether they are in prescribed limits. Traditionally, univariate Statistical Process Control tests are also applied on individual variables for reducing the effects of faults. However, these tests are applied on each individual measurements and not on all measurements together, hence, the interrelationships among the variables are not exploited for improving the accuracy.

The problem of detecting and finding the location of faults is referred to as Fault Detection and Isolation (FDI) in which fault detection is followed by fault isolation. A Fault Detection and Diagnosis (FDD) involves, alongwith FDI, also the determination of magnitudes and sources of faults. It may be noted that hereinafter the term 'FDI' is predominantly used, when generic concepts such as fault detection, isolation and estimation of magnitude and sources of faults are referred. It may also be noted that the use of the term 'FDI' is continued for the techniques capable of finding the magnitude of the fault, for the sake of alleviating the switching between the terminologies (FDI and FDD). FDI is regarded as the number one problem that needs to be solved in many industries such as petrochemical, pharmaceutical, power and so on, as it minimizes the losses due to accidents [121].

Significant development in the field of process automation in the last four decades led to improved product quality with increased economy. Process automation allows to obtain measurement data at high frequency for the purposes of control, protection and optimization. It significantly avoids errors in manual recording. The so obtained large measurement database can be exploited for further improvement in the accuracy of the data with the help of analytical redundancy. A simplified scheme of process automation can be seen in Fig. 1.1. Process automation integrates the tasks of control and supervision into the process operation. Control systems are applied to make the process meet the specified requirements. They may also involve random error filtering. Supervision includes monitoring the system for abnormal operations; detection of faults in one or more components, finding the locations, magnitudes and sources of faults. The supervision system obviates the human operator from the process, hence erroneous counteractions with respect to partial shut-downs of the process and re-scheduling the feedback control, can be avoided in case of operator errors. For example, after a fault is detected and isolated by the FDI scheme, the supervision scheme reconfigures the feedback control action by replacing the faulty feedback components, *i.e.*, either sensors or actuators by their substitutes, which are the duplicate devices or the techniques for performing the similar operations. If the faulty component is a sensor, estimate of its

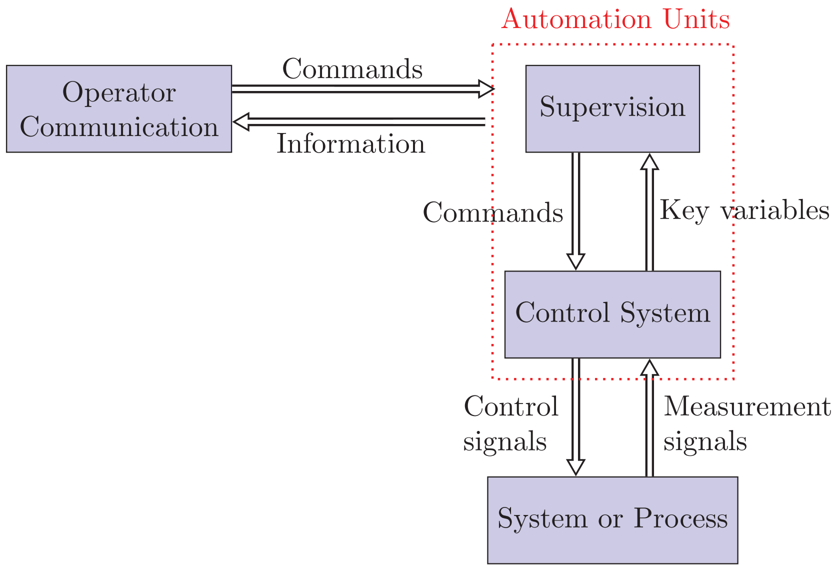

Figure 1.1: A simplified scheme of process automation [34].

signal is used for reconfiguration; and if the actuator is faulty, an identical and healthy or a substitute actuator is used. Therefore, the supervision scheme should encompass most reliable FDI systems for right counteractions in case of faults.

An FDI scheme is realized by either hardware redundancy or analytical redundancy. In hardware redundancy, many similar components instead of one and performing the same function are deployed. Their responses are checked for consistency and the components not obeying the consistency are faulty. However, the fault detection becomes ambiguous when two or more signals are drifting in the same direction. In addition, reconstruction of the redundant signals is also not possible. The major drawbacks of hardware redundancy are the extra equipment and maintenance cost, as well as the additional space required to accommodate the equipment. In analytical redundancy, more information is embedded into the supervision scheme in the form of either quantitative models (mathematical models or interrelationships among the variables) or qualitative models. These models facilitate in more efficient FDI. Analytical redundancy helps also in improving the accuracy by reconstruction of the redundant signals. So, it is preferable to employ analytical redundancy alongwith the hardware redundancy for efficient control, monitoring (supervision) and protection systems in safety-critical processes.

The FDI methods can either be quantitative model-based, qualitative model-based or process history-based, as will be explained in Section 2.1. In all these methods, the FDI system, based on analytical redundancy, generates discrepancies between the normal operation of the system and the actual behaviour. These discrepancies function as features to recognise the existence of faults or anomalies responsible for deviations. A suitable fault testing scheme, which tests the features, needs to be chosen based on the FDI technique adopted among the above classification, i.e., either quantitative model-based, qualitative model-based or process history-based methods. This scheme should mainly possess the characteristics such as quick detection of faults, minimum misclassification, robustness to noise and uncertainty, and efficient computational ability. The criterion for selection of a testing scheme, out of many, may be the fraction of the erroneous detection or identification of the faults. A test leading to less erroneous detection or identification of faults is to be selected. It should be noted that quantitative model-based and process history-based methods only are in the scope of this thesis.

Data Reconciliation (DR) is a technique based on analytical redundancy and adjusts the measurements such that the adjusted measurements satisfy the interrelations among the variables or a constraint model obtained either with quantitative model-based or process history-based methods. The adjusted measurements are more accurate than the original measurements, provided that there are no faults in the variables. However, if faults are present, erroneous adjustments are made to the variables as a result of faults. If the process is in steady-state, the reconciliation of the measurements alone is sufficient to bring enhanced accuracy. On the other hand, if the state of the process is dynamic, the reconciliation has to be done based on the dynamic model of the process. It should be noted that irrespective of the type of DR technique (whether static or dynamic), FDI techniques should function in a coordinative manner with DR for improving the accuracy of the measurements.

When compared to other industries listed earlier, *viz.*, petrochemical, pharmaceutical, power and so on, FDI in nuclear reactors is a more crucial task, since they have stringent requirements for safety and economy [50]. In reactors, neutrons are absorbed in the fissile nuclei present in the core and lead to the birth of new neutrons. The ratio of neutrons generated to those absorbed in the preceding generation is called multiplication factor. The relative change in the multiplication factor is called the reactivity, denoted by ρ. The reactor is called sub-critical, critical or super-critical respectively, when the ρ has the values lesser than, equal to or greater than 1. Reactor power can be raised by increasing the value of ρ and lowered by decreasing the value of ρ. The reactor power typically ranges from $1 \times 10^{-9}\%$ Full Power (FP) to 120% FP. However, being an unstable system, the nuclear reactor may become super-critical at any stage right from the reactor start-up. If it is left uncontrolled, the reactor may reach dangerous operating conditions posing threat to the safety and environment. However, the instantaneous fission power generated in the reactor is readily known from neutron flux, which is the number of neutrons per unit volume moving with a certain speed or number of neutrons travelling past a surface of unit area per second. Since a single detector cannot cover entire power range of the reactor (of the order of 10^{14}), different detectors are envisaged for the source range, intermediate range and power range. These ranges vary typically from $1 \times 10^{-9}\%$ FP to $1 \times 10^{-3}\%$ FP, $1 \times 10^{-5}\%$ FP to $1 \times 10\%$ FP and 1% FP to 120% FP respectively, ensuring sufficient overlap between successive ranges. Again, a large number of neutron flux detectors are used in each range.

In large reactors, the detectors for power range are placed both inside and outside the core for better monitoring and protection functions. The ex-core detectors, which are outside the core, sense the leakage flux from the core which is proportional to the core average flux or global flux. The ex-core measurement information is used not only for performing control of the thermal power but also for different monitoring and protection functions. Apart from this, functions such as monitoring spatial flux transients, flow changes in coolant channels, reactivity device movements and ensuring that peaking factors are within analyzed safety limits, are also required in large reactors. These functions are performed from the information about axial, azimuthal and radial flux distributions obtained through an in-core detectors (those placed within the core) -based flux mapping system.

Ex-core detectors are calibrated based on the steam flow rate. Ion chambers are used in major reactors because of their insensitivity to applied voltage, proportionality to the energy deposited and less vulnerability to gas deterioration. Faults in ion chambers are due to factors such as humidity, gas leakage, operating pressure, temperature, vibration and mechanical shocks, and degradation of the insulation cables [1, 44]. In addition to occasional faults, the ion chamber signals also contain random errors, contributed by slight variations in operating conditions of the ion chambers and probabilistic nature of the neutron interactions with the detector materials. Coming to in-core detector applications, Self-Powered Neutron Detectors (SPNDs) are more prevalent because of their small size, and requirement of simple electronics. Accurate signals from SPNDs, which are placed at strategic locations within the core, can help in successful implementation of both the flux mapping systems and flux tilt control. However, these SPND signals are corrupted by random noise because of the probabilistic nature of the neutron flux hitting the emitter material of the SPNDs and other factors related to operation of SPNDs [115]. Apart from random errors, these SPNDs might also develop failures. Failures in SPNDs can be broadly classified as hard failures (complete loss of signal, *e.g.*, due to sheath failure) and soft failures or faults (signal changes gradually or suddenly by a relatively small amount). Hard failures in SPNDs can be easily identified and those SPNDs can be replaced. However, faults are difficult to detect since they produce degraded signals over a period of time, because of changes in the parameters, which lead to changes in the sensitivity; improper calibration; and systematic biases. These factors reflect as faults in their output signals from the respective nominal values. Apart from random errors and faults, the response of SPNDs is significantly delayed because of the inherent dynamics when materials like Vanadium are used as emitter. The Vanadium SPNDs (VSPNDs) are generally preferred because of better life span, simple response characteristics, ease of handling the replaced VSPNDs *etc.* The delayed nature can be compensated with the use of a dynamic compensator, which uses the dynamic model of the VSPNDs.

Random errors and faults in ion chambers may lead to erroneous inferences about the operation of the reactor. This in turn would cause degradations in the performances from control, monitoring and protection systems. Similarly, they make the SPND signals inaccurate, which results in degraded performance of flux mapping and flux tilt control systems. Therefore, the ion chamber and SPND signals should be very much reliable such that random errors are filtered and any faults are timely identified.

For the detection of incipient faults in ion chambers and SPNDs, a dynamic model-based FDI can be implemented in which all the dynamics of the reactor and the detectors are included. Estimation of signals may be performed with the help of a Kalman filter. This formulation of the problem is referred to as the dynamic DR-based FDI since it uses the dynamic models. For the successful implementation of this scheme, the dynamic models should be so accurate that even the faults of small magnitudes are timely detected. However, it is extremely difficult to develop such an accurate model when the complexity of the model increases as in the case of large reactors.

In this context, considering the limitations of model-based FDI in nuclear reactors, the role of a data-based FDI system not relying on the dynamic models is very much significant. When the reactor is in steady-state, a steady-state DR scheme can be implemented on the detector signals. This scheme can handle both the incipient and abrupt faults in the ion chambers and SPNDs. This scheme may be of great use for FDI of ion chambers, since ion chambers provide gross information on the core average flux and are least affected by the local flux variations in the core. Steady-state algebraic relations (constraint models) among ion chamber signals can be obtained, which can further be used for DR and FDI.

Generally, in a plant with many detectors, the constraint model developed on all the detectors is not consistent as a result of varying correlation patterns among the detector signals in the course of a transient. This situation leads to infeasible performances from DR and FDI schemes reflected in their indices. The control systems deployed in nuclear reactors maintain the global power at the desired set point and the operating flux close to the desired flux shape within the core, but during transients, the operating flux might deviate from the desired flux shape for several hours. This leads to inconsistent algebraic relationships among the SPND signals, which are strong functions of the local core flux. This prohibits the use of steady-state DR coupled with FDI for SPNDs. However, even during the transients, significant performances can be extracted from the DR and FDI schemes, when applied on the set of SPNDs with consistent correlation structures. Hence, the SPNDs may be grouped into different clusters based on their correlations such that DR and FDI analyses performed on each cluster are effective.

However, one drawback of the process history-based models is that they are very sensitive to the operating mode of the plant. It is highly desirable to test their applicability to different operating modes of the plant [123]. The operating modes can be obtained either from real-time process or from a simulated process. The simulated process gives the wide-degree of flexibility in obtaining different operating modes representing the system behaviour. The simulation requires a dynamic model of the process obtained either through the first principles or through empirical modeling. In the perspective of FDI of neutron detectors of a nuclear reactor, as considered in this thesis, the dynamic model should also include the determination of signals from the neutron detectors. Once the reactor behaviour under different transients is simulated with the help of such a model, covariance models can be built from the operating data under healthy conditions for facilitating FDI during actual run of the reactor.

In this thesis, the FDI schemes have been tested on the neutron detectors of the Advanced Heavy Water Reactor (AHWR) [103]. AHWR is a vertical, pressure tube type, heavy water moderated and boiling light water cooled natural circulation reactor, designed to generate 920 MW (thermal) power. AHWR core is very large in radial dimensions as a result of which, situations such as flux-tilt and variation of the transient flux shape are possible. Hence, ex-core ion chambers and in-core VSPNDs in a large number are used for control, monitoring and protection of the reactor. A detailed (non-linear) mathematical model of AHWR is developed for the simulation of measurement data from the ion chambers and VSPNDs. The effectiveness of the DR has been established through simulations performed on the simulated measurement data with the help of different FDI schemes capable of detecting multiple faults.

However, when the reactor is in transient state, since the steady-state relations are no longer trusted for FDI, dynamic models of the ion chambers and VSPNDs can be used for the detection of atleast the abrupt jumps (additive biases) in the signals arising from faults. This later scheme can be of use with VSPNDs. Using the dynamic models of VSPNDs, a random error filtering technique coupled with an FDI scheme can be developed, which also compensates for the slow response of the VSPNDs. A hybrid scheme, which dynamically compensates the VSPND signal for promptness; minimizes the random errors through Kalman filter; performs FDI; and corrects the faulty measurements on-line has also been proposed in this thesis. The performance of the proposed strategy is established through simulations using the mathematical model of AHWR.

Note that the steady-state DR and FDI; and Kalman filter-based FDI in this thesis are performed based on sampled data since the controllers and protection systems in modern nuclear reactors are based on digital or discrete-time control theory. Hence, a discrete-time, as opposed to a continuous-time, Linear Time-Invariant (LTI) system also has been considered for the Kalman filter-based FDI.

Objectives of the Thesis

In large reactors like AHWR, there is an adequate degree of hardware redundancy in the neutron detectors to ensure that faults do not hamper the intended functionality. For example, each of the control, monitoring and protection systems are provided with more than two ion chambers and the signal that deviates considerably from the signals of other detectors is rejected. As there are redundant detectors, analytical redundancy among these detectors can be derived for the purpose of cross-checking of the data of the detectors or to continuously monitor the detectors for occurrence of faults and to isolate the faulty reading. The main objectives of the thesis are:

- to develop a mathematical model of AHWR for the simulation of measurement data of the neutron detectors as this data helps in the FDI of the detectors. This is required since the applicability of constraint models is affected by the operating mode of the reactor. For example, ion chamber signals may considerably differ from each other during occurrence of flux-tilt in the reactor.

- to work out a best FDI scheme capable of detecting multiple faults.

- to investigate the effectiveness of the steady-state DR scheme for the FDI of both the ex-core and in-core neutron detectors of AHWR under different operating transients of the reactor.

- to examine the effectiveness of DR-based FDI when applied to a cluster of VSPNDs with consistent correlation. This is important, since the constraint model developed on all the VSPNDs as a whole may not be consistent while the models developed on different groups of VSPNDs may be consistent during various operating transients of the reactor.

- to test the performance of the Kalman filter-based FDI of VSPNDs.

Contributions of the Thesis

The contributions of the thesis are as follows:

1. The space-time kinetics model of the AHWR has been extended to include the determination of the signals from the ion chambers and VSPNDs whose responses are the functions of the neutron fluxes at their respective locations.

2. The effectiveness of the DR-based scheme for FDI has been established under various simulated operating transients, which the reactors generally undergo. It was revealed that the constraint model developed during one transient has successfully worked for other transients, provided the reactor is in steady-state. This kind of procedure for knowing the accuracy characteristics of the neutron flux detectors is the first attempt in the field.

3. The IPCT, a modified version of the conventional Principal Component test, has been proposed in this work. This test proved to be efficient among its counterparts.

4. A scheme that simultaneously compensates for the slow response of the VSPNDs and performs FDI is also proposed in this work. This scheme also corrects the signals for faults online.

The developed techniques are of use to the nuclear power sector and any other field interested in the sensor fault detection.

Organisation of the Thesis

The rest of the thesis is organised as follows. Chapter 2 presents the literature survey on fundamental FDI methods, DR, FDI tests, data driven methods for constraint model development and FDI, clustering of the data, modeling of the AHWR and model-based FDI. It may be noted that Chapter 2 is aimed at the techniques that are of use in DR-based FDI and Kalman filter-based FDI. In Chapter 3, general approaches for the data driven modeling, data reconciliation and FDI techniques are presented. Chapter 4 gives the detailed modeling of the AHWR; principle of operation, constructional details, fault modes and locations of both ex-core ion chambers and in-core VSPNDs; and methods for the generation of signals from these ion chambers and VSPNDs. In Chapter 5, the results of the steady-state DR-based FDI scheme are presented when applied on ion chambers and VSPNDs of AHWR. In Chapter 6, a model-based scheme has been proposed for the simultaneous response time improvement and the FDI. Chapter 7 draws the important conclusions from the work and presents the future scope.

Chapter 2

Literature Survey

This chapter presents some of the literature on various key concepts involved in the solution for FDI of ion chambers and VSPNDs. The survey includes fundamental FDI methods, DR, data driven modeling techniques, FDI tests that are suitable to be used with DR, clustering of the data, modeling of nuclear reactors and model-based FDI for VSPNDs. However, the survey is not intended to be exhaustive.

2.1 Fundamental FDI Methods

This section provides an overview of FDI methods across the broad spectrum of approaches using analytical redundancy. FDI basically involves methods for detecting and diagnosing the faults. There are different approaches for detecting and diagnosing the faults, the major difference being the knowledge used for formulating the diagnostics. All the FDI methods compare the actual measurements with the predicted measurements for the generation of features, which are thus used for the detection and diagnosis of faults. The diagnostic approaches differ from one another by the theory behind the 'prediction' of the measurements. They can be based either on *a priori* knowledge or empirical formulation. The approaches that use *a priori* knowledge are called as the model-based methods, and the latter are called as the process history-based methods in which case the models may not have any direct physical significance. The detailed classification of FDI approaches is shown in Fig. 2.1.

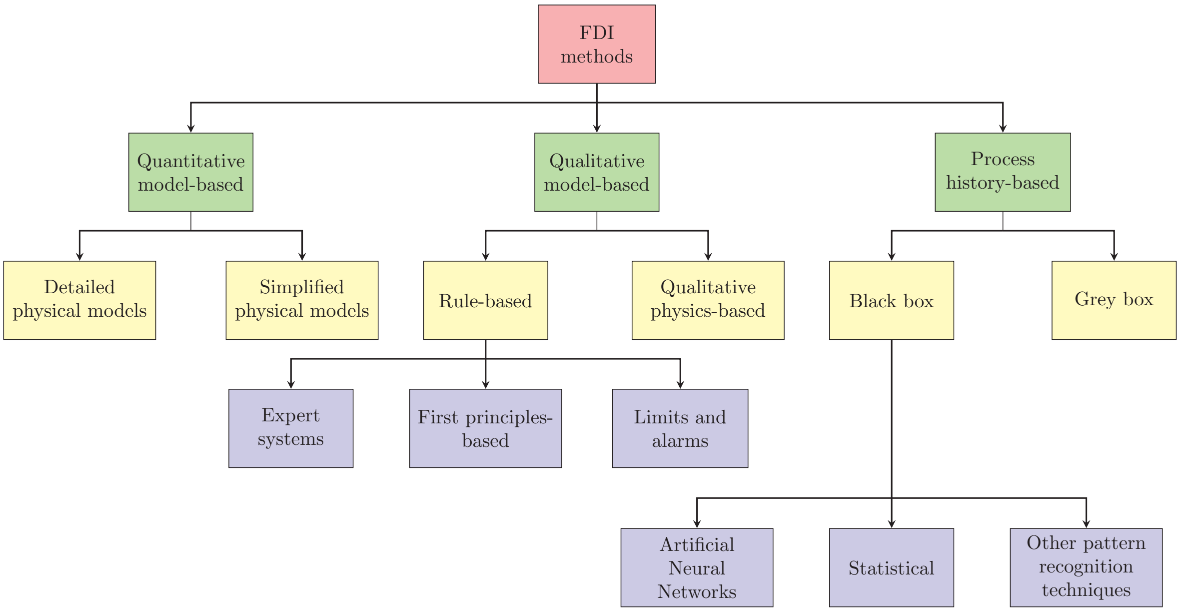

Figure 2.1: Classification of FDI methods

The model-based methods can again be classified as the quantitative model-based methods and qualitative model-based methods. Quantitative model-based methods depend on first-principles model or equations obtained after mathematical analysis of the process. They use either detailed or simplified models [59, 121]. In general, every physical system can be represented by a non-linear dynamic model, which is a detailed model. The simplified models can be represented by steady-state, linear dynamic models.

For the systems approximated by linear dynamic models, a Kalman filer algorithm [41, 58] can be implemented which performs FDI by estimating the 'state' of the system. Any discrepancy between the actual measurements and the estimated measurements (functions of estimated state) indicate the existence of faults. The Kalman filer works in the presence of uncertainties in the dynamic model and the measurements and it predicts and update the state estimates in a recursive manner. In other words, it uses only the present measurements and the previously calculated state and its uncertainty matrix; no additional past information is required. Extensions to the Kalman filter have also been developed, such as the Extended Kalman filter and the Unscented Kalman filter, which work on non-linear systems [39, 94].

Quantitative models have an advantage in modeling the transient behaviour of the systems more precisely than any other modeling technique. The estimation and the FDI of signals is most accurate, when the quantitative models are properly formulated. However, the formulation is not only complex and cumbersome but also computationally intensive. Their effectiveness reduces when the non-linear systems are approximated as linear systems. Modeling uncertainties also limit the application of these methods. In addition, model-based FDI schemes should be initially tuned for the detection and isolation of each anticipated fault. Any shortcoming in this process doesn't guarantee the detection of unexpected faults. In addition, these models should manage noises, disturbances and modeling uncertainties, for being effective. However, these problems may be overcome with powerful computational ability and linear nature of the process.

Qualitative models use qualitative relationships or knowledge bases to draw conclusions regarding the state of a system and its components [122]. Qualitative model-based methods include rule-based and qualitative physics-based systems. Rule-based systems may be categorized as those based on expert rules (human experience with the process is used to derive rules), rules derived from first principles, and those based on limit checks, which can be viewed as a limiting case of rule-based systems. In expert systems, computer programs mimic the cognitive behaviour of human experts who solve problems in a particular domain. The previous human experiences with the abnormalities can be used to generate if-then-else rules that relate a set of observations with specific causes. The programs contain such if-then-else rules and an inference engine, which searches through the knowledge base to derive conclusions. The set of these rules grows substantially with the behavioural complexity of the system. The expert systems have no understanding of the underlying physics of the system. This makes them fail for the cases in which there is a new condition not defined in the knowledge base [83]. However, the knowledge base can be updated with the experience newly encountered [84]. Rule-based systems based on first principles use reasoning about the cause and effect relationships. They aim at identifying functional changes, which resulted in malfunctioning of the process [15, 83, 120]. Fault tree analysis, which also needs a complete understanding of the system, can also be constructed by asking questions such as what could cause a hazard [25]. Qualitative physics, which only requires a nominal information about the process, employs a common sense reasoning [35, 42, 101]. The drawbacks of qualitative models are that (i) they are specific to a given system; (ii) difficulty to set-up and test the applicability of rules; and (iii) they depend on the expertise and knowledge of the developer.

Process history-based models employ empirical modeling based on input and output data from the plant [123]. However, output data is sufficient for the detection of faults in sensors. In these models, some transformations are performed on the data to obtain parameters or features for FDI. Process history-based models may be classified as black-box models when the features have no physical significance, and grey-box models that use first principles or engineering knowledge to specify the mathematical terms in the model, and the features have some physical significance. For black box models, various statistical and non-statistical methods are used to develop the relationship between inputs and outputs. Extensive survey of statistical methods is presented in Section 2.3. Non-statistical methods include artificial neural networks and other pattern-recognition methods. Examples of grey-box modeling techniques are linear or multiple linear regression carefully performed for retaining the physical significance of terms appearing in the models. Process history-based models are well suited to problems where there is abundant data and development of first principles model is not only complex but also involves non-realistic assumptions. The drawbacks are that these models cannot be used to extrapolate beyond the range of the training data, and are specific to the system for which they are trained. As stated in Chapter 1, quantitative model-based and process history-based methods only are in the scope of this thesis.

2.2 Data Reconciliation

DR technique is widely used in the field of chemical engineering. It was developed to improve the accuracy of measurements by reducing the effect of random errors. It makes use of a constraint model to obtain the reconciled estimates of signals, by adjusting the measurements so that they satisfy the constraints. This problem was first posed by Kuehn and Davidson in [45], where the analytical solution for a linear material balance problem is obtained. This is further discussed in [118, 119] with respect to the cases involving some unmeasured variables. It is elaborated that the use of graph-theory can solve for both the measured and unmeasured variables in DR framework. Estimation of unmeasured variables in the DR problem is also dealt in [55]. Crowe et al. [12] brought the concept of projection matrix based on Q-R factorization into the static DR problem for the estimation of some unmeasured variables and for reconciled estimates of the measured variables. This concept was further enhanced in [92]. Some of the earliest applications of DR for steady-state processes can be found in [31, 102, 126].

DR can also be applied to dynamic LTI systems using the Kalman filter [105]. The estimates of the variables obtained through the Kalman filter are regarded as the reconciled estimates. Equality constraints can also be imposed in this problem [100]. However, inequality constraints cannot be handled with this framework.

For non-linear processes, DR was first used by Knepper and Gorman for parameter estimation [43]. This work was followed by [73] in which successive linearization and projection matrix were used. The application of DR when there are bounds and inequality constraints on the variables is addressed in [112] with the use of constrained non-linear optimization.

A good review of DR can be found in [14]. For the cases in which the process is almost steady and the linear relationships are not violated, a linear steady-state DR is sufficient for random error reduction. In this case, the DR problem is minimization of square of the differences between the true and the measured values weighted by the variance of the measurements subject to one or more sets of constraints. This least squares problem can also be represented in Maximum Likelihood [37] and information theory [13] frameworks. For the cases involving significant changes in the state of the system, dynamic model-based reconciliation or dynamic data reconciliation is required. However, DR, whether static or dynamic, works with the assumption that only random errors are present in the data and it fails to give accurate estimates in the presence of faults. Suitable FDI scheme needs to applied not only for the early detection of faults but also for accurate reconciled estimates.

It should be noted that linear steady-state DR problem with no bounds on the variables only is in the scope of the thesis. A steady-state linear model is required for the implementation of the steady-state DR technique. A linear model can be built when the process topology is known as in the case of process flow reconciliation problem. However, when such a topology is not available, linear model identification from the process history or data driven modeling would be the first step.

2.3 Data Driven Modeling

In the early stages of development of data driven modeling techniques, the problem was concerned about detection of process changes from one mode to another [7]. Univariate control charts, such as Shewhart control charts [96], cumulative control charts [72] and Exponentially Weighted Moving Average charts [86], are also developed. These charts can be used to detect abnormal events, and thereby to correct and bring the process to normal operation. However, when the parameters being monitored are not independent, univariate control charts, which cannot handle correlation among variables, are misleading.

On the other hand, multivariate statistical techniques are powerful tools for data reduction while retaining the most of the variability of the data, and for handling correlation to extract the true information. The extensively used multivariate statistical techniques are Ordinary Least Squares, Principal Component Analysis (PCA), Partial Least Squares (PLS) and Canonical Variate Analysis (CVA). PCA, proposed by Pearson [74] and later developed by Hotelling [32], has capability to transform a set of correlated variables to a smaller set of uncorrelated variables. It is the most commonly used technique for dimensionality reduction. It relies on orthogonal transformation of the data matrices. In this process, PCA splits the multidimensional space into subspaces based on the data variabilities they hold. In other words, PCA aims at splitting the multidimensional space of the multivariate data into two subspaces namely the principal component subspace and the residual subspace that respectively hold maximum and minimum variability in the data. PCA initially found its uses in detection of changes in the mode of operation of the process. Statistic based on χ^2 distribution, Hotelling's T^2 statistic or Q statistic (squared prediction error), obtained from the data of one of the subspaces, can be used for process monitoring. Multiway PCA [70] for batch processes, nonlinear PCA [18] for handling nonlinearities in batch processes are also developed. In [20], authors used PCA for FDI of sensors via reconstruction. In that work, one sensor is assumed to be faulty at a time and then the remaining sensor signals are reconstructed. In recursive PCA [48], mean, covariance, principal components including number of components to be retained, and thresholds are recursively updated for adaptive modeling. Structured residuals approach wherein each residual is insensitive to one type of fault while sensitive to other types of faults is discussed in [78] for sensor FDI. Fault subspace analysis for process and sensor FDI is presented in [21]. Multi-scale PCA, which integrates PCA with wavelet analysis is proposed in [5].

PLS, proposed by Wold [129], is conceptually similar to PCA and also useful in data reduction. Unlike PCA, which is a procedure used for a single data matrix, PLS also has an additional group of data, *e.g.* product quality variables. PLS models these two blocks of data while compressing them simultaneously. There have been numerous extensions of PLS like neural-net PLS [76] for incorporating feed-forward neural networks into the PLS modeling to deal with nonlinearity and multi-block PLS [52] to facilitate FDI for very large processes. Recursive PLS [77] is also developed to make the PLS model time variant to cope up with the time varying processes.

CVA is another technique for data reduction. It is similar to PLS in the sense that it normalizes eigenvectors in the two blocks of data while maximizing the correlation between them. The use of CVA in regression and system identification can be found in [46, 93].

Much of the improvements proposed for PLS and PCA are with respect to adaptive modeling of the methods to time varying process conditions and enhancing the resolution properties. Compared to its counterparts like PLS and CVA, PCA is suitable for FDI of sensors as there is no involvement of quality variables. The power of PCA lies in its ability to also obtain the existing algebraic relations among the variables. These relations are called 'constraint models' or 'models', which are further used for DR and FDI. These models are different from 'dynamic models', which are dominantly used for control analysis and design. An ordinary PCA can be suited to most of the sensor FDI applications, subjecting to the condition that algebraic relations among the sensors' signals do not vary. The residual subspace helps in identifying the process constraint model [124], which is required for estimating the covariances of the measurement errors of the variables and for DR and FDI analyses. However, the order of the residual subspace, called as model order, is not known exactly from PCA. As an immediate consequence of this, fault diagnosis could become erroneous. With an assumption that the measurement error covariance matrix is known, the maximum likelihood PCA has been proposed [125] as an improved version of PCA. Recently, an iterative method known as Iterative Principal Component Analysis (IPCA) has also been developed to combine PCA with a maximum likelihood estimation procedure [66]. This technique aims at obtaining an estimate of the error covariance matrix simultaneously with the constraint model that exactly represents the residual subspace. It should be noted that the scope of the thesis is limited only to PCA and IPCA techniques. The outcomes of these techniques such as the constraint model and the error covariance matrix are then used in DR for obtaining reconciled estimates of the detector signals. However, faults in the signals invalidate reconciled estimates. Hence, a suitable FDI test needs to be applied.

Efficient applications of PCA-based FDI are widely reported in literature [40, 49, 75, 80, 117, 130]. In [80], FDI of in-core detectors of Pressurized Heavy Water Reactor (PHWR) has been achieved using PCA and IPCA techniques developed for static DR, based on the operating data from the plant. In [75], authors attempted FDI of in-core SPNDs of a reactor and reconstructed their signals.

2.4 FDI Tests

Excellent reviews of various fault detection and diagnosis methods can be found in [121, 122, 123]. In this section, FDI tests used for process history-based methods (refer to Section 2.1) are discussed.

For detecting the faults, threshold tests like $k-$sigma and sequential probability ratio tests [57, 128] are traditionally used due to their simplicity and ease of implementation. These tests, being univariate type, do not take other measurements into consideration. Hence, they lead to false alarms when the operating point or the state of the process changes from one to another. To get rid of these drawbacks, FDI tests that can be applied on all measurements together are highly desirable.

Tests for single fault detection such as Global Test (GT) [3, 54, 85], Measurement Test [3, 56], and Nodal Test [55, 82] were proposed in the early years of development in this field. These techniques were developed in the years 1975 and 1976. In a well maintained process, multiple faults (faults more than one in number) rarely occur. However, the tests to detect the faults should be capable of detecting multiple faults. The main mechanism for fault detection is the statistical distance. The errors (whether random errors or faults) make the signal deviate from the true values. The random errors are assumed to be always present in the measurements. For the measurements to be healthy or fault-free, the square of the deviations between the measured values and their respective estimates; normalized by the variance of the random errors must be lying within a limit specified by the variance of the random errors. Note that the limit specified and the normalized deviations are in standard deviation units. If the normalized deviations are outside this limit, the classical way is to declare the presence of faults.

In maximum likelihood estimation techniques, unknown parameter values of the random population are selected so that the joint probability density of the ensemble of observations is maximized. They can be used in radiation detection in the applications of localization of the radiation sources [9, 10, 11, 16, 17]. The Generalized Likelihood Ratio (GLR) method uses the maximum likelihood estimation in the sense that a likelihood ratio is derived from the probability density functions of the observations under the possible hypothesis and the unknown parameters are obtained as the maximum likelihood estimates which best explain the likelihood ratio. A GLR approach to the detection and estimation of jumps in linear systems was developed by Willsky and Jones in 1976 [127]. Inspired from this work, Narasimhan and Mah developed GLR method of fault detection for steady-state systems [63]. In [63], authors also proposed a serial fault compensation strategy for identification of multiple faults. Multiple FDI was also proposed in [88]. Following these developments, Tong and Crowe illustrated the efficacy of Principal Component Test in fault detection in their work [113].

With this background, few more multiple FDI strategies were developed in [89, 95]. These papers also presented serial elimination strategy for multiple fault identification and comparison among different methods with respect to their performances. In [33], the role of simulation in evaluating the performances of different FDI methods and strategies was demonstrated. Some performance indices that can be used for evaluation were also presented in [33, 89, 95]. In contrast to serial strategies mentioned above, simultaneous strategies for multiple FDI were also proposed by Rosenberg et al. [89] and Rollins and Davis [87]. However, there has not been any concrete stand point regarding the best FDI method. One of the FDI methods can be used in accordance with the type of the process and limitations of the methods.

In all the above mentioned methods, residuals which are the discrepancies between the actual and predicted quantities play the key role. If multi-variate statistical techniques are employed, contribution plots [51, 52] based on T^2 and Q statistics can also aid for FDI. However, fault isolation is difficult with this approach. For steady-state processes, tests with no-bounds on the variables such as GLR method, Iterative Measurement Test (IMT) and Iterative Principal Component Test (IPCT), proposed in this thesis, are suitable for dealing with multiple faults. These tests only are in the scope of this thesis and they proved to be efficient when used alongwith the steady-state DR scheme that requires the algebraic relations among the variables.

However, since the FDI techniques detect the faults based on the distance of residuals (constraint residuals, measurement adjustments, or innovations) from the origin, they should always be around the zero-mean, and there should not be any trend in them, i.e., they should be temporally independent. This suggests the whiteness of the residuals [58]. A Whiteness Test (WT) may be conducted to test the whiteness of the residuals [106].

Coming to the application of FDI techniques in nuclear reactors, FDI of in-core detectors and other nuclear reactor components are widely reported in [40, 47, 49, 50, 57, 68, 80, 90, 91, 116, 117]. A review of the applications of different FDI schemes to nuclear plants, is given in [50]. When the constraint model and the error covariance matrix are available and there are a fewer number of measurements, DR and FDI are straight forward, provided that there is a consistent correlation pattern among the variables. However, clustering or grouping of the measurements with consistent correlation may be required, when there are a large number of measurements as discussed in Chapter 1.

2.5 Clustering of the Data

Clustering helps in dealing with statistical analysis of large number of variables, as explained in Chapter 1 for the case of VSPNDs. It is the task of grouping the most similar variables into a group or cluster such that intra-cluster variables are more similar to each other than to those in other clusters. The similarity index can be Minkowski metric, Euclidean distance, Canberra metric, or Czekanowski metric [36]. Cluster analysis finds its use in many fields [114], *viz.*, biology, medicine, business and marketing, world wide web, computer science, social science, robotics, and others; apart from FDI. Clustering can be implemented by numerous algorithms, which may be classified as hierarchical or connectivity-based clustering [4, 22], non-hierarchical or centroid-based clustering [4, 22, 29, 53] and statistical distribution-based clustering. Hierarchical methods can be classified as agglomerative and divisive methods. In agglomerative methods, initially there are as many clusters as there are variables. In divisive methods, initially there is one cluster for all the variables. Either of these methods are followed to arrive at a suitable cluster configuration. Non-hierarchical methods assume an initial number of clusters and employ random assignment of the variables into the groups or initial set of cluster centroids. Iterative schemes lead them to work out the variables in each cluster. When there are a large number of variables to be grouped, it is the most used method. Statistical distribution-based clustering [36] use the probability density functions for clustering the variables. However, there is no stand-point for the best clustering method. The $k-$means algorithm in non-hierarchical clustering is the mostly used method by the practising engineers [80, 81]. In [81], FDI of SPNDs based on clustering is explained. In this work also, the $k-$means algorithm [36, 53] is used for clustering the VSPNDs. However, the need of clustering and the consistencies in the correlation patterns among the variables can be efficiently checked with the help of a simulated process. As stated earlier, for extracting the actual behaviour under different operational transients, the simulated process needs to be built on first principles. Hence, a model of the reactor with significant dynamics needs to be developed for this case of sensor FDI.

2.6 Modeling of Nuclear Reactors

In large nuclear reactors, operational transients occur on time scales of seconds to minutes. While the prompt neutrons have influence till some milliseconds, delayed neutrons, xenon build-up and core composition changes are responsible for longer transients. For the analysis of these transients and for ensuring safety and economy, mathematical models need to be developed from first principles. The fundamental equation that represents the dynamics of the nuclear reactors is the time-dependent Boltzmann transport equation for the angular flux [19]. However, its use coupled with delayed neutron precursors' equations is prohibitively difficult for neutron kinetics problems of practical interest [108]. Nevertheless, these problems can be solved with approximate methods like the time dependent group diffusion equation derived from the original Boltzmann equation.

The simplest form of mathematical model that can be derived from the diffusion equation is the point reactor kinetics model [19, 26] in which space and time dependence of neutron energy is omitted. In other words, all the neutrons have the same speed, and the neutron flux distribution is assumed to be time invariant. The material properties are also considered to be uniform. Essentially the diffusion equation is coupled with the set of delayed neutron precursor equations. The point reactor kinetics model, though suitable for very small reactors, does not adequately describe large reactors.

Large reactors are heterogeneous in nature as they have functionally distinct materials, *e.g.* fuel, coolant, moderator, reflector and control mechanisms *etc.*, distributed in the core. In addition they have various regions with different burn-ups and coolant densities. Within the core periphery, neutrons continuously either loose or gain energy, diffuse from one location to another, and undergo several interactions with matter. It is very important to determine the flux distribution under the operational transients for ensuring safety and economy. Hence, unlike the point reactor kinetics model, the time dependent group diffusion equation should be supported by the methods for treating the spatial variables. These methods may broadly be classified as space-time factorization methods, modal and synthesis methods and direct methods.

In space-time factorization methods, space, energy and time dependent neutron flux is factorized into the product of two components: one, called the amplitude function, depending only on the time variable and the other, called the shape function, depending only on the space and energy and not on time [30, 38, 71].

In modal methods, the instantaneous flux inside the reactor core is expressed by the linear combination of a set of pre-computed time independent flux distributions or modes. Each mode has an associated magnitude [24, 62, 104]. Modal synthesis methods, another class of modal methods, use expansion functions, which are static solutions of the diffusion equation for some specified initial conditions. Acceptable degree of accuracy from those methods can be guaranteed with small number of expansion functions.

In direct methods, the problem space is partitioned into a finite number of elemental volumes in which the material properties are assumed to be uniform. Based on this partitioning, spatially-discretized forms of the coupled diffusion and delayed neutron precursor equations are obtained. The direct methods may further be classified as Finite Difference Methods (FDMs), coarse-mesh methods and nodal methods [28, 108]. In FDMs, very fine mesh spacing is required for a good amount of accuracy. This increases the number of unknowns, and hence the computational time. In coarse-mesh and nodal methods, larger spacing can be used, *e.g.* uniform group diffusion parameters are used for the entire fuel assemblies to treat them as spatially homogeneous. These methods are computationally efficient, as they work on relatively smaller number of unknowns. In coarse-mesh methods, determination of the multi-dimensional flux distribution within a node is the integral part of the solution. In nodal methods [19, 26, 104], it is first necessary to partition the reactor spatial domain into relatively large rectangular right parallelepipeds, called nodes, to derive the nodal equations. Nodal methods are promising with respect to their formulations in terms of differential equations and computation time, when they are used for control system studies [97].

AHWR is a large reactor, which necessitates a space-time kinetics modeling for accurately determining the space and time-dependent flux behaviour. A nodal model with finite difference approximation of multi-group diffusion equation has been developed for PHWR [111]. A nodal model of AHWR has been developed [97] aiming at finding a model of reasonable order that maintains the requisite accuracy. In this work, the same methodology has been adopted to develop the model of the AHWR in terms of neutron fluxes. The treatment of the problem in terms of the nodal fluxes helps in the FDI of neutronic sensors, which generate the output signals as functions of the neutron flux at their respective locations. The methodology in [97] has been extended in this thesis to develop the model of the AHWR in terms of neutron fluxes with the objective of generating the in-core and ex-core detector signals from the mathematical model. This signal data is just sufficient for the DR and the process history-based FDI. Model-based FDI is also possible using signal data (process history) from the model of AHWR and the model of the detectors.

2.7 Model-based FDI for VSPNDs of AHWR

VSPNDs are known for their delayed response characteristics [60, 81] and need to be compensated for representing the prompt behaviour of the flux in the reactor. When they are used for in-core neutron flux monitoring and control, a system that can compensate for the delayed response of the VSPNDs could be deployed. If such a system is based on a very accurate model of the VSPNDs, it can also be exploited for detection and diagnosis of faults, if any, in the VSPNDs. A linear model developed for VSPNDs in [60] may be utilized for FDI. The design of residuals may be done using parity equations [8], state observers and state estimation techniques [34]. State estimation techniques such as Kalman filters differ from others in the sense that they can handle stochastic disturbances. A Kalman filter-based dynamic compensation scheme has been developed in [61] for improving the response time of VSPNDs. In that work, VSPNDs were formulated in an unknown-input observer framework.

For dynamic systems, a GLR-based FDI scheme relying on the temporal redundancy in the data is proposed in [127, 128] to overcome the limitations of threshold-based FDI schemes discussed in Section 2.4. This scheme gives all the information regarding the fault, *i.e.*, fault occurrence time, fault location and magnitude of the fault, but at the cost of increased computational effort. Therefore, it is further modified in [64] to reduce the computational burden so that it can be efficiently used for on-line FDI and fault correction. However, the on-line implementation of GLR-based FDI scheme requires prior knowledge of probable fault modes (state jump, state step, sensor jump, sensor step, hard-over actuator or sensor, increased actuator or sensor noise, dynamic shift *etc.*) and associated fault signature matrices of the system for which it is designed [64, 127, 128]. There is still a scope for the extension of Kalman filter formulation in [61] such that it also performs FDI using GLR method. In other words, a hybrid scheme can be developed which can dynamically compensate the VSPND signal for promptness; minimize the random errors through Kalman filter; and performs FDI with GLR method. This aspect also has been addressed in this thesis for the detection of abrupt jumps or measurement biases in the VSPND signal.

Different FDI techniques have been tried in the literature to chemical processes and rotating machinery. However, not enough evidence is found with respect to nuclear reactors. Also, the model-based FDI techniques are lacking. This thesis is an attempt to apply Steady-state DR and FDI and a model-based FDI techniques to a large reactor.

Chapter 3

Steady-state FDI Techniques

This chapter introduces the PCA and IPCA models, DR and FDI techniques. Success criteria, *viz.*, Average Error Reduction, Average Adjustments, Overall Detection Rate, and Overall Power are also introduced.

3.1 Data Driven Modeling using PCA and IPCA

A static linear model is required for the implementation of the steady-state DR technique for FDI of neutronic detectors, *viz.*, ion chambers and VSPNDs. Therefore, the first step would be the model identification. The PCA and IPCA techniques, which are used for model identification, are briefly described in the following:

3.1.1 Model Identification using PCA

PCA [36] is a multivariate statistical technique, which helps in obtaining the coordinate axes rotated to reveal the variability of the data. The new axes are termed as principal components, among which only a few represent the greater variability and the rest represent the lesser variability. When sufficient ratio of signal variability to noise variability is assured, principal components corresponding to lesser variability may represent the noise. In the presence of random errors, at a time instant k, the measurement vec-

A part of this chapter was published in *2015 IEEE International Conference on Control Applications (CCA)*, Sydney, Australia.

tor $\boldsymbol{y}(k)$ of variables is the summation of their true values $\boldsymbol{x}(k)$ and the corresponding random errors $\boldsymbol{\varepsilon}(k)$, given by

$$\boldsymbol{y}(k) = \boldsymbol{x}(k) + \boldsymbol{\varepsilon}(k),\ \boldsymbol{y}(k) \in \mathbb{R}^n,\ \boldsymbol{x}(k) \in \mathbb{R}^n,\ \boldsymbol{\varepsilon}(k) \in \mathbb{R}^n, \tag{3.1}$$

where it is assumed that $\boldsymbol{x}(k)$ and $\boldsymbol{\varepsilon}(k)$ are considered to be independent of each other and there exists sufficient signal to noise ratio.

Principal components depend entirely on the covariance matrix $\boldsymbol{\Sigma_y}$ of the measurement vector. Let $\boldsymbol{\Sigma_y}$ be decomposed into eigenvalue-eigenvector pairs $(\mu_i, \boldsymbol{p}_i)\ \forall\ i = 1, ..., n$, with $\mu_1 \geq \mu_2 \geq ... \geq \mu_n \geq 0$. Then principal components are given by $\bar{Z}_i = \boldsymbol{p}_i^T \boldsymbol{y}\ \forall\ i = 1, ..., n$. With this arrangement, the first principal component is the linear combination of the measurement variables and the elements of the eigenvector with maximum variance and the second principal component is the one with second maximum variance and so on.

Let $\boldsymbol{U}$, the matrix of ordered set of eigenvectors of $\boldsymbol{\Sigma_y}$ according to the eigenvalues in decreasing order of magnitude, be partitioned into two parts, as $\boldsymbol{U} = [\boldsymbol{U}_1\ \boldsymbol{U}_2]$, where for any $m < n$, $\boldsymbol{U}_1 = (\boldsymbol{p}_1, ..., \boldsymbol{p}_{n-m})$ represents the first $n - m$ eigenvectors corresponding to principal component subspace and $\boldsymbol{U}_2 = (\boldsymbol{p}_{n-m+1}, ..., \boldsymbol{p}_n)$ represents the remaining m eigenvectors corresponding to residual subspace.

The variations in measurement data along last m eigenvectors of residual subspace is negligible and $\boldsymbol{U}_2^T \boldsymbol{y} = \boldsymbol{r}$, the vector of residuals which are temporally uncorrelated with mean value $\approx \boldsymbol{0}$. Hence, it can be said that the residual subspace is attributed to the random errors in the measurement data, as the residuals obtained from the eigenvectors are approximately white. Now the m^{th} order constraint model, obtained with PCA is given as $\boldsymbol{A}_P = \boldsymbol{U}_2^T,\ \boldsymbol{A}_P \in \mathbb{R}^{m \times n}$, with the properties

$$\left.\begin{aligned} \boldsymbol{A}_P \boldsymbol{y}(k) &= \boldsymbol{r}(k) \\ \text{and} \quad \boldsymbol{A}_P \boldsymbol{x}(k) &= \boldsymbol{0}. \end{aligned}\right\} \tag{3.2}$$

If it is assumed that not all the variables of true signal vector $\boldsymbol{x}(k)$ are independent of each other, its covariance matrix, $\boldsymbol{\Sigma_x}$, is not of full rank and the eigenvectors corresponding to zero eigenvalues span the residual subspace. As noise $\boldsymbol{\varepsilon}(k)$ is random in nature, $\boldsymbol{\Sigma_y}$ is of full rank, making it impossible to get the exact order of residual subspace by looking at the eigenvalues. Hence, the exact model order is not known from PCA. Apart from this, error variances of the variables are also unknown. However, with a model of assumed order m, the residual vector given by $\boldsymbol{r}(k) = \boldsymbol{A}_P\boldsymbol{y}(k)$ is supposed to be a random vector with zero mean. The quadratic term $\boldsymbol{r}^T(k)\boldsymbol{\Sigma_r}^{-1}\boldsymbol{r}(k)$ where $\boldsymbol{\Sigma_r}$ is the covariance matrix of $\boldsymbol{r}(k)$, amounts to the sum of the squares of m independent standard normal random variables [36, 64]. Hence, it follows a central χ^2 distribution with m degrees of freedom. In the event of faults in one or more variables, this quadratic term is supposed to exceed a chosen χ^2 threshold and thus helps in FDI.

3.1.2 Model Identification using IPCA

IPCA [66], which is also a multivariate statistical method, is an improved version of PCA. Its strengths lie in simultaneous estimation of the constraint model $\boldsymbol{A}_I$ with exact order of residual subspace and covariance matrix of measurement errors $\boldsymbol{\Sigma_\varepsilon}$. To perform these functions, IPCA relies upon the concept of scaling of the data. It is assumed that initial estimates of the non-zero elements of $\boldsymbol{\Sigma_\varepsilon}$ are small fractions of those of the data covariance matrix and the solutions are obtained in an iterative manner. Let $[\boldsymbol{U}, \boldsymbol{M}, \boldsymbol{V}] = \mathrm{svd}(\boldsymbol{Y})$ denote the singular value decomposition of an $n \times N$ data matrix $\boldsymbol{Y}$, where $\boldsymbol{U}$ is the $n \times n$ matrix of left singular vectors, $\boldsymbol{M}$ is an $n \times n$ matrix containing the n non-zero singular values ordered from the largest to the smallest along the diagonal, and $\boldsymbol{V}$ is an $n \times N$ matrix of right singular vectors. If $\boldsymbol{\Sigma_y}$ is assumed to be equal to the sample covariance matrix of the data matrix (generally true for data with large number of samples), it can be expressed as

$$\boldsymbol{\Sigma_y} = \frac{1}{N}\sum_{k=1}^{N} \boldsymbol{y}(k)\boldsymbol{y}^T(k) = \frac{1}{N}\boldsymbol{Y}\boldsymbol{Y}^T. \tag{3.3}$$

Now, the iterative algorithm for simultaneous model identification and error covariance matrix estimation can be summarized as follows:

1. Initially, set iteration counter $\kappa = 1$ and non-zero elements of $\boldsymbol{\Sigma_{\varepsilon}}^{\kappa}$ as small fractions (say 0.0001) of the corresponding elements of $\boldsymbol{\Sigma_{y}}$; assume a model order m and sum of last m singular values $\lambda^{\kappa-1} = 0$.

2. Scale the data using the standard deviations of variables, *i.e.*, $\boldsymbol{Y}_s = \boldsymbol{L}^{-1}\boldsymbol{Y}$, where $\boldsymbol{L}\boldsymbol{L}^T = \boldsymbol{\Sigma_{\varepsilon}}^{\kappa}$.

3. Perform the singular value decomposition of $\boldsymbol{Y}_s$, *i.e.*, obtain $[\boldsymbol{U}, \boldsymbol{M}, \boldsymbol{V}] = \mathrm{svd}(\boldsymbol{Y}_s)$, for the assumed model order m. Pick $\boldsymbol{U}_2$, the $n \times m$ sub-matrix of $\boldsymbol{U}$ corresponding to the last m columns. Model corresponding to unscaled data $\boldsymbol{Y}$ is $\boldsymbol{A}^{\kappa} = \boldsymbol{U}_2^T\boldsymbol{L}^{-1}$.

4. Compute λ^{κ} as sum of last m singular values of $\boldsymbol{Y}_s$. If relative change in λ is less than a specified tolerance, output the results $\boldsymbol{A}^{\kappa} = \boldsymbol{A}_I$, $\boldsymbol{\Sigma_{\varepsilon}}^{\kappa} = \boldsymbol{\Sigma_{\varepsilon}}$, $\boldsymbol{M}$ and stop the procedure. On the other hand, if relative change in λ^{κ} is significant, the iteration should continue by returning to step 2 for the next instant, $k+1$. However, before returning to step 2, estimate the non-zero elements of the $\boldsymbol{\Sigma_{\varepsilon}}^{\kappa+1}$ which minimize the log-likelihood function of constraint residuals given by
$N \log|\boldsymbol{A}^{\kappa}\boldsymbol{\Sigma_{\varepsilon}}^{\kappa+1}(\boldsymbol{A}^{\kappa})^T| + \sum_{k=1}^{N} \boldsymbol{r}^{\kappa}(k)(\boldsymbol{A}^{\kappa}\boldsymbol{\Sigma_{\varepsilon}}^{\kappa+1}(\boldsymbol{A}^{\kappa})^T)^{-1}\boldsymbol{r}^{\kappa}(k)$
where $\boldsymbol{r}^{\kappa}(k) = \boldsymbol{A}^{\kappa}\boldsymbol{y}(k)$.

The above algorithm is represented in the form of a flowchart in Fig. 3.1. The measurement errors are assumed to be independent of each other, making $\boldsymbol{\Sigma_{\varepsilon}}$ a diagonal matrix. The vector of standard deviation of variables, σ_{ε} is obtained from converged $\boldsymbol{\Sigma_{\varepsilon}}$. Out of many, the maximum value of m for which the last m singular values of $\boldsymbol{\Sigma_{\varepsilon}}$ converge to 1 is the identified model order and the corresponding model is the identified model. However, the model order has to be selected carefully because relative magnitudes of standard deviations of measurement errors affect the detectability of faults in the variables. A model order with which there is not much deviation in the estimates

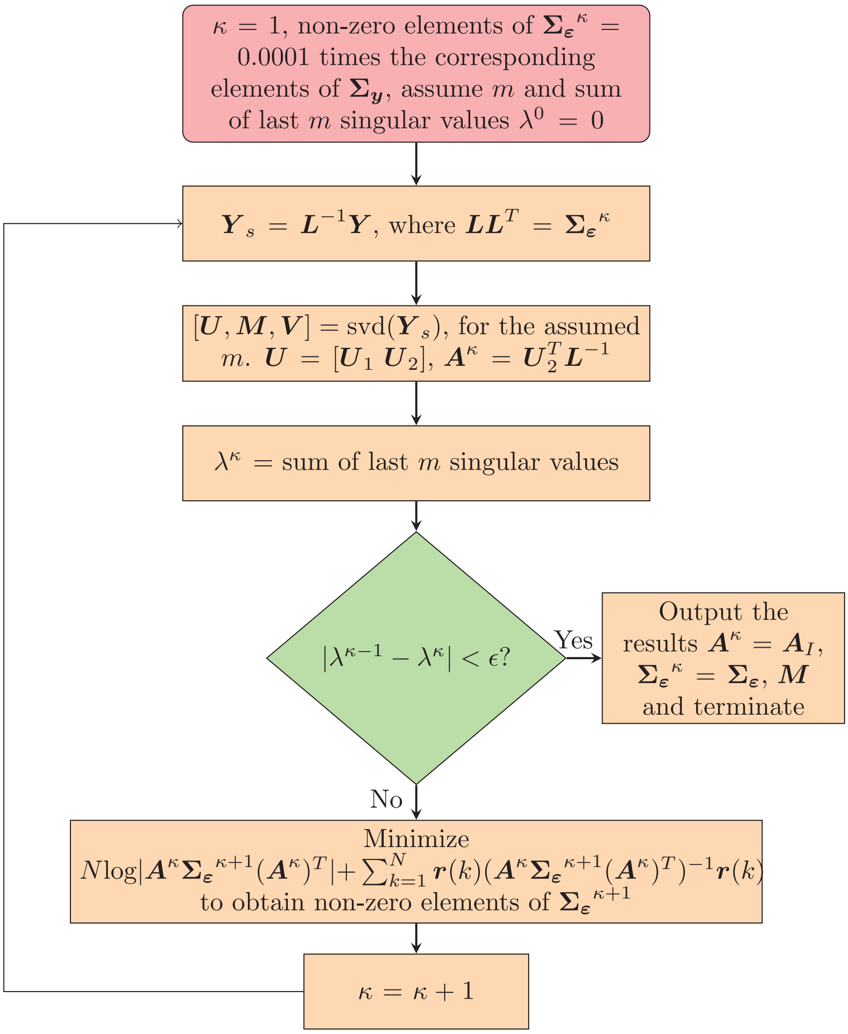

Figure 3.1: Flowchart of IPCA

of standard deviation of errors from the true ones is selected. Residual vectors can be obtained with the model and FDI can be attempted. It should be noted that the true standard deviations of errors can be known from the covariance matrix of measurement data, when the process is in steady-state.

The data used for PCA and IPCA constraint model development should have sufficiently large signal variability compared to the noise variability [79] in order to achieve the distinguishability between principal component subspace and residual subspace. However, the constraint model is expected to work successfully for any data holding the same correlations among the variables as exhibited by the training data.

3.2 Data Reconciliation

In the following, $\boldsymbol{A}$ denotes the linear constraint model, which is either $\boldsymbol{A}_P$ (if PCA is used to obtain the constraint model) or $\boldsymbol{A}_I$ (if IPCA is used).

3.2.1 DR Formulations: No-fault case

The estimates of the signals, at a time instant k, are obtained by minimizing the function

$$\begin{aligned}
&\min_{\boldsymbol{x}(k)}(\boldsymbol{y}(k)-\boldsymbol{x}(k))^T\boldsymbol{\Sigma_\varepsilon}^{-1}(\boldsymbol{y}(k)-\boldsymbol{x}(k)),\\
&\text{s.t.} \\
&\boldsymbol{A}\boldsymbol{x}(k)=\boldsymbol{0}.
\end{aligned} \tag{3.4}$$

The reconciled estimates of the true values of the measurements obtained from the above optimization problem are given by [65]

$$\hat{\boldsymbol{x}}(k)=\boldsymbol{y}(k)-\boldsymbol{\Sigma_\varepsilon}\boldsymbol{A}^T(\boldsymbol{A}\boldsymbol{\Sigma_\varepsilon}\boldsymbol{A}^T)^{-1}\boldsymbol{A}\boldsymbol{y}(k). \tag{3.5}$$

The adjustments made to the measurements are given by

$$\boldsymbol{a}(k)=\boldsymbol{y}(k)-\hat{\boldsymbol{x}}(k). \tag{3.6}$$

3.2.2 DR Formulations: With-fault case

For the DR to be effective, the measurements suffering from faults are to be eliminated before DR is performed. The $Q-R$ factorization [2, 69] does this job with the help of a projection matrix $\boldsymbol{P}$ constructed from the columns of $\boldsymbol{A}$ corresponding to unmeasured values or faulty signals [65]. In this method, overall estimation problem is divided into two sub-problems: one is reconciliation of measurements and the other is estimation of faulty signals, which are eliminated in the reduced DR problem.

The n number of true variables $\boldsymbol{x}(k)$ are decomposed into p number of measured variables, denoted by $\boldsymbol{x}_p(k)$, and $q = (n - p)$ number of unmeasured or faulty variables, denoted by $\boldsymbol{u}(k)$. The constraint equations are written as

$$\boldsymbol{A}_1\boldsymbol{x}_p(k) + \boldsymbol{A}_2\boldsymbol{u}(k) = \boldsymbol{0},\ \boldsymbol{x}_p(k) \in \mathbb{R}^p,\ \boldsymbol{u}(k) \in \mathbb{R}^q, \tag{3.7}$$

where $\boldsymbol{A}_1$ and $\boldsymbol{A}_2$ are columns of $\boldsymbol{A}$ corresponding to measured and unmeasured variables, respectively. Performing a $Q-R$ decomposition on matrix $\boldsymbol{A}_2$, matrices $\boldsymbol{Q}_u$, $\boldsymbol{R}_u$, and $\boldsymbol{\Pi}_u$ are obtained such that

$$\boldsymbol{A}_2\boldsymbol{\Pi}_u = \boldsymbol{Q}_u\boldsymbol{R}_u. \tag{3.8}$$

In this, $\boldsymbol{\Pi}_u$ is the permutation matrix whose columns are permuted columns of an identity matrix of appropriate dimensions such that

$$\boldsymbol{\Pi}_u^T\boldsymbol{u}(k) = \begin{bmatrix} \boldsymbol{u}_{r_u}(k) \\ \boldsymbol{u}_{q-r_u}(k) \end{bmatrix}, \tag{3.9}$$

where r_u is the rank of matrix $\boldsymbol{A}_2$.

Expressing

$$\boldsymbol{Q}_u = [\boldsymbol{Q}_{u1}\ \boldsymbol{Q}_{u2}],\ \boldsymbol{R}_u = \begin{bmatrix} \boldsymbol{R}_{u1} & \boldsymbol{R}_{u2} \\ \boldsymbol{0} & \boldsymbol{0} \end{bmatrix}, \tag{3.10}$$

where $\boldsymbol{Q}_{u1}$, $\boldsymbol{Q}_{u2}$, $\boldsymbol{R}_{u1}$ and $\boldsymbol{R}_{u2}$ are $m \times r_u$, $m \times (q - r_u)$, $r_u \times r_u$ and $r_u \times (q - r_u)$ matrices respectively, the constraint equation can be written as

$$\boldsymbol{A}_1\boldsymbol{x}_p(k) + [\boldsymbol{Q}_{u1}\ \boldsymbol{Q}_{u2}] \begin{bmatrix} \boldsymbol{R}_{u1} & \boldsymbol{R}_{u2} \\ \boldsymbol{0} & \boldsymbol{0} \end{bmatrix} \begin{bmatrix} \boldsymbol{u}_{r_u}(k) \\ \boldsymbol{u}_{q-r_u}(k) \end{bmatrix} = \boldsymbol{0}. \tag{3.11}$$

By pre-multiplying the above equation by $\boldsymbol{Q}_u^T$, the following relations are obtained:

$$\boldsymbol{Q}_{u1}^T\boldsymbol{A}_1\boldsymbol{x}_p(k) + \boldsymbol{R}_{u1}\boldsymbol{u}_{r_u}(k) + \boldsymbol{R}_{u2}\boldsymbol{u}_{q-r_u}(k) = \boldsymbol{0}, \tag{3.12}$$

$$\boldsymbol{Q}_{u2}^T\boldsymbol{A}_1\boldsymbol{x}_p(k) = \boldsymbol{G}_x\boldsymbol{x}_p(k) = \boldsymbol{0}, \tag{3.13}$$

where $\boldsymbol{P} = \boldsymbol{Q}_{u2}^T$ is the projection matrix and $\boldsymbol{G}_x = \boldsymbol{Q}_{u2}^T\boldsymbol{A}_1$ is the reduced constraint model of the healthy measurements. From (3.13), the reconciled estimates of measured variables are obtained as

$$\hat{\boldsymbol{x}}_p(k) = \boldsymbol{y}_p(k) - \boldsymbol{\Sigma}_{\boldsymbol{\varepsilon_p}}\boldsymbol{G}_x^T(\boldsymbol{G}_x\boldsymbol{\Sigma}_{\boldsymbol{\varepsilon_p}}\boldsymbol{G}_x^T)^{-1}\boldsymbol{G}_x\boldsymbol{y}_p(k), \tag{3.14}$$

where $\boldsymbol{y}_p(k)$ is the measurement values of the healthy signals and $\boldsymbol{\Sigma}_{\boldsymbol{\varepsilon_p}}$ is variance-covariance matrix of $\boldsymbol{y}_p(k)$. From (3.12) and (3.14), the estimates of unmeasured variables can be obtained as

$$\boldsymbol{u}_{r_u}(k) = -\boldsymbol{R}_{u1}^{-1}\boldsymbol{Q}_{u1}^T\boldsymbol{A}_1\hat{\boldsymbol{x}}_p(k) - \boldsymbol{R}_{u1}^{-1}\boldsymbol{R}_{u2}\boldsymbol{u}_{q-r_u}(k). \tag{3.15}$$

From (3.15), two cases are possible:

1. Rank of $\boldsymbol{R}_{u1} = r_u = q$

   In this case, $\boldsymbol{R}_{u2}$ and $\boldsymbol{u}_{q-r_u}(t)$ do not exist. The solution of unmeasured variables is, therefore

   $$\boldsymbol{u}_{r_u}(k) = -\boldsymbol{R}_{u1}^{-1}\boldsymbol{Q}_{u1}^T\boldsymbol{A}_1\hat{\boldsymbol{x}}_p(k). \tag{3.16}$$

   It is clear that all measured and unmeasured variables are estimable and a unique solution is guaranteed.

2. Rank of $\boldsymbol{R}_{u1} = r_u < q$

   In this case, the variables $\boldsymbol{u}_{r_u}(k)$ are estimated from (3.15), when the variables $\boldsymbol{u}_{q-r_u}(k)$ are given. In this work, estimates for $\boldsymbol{u}_{q-r_u}(k)$ are taken from the reconciled measurements values of all the variables given by (3.5), leading to a non-unique solution for the variables.

In either of the above two cases, the vector of reconciled values of all the variables, $\hat{\boldsymbol{x}}(k)$ is obtained by suitably coupling the solutions for each variable from $\hat{\boldsymbol{x}}_p(k)$ and $\hat{\boldsymbol{u}}(k)$.

For the evaluation and comparison of the performances of PCA and IPCA techniques, following DR indices are computed from the data window with N_g number of observations corresponding to a fault scenario. One of the indices, namely Average Error Reduction (AER), is already found in the literature, while the terminology Average Adjustments (AA) is introduced in this thesis.

1. *AER:* Defining

$$E_1 = \textstyle\sum_{j=1}^{N_g} (\sum_{i=1}^{n} |y_{ij} - x_{ij}|) \tag{3.17}$$

$$\text{and} \quad E_2 = \textstyle\sum_{j=1}^{N_g} (\sum_{i=1}^{n} |\hat{x}_{ij} - x_{ij}|), \tag{3.18}$$

   the AER [63] is given by

$$\text{AER} = \frac{(E_1 - E_2)}{E_1} \times 100, \tag{3.19}$$

   where y_{ij}, x_{ij} and $\hat{x}_{ij}$ are respectively the measurement, true and reconciled values of i^{th} sensor signal in the j^{th} observation.

2. *AA:* This is the vector of the mean values of the measurement adjustments, which are the differences between the measurements and reconciled values. Its element corresponding to i^{th} sensor is given by

$$AA_i = \frac{1}{N_g} \sum_{j=1}^{N_g} (y_{ij} - \hat{x}_{ij}). \tag{3.20}$$

The following are the desirable properties of the above DR indices:

1. AER should increase in magnitude when conditions of detectors change from fault-free to faulty.

2. AAs of the faulty detectors should be equal to the fault magnitudes of the respective detectors, while the AAs of healthy detectors are not affected.

3.3 Fault Detection and Isolation

As discussed in Section 3.2, when the knowledge of faulty sensors is available, DR is helpful in obtaining reconciled estimates even in situations involving presence of faults. This knowledge is provided by FDI, which has three sub-problems, *viz.,* detection problem, multiple fault identification problem, and estimation of magnitudes of faults.

As a part of detection problem, hypothesis testing is considered, which is basically a method for testing a claim or hypothesis about a parameter in a population, using data measured in a sample. A hypothesis regarding population parameter is assumed to be true a priori, and some hypothesis is tested by determining the likelihood that a sample statistic was obtained from the population.

In case of no fault, the constraint residual or measurement adjustment vectors, whose elements are independent standard normal random variables, are of zero mean provided that there is an accurate constraint model. This condition is assumed to be true in hypothesis testing. In case of fault(s), the mean vector deviates from the zero. However, the vector has the same covariance in both the situations. For the detection problem, the null hypothesis H_0 is that no fault is present or residual or adjustment mean is close to zero and the alternative hypothesis H_1 is that fault is present in one or more signals or residual or adjustment mean is non-zero. Some suitable test statistic, which is a measure of distance spanned by the residual or adjustment vector from zero or origin, is computed. The value of this statistic is compared with a criterion to take a decision about the fault. The criterion is usually obtained by the level of significance to be applied on the distance metric of the residual vector from zero. The level of significance should be carefully selected such that there is a compromise between the Type-I error probability (the probability of declaration of H_1 when H_0 is true) and Type-II error probability (the probability of declaration of H_0 when H_1 is true), as it largely affects these probabilities.

The FDI strategy can be chosen to deal with all the three sub-problems listed above. Some of the FDI methods capable of handling multiple faults and suitable to be used with the steady-state DR problem are described in the following:

3.3.1 GLR Method

For GLR method, GT [3, 54, 65, 85] is considered for the detection of faults. GT statistic is derived from the constraint residual vector $\boldsymbol{r}(k)$ obtained from (3.2), as

$$\gamma(k) = \boldsymbol{r}^T(k)\boldsymbol{\Sigma}_{\boldsymbol{r}}{}^{-1}\boldsymbol{r}(k), \tag{3.21}$$

where $\boldsymbol{\Sigma_r} = \boldsymbol{A\Sigma_\varepsilon A}^T$ is the covariance matrix of $\boldsymbol{r}(k)$. It is obvious that $\gamma(k)$ has a χ^2 distribution of m degrees of freedom as $\boldsymbol{A} \in \mathbb{R}^{m\times n}$, if all m rows of $\boldsymbol{A}$ are linearly independent. At a specified level of significance (α), $P\{\gamma \geq \chi^2_{1-\alpha}(m)\} = \alpha$, where α is taken as 0.05. If $\gamma \geq \chi^2_{1-\alpha}(m)$, alternative hypothesis, H_1 is declared. However, GT declares only the presence of faults but not their origin, which necessitates a separate procedure to identify their origin.

If H_0 is rejected by the GT, the identification problem arises. Then GLR test is conducted for all possible combinations of a single and multiple faults in the data and test statistics are derived for each of these alternatives. At a time instant k, fault signature vectors $\boldsymbol{f}_j = \boldsymbol{Ae}_j$ are developed for each measurement j, where $\boldsymbol{e}_j$ is the unit vector with 1 at position j. Suppose the fault signature matrix $\boldsymbol{F}_i = \{\boldsymbol{Ae}_{i_1},\ i_1 = 1,...,n; \boldsymbol{A}(\boldsymbol{e}_{i_1}, \boldsymbol{e}_{i_2}),\ \forall i_1, i_2 = 1,...,n,\ i_1 \neq i_2; ...; \boldsymbol{A}(\boldsymbol{e}_{i_1}, \boldsymbol{e}_{i_2}, ..., \boldsymbol{e}_{i_g}),\ \forall i_1, i_2, ..., i_g = 1,...,n,$ $i_1 \neq i_2 \neq ... \neq i_g\}$ has fault signature vectors as its columns. The subscript i refers to the set of combinations in which $i_1, i_2, ..., i_g$ are chosen to exhaustively consider all possible combinations of faults from $1, 2, ..., g$. The residuals have a mean of $\boldsymbol{0}$ and $\boldsymbol{F}_i\boldsymbol{b}$ in the presence of no and g faults hypothesized respectively, where $\boldsymbol{b}$ is a column vector of unknown magnitudes of faults. It may be noted that the sizes of $\boldsymbol{F}_i$ and $\boldsymbol{b}$ depend on the number of faults hypothesized.

If $f(\boldsymbol{r})$ denotes the probability density function of the m-variate residuals, then the GLR can be written as

$$\lambda(\boldsymbol{r}) = \sup \frac{f(\boldsymbol{r}|H_1)}{f(\boldsymbol{r}|H_0)}. \tag{3.22}$$

Using the normal probability density function for the constraint residuals $\boldsymbol{r}$, (3.22) can be written as

$$\lambda(\boldsymbol{r}) = \sup_{\boldsymbol{e}_i, b} \frac{\exp\left\{-\frac{1}{2}\boldsymbol{\varrho}_i^T(k)\boldsymbol{\Sigma_r}^{-1}\boldsymbol{\varrho}_i(k)\right\}}{\exp\left\{-\frac{1}{2}\boldsymbol{r}^T(k)\boldsymbol{\Sigma_r}^{-1}\boldsymbol{r}(k)\right\}}, \tag{3.23}$$

where

$$\boldsymbol{\varrho}_i(k) = \boldsymbol{r}(k) - \boldsymbol{F}_i\boldsymbol{b}. \tag{3.24}$$

For simplicity, define

$$T = 2\ln\lambda(\boldsymbol{r}) = \sup_{\boldsymbol{e}_i} T_i, \tag{3.25}$$

where

$$T_i = \boldsymbol{r}^T(k)\boldsymbol{\Sigma_r}^{-1}\boldsymbol{r}(k) - \sup_{\boldsymbol{b}} \boldsymbol{\varrho}_i^T(k)\boldsymbol{\Sigma_r}^{-1}\boldsymbol{\varrho}_i(k). \tag{3.26}$$

The maximum likelihood estimates of the fault magnitudes $\hat{\boldsymbol{b}}$ is obtained by equating the first derivative of (3.26) with respect to $\boldsymbol{b}$ to zero, and is

$$\hat{\boldsymbol{b}} = (\boldsymbol{F}_i^T\boldsymbol{\Sigma_r}^{-1}\boldsymbol{F}_i)^{-1}(\boldsymbol{F}_i^T\boldsymbol{\Sigma_r}^{-1}\boldsymbol{r}(k)), \tag{3.27}$$

and the corresponding test statistics are

$$T_i = (\boldsymbol{F}_i^T\boldsymbol{\Sigma_r}^{-1}\boldsymbol{r}(k))^T(\boldsymbol{F}_i^T\boldsymbol{\Sigma_r}^{-1}\boldsymbol{F}_i)^{-1}(\boldsymbol{F}_i^T\boldsymbol{\Sigma_r}^{-1}\boldsymbol{r}(k)). \tag{3.28}$$

The Type-I error probabilities for each of the test statistics are given by

$$\alpha_i(k) = \Pr(\chi_g^2 \geq T_i(k)), \tag{3.29}$$

where χ_g^2 is a random variable following a central chi-square distribution with g degrees of freedom. The combination i chosen out of $\{i_1 = 1, ..., n; i_1, i_2 = 1, ..., n,\ i_1 \neq$

$i_2; ...; i_1, i_2, ..., i_g = 1, ..., n, i_1 \neq i_2 \neq ... \neq i_g\}$ and corresponding to minimum Type-I error probability gives the number and locations of faults and the corresponding bias magnitudes. From the outcomes of GLR method, two versions for FDI are possible:

1. Compensation for faults: Constraint residuals compensated for faults are formulated from original residuals as $\boldsymbol{r}_c(k) = \boldsymbol{r}(k) - \boldsymbol{F}_g(k)\hat{\boldsymbol{b}}(k)$. These residuals can be substituted in (3.5) in place of $\boldsymbol{Ay}(k)$, so that reconciled estimates are obtained. This approach is known as GLR-Compensation method [63], denoted here as GLR-C.

2. Elimination of faults: Eliminate signals in faults with the help of $Q - R$ factorization explained in Sec. 3.2, to get the reconciled estimates. This method is denoted here as GLR-E.

The flowchart of the GLR method with reference to above steps is shown in Fig. 3.2.

3.3.2 IMT

IMT has two sub-problems, *viz.*, detection problem and multiple fault identification problem. IMT uses an iterative method for identification of multiple faults. However, the number of allowable faults at the most is m, since the faulty variables need to be discarded and, thus, there is no analytical redundancy if there are faults equal to m (model order or the number of rows of matrix $\boldsymbol{A}$). When H_0 is rejected in one of the measurements, that variable is declared as faulty and is added to a set of faulty signals, which are eliminated from the DR problem with the help of $Q - R$ factorization [2, 69], leading to a reduced DR problem. In the next step of iteration, a check for a single fault in one of the remaining variables is carried out. The procedure is continued either till no additional fault is found or till the declared number of faults is less than the model order m. On the other hand, when H_0 is not rejected, IMT declares the hypothesis of no gross error. The IMT algorithm is summarized as follows:

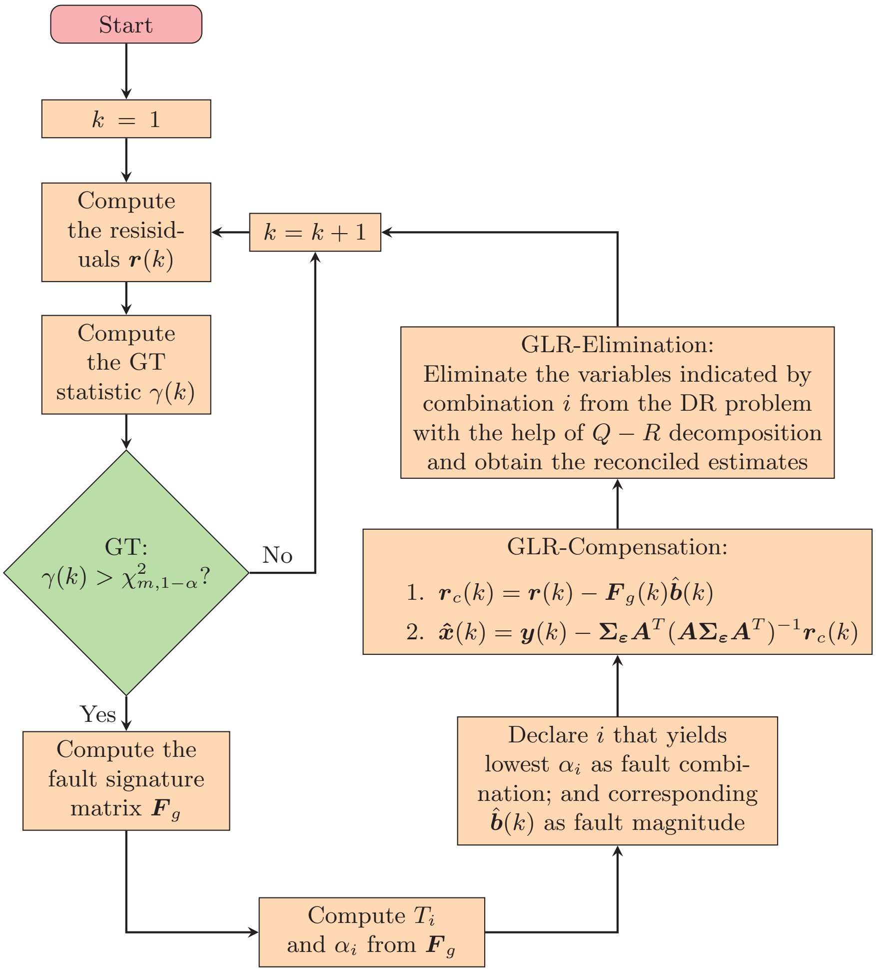

Figure 3.2: Flowchart of GLR method

Suppose either $\boldsymbol{A}_P$ or $\boldsymbol{A}_I$ is considered as the constraint model $\boldsymbol{A}$. Let S be the set of all the healthy measurements, C be the set of all faulty measurements and T be the set of measured variables in the reduced DR problem. Initially T has all the measurements and C is empty.

1. Solve for reconciled estimates from (3.5) and measurement adjustments from (3.6). Now determine the test statistics with maximal power [65, 109]

$$\boldsymbol{d}(k) = \boldsymbol{\Sigma}_{\boldsymbol{\varepsilon}}^{-1}\boldsymbol{a}(k) \tag{3.30}$$

and covariance matrix of $\boldsymbol{d}(k)$, given by

$$\boldsymbol{\Sigma_d} = \boldsymbol{A}^T(\boldsymbol{A}\boldsymbol{\Sigma_\varepsilon}\boldsymbol{A}^T)^{-1}\boldsymbol{A}. \tag{3.31}$$

2. Compute the measurement test statistics

$$z_{d,j}(k) = \frac{|d_j(k)|}{\sqrt{\Sigma_{d,(j,j)}}} \tag{3.32}$$

for each measurement j in the set T, where $d_j(k)$ is the j^{th} element of $\boldsymbol{d}(k)$ and $\Sigma_{d,(j,j)}$ is the j^{th} diagonal element of $\boldsymbol{\Sigma_d}$. Each $z_{d,j}(k)$ follows a standard normal distribution under H_0.

3. Compare each $z_{d,j}(k)$ with the critical test value $Z_c = Z_{1-\frac{\bar{\beta}}{2}}$, where $\bar{\beta} = 1-(1-\alpha)^{1/n_h}$ is the modified level of significance [56] for a Type I error probability α, and n_h is the number of healthy measurement signals in T. If $|z_{d,j}(k)| \leq Z_c \forall j \in T$, proceed to step 5. Otherwise, select the signal corresponding to the largest value of $|z_{d,j}(k)|$ and add it to the set C of faulty signals. If two or more signals have the same maximum value of $|z_{d,j}(k)|$, select the one with the lowest index j.

4. Remove the measurements contained in C from set S, and solve for reduced DR problem by using the projection matrix $\boldsymbol{P}$ as explained in Section 3.2.2. Obtain T, the set of measurements in the reduced DR problem, $\hat{\boldsymbol{x}}_p(k)$ from (3.14) and $\boldsymbol{u}_{r_u}(k)$ suitably from either (3.15) or (3.16). Also the vectors $\boldsymbol{a}(k)$ and $\boldsymbol{d}(k)$ corresponding to these measurements are computed from (3.6) and (3.30). Go to Step 2.

5. The measurements $y_f(k)\ \forall f \in C$ are suspected of containing faults. The estimates of healthy and faulty measurement signals after removal of the variables in C are those obtained in Step 4 of the last iteration.

The flowchart of IMT is shown in Fig. 3.3.

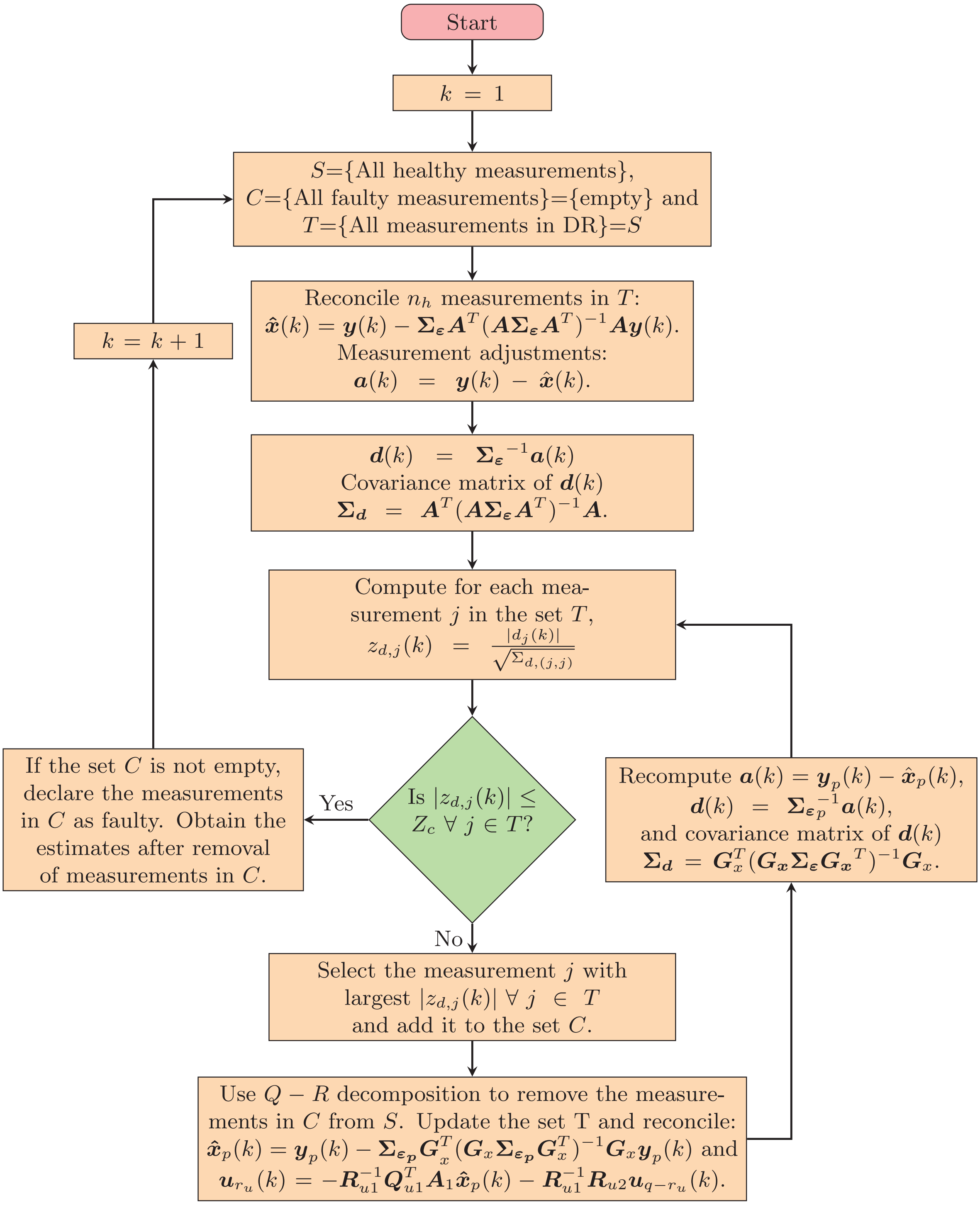

Figure 3.3: Flowchart of IMT

3.3.3 IPCT

Principal component tests are especially intended for detection and identification of subtle gross errors, that are not traced by other techniques [113]. Principal component test uses the PCA on measurement adjustments given in (3.6). IPCT, which is a modification of the principal component test for better isolation of faulty sensors, is explained in the following:

The measurement adjustments are considered for the generation of test statistics and principal components are derived from the covariance matrix $\boldsymbol{\Sigma_a}$ of the same [113], given by $\boldsymbol{\Sigma_a} = \boldsymbol{\Sigma_\varepsilon A}^T \boldsymbol{\Sigma_r}^{-1} \boldsymbol{A\Sigma_\varepsilon}$. Singular value decomposition is performed on $\boldsymbol{\Sigma_a}$, denoted by

$$[\boldsymbol{H}, \boldsymbol{N}, \boldsymbol{J}] = \mathrm{svd}(\boldsymbol{\Sigma_a}), \tag{3.33}$$

where $\boldsymbol{H}$ is the $n \times n$ matrix of left singular vectors, $\boldsymbol{N}$ is an $n \times n$ matrix containing the n non-zero singular values ordered from the largest to the smallest along the diagonal, and $\boldsymbol{J}$ is an $n \times n$ matrix of right singular vectors. Principal components are derived as

$$z(k) = \boldsymbol{D}^T \boldsymbol{a}(k), \tag{3.34}$$

where $\boldsymbol{D} = \boldsymbol{H}_1 \boldsymbol{N}_1^{-1/2}$; $\boldsymbol{H}_1$ and $\boldsymbol{N}_1$ are the matrices holding the first r_a columns of $\boldsymbol{H}$ and the diagonal sub-matrix of $\boldsymbol{N}$ holding the dominant singular values corresponding to $\boldsymbol{H}_1$, where r_a is the rank of $\boldsymbol{\Sigma_a}$. Faults can be detected and identified in measurements by inspecting the contribution from j^{th} adjustment $a_j(k)$ to a suspect principal component i, calculated as

$$g_{i,j}(k) = \boldsymbol{D}_{i,j} a_j(k),\ j = 1, ..., n, \tag{3.35}$$

where $\boldsymbol{D}_{i,j}$ is the j^{th} element of i^{th} singular vector in $\boldsymbol{D}$. For this principal component i, let $\boldsymbol{g}_i'(k)$ be the same as the principal component statistic vector $\boldsymbol{g}_i(k) = [g_{i,1}(k)\ g_{i,2}(k)...g_{i,n}(k)]$, except that its elements are sorted in descending order based on their absolute values. The contributions of signals to principal components, are revealed from $\boldsymbol{G}'(k) = \{\boldsymbol{g}_i'(k), \forall i = 1, ..., r_a\}$.

The identification is carried out as follows: Based on Sidak's inequality [65], a χ^2 variable with assumed confidence level (generally 95%; Type I error probability $\alpha = 0.05$) with r_a degrees of freedom, is taken as the threshold Z_c. Those principal components in $z(k)$ for which the statistic given by (3.34) exceeds the threshold, are the suspect principal components, *i.e.*, in all columns of $\boldsymbol{G}'(k)$ the first few components whose sum exceeds the threshold are found. In other words, in suspect principal components, those variables whose contributions are dominant enough for the test statistic to exceed the threshold are the variables identified to have faults.

However, incorrect identification may be possible with the above formulation. To minimize this, it is proposed to adopt the following iterative procedure, since for n_f number of suspected measurements, $2^{n_f} - 1$ combinations are possible each representing a fault scenario (*e.g.*, for 3 suspicious faulty measurements $1, 2$ and 3, the 7 possible combinations are: $\{1\}, \{2\}, \{3\}, \{1, 2\}, \{1, 3\}, \{2, 3\}$ and $\{1, 2, 3\}$.).

1. Identify all $2^{n_f} - 1$ fault combinations. Choose a combination with number $c = 1$ and take an empty set O.

2. Let T_c be the set of all healthy signals for combination c. Eliminate the variables pointed by the chosen fault combination, such that a reduced DR problem arises, as explained in Sec. 3.2.

3. Calculate the measurement adjustments $\boldsymbol{a}_c(k) = \boldsymbol{y}_c(k) - \hat{\boldsymbol{x}}_c(k)$, where $\boldsymbol{y}_c(k)$ and $\hat{\boldsymbol{x}}_c(k)$ are the vectors of measurements and reconciled estimates respectively for the reduced DR problem [12] corresponding to T_c. Compute covariance matrix of $\boldsymbol{a}_c(k)$, given by

$$\boldsymbol{\Sigma}_{\boldsymbol{a}c} = \boldsymbol{\Sigma}_{\boldsymbol{\varepsilon}c}\boldsymbol{G}_{xc}^T(\boldsymbol{G}_{xc}\boldsymbol{\Sigma}_{\boldsymbol{\varepsilon}c}\boldsymbol{G}_{xc}^T)^{-1}\boldsymbol{G}_{xc}\boldsymbol{\Sigma}_{\boldsymbol{\varepsilon}c}, \tag{3.36}$$

   where $\boldsymbol{\Sigma}_{\boldsymbol{\varepsilon}c}$, $\boldsymbol{G}_{xc}$ are the measurement error covariance matrix and the reduced constraint matrix, respectively for combination c.

4. Perform singular value decomposition of $\boldsymbol{\Sigma}_{\boldsymbol{a}c}$, denoted by $[\boldsymbol{H}_c, \boldsymbol{N}_c, \boldsymbol{J}_c] = \text{svd}(\boldsymbol{\Sigma}_{\boldsymbol{a}c})$, where all the quantities on LHS are analogous to those in (3.33) with appropriate dimensions.

5. Derive the principal components as $\boldsymbol{z}_c(k) = \boldsymbol{D}_c^T \boldsymbol{a}_c(k)$, where all the quantities are analogous to those in (3.34).

6. Find whether the new principal components exceed the threshold. If $|z_{c,j}(k)| \leq Z_c \forall j \in T_c$, add c to set O.

7. If $c = 2^{n_f} - 1$, conclude the algorithm. Otherwise, increment c by 1 and go to step 2.

After considering all the combinations, set O contains all the combinations of faulty variables removal of which results in no further alarm regarding the faults. Since the number of faulty variables is assumed to be as low as possible for a well maintained plant, a combination in set O with least number of variables is declared as the faulty measurement combination. In case of many combinations having least number of variables, declare a combination c among them for which the inner product of adjustment vector, given by $\boldsymbol{a}_c^T(k)\boldsymbol{a}_c(k)$ is minimum. The idea behind this approach is that, if exact faulty detectors are eliminated, variables in reduced DR problem have only random errors leading to minimum adjustments to the retained measurements. The flowchart of IPCT is shown in Fig. 3.4.

For successful FDI, the number of faults must not exceed m, the model order. However, for good identification rate, the number of faulty detectors (g) should be less than one-half of n, the total number of detectors, *i.e.*, $g < \frac{n}{2}$. In addition, 100% identification rate may not be achieved for $g = \frac{n}{2}$. This is because for $g \geq \frac{n}{2}$, the number of healthy detectors $(n-g) \leq g$, and these minority detectors might wrongly be portrayed as faulty detectors by g number of actual faulty detectors with their unbroken covariance structures. However, incorrect identification may be possible with the above FDI techniques

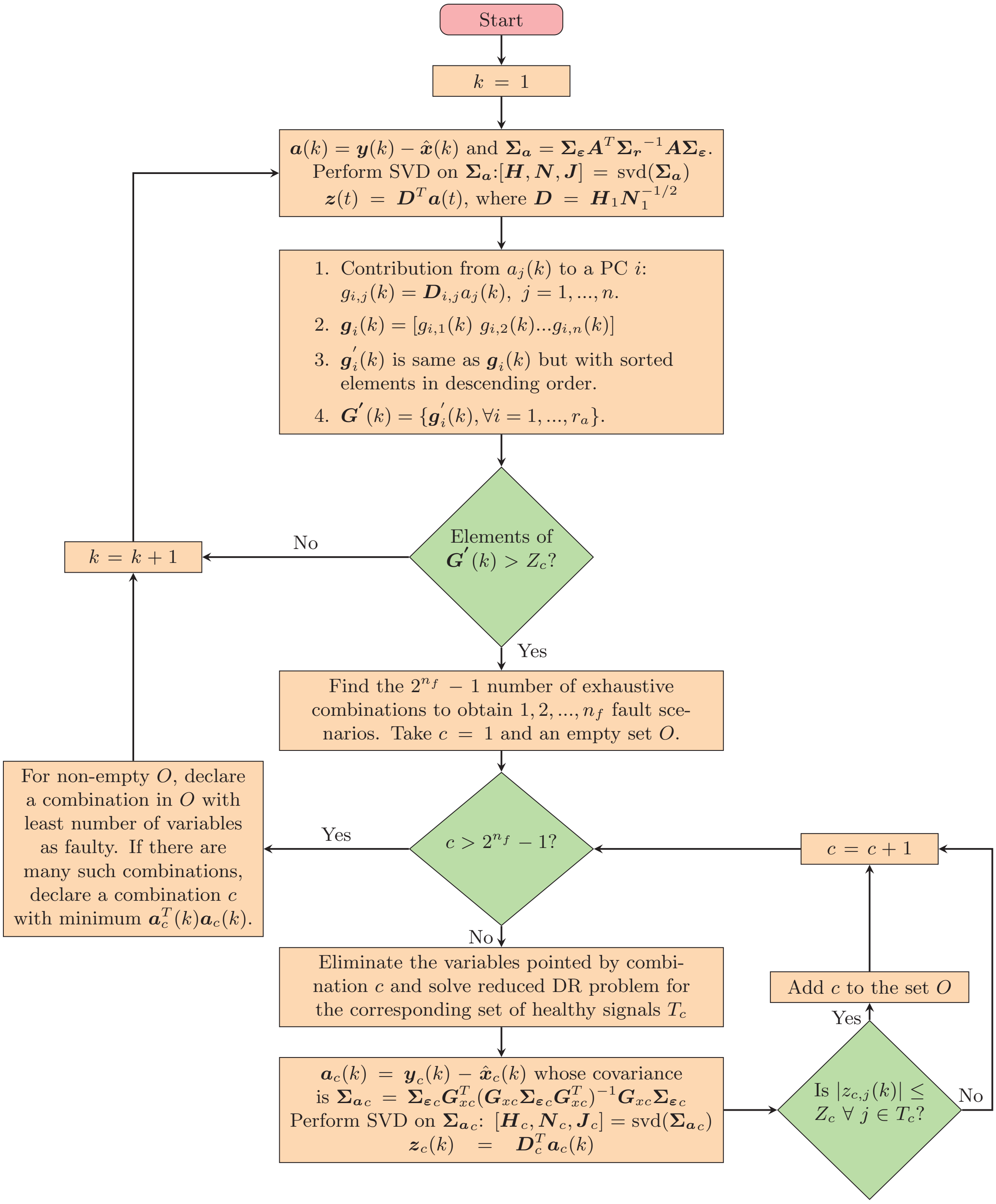

Figure 3.4: Flowchart of IPCT

and probability of correct identification largely depends on the columns of the constraint model and magnitude of the fault [33]. Evaluation of the above FDI techniques needs to be carried out through simulations. In Chapter 5, evaluation results of all the above FDI methods are presented based on extensive simulations. The following FDI indices can be computed for the evaluation of the performances of the FDI techniques.

1. *Overall Detection Rate (ODR):* It is the percentage of detection of one or more faults or rejection of H_0 out of total number of trials. It involves detection, even during the cases where H_0 is true.

2. *Overall Power (OP):* It is the percentage of trials when one or more faults are correctly identified for a true H_1.

The following are the desirable properties of the FDI indices:

1. ODR should be close to 100%.

2. OP should be close to 100%.

3.4 Clustering the VSPND Data

Since there is no stand point in selection of the clustering algorithm or method and as selection completely depends on one's expertise in the solution, the popular $k-$means algorithm is chosen for clustering the large number of VSPNDs of AHWR. This algorithm is centroid-based and falls under non-hierarchical clustering techniques. According to this method, the number of clusters k is chosen in advance. Then k centroids (points of mean) of the data are randomly chosen. The matrix $\boldsymbol{Y} \in \mathbb{R}^{n\times N}$, where n is the number of items (or detector signals for the case of $\boldsymbol{Y}$ being a measurement matrix) and N is the number of observations, is supplied to the $k-$means algorithm. It may be noted that in applications like FDI, it is the items, rather than the observations, that must be grouped. Hence, the data is visualized as n items in N dimensional space. The algorithm is explained as follows:

1. The items are assigned to one of the k clusters.

2. The Euclidean distance between each item to all the centroids are computed. An item is assigned to the cluster whose centroid is nearest. The centroids are recalculated for the cluster receiving the item and for the cluster loosing the item.

3. Step-2 is repeated until no more reassignments of the items take place.

The procedure for selection of number of clusters into which the items are to be grouped is described in the following: The $k-$means algorithm is run for values of number of clusters from 1 to k_f. It should be noted here that k_f is any number less than n. In each case, for each cluster, the quantity $1 - \bar{\rho}_{min}$ is calculated, which gives maximum spread within each cluster, where $\bar{\rho}_{min}$ is the minimum pair-wise correlation between two items in the cluster. Then, average of $1 - \bar{\rho}_{min}$ is taken over all the clusters, which is averaged maximum spread. The averaged maximum spread is plotted against the number of clusters, and the cluster configurations near the knee point of the curve are taken as the candidates for the final number of clusters.

3.5 Discussions

The general techniques for development of steady-state constraint relations among the detector signals are discussed and the constraint models are derived. The DR problem that utilizes the constraint model for the accurate estimates of the measurements has been addressed under the situations of both healthy and faulty detectors. A fault detection and diagnosis scheme should also work in a coordinated manner with the DR scheme for the timely detection and location and identification of the faults.

The above techniques can be applied to the ion chamber and VSPND data of the AHWR for the assessment of the performance. However, for the VSPND data a clustering scheme has been suggested, which can achieve better performance when applied on individual clusters or groups of VSPND worked out based on the correlations among the signals. The next chapter derives a dynamic model of AHWR, which helps in the generation of data for the development of the constraint model, the key concept in DR-based FDI.

Chapter 4

The AHWR and its Modeling

The AHWR, designed with the aim of direct utilization of large thorium reserves in India, uses uranium-thorium and plutonium-thorium mixed oxide fuel [103]. The reactor employs various passive safety features for decay heat removal and mitigation of postulated accident conditions. Removal of core heat by natural circulation, another passive feature, makes the reactor to be of vertical type.

There are three regions with burn-up decreasing towards the periphery of the core. Control of reactivity in AHWR is achieved by on-line fuelling, boron dissolved in moderator and control rods. Boron in moderator is essentially used for reactivity management of equilibrium xenon load. In the core, there are 513 lattice locations out of which 452 are meant for fuel assemblies and the remaining 61 are reserved for control rods, as shown in Fig. 4.1. Control rods include Regulating Rods (RRs), Absorber Rods and Shim Rods, each are 8 in number; and 37 Shut-Off Rods. RRs are used to regulate the rate of nuclear fission, Absorber Rods and Shim Rods, fully inside and outside the core respectively, are used to meet the reactivity demands beyond the worth of RRs. RRs, Absorber Rods and Shim Rods are used by RRS; Shut-Off Rods are used by SDS-1. SDS-2, another independent protection system, is based on liquid poison injection into

A part of this chapter was published in *2013 IEEE International Conference on Control Applications (CCA)*, Hyderabad, India.

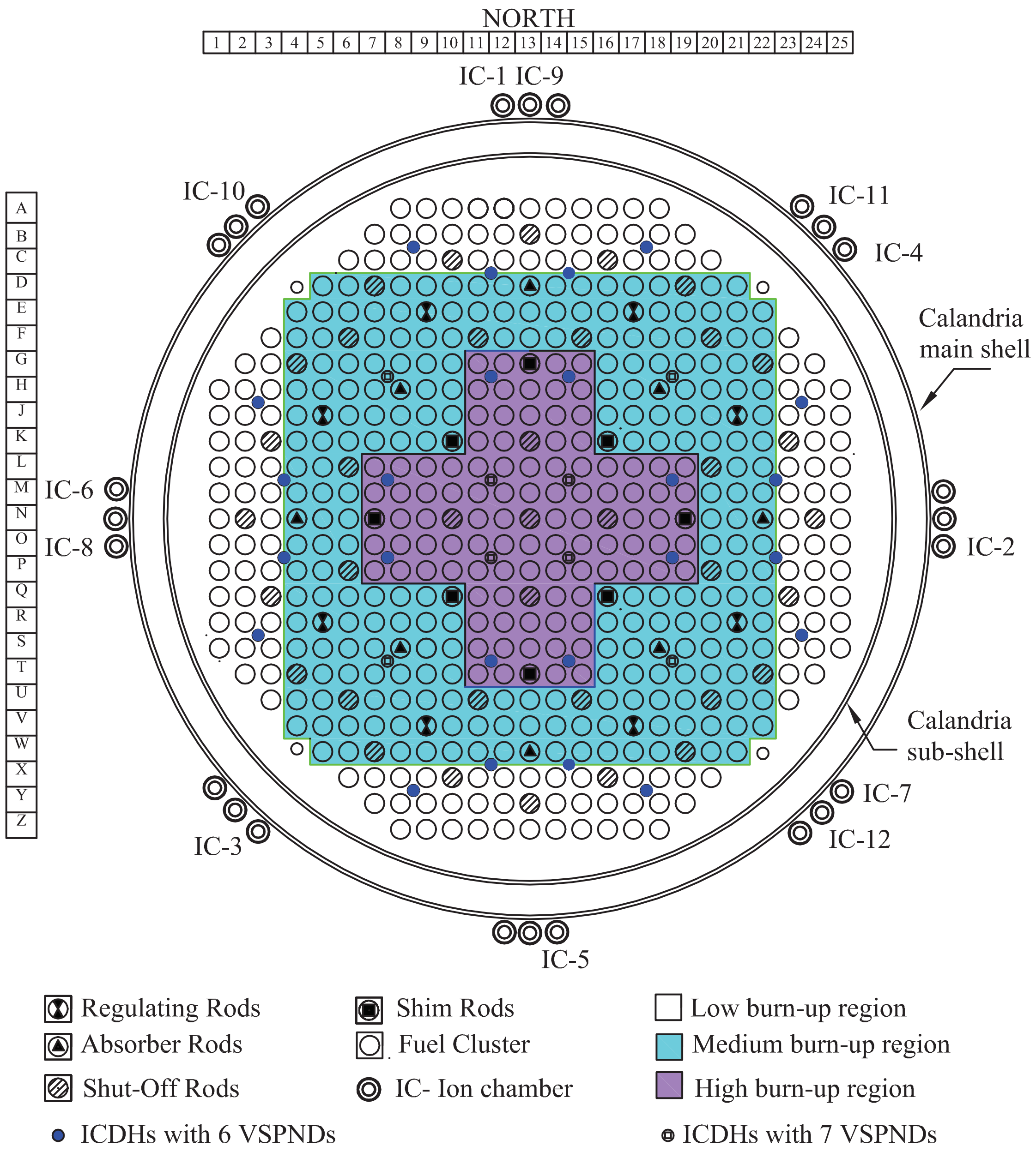

Figure 4.1: Core map with detector locations

the moderator. The radially large AHWR core is placed in a vessel called calandria containing heavy water (D_2O), which acts both as the moderator and the reflector. The calandria is in turn surrounded by a light water filled vault that acts as an effective radiation shield.

The neutronic instrumentation system of AHWR monitors the power levels from 5×10^{-14} FP to 5×10^{-6} FP with the help of start-up detectors; and from 5×10^{-8} FP to 1.5 FP with the help of power range detectors. The reactor is under manual control when the power is in start-up range, and under manual as well as automatic control when it lies in power range. In this thesis, since the DR-based FDI is a part of automation, the detectors in power range are of importance. Hence the discussion is restricted to boron coated ion chambers with gamma compensation and VSPNDs, which are the ex-core and in-core detectors in power range, respectively. In this chapter, a mathematical model of AHWR is developed for the simulation of measurement data of the ion chambers and VSPNDs as this data helps in achieving the objectives such as estimation of the core neutron flux and its shape, ensuring non-violation of various safety limits on fuel pellets and fuel clad barriers, validation of algorithms meant for generation of the three dimensional flux map of the entire core alongwith the FDI of the detectors.

4.1 Ion Chambers and VSPNDs of AHWR

The internal construction details and the fault modes of the ion chambers and VSPNDs of AHWR are given in this section.

4.1.1 Ion Chambers

Standard ex-core ion chambers are almost insensitive to core leakage flux due to low neutron interaction probability in the usual filling gases [1]. Hence, Boron-10 coated ion chambers are generally used. They work on the principle that Boron-10 and filling gas respectively get ionized as a result of the neutron flux and gamma radiation and thereby emit alpha particles. The collection of these particles result into an electrical signal proportional to the radiation dose. However, determination of slow neutron flux,

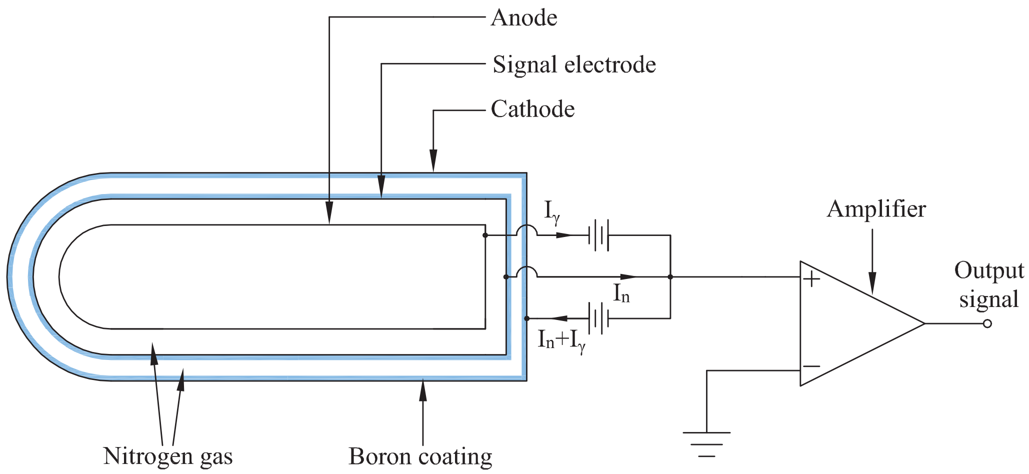

Figure 4.2: Basic configuration of ion chambers.

which is representative of the core average flux, is difficult due to the presence of high gamma radiation. Boron-10 coated gamma compensated ion chambers alleviate this problem. These detectors, which are also used in AHWR, necessitate the construction of a segmented ion chamber for the simultaneous measurement of the core leakage flux and the gamma radiation, such that one segment of this detector is boron-lined, sensitive to both neutrons and gamma-rays; the other is an ordinary ion chamber capable of measuring only the gamma flux. The detectors consist of three coaxial cylindrical Aluminium electrodes as shown in Fig. 4.2 with the annular volume filled with Nitrogen gas so that a polarized voltage results in current flow. The outer and inner electrodes are cathode and anode respectively, and the middle electrode is called the signal electrode. The inner surface of cathode and the outer surface of signal electrode are coated with Boron-10. The gamma radiation induced current I_γ is then subtracted from the total current $I_n + I_\gamma$ to obtain the neutron induced current I_n.

Some of the major fault modes of the ion chambers are listed as follows:

1. *Leakage of gas:* Leakage of gas from the volume of ion chamber results in reduction of the insulation resistance. This could result in high leakage current.

2. *Changes in the operating pressure:* Reduction in operating pressure lowers the insulation resistance thereby results into high leakage current.

3. *Humidity:* Humidity reduces the insulation resistance and thereby increases the leakage current from the ion chamber.

4. *Changes in the polarization voltage:* Ion chamber signal is directly related to the polarization voltage. Any change in polarization voltage leads to degraded signal from the ion chamber.

5. *Radiation damage:* Contamination of the anode and cathode components by dissociation products of avalanche reactions degrades the ion chamber signals.

6. *High temperature:* Leakage current increases with high temperatures. This makes the ion chamber signal faulty.

7. *High neutron flux:* This introduces non-linearity in the relationship between the flux and current. This degrades the ion chamber signal.

8. *Vibration and shock:* Mechanical shocks against high voltage detector cables or detectors themselves result in large noise pulse. This may be interpreted as a faulty signal.

4.1.2 VSPNDs

In SPNDs, current is generated by means of emission of beta particle or an electron by the emitter material as a result of interactions with neutron flux and gamma radiation. This current is measured between the emitter and an outer shell or sheath, called the collector. The intervening space is filled with an insulator that can withstand extreme temperature and radiation environment in the reactor core. Performance of SPNDs is solely governed by the choice of emitter material. The material with a moderate capture cross section should be selected, because a too high value results in rapid burnup and a too low value leads to detectors with low sensitivity. Also, the half-life of the induced activity should be as short as possible for the quick response and sufficiently high energy beta rays should be produced to avoid self absorption.

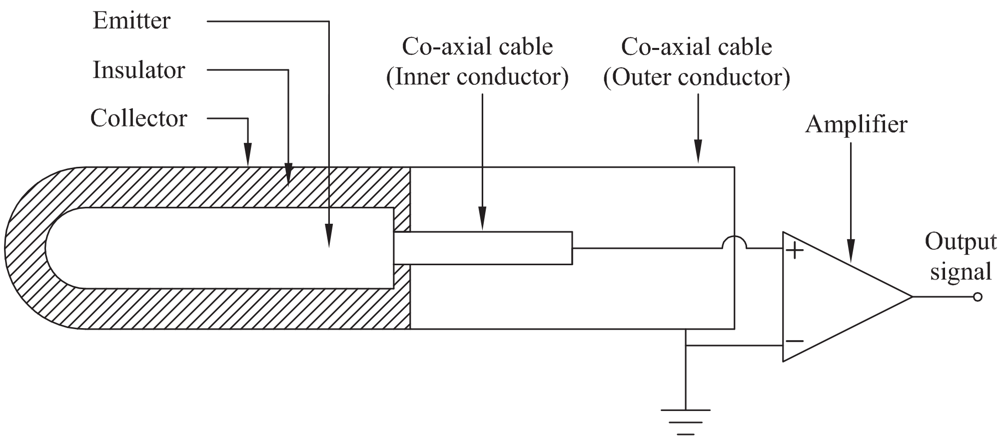

Figure 4.3: Basic configuration of VSPNDs.

In a VSPND, the in-core detector in power range for AHWR, the material of emitter is Vanadium. A typical VSPND, as shown in Fig. 4.3, has a co-axial configuration with four parts, *viz.*, emitter, insulation, collector, and mineral insulated co-axial cable. Generally Magnesium Oxide (MgO) or Aluminium Oxide (Al_2O_3) are used as insulator and Inconel as the sheath [60].

The following are the different fault modes of the in-core SPNDs [6, 116]:

1. *Sensitivity changes:* Sensitivity (S_v) is the current signal produced per unit neutron flux received in a unit length of the SPND. With increase in fluence, the sensitivity is observed to reduce because of burn-up of emitter material. It can be compensated by increasing the amplifier gain.

2. *Reduction in insulation resistance:* Insulation resistance reduces from the nominal value (of the order of 10^{12} ohms) mainly due to moisture contamination. This increases the leakage current thereby reducing the signal from the SPND. This has a gradual effect on the SPND signal.

3. *Failure of seal:* Detectors are filled with inert gases such as helium and sealed in order to avoid corrosion. When seal gets deteriorated, conducting media like air and moisture replace the inert gas thereby corrupting the signal.

4. *Corrosion:* Because of oxidizing and nitriding atmosphere surrounding the SPND assembly, embrittlement of the Inconel sheath may happen when encapsulation deteriorates. This gradually deteriorates the signal.

5. *Ageing and activation products:* Due to activation products, sheath and electrode alloys are degraded leading to signal degradation.

6. *Clipping and modulation:* The SPND signal may be restricted at a particular level or the signal may be modulated because of saturation of either the SPND or the associated electronic circuitry. These effects are similar to faults in the SPNDs.

7. *Bias error:* Sudden jumps in the signal due to degradation of either the SPND or the associated electronic circuitry can also manifest as faults in the SPNDs.

All the faults listed in the above subsections give rise to either a sudden change or a slow change in the signals of the detectors. Though it is desirable to find out a FDI method capable of detecting all these faults, formulating such strategy is rather impractical due to computational limitations. However, since all these faults eventually lead to a bias, a bias detection scheme is generally adequate. Hence, FDI techniques for bias detection are presented in the subsequent chapters.

4.2 Locations of Neutron Detectors in AHWR

There are 8 out-of-core locations containing 9 ion chambers, with 3 detectors each for the RRS, SDS-1 and SDS-2. There are 3 more spare ion chambers with one for each of the RRS and SDSs. Ion chambers are placed in vault water around the calandria vessel [103], in lattice tubes placed close to calandria as shown Fig. 4.1. Hence, each ion chamber gives a current signal proportional to the core leakage flux at its location, which is representative of the core average flux. Ion chambers 1, 2 and 3 are for RRS; ion chambers 4, 5 and 6 are for SDS-1; ion chambers 7, 8 and 9 are for SDS-2; ion

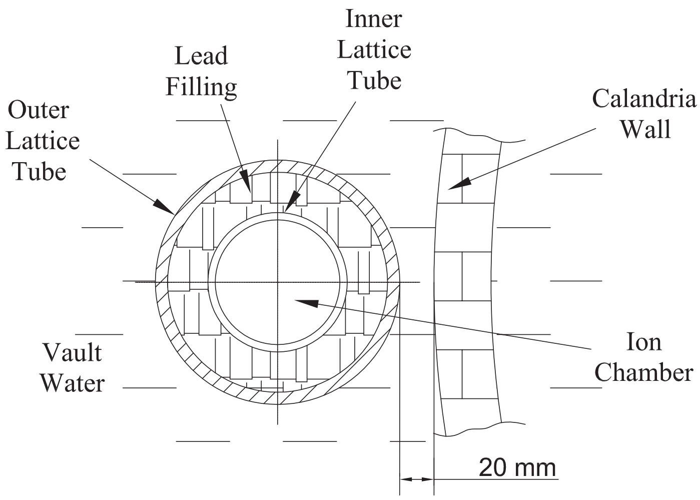

Figure 4.4: Location of an ion chamber near calandria (Top view).

chambers 10, 11 and 12 are the respective spare detectors for RRS, SDS-1 and SDS-2. The aluminium lattice tubes of ion chambers are positioned vertically and are to be installed through stainless steel lattice tubes provided in the top end shield, with lead filling separating the inner and outer tubes. The outer lattice tube for the ion chamber housing extends to an elevation of 700 mm below the centre of the AHWR fuel assembly. As neutron flux attenuates quickly in vault water, these lattice tubes are located close to calandria, at a distance of about 20 mm. The detailed sketch of the ion chamber placement near calandria is given in Fig. 4.4.

On the other hand, 200 VSPNDs for in-core measurement are distributed in different layers in 32 In-Core Detector Housings (ICDHs) at inter-lattice locations surrounded by 4 lattices each, as shown in Fig. 4.1. For each of the ICDHs, the surrounding lattices are indicated in Table 4.1, and the locations are shown in Fig. 4.5(a). Each ICDH can accommodate up to 7 VSPNDs at the positions indicated in Fig. 4.5(b). The VSPNDs, numbered as $V_i,\ i = 1, ..., 200$, are placed in ICDHs at the positions given in Table 4.1. Only eight ICDHs, *i.e.*, ICDHs numbered as 5, 8, 13, 14, 19, 20, 25 and 28 contain 7 SPNDs each while the remaining 24 ICDHs contain 6 VSPNDs each. ICDHs are depicted in Fig. 4.5(a). It can also be observed that each zone (one of the quadrants of the core, shown in Fig. 4.5(a)) contains 50 VSPNDs.

Table 4.1: Placement of 200 number of VSPNDs in 32 ICDHs

ICDH No.	Surrounding lattices	Layer No.							No. of VSPNDs
		Z1	**Z2**	**Z3**	**Z4**	**Z5**	**Z6**	**Z7**	
1	X8, X9, Y8 and Y9	V_1	-	V_{41}	V_{73}	V_{105}	V_{137}	V_{169}	6
2	X17, X18, Y17 and Y18	V_2	-	V_{42}	V_{74}	V_{106}	V_{138}	V_{170}	6
3	W11, W12, X11 and X12	V_3	-	V_{43}	V_{75}	V_{107}	V_{139}	V_{171}	6
4	W14, W15, X14 and X15	V_4	-	V_{44}	V_{76}	V_{108}	V_{140}	V_{172}	6
5	S7, S8, T7 and T8	V_5	V_{33}	V_{45}	V_{77}	V_{109}	V_{141}	V_{173}	7
6	S11, S12, T11 and T12	V_6	-	V_{46}	V_{78}	V_{110}	V_{142}	V_{174}	6
7	S14, S15, T14 and T15	V_7	-	V_{47}	V_{79}	V_{111}	V_{143}	V_{175}	6
8	S18, S19, T18 and T19	V_8	V_{34}	V_{48}	V_{80}	V_{112}	V_{144}	V_{176}	7
9	R2, R3, S2 and S3	V_9	-	V_{49}	V_{81}	V_{113}	V_{145}	V_{177}	6
10	R23, R24, S23 and S24	V_{10}	-	V_{50}	V_{82}	V_{114}	V_{146}	V_{178}	6
11	O3, O4, P3 and P4	V_{11}	-	V_{51}	V_{83}	V_{115}	V_{147}	V_{179}	6
12	O7, O8, P7 and P8	V_{12}	-	V_{52}	V_{84}	V_{116}	V_{148}	V_{180}	6
13	O11, O12, P11 and P12	V_{13}	V_{35}	V_{53}	V_{85}	V_{117}	V_{149}	V_{181}	7
14	O14, O15, P14 and P15	V_{14}	V_{36}	V_{54}	V_{86}	V_{118}	V_{150}	V_{182}	7
15	O18, O19, P18 and P19	V_{15}	-	V_{55}	V_{87}	V_{119}	V_{151}	V_{183}	6
16	O22, O23, P22 and P23	V_{16}	-	V_{56}	V_{88}	V_{120}	V_{152}	V_{184}	6
17	L3, L4, M3 and M4	V_{17}	-	V_{57}	V_{89}	V_{121}	V_{153}	V_{185}	6
18	L7, L8, M7 and M8	V_{18}	-	V_{58}	V_{90}	V_{122}	V_{154}	V_{186}	6
19	L11, L12, M11 and M12	V_{19}	V_{37}	V_{59}	V_{91}	V_{123}	V_{155}	V_{187}	7
20	L14, L15, M14 and M15	V_{20}	V_{38}	V_{60}	V_{92}	V_{124}	V_{156}	V_{188}	7
21	L18, L19, M18 and M19	V_{21}	-	V_{61}	V_{93}	V_{125}	V_{157}	V_{189}	6
22	L22, L23, M22 and M23	V_{22}	-	V_{62}	V_{94}	V_{126}	V_{158}	V_{190}	6
23	H2, H3, J2 and J3	V_{23}	-	V_{63}	V_{95}	V_{127}	V_{159}	V_{191}	6
24	H23, H24, J23 and J24	V_{24}	-	V_{64}	V_{96}	V_{128}	V_{160}	V_{192}	6
25	G7, G8, H7 and H8	V_{25}	V_{39}	V_{65}	V_{97}	V_{129}	V_{161}	V_{193}	7
26	G11, G12, H11 and H12	V_{26}	-	V_{66}	V_{98}	V_{130}	V_{162}	V_{194}	6
27	G14, G15, H14 and H15	V_{27}	-	V_{67}	V_{99}	V_{131}	V_{163}	V_{195}	6
28	G18, G19, H18 and H19	V_{28}	V_{40}	V_{68}	V_{100}	V_{132}	V_{164}	V_{196}	7
29	C11,C12, D11 and D12	V_{29}	-	V_{69}	V_{101}	V_{133}	V_{165}	V_{197}	6
30	C14, C15, D14 and D15	V_{30}	-	V_{70}	V_{102}	V_{134}	V_{166}	V_{198}	6
31	B8, B9, C8 and C9	V_{31}	-	V_{71}	V_{103}	V_{135}	V_{167}	V_{199}	6
32	B17, B18, C17 and C18	V_{32}	-	V_{72}	V_{104}	V_{136}	V_{168}	V_{200}	6

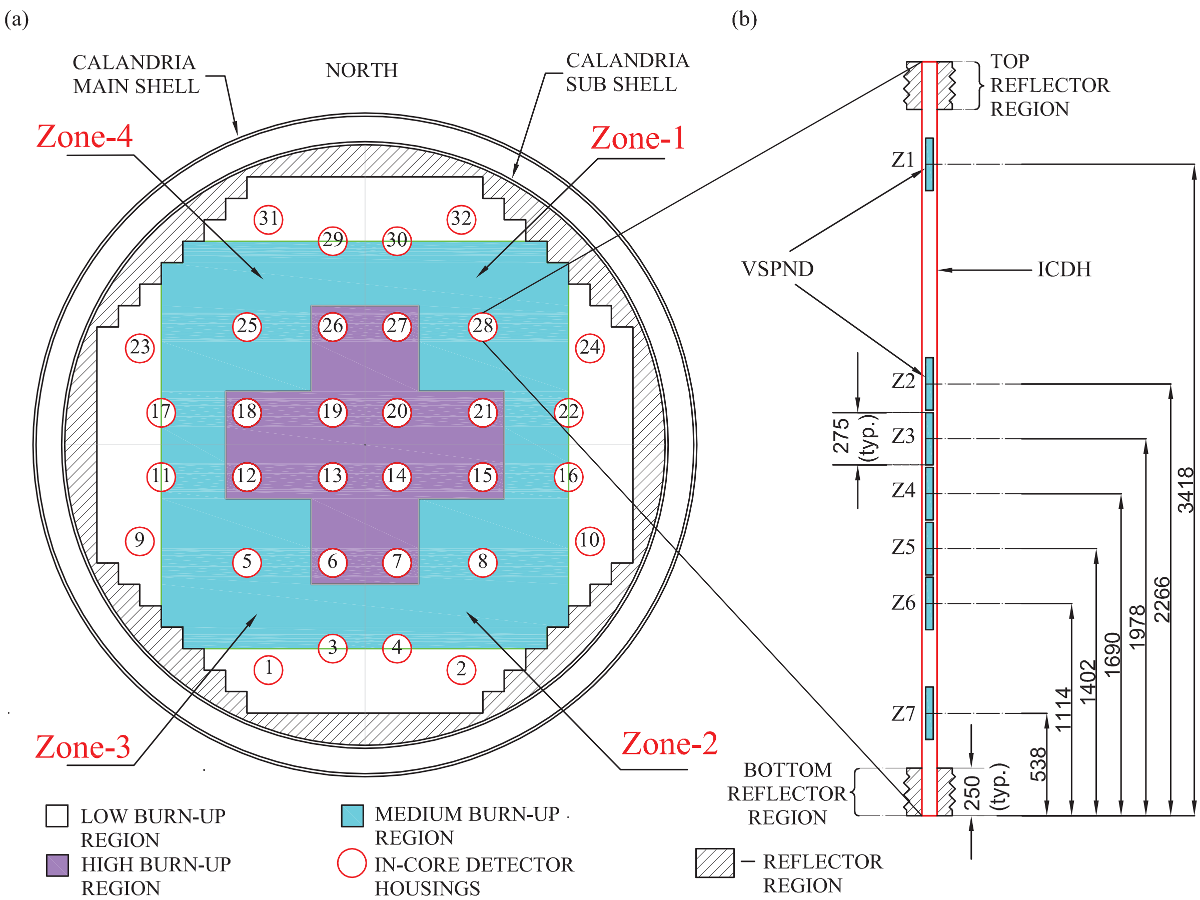

Figure 4.5: (a) Cross-section of the AHWR core, showing the location of ICDHs (schematic) (b) Placement of 7 VSPNDs along an ICDH in AHWR (all the dimensions are in mm).

4.3 Model Derivation for AHWR

The neutrons are born as fast neutrons (having high energy) and eventually slow down to become thermal neutrons. There are numerous other interactions with the matter. Each interaction, *viz.*, absorption, scattering, fission *etc.*, has a certain probability of occurrence called as cross-section. The cross-sections are different for different regions and also for different neutron energies. However, for the usual reactor kinetics modeling, it is adequate to work with two-group neutron fluxes. The nodal model developed in this thesis is in terms of an equivalent flux derived from two-group fluxes.

Benchmark problems and their reference solutions useful for validation of simplified models are not available for AHWR, unlike Light Water Reactors and PHWRs. Hence,

Table 4.2: Dimensional Details of the mesh boxes

S. No.	**Region**	**Dimension (mm)**	
		Height	**Length**
1	Core	143.83	225
2	Side reflector	143.83	133.33
3	Top reflector	133.33	225
4	Bottom reflector	150	225

validation of the mathematical model is carried out by comparing the flux distributions with those generated using more accurate core physics calculation codes such as the FDM. In other words, an FDM similar to that described in [67] is taken as the benchmark. In this FDM, the core including reflector is considered to be divided into 22950 fictitious meshes, distributed in 30 horizontal planes along the axis of the core. The detailed core map with reflector region of one of the planes is shown in Fig. 4.6. First 3 planes from the top and last 3 planes from the bottom respectively form the top and bottom reflector regions. The middle 24 number of meshes in 24 other planes belong to either side-reflector region or the core region, depending on their position in the core, as shown in Fig. 4.6. The dimensional details such as height and length of the 22950 finite difference meshes are given in Table 4.2. In Table 4.2, as the mesh boxes in the side, top and bottom reflector regions are cubicles, the dimension of one of their two sides only is given. However, their width is based on the dimension of the neighbouring mesh boxes. Under nominal steady-state condition, reactor exhibits a quadrant core symmetry in flux distribution and the FDM generates a fast and a thermal flux in each of the 22950 mesh boxes.

4.3.1 The Nodal Method

The AHWR core is considered to be divided into 17 nodes, as shown in Fig. 4.7(a) by the segments labelled from 1 to 17. The top and bottom reflector regions are divided into 17 nodes in an identical pattern as the core, whereas the side reflector region is divided into 8 nodes, giving 59 nodes in total. The side reflector region is shown in Fig.

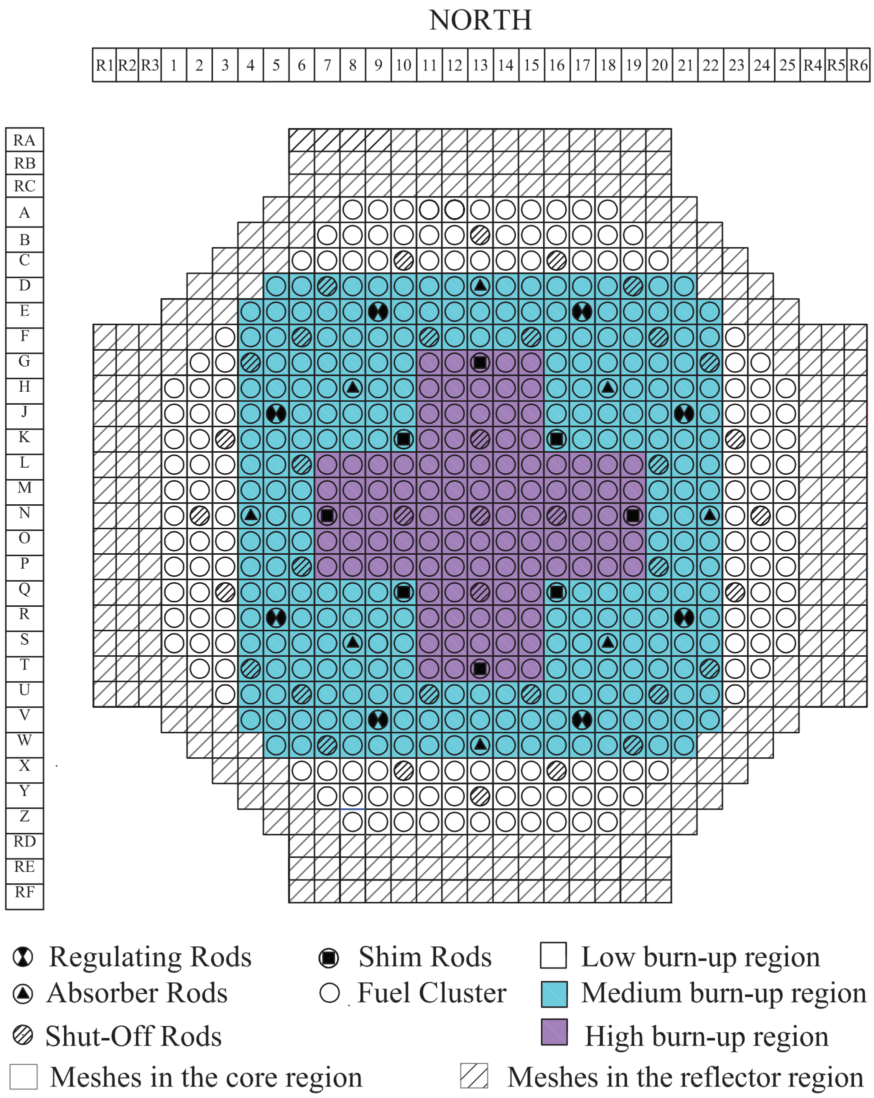

Figure 4.6: Cross-sectional views of AHWR core layout including reflector region (top view).

4.7(a) by the segments labelled from 18 to 25. The top and bottom reflector regions alongwith their nodal division are shown in Fig. 4.7(b) and 4.7(c) respectively.

AHWR operates with a slightly harder spectrum in the epithermal region and the contribution of up-scattering, though small, needs to be accounted. Starting with the two-group neutron diffusion equations and delayed neutron precursor concentration equation, the following set of equations characterizing the nodal model of AHWR

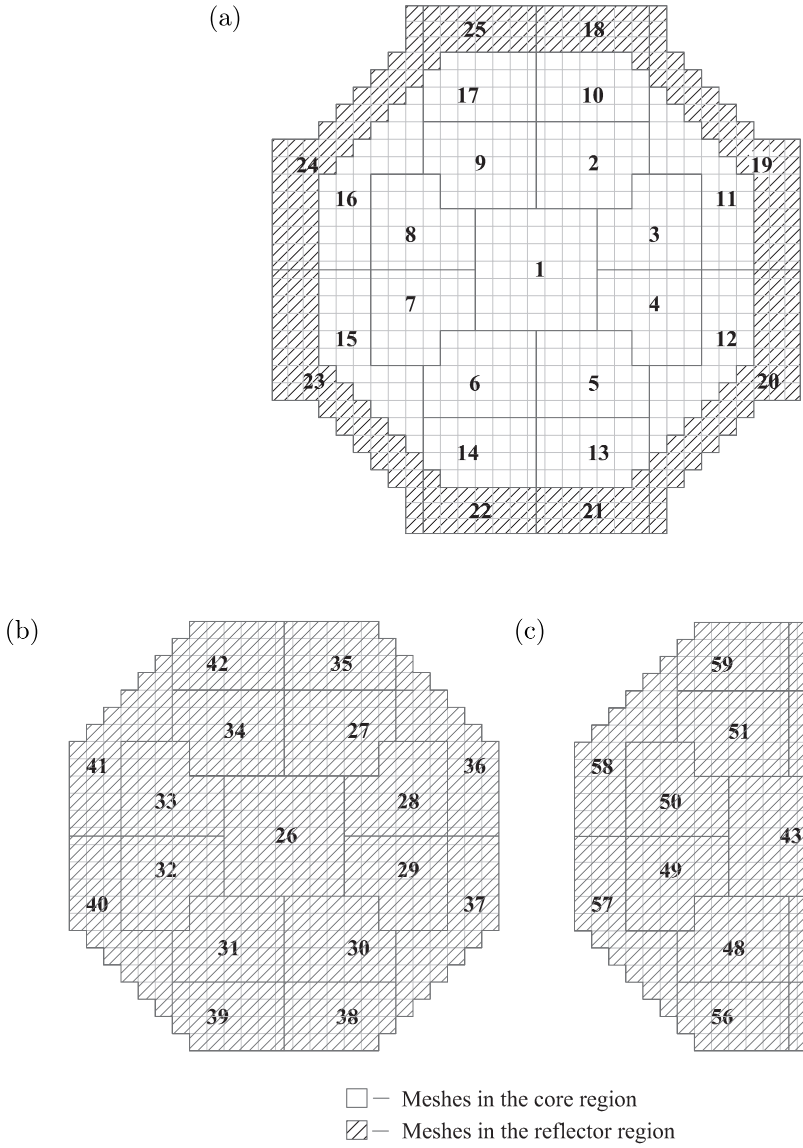

Figure 4.7: 17 node AHWR core nodalization for (a) the active core (17 nodes in core and 8 nodes in side reflector) (b) top reflector region (c) bottom reflector region.

are obtained:

$$\frac{1}{\upsilon_1}\frac{\partial \phi_1}{\partial t} = \nabla D_1 \nabla \phi_1 - \Sigma_{a1}\phi_1 - \Sigma_{12}\phi_1 + \Sigma_{21}\phi_2 + (1-\beta)(\nu\Sigma_{f1}\phi_1 + \nu\Sigma_{f2}\phi_2) + \sum_{i=1}^{m_d} \lambda_i C_i, \quad (4.1)$$

$$\frac{1}{\upsilon_2}\frac{\partial \phi_2}{\partial t} = \nabla D_2 \nabla \phi_2 - \Sigma_{a2}\phi_2 + \Sigma_{12}\phi_1 - \Sigma_{21}\phi_2, \quad (4.2)$$

$$\frac{\partial\ C_i}{\partial t} = \beta_i(\nu\Sigma_{f1}\phi_1 + \nu\Sigma_{f2}\phi_2) - \lambda_i C_i; i = 1, 2, ..., m_d, \quad (4.3)$$

where the subscripts 1 and 2 represent the parameters of fast and thermal group fluxes. υ_g, ϕ_g, D_g, Σ_{ag}, Σ_{fg} are mean velocity of neutrons, neutron flux, diffusion coefficient, absorption cross section, fission cross section for energy group-g, $g = 1, 2$. Σ_{12} and Σ_{21} are the scattering cross sections from group-1 to group-2 and from group-2 to group-1 respectively. ν is the mean number of fission neutrons and $m_d = 6$ is the total number of delayed neutron precursors' groups. C_i, β_i, λ_i are the concentration, fraction and decay constant of delayed neutrons of i^{th} group precursors. Effective fraction of delayed neutrons $\beta = \sum_{i=1}^{m_d} \beta_i$. The neutron fluxes ϕ_1 and ϕ_2 are functions of both space co-ordinates and time. The parameters D_1, D_2, Σ_{a1}, Σ_{a2}, Σ_{f1} and Σ_{f2} are different for different core locations as given in Table 4.3. If the spatial variations of D_1 and D_2 are neglected, $\nabla D_1 \nabla \phi_1 = D_1 \nabla^2 \phi_1$ and $\nabla D_2 \nabla \phi_2 = D_2 \nabla^2 \phi_2$.

The discussion is restricted to the more tractable reactor kinetics problem, hence the coefficients in the partial differential equation system are treated as piecewise constants in space, with possible iterative updating in time in the course of a transient.

When two nodes h and k are considered,

$$D_1 \frac{d^2\phi_1}{du^2} \bar{V}_h = J_u A_{hk}, \tag{4.4}$$

where $\bar{V}_h$ is the volume of the node-h, J_u is the neutron current density in the direction-u and A_{hk} is the area of interface between nodes h and k. From Fick's law,

$$J_u = D_1 \frac{d\phi_1}{du}. \tag{4.5}$$

From (4.4) and (4.5),

$$D_1 \frac{d^2\phi_1}{du^2} = \frac{A_{hk}}{\bar{V}_h} D_1 \frac{d\phi_1}{du} = \frac{D_1 A_{hk}}{\bar{V}_h} \frac{(-\phi_{1h} + \phi_{1k})}{\Delta_{hk}}, \tag{4.6}$$

$$\Rightarrow D_1 \nabla^2 \phi_1|_h = -\omega_{1hh}\phi_{1h} + \sum_{k=1}^{\bar{N}_h} \omega_{1hk}\phi_{1k}, \tag{4.7}$$

and similarly,

$$D_2 \nabla^2 \phi_2|_h = -\omega_{2hh}\phi_{2h} + \sum_{k=1}^{\bar{N}_h} \omega_{2hk}\phi_{2k}, \tag{4.8}$$

where

$\omega_{ghk} = \frac{D_g A_{hk}}{V_h \Delta_{hk}}$ and $\omega_{ghh} = \sum_{k=1}^{\bar{N}_h} \omega_{ghk}$, $g = 1, 2.$; and $\bar{N}_h$ is the number of all the neighbouring nodes to node-h.

Substituting (4.6) to (4.8) in (4.1) and (4.2),

$$\begin{aligned} \frac{1}{\upsilon_1}\frac{d\phi_{1h}}{dt} = -\omega_{1hh}\phi_{1h} + \sum_{k=1}^{\bar{N}_h} \omega_{1hk}\phi_{1k} - (\Sigma_{a1h}\phi_{1h} + \Sigma_{12h}\phi_{1h}) \\ + \Sigma_{21}\phi_2 + (1-\beta)(\nu\Sigma_{f1h}\phi_{1h} + \nu\Sigma_{f2h}\phi_{2h}) + \sum_{i=1}^{m_d} \lambda_i C_{ih}, \end{aligned} \tag{4.9}$$

$$\frac{1}{\upsilon_2}\frac{d\phi_{2h}}{dt} = -\omega_{2hh}\phi_{2h} + \sum_{k=1}^{\bar{N}_h} \omega_{2hk}\phi_{2k} - \Sigma_{a2h}\phi_{2h} + \Sigma_{12h}\phi_{1h} - \Sigma_{21}\phi_2. \tag{4.10}$$

Adding (4.9) and (4.10), and defining equivalent flux $\phi_h = \phi_{1h} + \phi_{2h}$,

$$\left.\begin{aligned} R_h &= \frac{\phi_{2h}}{\phi_{1h}}, \\ \upsilon_h &= \frac{(1 + R_h)}{\left(\frac{1}{\upsilon_1} + \frac{R_h}{\upsilon_1}\right)}, \\ D_h &= \left(\frac{D_{1h} + D_{2h}R_h}{1 + R_h}\right), \\ \omega_{hh} &= \left(\frac{\omega_{1hh} + \omega_{2hh}R_h}{1 + R_h}\right), \\ \omega_{hk} &= \left(\frac{\omega_{1hk} + \omega_{2hk}R_h}{1 + R_h}\right), \\ \Sigma_{ah} &= \left(\frac{\Sigma_{a1h} + \Sigma_{a2h}R_h}{1 + R_h}\right), \\ \Sigma_{fh} &= \left(\frac{\Sigma_{f1h} + \Sigma_{f2h}R_h}{1 + R_h}\right), \end{aligned}\right\} \tag{4.11}$$

lead to

$$\frac{1}{\upsilon_h}\frac{d\phi_h}{dt} = -\omega_{hh}\phi_h + \sum_{k=1}^{\bar{N}_h}\omega_{hk}\phi_k - \phi_h\Sigma_{ah} + (1-\beta)\nu\phi_h\Sigma_{fh} + \sum_{i=1}^{m_d}\lambda_i C_{ih}. \tag{4.12}$$

Delayed-neutron precursor density can be expressed as

$$\frac{dC_{ih}}{dt} = \beta_i\nu\phi_h\Sigma_{fh} - \lambda_i C_{ih}. \tag{4.13}$$

Further defining prompt neutron life-time l_h , multiplication factor K_h and reactivity ρ_h as follows,

$$l_h = \frac{1}{\Sigma_{ah}\upsilon_h}, K_h = \frac{\nu\Sigma_{fh}}{\Sigma_{ah}}, \rho_h = \frac{K_h - 1}{K_h}, \tag{4.14}$$

(4.12) and (4.13) can be written in a modified form as

$$\frac{d\phi_h}{dt} = -\omega_{hh}\upsilon_h\phi_h + \sum_{k=1}^{\bar{N}_h}\omega_{hk}\upsilon_h\phi_k + (\rho_h - \beta)\frac{\phi_h}{l} + \sum_{i=1}^{m_d}\upsilon_h\lambda_i C_{ih}, h = 1, 2, ...Z, \tag{4.15}$$

$$\frac{dC_{ih}}{dt} = \frac{\beta_i\phi_h}{\upsilon_h l_h} - \lambda_i C_{ih}, i = 1, 2, ...m_d. \tag{4.16}$$

Equations (4.15) and (4.16) give the neutronics model of the reactor core without internal feedbacks, where $Z = 17$ is the number of nodes in the core. In reflector nodes, delayed neutron precursors' concentration, fraction of delayed neutrons and reactivity are not considered as there is no fuel material and no direct reactivity introduced into them. Hence, the following equation holds good for the reflector region nodes.

$$\frac{d\phi_h}{dt} = -\omega_{hh}\upsilon_h\phi_h + \sum_{k=1}^{\bar{N}_h}\omega_{hk}\upsilon_h\phi_k, h = Z+1, ..., Z+R, \tag{4.17}$$

where $R = 42$ is the number of nodes in the reflector region. It may be noticed that the total number of model equations would be $Z(m_d + 1) + R$.

In order to account for the reactivity variations due to internal feedbacks and control devices, the reactivity term ρ_h in (4.15) is expressed as the sum of reactivity feedback due

Table 4.3: Two-group cross-section data for different reactor elements (all cross-sections (Σ) in cm^{-1} and diffusion coefficients (D) in cm).

Material	Σ_{a1}	Σ_{a2}	Σ_{f1}	Σ_{f2}	$\nu\Sigma_{f1}$	$\nu\Sigma_{f2}$	Σ_{12}	Σ_{21}	D_1	D_2
Fuel										
High burnup region-top	0.00333	0.0118	0.000815	0.00481	0.00215	0.0126	0.00732	1.55	0.896	0.000221
High burnup region-bottom	0.0035	0.012	0.000803	0.00475	0.00209	0.0124	0.00792	1.55	0.895	0.000218
Medium burnup region-top	0.00332	0.0118	0.000814	0.0048	0.00213	0.0125	0.00729	1.55	0.896	0.00022
Medium burnup region-bottom	0.00356	0.0124	0.000846	0.00508	0.00221	0.0133	0.00787	1.55	0.897	0.000224
Low burnup region-top	0.0033	0.0116	0.000802	0.00474	0.00202	0.0121	0.00728	1.55	0.896	0.000219
Low burnup region-bottom	0.00357	0.0126	0.000863	0.00522	0.00221	0.0137	0.00785	1.55	0.897	0.000227
AR,RR	0.002922	0.007255	0	0	0	0	0.009011	9.92×10^{-5}	1.2994	0.8514
SR,SOR	0.006072	0.019909	0	0	0	0	0.006621	0.000258	1.27414	0.85382
Reflector	9.05×10^{-6}	6.48×10^{-5}	0	0	0	0	0.011427	9.26×10^{-7}	1.3259	0.8374

to Xenon and that due to control rods, *i.e.*, $\rho_h = \rho_{hx} + \rho_{hu}$. Other factors for reactivity contribution such as fuel, coolant, moderator temperature feedbacks are ignored due to their less significance in AHWR.

In the solution process, the physical parameters such as volume of the nodes, area of interface, distance between the nodes, and the homogenized neutron cross-sections for the nodes under consideration are essential for computation of coupling coefficients. The average coolant densities in the bottom half (for a length of 1.75 m from the core bottom) and top half (remaining 1.75 m length of the lattices) of the reactor core under full power operating conditions are calculated as 0.74 g/cc and 0.45 g/cc respectively, and corresponding cross-sections as given in Table 4.3 are used in the analysis. The neutronic data of AHWR is given in Table 4.4.

4.3.2 Formulation of Xenon Reactivity Feedback

To formulate Xenon reactivity feedback, Iodine and Xenon dynamics in each node h in the core region can be modelled as:

$$\frac{dI_h}{dt} = \gamma_I \Sigma_{fh} \phi_h - \lambda_I I_h, \tag{4.18}$$

Table 4.4: Neutronic data of AHWR

Parameter	**Value**
β_1	0.000136
β_2	0.000745
β_3	0.000575
β_4	0.000855
β_5	0.000234
β_6	0.000098
λ_1	0.0127 s^{-1}
λ_2	0.0323 s^{-1}
λ_3	0.133 s^{-1}
λ_4	0.328 s^{-1}
λ_5	1.21 s^{-1}
λ_6	2.68 s^{-1}
λ_I	2.83×10^{-5} s^{-1}
λ_X	2.09×10^{-5} s^{-1}
γ_I	0.061
γ_X	0.003
σ_{aX}	2.65×10^{-18} cm^2
υ_1	1×10^7 cm/s
υ_2	3×10^5 cm/s

$$\frac{dX_h}{dt} = \gamma_X \Sigma_{fh}\phi_h + \lambda_I I_h - (\lambda_X + \sigma_{aX}\phi_h)X_h, \tag{4.19}$$

where I_h and X_h are respectively the iodine and xenon concentrations in node- h , γ_I and γ_X are their respective fractional yields, λ_I and λ_X are respective decay constants. The Xenon reactivity feedback in a node h is given by

$$\rho_{hX} = -\frac{\sigma_{aX} X_h}{\Sigma_{ah}}. \tag{4.20}$$

4.3.3 Formulation of RR Reactivity Variation

For small-scale transients involving normal operational and control situations, reactivity control requirements are met by RRs, *i.e.*, ρ_{hu} is essentially on account of RR movements. The AHWR has 8 RRs, each situated in a distinct lattice location of the core, as shown in Fig. 4.10. Reactivity contributed by the movement of a RR is a non-linear function of its position, but for the normal range of operation it can be approximated by a linear

Table 4.5: Location of RRs in the core

Aspect	**RR**							
	RR-1	**RR-2**	**RR-3**	**RR-4**	**RR-5**	**RR-6**	**RR-7**	**RR-8**
Lattice Location	E17	J21	R21	V17	V9	R5	J5	E9
Node	2	3	4	5	6	7	8	9

function. Thus, if node h contains the RR l, the node reactivity due to RR movement is given by

$$\rho_{hu} = (-21.604P_l + 1440.311) \times 10^{-6}, \tag{4.21}$$

where P_l is the %-in position of the l^{th} RR. ρ_{hu} is zero for nodes not containing RRs.

The 8 RRs given in Table 4.5 are grouped into two banks, with one bank containing 4 RRs (*viz.*, RR-1, RR-3, RR-5 and RR-7) is used for the automatic control of the reactor while the other bank containing remaining RRs (*viz.*, RR-2, RR-4, RR-6 and RR-8) is used for manual control. Each RR is driven by its individual reversible variable speed type three phase induction motors through a rope-pulley mechanism. Neglecting the friction, damping and rotational to linear motion transmission dynamics, the speed of RR-l is directly proportional to the applied voltage to the drive motor, *i.e.*,

$$\frac{dP_l}{dt} = G_{RR}\vartheta_l, l = 1, ..., N_{RR}, \tag{4.22}$$

where N_{RR} is the number of RRs available for control, ϑ_l is the control signal (in the range of ± 1 V) applied to the l^{th} RR drive and G_{RR} is a constant decided by the constraint in maximum speed of movement of RRs (thereby the maximum rate of reactivity insertion) under the maximum control signal, as $G_{RR} = 0.56$.

4.3.4 Homogenization of Nodes

The practical application of any coarse-mesh formulation requires a means of obtaining spatially homogenized group-diffusion cross-sections, and a method of reconstructing local pin power densities for actual heterogeneous sub-assemblies from the results of the

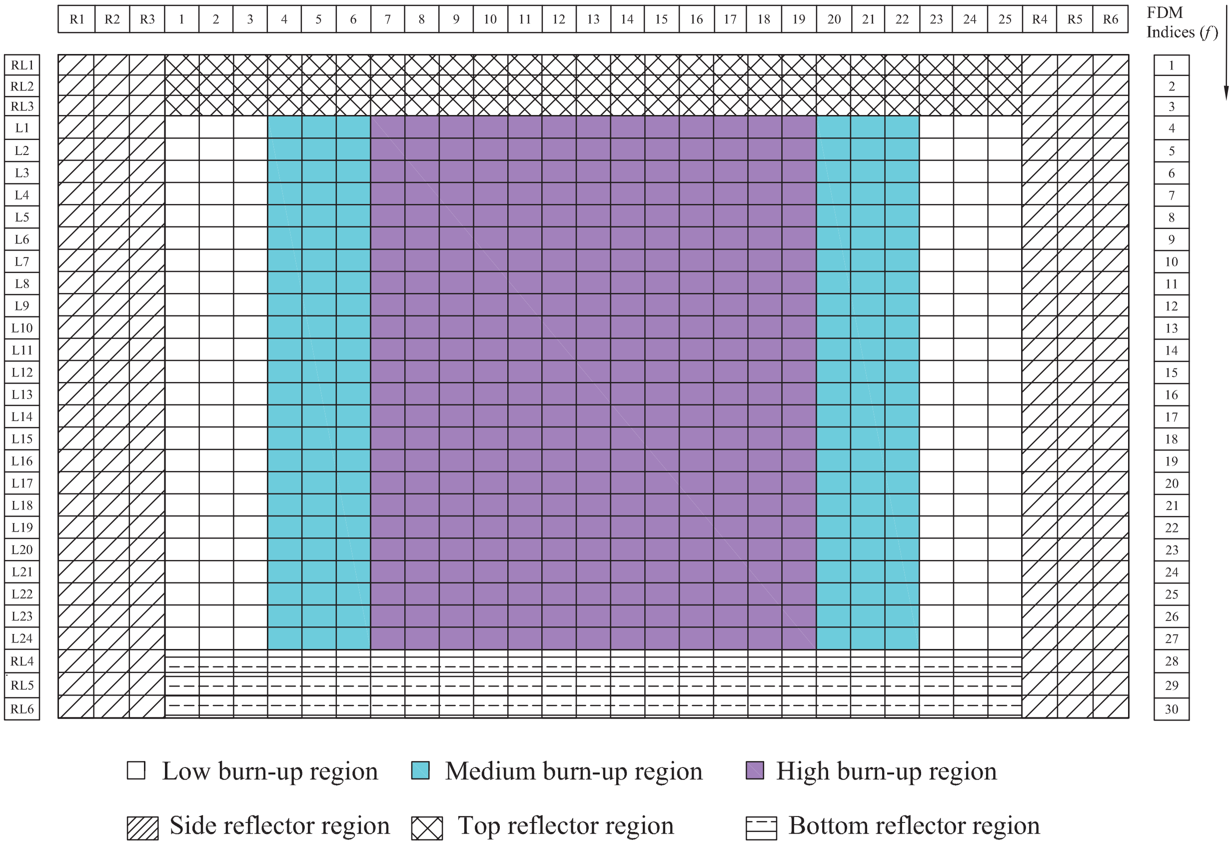

Figure 4.8: Vertical sections and mesh boxes in all regions.

coarse-mesh calculation. These two steps are intimately related, since the accuracy in reconstructing local information from a converged coarse-mesh solution largely depends on an effective method of spatially averaging group reaction cross-sections or homogenized cross-sections and diffusion constants for a node. Homogenized cross sections [19, 97] are obtained for each node by performing a series of local fine-mesh calculations. The vertical alignment of the fictitious meshes in the top, bottom and side reflector regions; and the core region is evident from Fig. 4.8.

When Σ represents the cross section, ζ denotes a neutron interaction, j denotes a vertical section in the core (j may have 3 or 24 or 30 FDM mesh boxes depending on its location whether in top and bottom reflector regions; or active core; or side reflector regions respectively), f gives the indices of the mesh boxes, two group cross-sections are computed through volume-flux weighted homogenization as follows:

1. For active core region:

$$\Sigma_{\zeta gj} = \frac{\sum_{f\in j, f=4}^{27} \Sigma_{\zeta gf}\phi_{gf}\bar{V}_f}{\sum_{f\in j, f=4}^{27} \phi_{gf}\bar{V}_f}, g = 1, 2. \tag{4.23}$$

2. For side reflector region:

$$\Sigma_{\zeta gj} = \frac{\sum_{f\in j, f=1}^{30} \Sigma_{\zeta gf}\phi_{gf}\bar{V}_f}{\sum_{f\in j, f=1}^{30} \phi_{gf}\bar{V}_f}, g = 1, 2. \tag{4.24}$$

3. For top reflector region:

$$\Sigma_{\zeta gj} = \frac{\sum_{f\in j, f=1}^{3} \Sigma_{\zeta gf}\phi_{gf}\bar{V}_f}{\sum_{f\in j, f=1}^{3} \phi_{gf}\bar{V}_f}, g = 1, 2. \tag{4.25}$$

4. For bottom reflector region:

$$\Sigma_{\zeta gj} = \frac{\sum_{f\in j, f=28}^{30} \Sigma_{\zeta gf}\phi_{gf}\bar{V}_f}{\sum_{f\in j, f=28}^{30} \phi_{gf}\bar{V}_f}, g = 1, 2. \tag{4.26}$$

In (4.23)-(4.26), $\bar{V}_f$ is the volume of the mesh boxes. The group wise homogenized constants of each node h are found using the relation,

$$\Sigma_{\zeta gh} = \frac{\sum_{\forall j\in h} \Sigma_{\zeta gj}\phi_{gj}\bar{V}_j}{\sum_{\forall j\in h} \phi_{gj}\bar{V}_j}, g = 1, 2, \tag{4.27}$$

where $\bar{V}_j$ is the volume of the vertical section. The steady-state equivalent flux in the vertical section j for both the fast and thermal energy groups is given by

$$\phi_j^0 = \phi_{1j}^0 + \phi_{2j}^0, \tag{4.28}$$

where ϕ_{1j}^0 and ϕ_{2j}^0 are the volume weighted homogenized fluxes for the fast and thermal groups respectively in vertical section j. The steady-state equivalent flux in the node h

obtained from both the fast and thermal energy groups is given by

$$\phi_h^0 = \phi_{1h}^0 + \phi_{2h}^0, \tag{4.29}$$

where ϕ_{1h}^0 and ϕ_{2h}^0 are the volume weighted homogenized fluxes for the fast and slow groups respectively in node h.

All the one-group homogenized constants of each parameter such as $\Sigma_{ah}, \Sigma_{fh}, D_h$ are to be found from (4.11) by using the value of R_h given by,

$$R_h = \frac{\phi_{2h}^0}{\phi_{1h}^0}. \tag{4.30}$$

In the course of a transient, the nodal fluxes vary according to (4.15) alongwith dynamics of delayed neutron precursors concentration and xenon; and RR movements. The core average flux at any instant during the transient is obtained by the volume weighted average of all the nodal fluxes in the core region given by

$$\phi_C = \frac{\sum_{h=1}^{Z} \phi_h \bar{V}_h}{\sum_{h=1}^{Z} \bar{V}_h}. \tag{4.31}$$

4.4 Reconstruction of Three-Dimensional Fluxes from Nodal Fluxes

The methods for developing homogenized parameters for large nodes from detailed heterogeneous solutions and the problem of deducing local pin powers from the nodal solutions are generally applied to time-independent problems but these could also be extended to situations involving slow variations. The pin-by-pin flux distribution within each node is calculated using a de-homogenization method or Flux Reconstruction Method (FRM) [27] from nodal solutions. The FRM is superior than FDM in terms of computational time and it is based on the assumption that the fine-mesh point flux

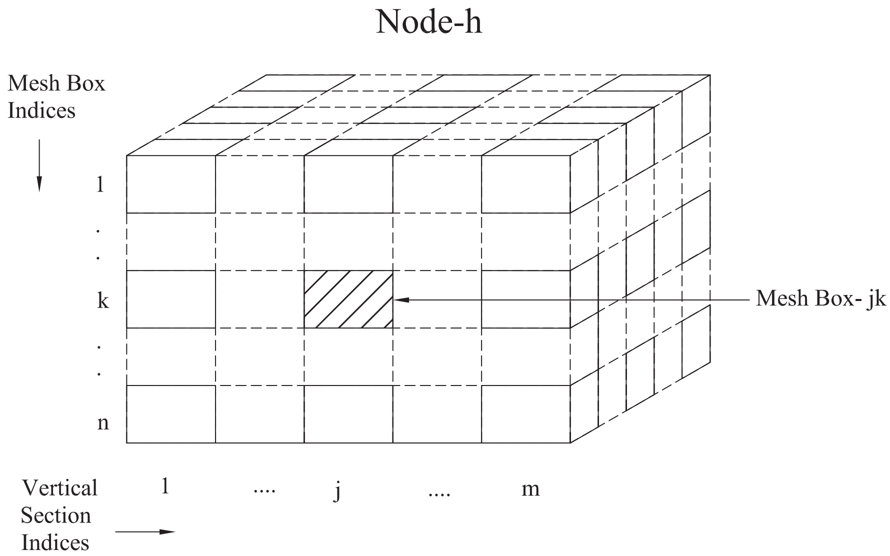

Figure 4.9: A node with vertical sections and mesh boxes.

can be expressed as the product of flux of the assembly to which it belongs, which is obtained through a vertical grid level weighting factor applied on the global flux, and a mesh box level weighting factor corresponding to it. A simple diagram representing a fictitious node h, with vertical sections, mesh boxes and their indices is shown in Fig. 4.9.

From (4.28) and (4.29), the weighting factor for each vertical section j in a node h is given by $\kappa_j = \phi_j^0/\phi_h^0$. The weighting factor for each mesh box f in any vertical grid j can be found from the axial flux distribution obtained from the steady-state FDM computation. The weighting factor for each mesh box f in a vertical grid j is defined as $\kappa_{jf} = \phi_{jf}^0/\phi_j^0$. During a transient, the fluxes in vertical grids and mesh boxes vary according to the transient value of the nodal flux and weighting factors κ_j and κ_{jf} corresponding to vertical grid j and mesh box f. Transient value of flux in any vertical grid j is given by $\phi_j = \kappa_j.\phi_h$, where ϕ_h is the transient value of flux of node h, in which vertical grid j is a member. On the other hand, transient value of flux in any mesh box f in vertical grid j is given by $\phi_{jf} = \kappa_{jf}.\phi_j$. From the expression of ϕ_j,

$$\phi_{jf} = \kappa_{jf}.\kappa_j.\phi_h. \tag{4.32}$$

Substituting the values of κ_{jf} and κ_j, (4.32) can be written as

$$\phi_{jf} = \left(\frac{\phi_h}{\phi_h^0}\right)\phi_{jf}^0. \tag{4.33}$$

Hence the transient value of flux in any mesh box is expressed as the ratio of transient to steady-state flux value of the node it belongs to, multiplied by its own steady-state value. This way the flux distribution is reconstructed in all 22950 mesh boxes.

4.5 Signals from Ion Chambers

The fluxes at the locations of ion chambers whose axis is parallel to the calandria wall in a distance of 20 mm (refer to Fig. 4.4), can be determined if the diffusion equation is solved for the case in which reflector is considered as a plane source and the surrounding vault water is taken as a non-multiplying medium consisting of a slab of infinite extent as far as length and breadth are concerned and having finite thickness [19, 26]. The calandria vault which holds light water is surrounded by air, which is treated as vacuum. With this assumption, there is a flow of neutrons in only one direction, neglecting very small scattering back from the air. So the boundary condition is then postulated as if near the boundary between a diffusion medium and air, the neutron flux gradient is such that linear extrapolation would lead to the flux vanishing at a certain distance beyond the boundary. The diffusion coefficient for this case is

$$\frac{d^2\phi}{dx^2} - \frac{1}{L^2}\phi = 0, \tag{4.34}$$

where x is the distance in the radial direction to the reflector, and L is the diffusion length. The general solution of the above diffusion equation is

$$\phi(x) = Ae^{\{\frac{-x}{L}\}} + Ce^{\{\frac{x}{L}\}}, \tag{4.35}$$

where A and C are constants determined by the boundary conditions. When x is equal to $\widetilde{a}$, the hypothetical extrapolated boundary, the solution is

$$\phi(x)|_{x=\widetilde{a}} = Ae^{\{\frac{-\widetilde{a}}{L}\}} + Ce^{\{\frac{\widetilde{a}}{L}\}} = 0. \tag{4.36}$$

Here $\tilde{a}$ is the thickness of the medium including the extrapolation distance. The constant C can be evaluated as

$$C = -Ae^{\{\frac{-2\widetilde{a}}{L}\}}. \tag{4.37}$$

Substituting (4.37) in (4.36),

$$\begin{aligned}\phi(x) &= Ae^{\{\frac{-x}{L}\}} - Ae^{\{\frac{-2\widetilde{a}}{L}\}}e^{\{\frac{x}{L}\}} &(4.38)\\ &= A(e^{\{\frac{-x}{L}\}} - e^{\{\frac{x-2\widetilde{a}}{L}\}}). &(4.39)\end{aligned}$$

At the location of the source, *i.e.*, when $x = 0$,

$$S = \lim_{x\to 0} = \phi(x) = A(1 - e^{\{\frac{-2\widetilde{a}}{L}\}}) \tag{4.40}$$

From this,

$$A = \frac{S}{(1 - e^{\{\frac{-2\widetilde{a}}{L}\}})} \tag{4.41}$$

Substituting from (4.41) in (4.39),

$$\begin{aligned}\phi(x) &= \frac{S}{(1 - e^{\{\frac{-2\widetilde{a}}{L}\}})}(e^{\{\frac{-x}{L}\}} - e^{\{\frac{x-2\widetilde{a}}{L}\}})\\ &= \frac{Se^{\{\frac{-\widetilde{a}}{L}\}}(e^{-\{\frac{x-\widetilde{a}}{L}\}} - e^{\{\frac{x-\widetilde{a}}{L}\}})}{(1 - e^{\{\frac{-2\widetilde{a}}{L}\}})}\\ &= \frac{S(e^{-\{\frac{x-\widetilde{a}}{L}\}} - e^{\{\frac{x-\widetilde{a}}{L}\}})}{(e^{\{\frac{\widetilde{a}}{L}\}} - e^{\{\frac{-\widetilde{a}}{L}\}})} &(4.42)\end{aligned}$$

Simplifying (4.42), the flux at a point x in the radial direction of the core is given by

$$\phi(x) = S \times \frac{\sinh\left(\frac{\widetilde{a}-|x|}{L}\right)}{\sinh\left(\frac{\widetilde{a}}{L}\right)}, \tag{4.43}$$

where the source strength S is the node average flux value of the reflector node near which the point x is located. Hence, fluxes at the locations of various ion chambers are obtained from the flux values of the nearby reflector nodes shown in Fig. 4.7(a) which act as sources of neutrons. Fig. 4.10 shows the nodal division of AHWR core and the side reflector, and the locations of ion chambers(refer to Fig. 4.1 also). Unlike others, ion chamber-9 is in the interface of nodes 18 and 25, so that average flux of the two nodes is taken as the source strength. All ion chambers are mounted in the calandria vault of thickness 88.75 cm, filled with light water. Hence, extrapolation distance $\widetilde{a}$ expressed as $\widetilde{a} = a + 0.7108 \times \lambda_{tr}$ is found as $\widetilde{a} = (88.75 + 0.151)$ cm, where λ_{tr} is the transport mean free path of light water. Diffusion length (L) of light water is taken as 2.73 cm.

Flux at any ion chamber with source strength S located at a distance of 2 cm radially from the calandria vessel or from the reflector is given by

$$\phi(x = 2 \text{ cm}) = 0.4819 \times S. \tag{4.44}$$

The signals from ion chambers are proportional to the local neutron flux, which in turn is proportional to the core-average neutron flux. Hence the current of an ion chamber-j can be represented as

$$i_{IC_j} = G_{IC}\phi_{IC_j} + 4 \qquad \text{mA}, \; j = 1, \cdots, 9, \tag{4.45}$$

where $G_{IC} = 10.667$ is the product of detector sensitivity and the gain of the amplifier stages. ϕ_{IC_j} denotes the per-unit (pu) value of the local neutron flux at the j^{th} ion chamber location. It is directly proportional to the core average flux ϕ_C for nominal

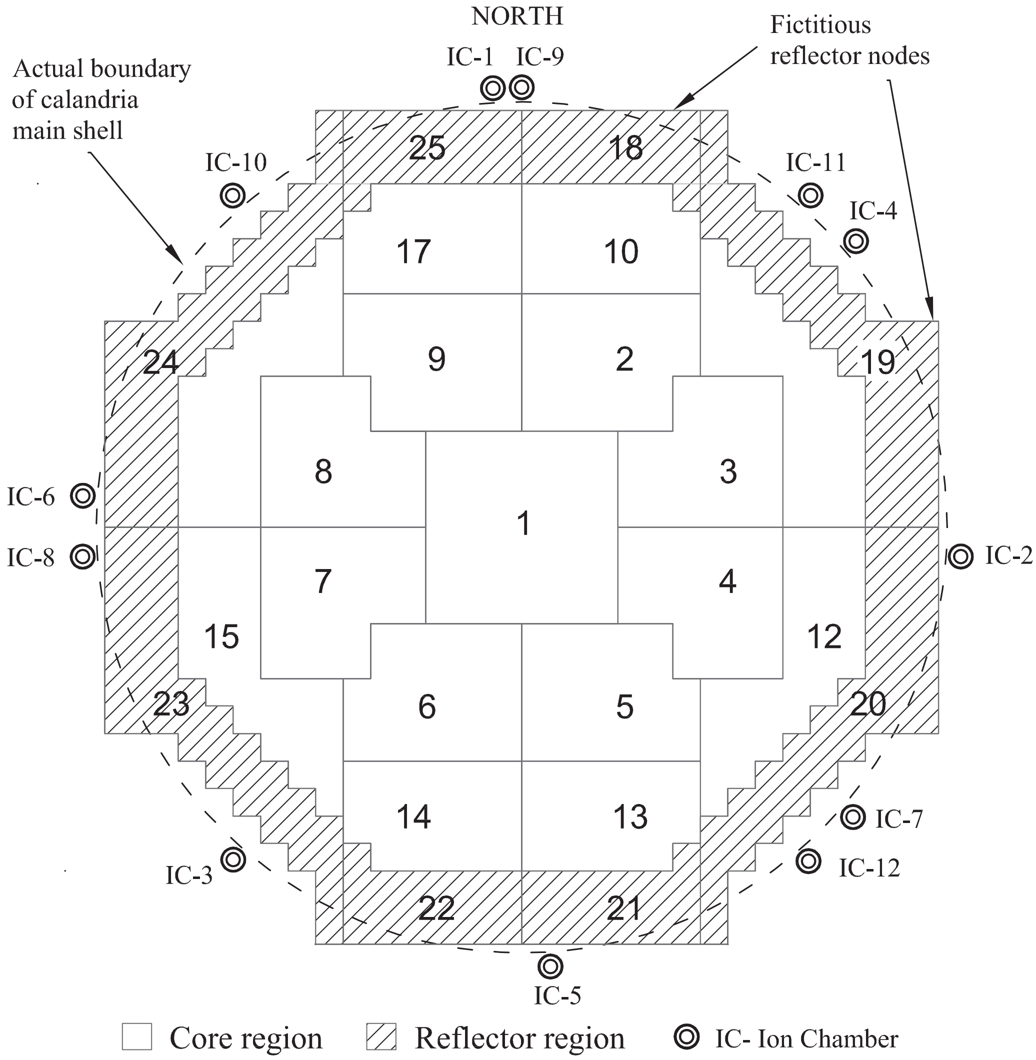

Figure 4.10: Nodalization of AHWR core and side-reflector; and ex-core ion chambers (schematic).

flux distribution. The above model brings the signal to $(4 - 20)$ mA calibrated range, during different operational power levels of the reactor.

4.6 Signals from VSPNDs

Each ICDH is surrounded by 4 fuel channels and accommodates an assembly containing in-core detectors for neutron flux measurement. The location of VSPNDs in each ICDH is such that each VSPND is surrounded by 8 number of FDM meshes as shown in

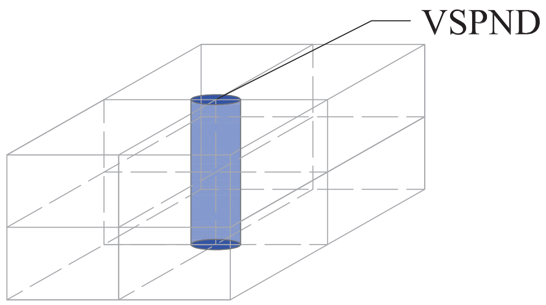

Figure 4.11: VSPND in an ICDH surrounded by 8 mesh boxes.

Fig.4.11. Flux reaching an VSPND d is computed by weighted average of fluxes in the surrounding 8 meshes [23] as follows:

$$\phi_d = \frac{\sum_{i=1}^{8} \phi_i^d D_i^d}{\sum_{i=1}^{8} D_i^d}, \tag{4.46}$$

where ϕ_i^d and D_i^d are the one-group flux and the diffusion coefficients of the surrounding mesh box i.

Each VSPND signal is a function of the flux at its location and is amplified using a linear amplifier. The response of each VSPND is characterized by a large delay but a suitable dynamic compensation scheme such as Dominant Pole Tustin Method or Direct Inversion Method can be deployed to reconstruct the prompt flux variations from the delayed signal of a VSPND [60]. Hence, a VSPND, its amplifier and a dynamic compensator can be lumped as a prompt VSPND and an amplifier. A linear amplifier is considered as the amplifier of a VSPND signal. Thus the output signal of the amplifier of a VSPND is

$$i_V = G_V \phi_V + 4 \qquad \text{mA}, \tag{4.47}$$

where gain $G_V = 10.667$, and ϕ_V is the pu value of the flux observed at the VSPND location.

4.7 Validation of the Model

The methods of generation of core flux (Section 4.3) and detector signals (Sections 4.5 and 4.6) are now applied to the AHWR. For a given transient, responses obtained from the FDM are taken as the reference solutions and comparison is made with the open loop responses of the 17-node model for the same transient. Two different transients are considered for simulations and in both, the reactor was assumed to be initially operating on full power, with each RR equally at 16 mesh boxes from the top of the core or at 66.66 %-in position, absorber rods are fully in; shim rods, and shut-off rods are fully out. In both the simulations, steady-state is maintained until 10 s, at which the transient commences. Reference solutions were obtained from the detailed three-dimensional FDM computations based on a quasi-static approach, with shape calculations performed whenever the rods reach a new mesh box level from the top of the core besides at time $t = 10$ s, and amplitude calculations carried out with a time step of 2 ms. For each transient, errors were computed between the nodal method and the reference solution. During both the transients, the maximum root-mean-square error and the instance of its occurrence were computed for three aspects: all the 22950 mesh box fluxes, the flux values at the ion chamber locations, and those at the VSPND locations. The first 3 ion chambers and VSPNDs with large relative absolute errors are listed in Table 4.7, at the instances of their respective maximum root-mean-square error. Under each transient, the plots of the fluxes at these detector locations during the simulation are also given. For each transient, for the sake of evaluating the established model, the errors in zonal and bulk fluxes were computed from the flux values at the VSPND locations. The four zones (quadrants) of the core, with their designations, are given in Fig. 4.12.

The zonal and bulk fluxes, from the reference and nodal solutions, are computed as follows: quadrant fluxes are obtained as an average of all the fluxes at the VSPND locations in each quadrant; and the bulk flux is computed as the average of all the quadrant fluxes. The relative errors in zonal and bulk fluxes are computed, and their

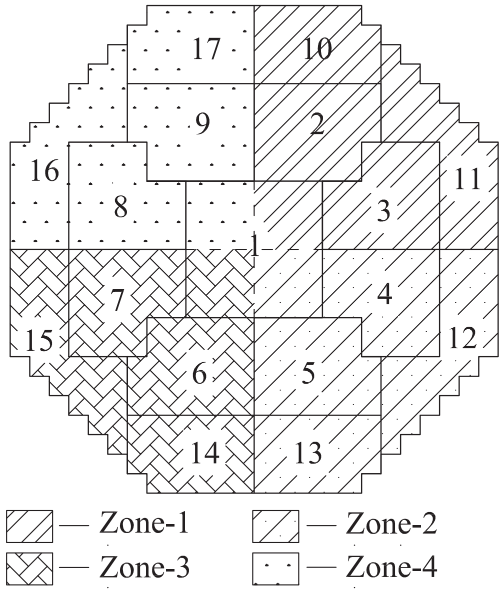

Figure 4.12: Four quadrants of the core

plots are shown under each transient. The transients are described in the following.

4.7.1 Simultaneous Movement of 4 RRs

In this transient, all 4 RRs meant for automatic control, *i.e.*, RR-1, RR-3, RR-5 and RR-7, respectively located in nodes 2, 4, 6 and 8 were considered to be moved simultaneously (refer to Table 4.5). At time $t = 10$ s, when a control signal of 1 V was applied to the drives of these RRs, the rods moved linearly into the reactor core according to (4.22) and secured a new position of 17 mesh boxes from the top of the core in 7.44 s. Then control signals were made zero in order to hold the rods at their new positions. After a small interval of time, these rods were driven out linearly back to their nominal positions under a control signal of -1 V. After another short interval of time, an outward movement of these rods followed by inward movement back to nominal position was simulated. Fig.4.13(a) shows the position of these RRs during the transient. During this transient, all other reactivity devices were kept stationary at their respective nominal positions. Responses for the core average flux in pu were obtained from the nodal model and the quasi-static method and are shown in Fig. 4.13(b). The

Table 4.6: Relative absolute error (%) at different detector locations under simultaneous movement of 4 RRs

S.No.	Ion chamber	Error	VSPND	Error
1	2	6.89	V_{152}	7.76
2	7	5.98	V_{151}	7.43
3	4	5.16	V_{82}	6.85

comparison makes clear that the nodal model shows a very good agreement with the reference response throughout. The maximum values of root-mean-square error in the fluxes in the mesh boxes, at ion chamber and at VSPND locations are 4.15 %, 4.05 %, and 4.15 % respectively; these errors occurred at 43.88 s, 43.9 s, and 43.86 s respectively. The first 3 ion chambers and VSPNDs that exhibited maximum error are given in Table 4.6. Fluxes at these ion chambers, i.e., ion chamber-2, ion chamber-7, ion chamber-4, are respectively shown in Fig. 4.14(a), 4.14(b), and 4.14(c). Similarly, fluxes at V_{152}, V_{151} and V_{82} are respectively shown in Fig. 4.15(a), 4.15(b), and 4.15(c). As the detector signals are proportional to the fluxes at their locations, major errors in the signals are exhibited in the same detectors. The relative errors observed in quadrant and bulk fluxes are shown in Fig. 4.16. As the typical values of these errors are within ±5 % during the entire simulation, the established nodal model can be said to be accurate enough for the transient considered.

4.7.2 Differential Movement of 2 RRs

As scenarios in which the power distribution in the reactor core undergoes variations in spite of the total power remaining constant are of great significance in spatial reactor control applications, a transient involving simultaneous counter-movement of two diagonally opposite RRs was simulated. At time $t = 10$ s, the RR-5 in node 6 was driven linearly into the reactor core from its nominal position under a signal of 1 V while the RR-1 at the diagonally opposite lattice location in node 2 was driven out simultaneously at the same speed under a signal of -1 V. Movement of the two RRs, as shown in Fig.

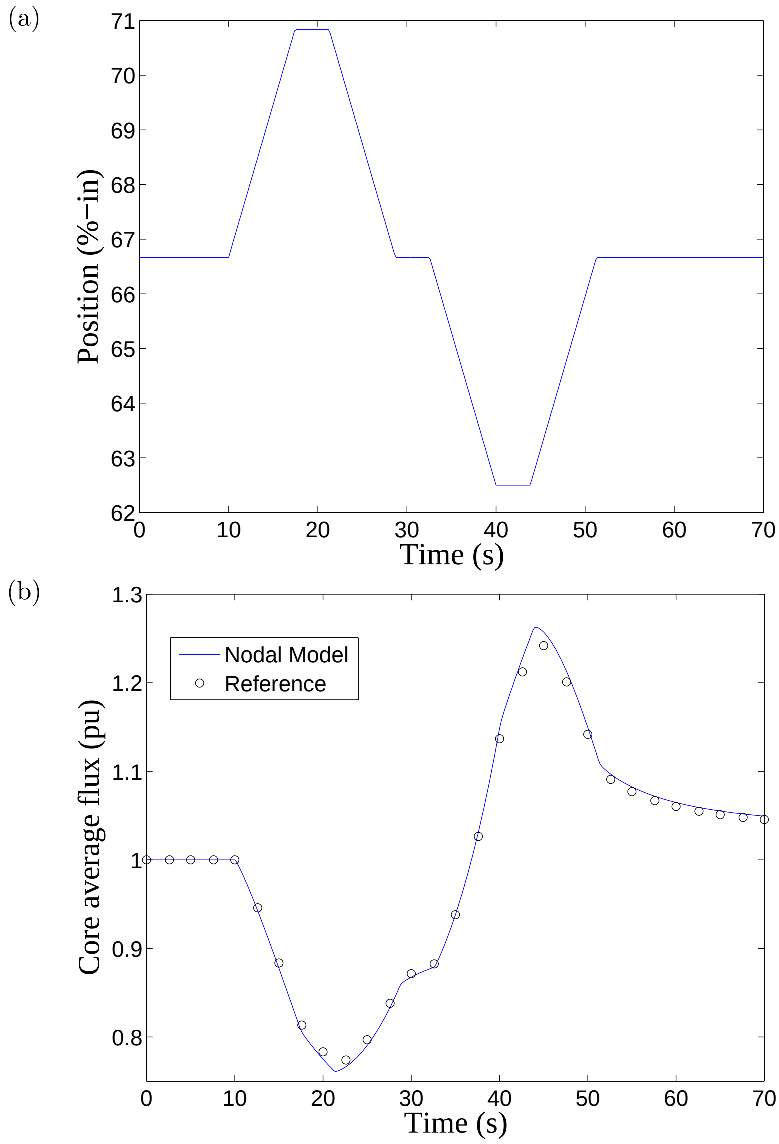

Figure 4.13: Simultaneous movement of 4 RRs: (a) Position of RRs (b) Comparison of the nodal model response with the reference solution.

4.17(a), maintains the net reactivity near to zero and the total power is kept almost constant. All other control rods were kept stationary at their nominal positions during the transient. Responses for the core average flux in pu were obtained from the nodal model and the quasi-static method and are shown in Fig. 4.17(b). The maximum values of root-mean-square error in the fluxes in the mesh boxes, at ion chamber and at VSPND locations are 9.77 %, 5.91 %, and 10.37 %; at 70 s, 62.1 s and 70 s respectively. The first 3 ion chambers and VSPNDs with large root-mean-square error are given in Table

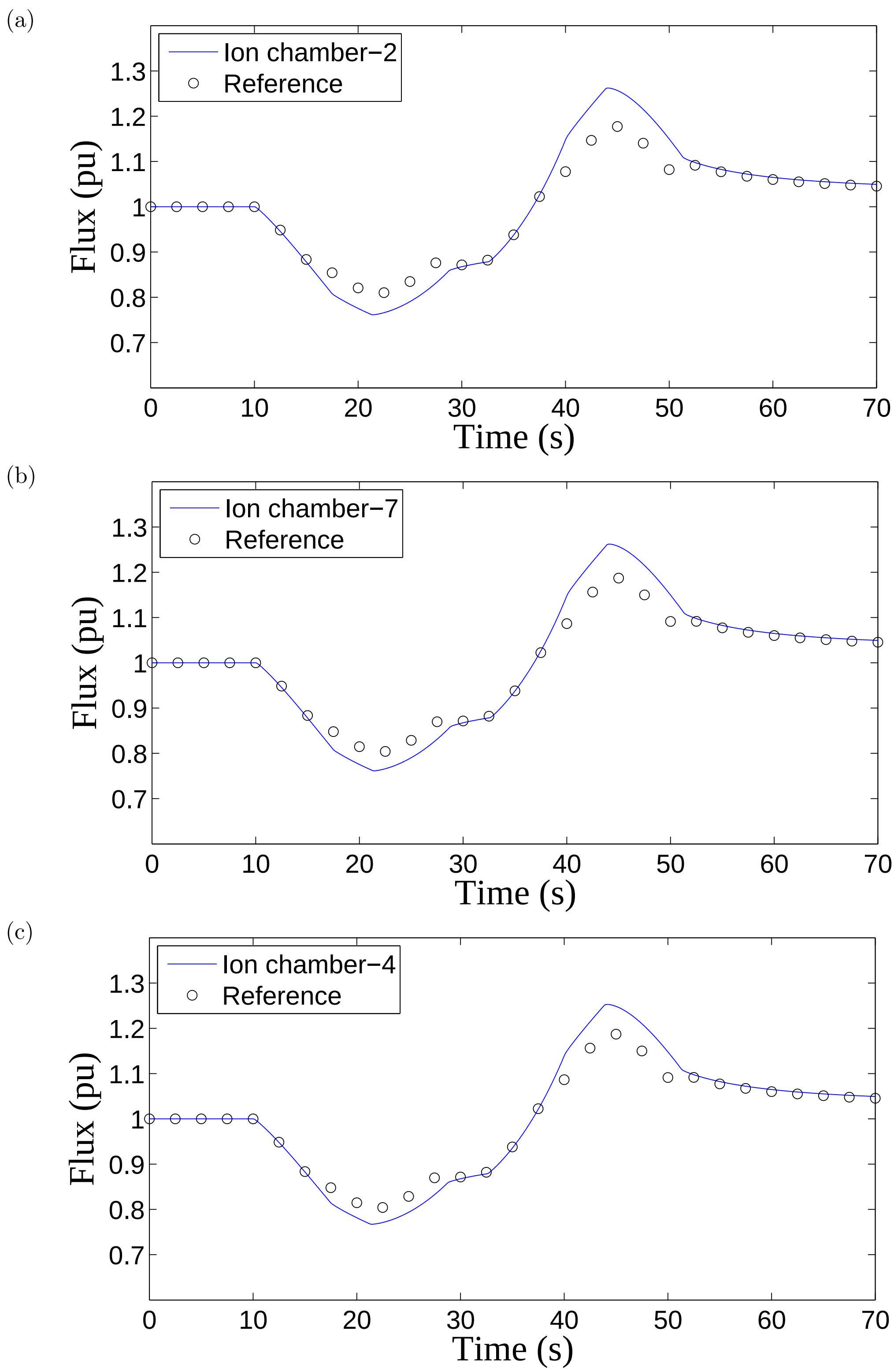

Figure 4.14: Simultaneous movement of 4 RRs: flux values at the 3 ion chambers that exhibited maximum error.

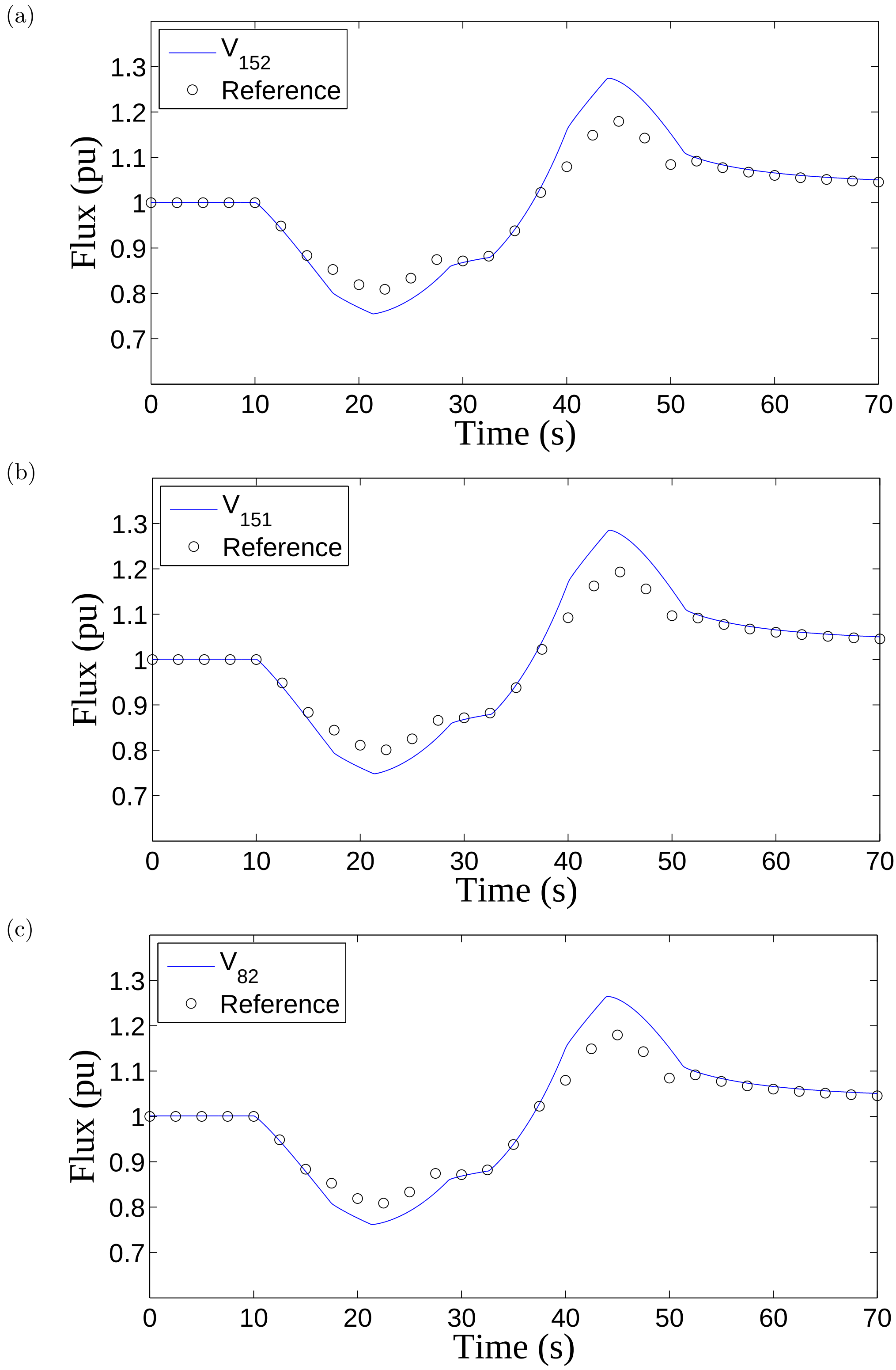

Figure 4.15: Simultaneous movement of 4 RRs: flux values at the 3 VSPNDs that exhibited maximum error.

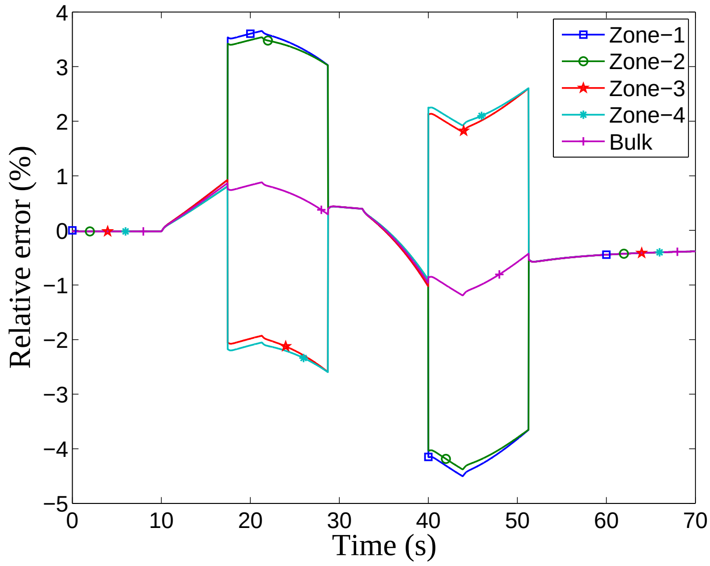

Figure 4.16: Relative errors in zonal and bulk fluxes during the simultaneous movement of 4 RRs.

4.7 and fluxes at their locations are shown in Figs. 4.18(a) and 4.18(b). The relative errors observed in zonal and bulk fluxes are shown in Fig. 4.19. The typical values of these errors are within ±5 %, for 40 s from the commencement of the transient. Hence, within ± 22.4 % movement of the manoeuvred RRs, from their nominal position, the established nodal model can be said to be accurate enough for the transient considered.

Table 4.7: Relative absolute error (%) at different detector locations under differential movement of 2 RRs

S.No.	**Ion chamber**	**Error**	**VSPND**	**Error**
1	6	9.96	V_6	37.61
2	8	8.55	V_5	28.14
3	1	6.34	V_{27}	27.50

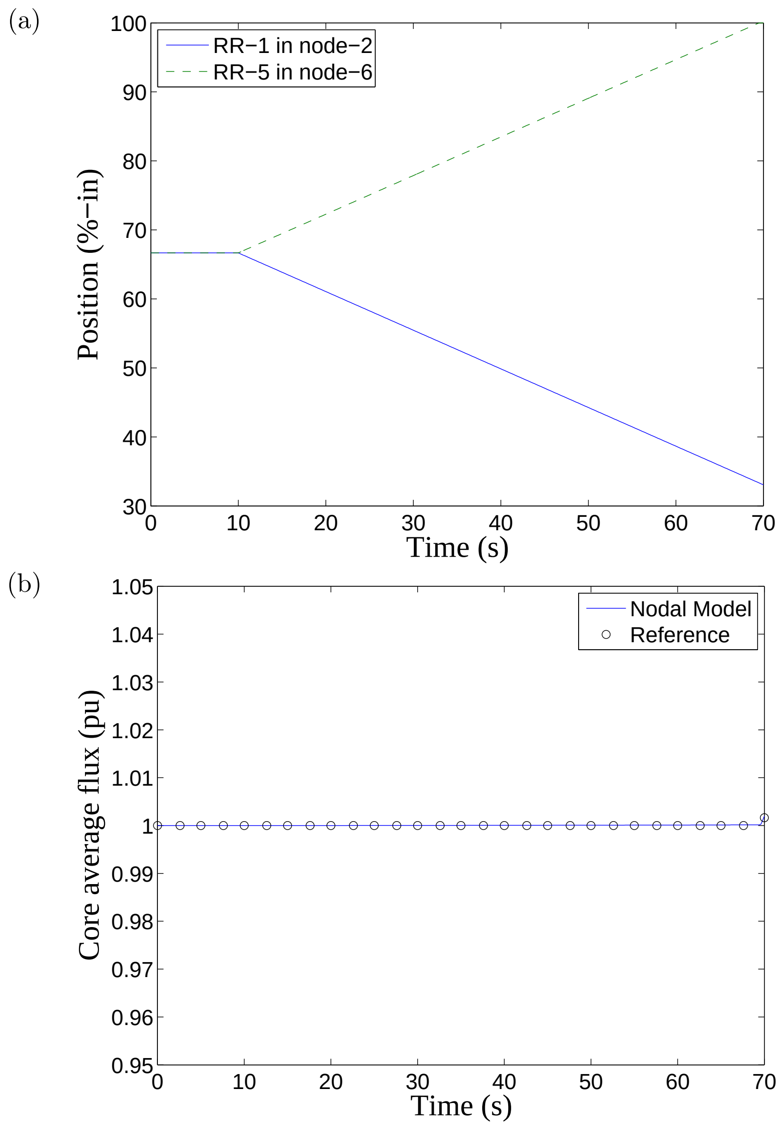

Figure 4.17: Differential movement of 2 RRs: (a) Position of RRs (b) Comparison of the nodal model response with the reference solution.

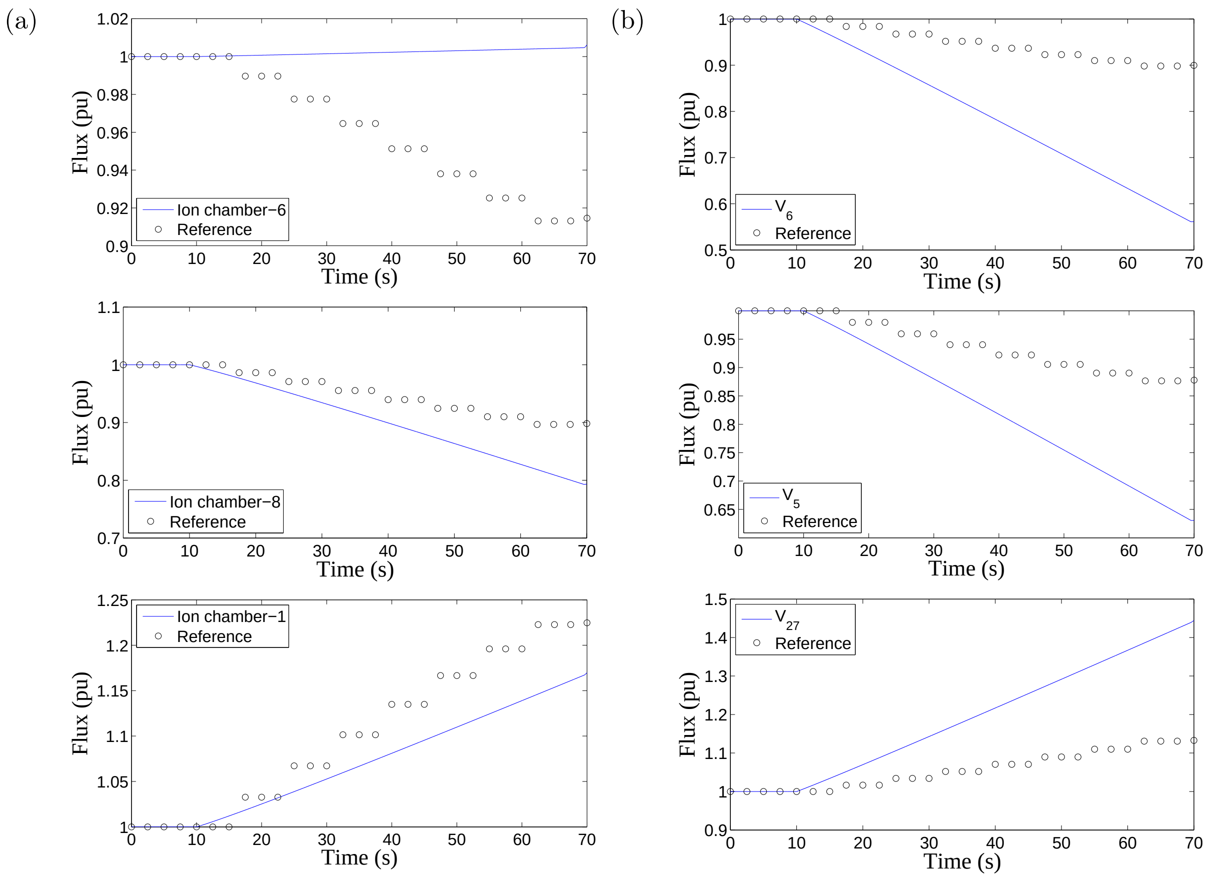

Figure 4.18: Differential movement of 2 RRs: (a) Flux values at the 3 ion chambers (b) Flux values at the 3 VSPNDs.

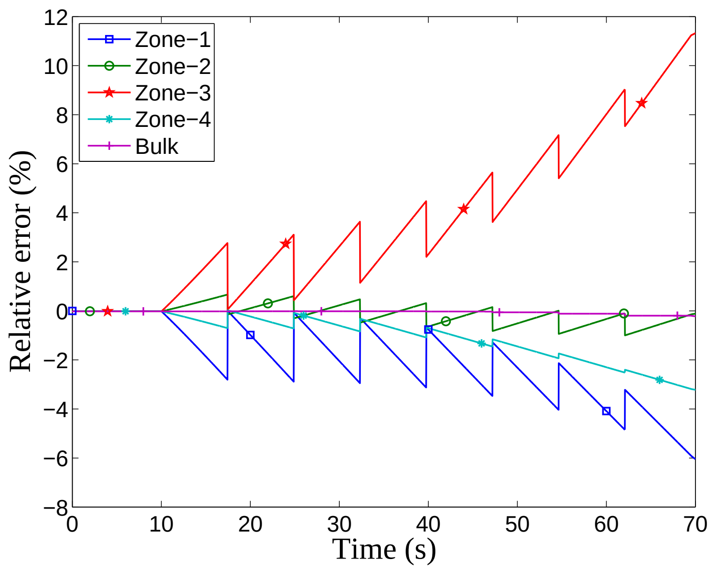

Figure 4.19: Quadrant and bulk fluxes during the differential movement of RRs.

4.8 Discussions

Knowledge of the in-core and ex-core detector signals is of much importance in the nuclear reactors. Large physical dimensions of the AHWR make this requirement more stringent. In this chapter, ion chamber and VSPND signals of AHWR have been simulated using the nodal method, flux extrapolation and flux reconstruction methods. Within a considerable region of perturbation around the steady-state operating point, the core average flux, fluxes at the detector locations and the detector signals from the nodal method are found to be in good agreement with the benchmark. As a result of this, the flux values at the ion chamber and VSPND locations and the detector signals are treated to be accurate enough for the subsequent analyses. From the signal data of ion chamber and VSPND during different transients under healthy conditions of the reactor, covariance models can be obtained enabling their use in further analyses such as DR-based FDI. The outcomes of the DR-based FDI, when applied on the signal data of ion chambers and VSPNDs, are presented in the next chapter.

Chapter 5

Steady-state DR and FDI

In this chapter, the DR and FDI techniques presented in the preceding chapters are applied to ion chambers and VSPNDs of AHWR. Although the ion chambers are expected to give signals proportional to the core average flux, the signals of the 9 ion chambers are seldom equal. Their outputs differ from each other due to differences in leakage flux at their respective locations, caused due to rod shadowing effects. Also, the core power distribution could be unsymmetrical due to refuelling or xenon-induced spatial variations. Such regularly occurring variations are, of course, not to be treated as faults in ion chambers. Accordingly, the DR and FDI analysis should be made robust to such effects by proper tuning of PCA and IPCA algorithms. For the case of VSPNDs, since the local flux variation within the core affect the performance of DR and FDI, they need to be performed on individual clusters.

5.1 Steady-state DR and FDI of Ion Chambers

Data of ion chambers in typical situations have been obtained from simulations using space-time kinetics model of the reactor. Suitable random noise has been superimposed on this data for realistic representation. These data serve for development of constraint

Parts of this chapter were published in *Annals of Nuclear Energy,* Vol. 85 and in *3rd National Symposium on Advances in Control & Instrumentation (SACI),* Mumbai, India.

model of ion chamber signals and subsequent DR and FDI analyses. Four different transients are considered for DR and FDI analysis, out of which three transients involve simulation under the action of an output feedback controller [99].

Fig. 5.1 depicts the implementation of the proposed IPCA-based scheme for DR and FDI in the control of the reactor. Each of the control and protection systems is fed with signals from the linear amplifiers of the ion chambers meant for them. Although signals are tapped from the 9 ion chambers before being fed to the DR and FDI system, physical separation and electrical isolation among control and each of the protection systems are maintained. The reconciled estimates of ion chamber signals for control channels (ion chamber-1, ion chamber-2 and ion chamber-3) are sent to the RRS, which in accordance to appropriate control algorithms, generate signals to reactivity control devices.

For DR and FDI, it is proposed to use data from all 9 ion chambers for two reasons. Firstly, the convergence of the IPCA algorithm (refer to Section 3.1.2) is usually not achieved with the individual sets of 3 ion chamber data corresponding to control and protection systems. This is due to the fact that a non-degenerate estimate for the error covariance matrix is obtained only if $m(m+1) \geq 2n$ [66]. For the data of individual systems to be fed as the input to the IPCA algorithm, this condition requires the model order m to be equal to only 2, since $n = 3$. This strict restriction does not guarantee the convergence of the IPCA algorithm. In addition, the deployment of the data from all the ion chambers enhances the redundancy which can be exploited for the better reconciled estimates even in the presence of faults. However, the reconciled estimates of the signals are used only for control, whereas for protection purposes, original measurement signals are used. This is because of the protection functions are of safety-critical nature and employing a complex computationally intensive algorithms are generally not permitted in safety-critical systems.

Extensive simulations are carried out using a mathematical model of the reactor core and the ion chamber model given by (4.45) to generate time-series data of all 9 ion chambers in steady-state and a number of transient situations. Some of these data are used in the PCA and IPCA algorithms (refer to Section 3.1) to obtain the constraint model and standard deviation of measurement errors, while the remaining data are used for evaluation of the performance of the proposed DR and FDI schemes. However, IPCA, owing to its mathematical advancements, is preferred over PCA in the control of the reactor.

The noise levels of real-time data corresponding to ion chambers of various plants [61] have been considered for simulating the measurement data of the ion chambers. From the plant data it was revealed that, the noise takes almost a normal probability distribution with a standard deviation of nearly 2% of the nominal value of the signal. Simulations based on space-time kinetics modeling, in four representative situations of reactor operation are considered. In one of the cases, the reactor power is assumed to be unregulated while the signal to control rods is varied from the steady-state value, in a preprogrammed manner. The other three cases correspond to typical operational situations in which the reactor power is regulated by means of the RRS, but either the demand power is changed or one coolant channel is being refuelled on-power, or the closed loop system is experiencing xenon-induced spatial instability. In all these cases, signals of all the 9 ion chambers belonging to regulating and protection systems are generated and in order to represent realistic behaviour, a noise is added to these signals. The added noise is intended to be in line with the real-time noise. Hence, it has a normal distribution and standard deviation of 0.2933 mA, which is it is equivalent to 2% random fluctuations around the full power steady-state.

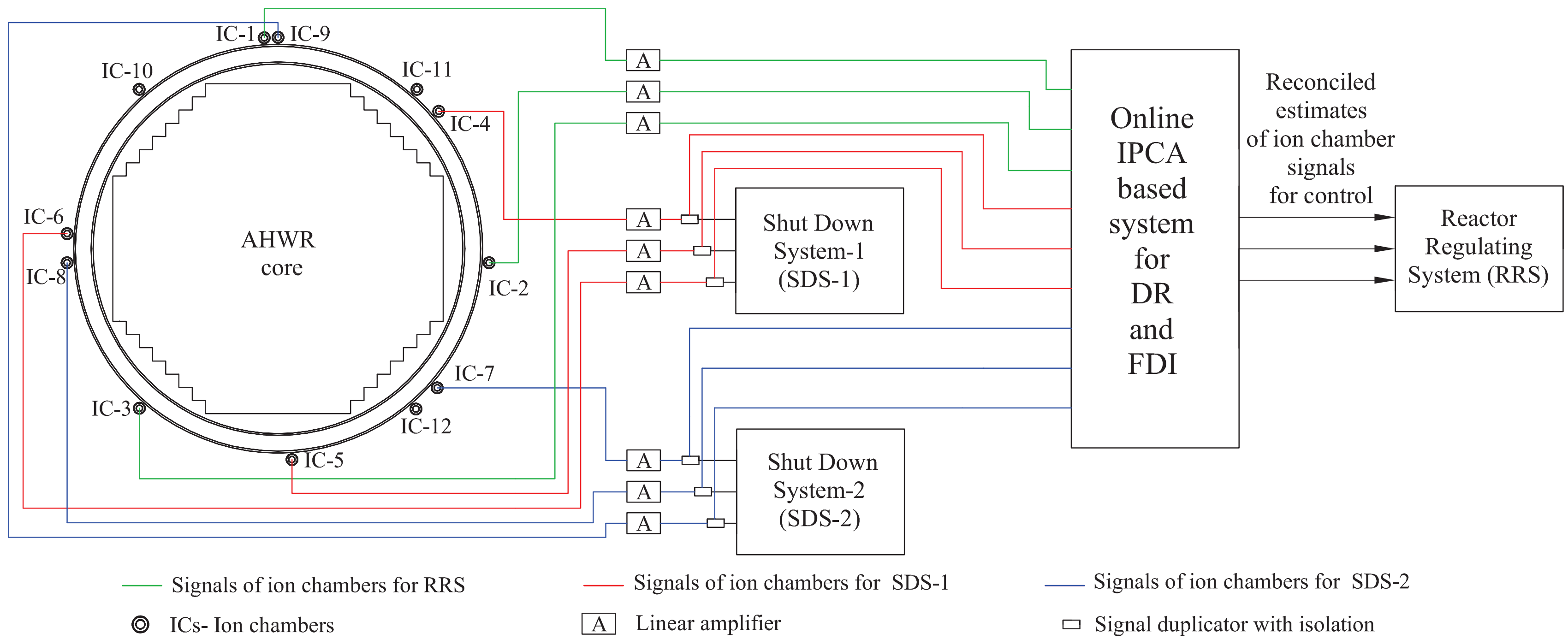

Figure 5.1: Implementation of the proposed IPCA-based method for reactor control.

For the case of ion chamber data, we have $n = 9$ and fault scenarios in which $g \in \{1, 2, 3\}$ are considered for the analyses (refer to Chapter 3). In all the four cases, additive biases (equivalent to faults) are introduced into the sensor data corresponding to three different variables, in a sequential manner. Initial $\frac{1}{4}^{\text{th}}$ length of data corresponds to the case of no fault. Bias is added to signal of an ion chamber-a, $a \in \{1, 2, 3\}$, from the instant corresponding to $\frac{1}{4}^{\text{th}}$ of the length of data. Again bias is added to ion chamber-b, $b \in \{4, 5, 6\}$, from $\frac{1}{2}$ of the data, and finally in ion chamber-c, $c \in \{7, 8, 9\}$, for the last $\frac{1}{4}^{\text{th}}$ length of data. In this way, the data is contaminated by a single fault, 2 faults and 3 faults during second, third and fourth quarters length of data respectively, leading to fault scenarios with up to 3 simultaneous faulty sensors. It is to be reckoned that reactor control and protection systems are designed to address 1-fault scenarios. In 2 or more-fault scenarios, reactor is shut down. Hence, care has been taken not to simulate two simultaneous faults in the ion chambers corresponding to a single system, *viz.*, RRS, SDS-1 and SDS-2. Hence, 27 different ion chamber combinations, as listed in Table 5.1, are identified for the simulation of 3-fault scenarios. In these scenarios, m can range from 3 to 8, by allowing at least one eigenvector to represent principal component subspace. However, the maximum value of m with which the estimated standard deviations of errors (from IPCA) are close to the true values is preferred to represent residual subspace.

The DR and FDI statistics, *viz.*, AER, AA, ODR and OP, (refer to Sections 3.2 and 3.3), are computed for each fault scenario for different additive biases, expressed as percentage of the nominal values of the sensor signals. The additive biases are representatives of the extents of degradation of the signals. The detection system is effective if the extent of detectable degradation is small. Different bias magnitudes are considered in increasing magnitudes, in increased number of ion chambers, so that detectable bias levels in different gross error scenarios are known. Bias percentages are considered from 0% to 20%, separated by 0.5%. In order to avoid infinite number of combinations of the

Table 5.1: Different ion chamber combinations under consideration

Case No.	Faulty ion chambers	Healthy ion chambers
1	{1,4,7}	{2,3,5,6,8,9}
2	{1,4,8}	{2,3,5,6,7,9}
3	{1,4,9}	{2,3,5,6,7,8}
4	{1,5,7}	{2,3,4,6,8,9}
5	{1,5,8}	{2,3,4,6,7,9}
6	{1,5,9}	{2,3,4,6,7,8}
7	{1,6,7}	{2,3,4,5,8,9}
8	{1,6,8}	{2,3,4,5,7,9}
9	{1,6,9}	{2,3,4,5,7,8}
10	{2,4,7}	{1,3,5,6,8,9}
11	{2,4,8}	{1,3,5,6,7,9}
12	{2,4,9}	{1,3,5,6,7,8}
13	{2,5,7}	{1,3,4,6,8,9}
14	{2,5,8}	{1,3,4,6,7,9}
15	{2,5,9}	{1,3,4,6,7,8}
16	{2,6,7}	{1,3,4,5,8,9}
17	{2,6,8}	{1,3,4,5,7,9}
18	{2,6,9}	{1,3,4,5,7,8}
19	{3,4,7}	{1,2,5,6,8,9}
20	{3,4,8}	{1,2,5,6,7,9}
21	{3,4,9}	{1,2,5,6,7,8}
22	{3,5,7}	{1,2,4,6,8,9}
23	{3,5,8}	{1,2,4,6,7,9}
24	{3,5,9}	{1,2,4,6,7,8}
25	{3,6,7}	{1,2,4,5,8,9}
26	{3,6,8}	{1,2,4,5,7,9}
27	{3,6,9}	{1,2,4,5,7,8}

different bias magnitudes for different detector signals, uniform magnitudes of biases are taken for all the faulty sensors, in the scenarios of 2 and 3 faults. In all the four cases, the DR and FDI statistics obtained from either of the PCA and IPCA models with a known $\mathbf{\Sigma}_{\boldsymbol{\varepsilon}}$ obtained from IPCA, with its computed standard deviation vector $\boldsymbol{\sigma}_{\varepsilon}$, are found to be almost the same. Hence the statistics obtained from IPCA are only presented. Also, evaluation of different FDI techniques presented in Section 3.3, *viz.*, GLR, IMT and IPCT, is performed in Section 5.1.1 to work out the most suitable technique.

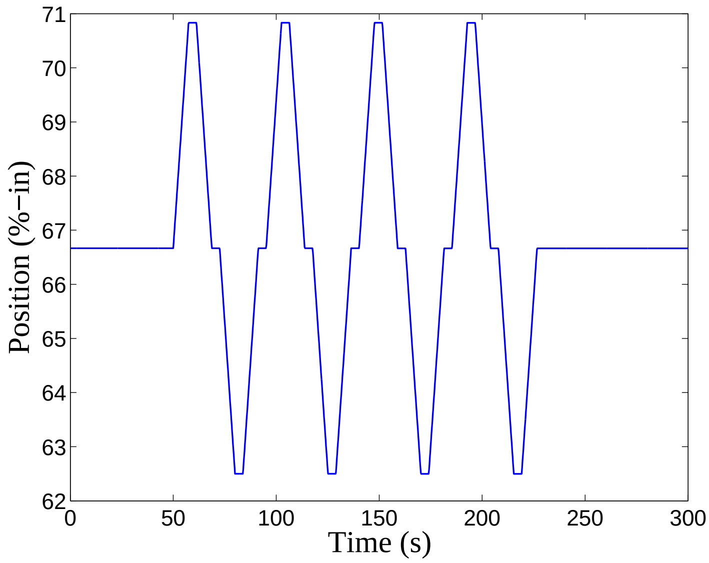

Figure 5.2: Simulated variation of position of RR-3

5.1.1 Data of Ion Chambers during Open-loop Response of the Reactor for an RR Movement

When the reactor is critical, all the RRs are at 66.66 % -in position. Starting from this configuration, movement of the RR-3 (refer to Fig. 4.10) was simulated in the manner as explained in Section 4.7.1. Fig. 5.2 shows the position of the RR during the transient. Other RRs remain at their original positions. During the transient, the signals of the ion chambers vary as shown in Fig. 5.3(a). As RR-3 is relatively closer to ion chambers 3, 5, 6 and 8 than ion chambers 1, 2, 4, 7 and 9, the signals of the former set of ion chambers are different from the signals of the later set of ion chambers, while at steady-state their signals are equal. Fig. 5.3(b) shows the ion chamber signals corrupted by noise. The sampling duration of 0.2 s led to the generation of 1500 observations. All ion chamber signals are healthy for first 375 observations. At observation $k = 375$ ($t = 75$ s), a fault is simulated in an ion chamber for RRS. From $k = 750$ ($t = 150$ s), in addition to the ion chamber for RRS, fault is present in an ion chamber for SDS-1 also. Finally after $k = 1125$ ($t = 220$ s), faults are present in 3 ion chambers corresponding to RRS, SDS-1 and SDS-2.

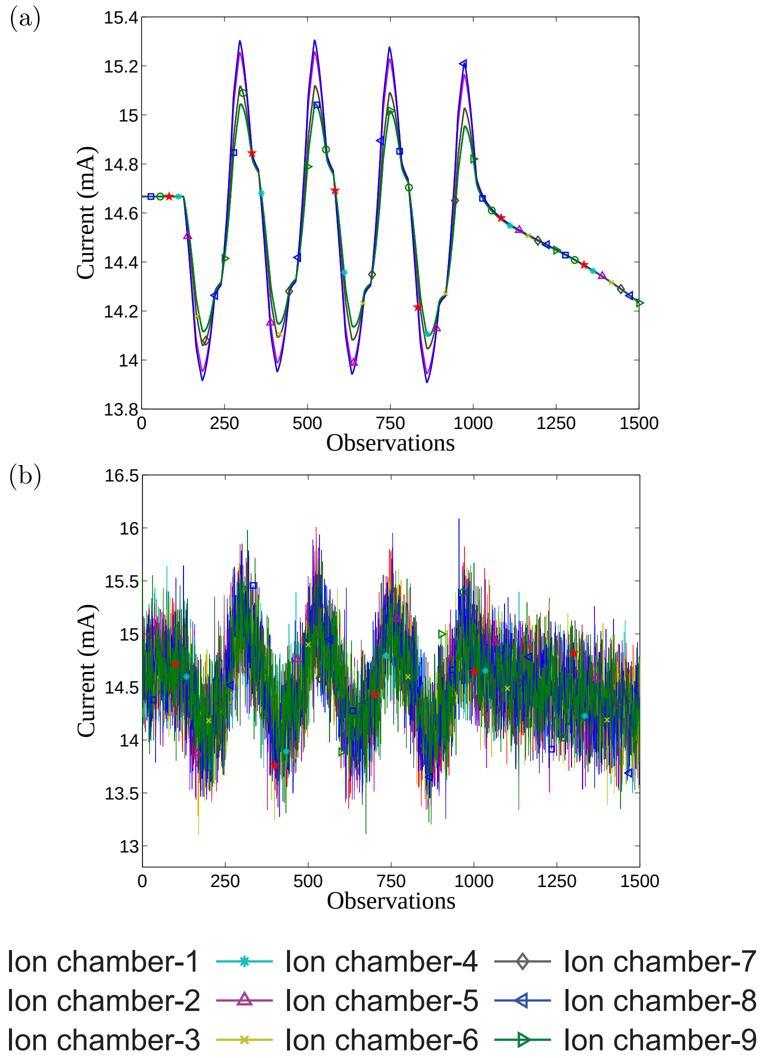

Figure 5.3: Ion chamber signals during the transient corresponding to RR movement (a) actual (noise-free) signals (b) signals with noise.

When the IPCA algorithm (refer to Fig. 3.1) is applied to the data shown in Fig. 5.3(b), the singular values of scaled data matrix $\boldsymbol{Y}_s$[†] and standard deviations of error for different model orders are obtained as given in Table 5.2. It can be observed that with a model order of 7 as well as 8, the standard deviations of the measurement errors are accurately estimated and the last 8 singular values are converged close to 1, while the detectability considerations are satisfied. As a higher model order is preferred for FDI, $m = 8$ is taken as model order for the residual subspace. The constraint model

[†]Singular values are slightly different for different model order values due to iterations converging differently.

Table 5.2: IPCA results for different model orders for the data corresponding to RR movement

(a) Singular values of $\boldsymbol{Y}_s$

S. No.	$m = 8$	$m = 7$
1	155.0112	154.9911
2	1.1595	1.1721
3	1.0911	1.0796
4	1.0582	1.0585
5	1.0496	1.0445
6	1.0381	1.0368
7	1.0279	1.0291
8	1.0164	1.0219
9	1.0000	1.0000

(b) Standard deviation vector ($\boldsymbol{\sigma}_\varepsilon$)

Ion chamber	True $\boldsymbol{\sigma}_\varepsilon$	Estimated $\boldsymbol{\sigma}_\varepsilon$	
		$m = 8$	$m = 7$
Ion chamber-1	0.2933	0.2908	0.2882
Ion chamber-2	0.2933	0.2962	0.2961
Ion chamber-3	0.2933	0.3062	0.2962
Ion chamber-4	0.2933	0.2928	0.2896
Ion chamber-5	0.2933	0.2888	0.2811
Ion chamber-6	0.2933	0.3024	0.2996
Ion chamber-7	0.2933	0.2944	0.2938
Ion chamber-8	0.2933	0.3117	0.2977
Ion chamber-9	0.2933	0.2917	0.2883

obtained by IPCA for $m = 8$ is given as follows:

$$\boldsymbol{A} \triangleq \boldsymbol{A}_I = \begin{bmatrix} 0.2703 & 0.1087 & -0.4557 & 0.2918 & -0.4632 & 0.2612 & 0.1618 & -0.4731 & 0.2987 \\ -0.2180 & -0.5647 & -0.0317 & -0.1032 & -0.0412 & -0.2132 & 0.5679 & 0.1151 & 0.4886 \\ 0.5022 & -0.1753 & 0.1693 & 0.4180 & -0.3693 & -0.5184 & 0.0444 & 0.1925 & -0.2632 \\ -0.5623 & 0.3607 & -0.1997 & 0.4959 & 0.1443 & -0.2903 & 0.3287 & -0.0474 & -0.2287 \\ 0.2789 & 0.5017 & 0.0016 & -0.5463 & 0.0650 & -0.4777 & 0.2879 & -0.2139 & 0.1032 \\ 0.0993 & -0.0936 & -0.1842 & 0.2617 & 0.4821 & -0.3822 & -0.5036 & -0.1523 & 0.4726 \\ -0.2894 & 0.0725 & 0.7369 & 0.1305 & -0.2735 & -0.0612 & -0.1186 & -0.4440 & 0.2470 \\ 0.2386 & -0.3588 & 0.1137 & 0.0644 & 0.5005 & 0.0977 & 0.2882 & -0.5349 & -0.4097 \end{bmatrix}. \quad (5.1)$$

Its reduced row echelon form [107] is given by the matrix

$$\boldsymbol{A} \triangleq \boldsymbol{A}_I = \begin{bmatrix} 1 & 0 & 0 & 0 & 0 & 0 & 0 & 0 & -1.0001 \\ 0 & 1 & 0 & 0 & 0 & 0 & 0 & 0 & -1.0007 \\ 0 & 0 & 1 & 0 & 0 & 0 & 0 & 0 & -1.0009 \\ 0 & 0 & 0 & 1 & 0 & 0 & 0 & 0 & -0.9996 \\ 0 & 0 & 0 & 0 & 1 & 0 & 0 & 0 & -0.9999 \\ 0 & 0 & 0 & 0 & 0 & 1 & 0 & 0 & -1.0002 \\ 0 & 0 & 0 & 0 & 0 & 0 & 1 & 0 & -1.0003 \\ 0 & 0 & 0 & 0 & 0 & 0 & 0 & 1 & -1.0001 \end{bmatrix}, \tag{5.2}$$

which indicates that all the ion chamber signals are almost equal for this data. It is evident from the pattern of the data shown in Fig. 5.3(b) that the data of all ion chambers are highly positively correlated holding larger variability of signals than that of noise. Hence, these outcomes are applicable for any other transient for which the same correlation pattern persists.

All the FDI techniques, i.e., GLR, IMT and IPCT (refer to Section 3.3), depend on the mismatch of the actual measurements from the expected measurements. This mismatch is captured in constraint residuals $\boldsymbol{r}(k) = \boldsymbol{A}\boldsymbol{y}(k)$ for GLR method and in measurement adjustments $\boldsymbol{a}(k) = \boldsymbol{y}(k) - \hat{\boldsymbol{x}}(k)$ for IMT and IPCT. Each element of the residuals and adjustments should be 'white' for proper distance measure to be used in FDI. The validity of the constraint model $\boldsymbol{A}$ plays an important role in the whiteness. In other words, the residuals and adjustments are white if the constraint model $\boldsymbol{A}$ is valid to represent the algebraic relationships among the variables (or ion chamber measurements). To test the validity of the constraint model (5.1) or (5.2), a whiteness test is conducted as follows:

For the case of fault-free ion chamber data simulated through the RR movement, as described above, the reconciled estimates are obtained from (3.5) and the whiteness of adjustments, obtained from (3.6), is tested [106]. A consistent estimate of covariance of measurement adjustments of i^{th} ion chamber signals is computed as

$$\sigma_0 = \frac{1}{N_w} \sum_{\kappa=0}^{N_w} a_i^2(\kappa), \tag{5.3}$$

Table 5.3: Violation index of measurement adjustments of ion chamber data in WT for RR movement transient

Measurement adjustments	a_1	a_2	a_3	a_4	a_5	a_6	a_7	a_8	a_9
Violation index (%)	1.86	1.46	1.99	1.73	1.66	1.26	1.46	1.99	1.06

where a_i is the i^{th} element of the adjustment vector and N_w is the number of observations in the time-window. If the innovations are white, the auto-covariance

$$\sigma_j = \frac{1}{N_w} \sum_{\kappa=0}^{N_w - j} a_i(\kappa) a_i(\kappa + j) \tag{5.4}$$

has the following properties:

$$\sigma_j \sim \mathcal{N}\left(0, \frac{\sigma_0^2}{N_w}\right), \forall j = 1, ..., k$$
$$\text{cov}[\sigma_j, \sigma_l] = 0, j \neq l, \ \forall j = 1, ..., k,$$

and

$$\frac{|\sigma_j|}{\sigma_0} \leq \frac{1.96}{\sqrt{N_w}}, \ \forall j = 1, ..., k, \tag{5.5}$$

is satisfied with a 5% violation. This test is called Whiteness Test (WT), while the threshold of $\frac{1.96}{\sqrt{N_w}}$ is called WT threshold. If the percentage of violation or violation index exceeds 5%, then the innovation sequence is declared as non-white.

Fig. 5.4 shows the adjustment sequence of all the 9 ion chambers, while Fig. 5.5 shows the auto-correlation characteristic as a function of the lag index j. It can be seen that there are no trends or serial correlation in the adjustment sequence. The whiteness violation index $\frac{|\sigma_j|}{\sigma_0}$ for each of the ion chambers is given in Table 5.3. Since the violation index is less than 5% for all the 9 ion chambers, the adjustments are white. This means that the constraint model of (5.2) is apt to carry out the DR and FDI analyses.

DR and FDI statistics (refer to Section 3.2 and 3.3) such as ODR or percentage of detection of faults; OP or percentage of correct isolation of faults; and AER or percentage

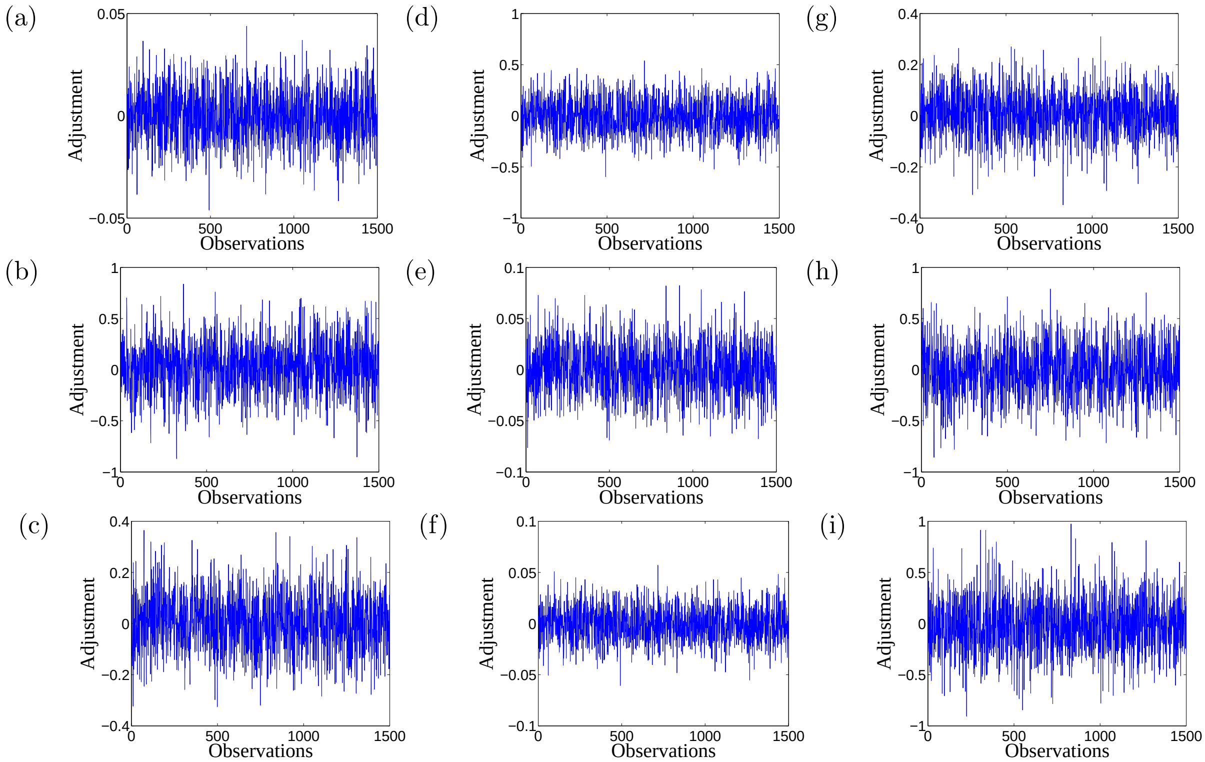

Figure 5.4: Open-loop RR transient: Adjustments for (a) ion chamber-1 (b) ion chamber-2 (c) ion chamber-3 (d) ion chamber-4 (e) ion chamber-5 (f) ion chamber-6 (g) ion chamber-7 (h) ion chamber-8 (i) ion chamber-9.

reduction in error due to DR, exhibited by all the FDI techniques of Section 3.3 when coupled with IPCA-model-based DR scheme are computed. When the IPCT (refer to Fig. 3.4) is applied in 3-fault scenarios, for bias magnitudes of 10% of the nominal steady-state signals, the smallest OP of 93.54% is observed with ion chamber-2, ion chamber-4 and ion chamber-9 being the faulty ion chambers (see Table 5.1). Signals of these ion chambers for the bias magnitudes of 10% of the nominal steady-state signals are shown in Fig. 5.6(a), 5.6(b), and 5.6(c) respectively. For the bias magnitudes of 10%, the largest OP of 100% is observed with ion chamber-3, ion chamber-6 and ion chamber-8 being the faulty detectors. Signals of this ion chamber combination for the bias magnitudes of 10% are shown in Fig. 5.7(a), 5.7(b), and 5.7(c) respectively. In other combinations of 3 faults, the OP was found to be in between these smallest and largest values.

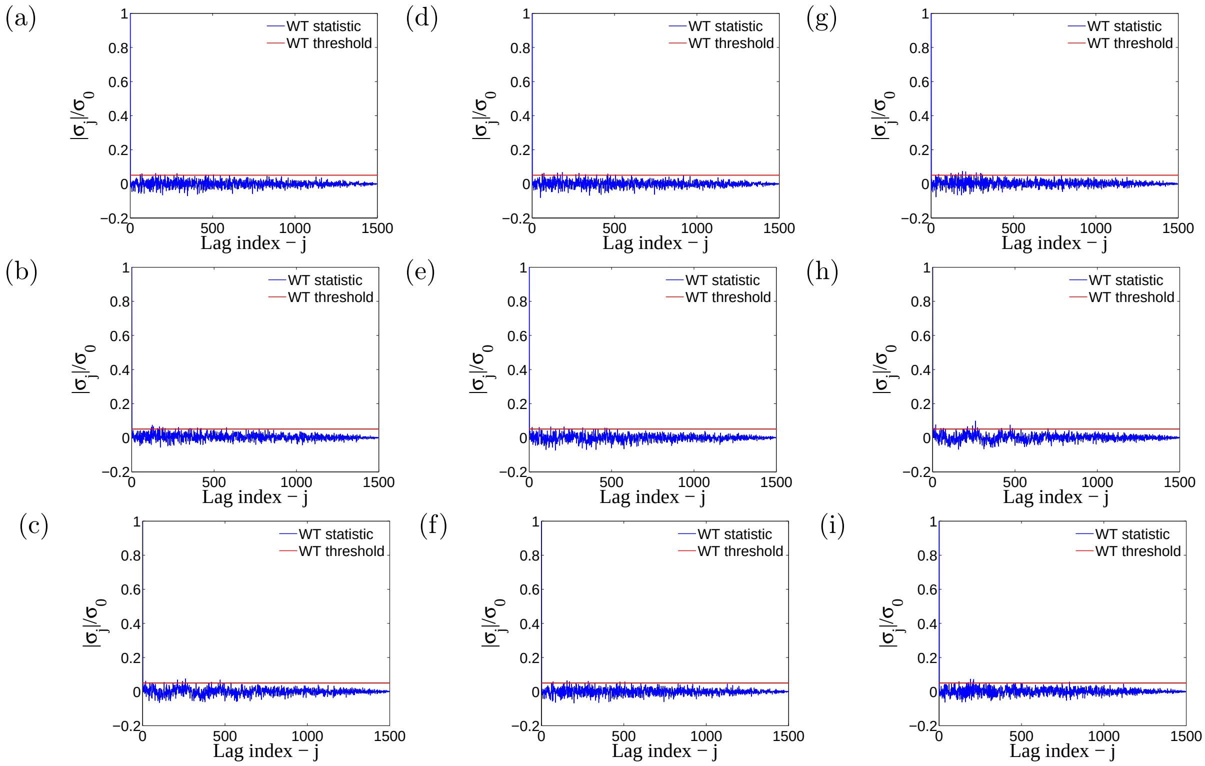

Figure 5.5: Open-loop RR transient: Whiteness test statistics for (a) ion chamber-1 (b) ion chamber-2 (c) ion chamber-3 (d) ion chamber-4 (e) ion chamber-5 (f) ion chamber-6 (g) ion chamber-7 (h) ion chamber-8 (i) ion chamber-9.

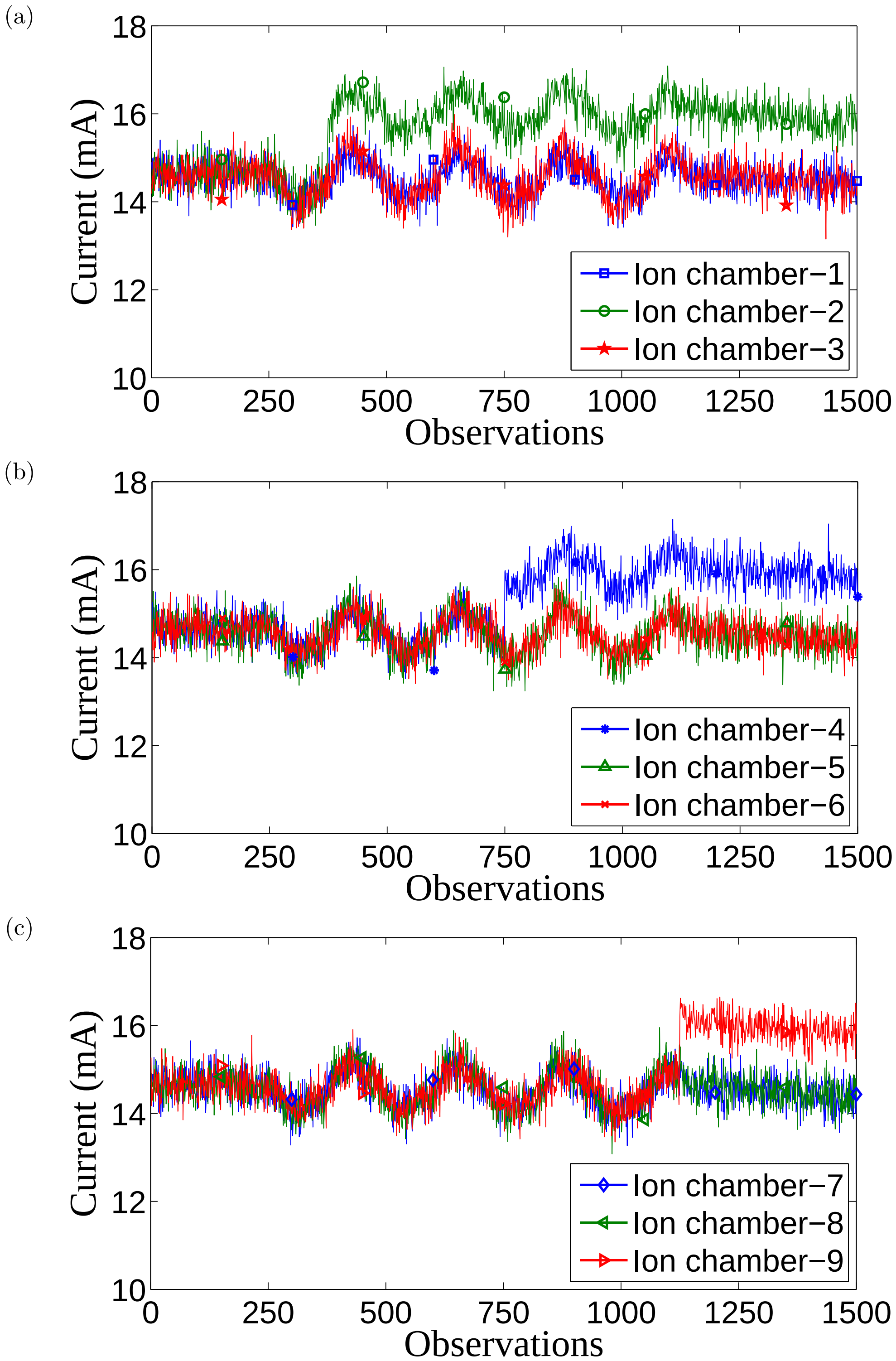

Figure 5.6: Data of ion chambers with smallest OP in the 3-fault scenarios during the transient involving RR movement: (a) Data to RRS (ion chamber-2 is faulty) (b) Data to SDS-1 (ion chamber-4 is faulty) (c) Data to SDS-2 (ion chamber-9 is faulty). (Note: Sudden jumps in the above figures are because of additive biases in the signals.)

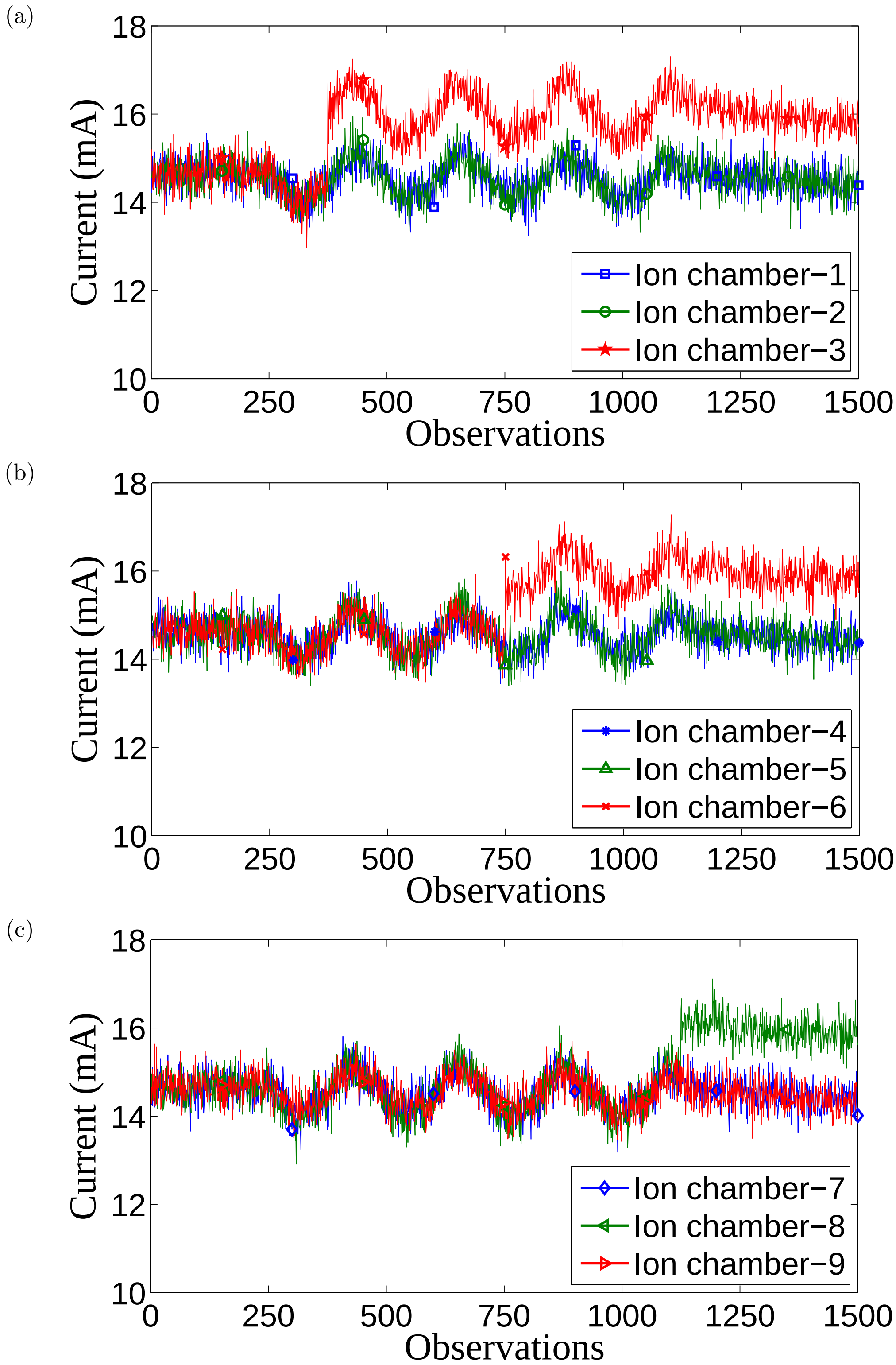

Figure 5.7: Data of ion chambers with largest OP in the 3-fault scenarios during the transient involving RR movement (a) Data to RRS (ion chamber-3 is faulty) (b) Data to SDS-1 (ion chamber-6 is faulty) (c) Data to SDS-2 (ion chamber-8 is faulty).

DR and FDI statistics exhibited by all the FDI techniques of Section 3.3 are given in Tables 5.4 and 5.5. Table 5.4 gives the statistics corresponding to the combination 'ion chamber-2, ion chamber-4 and ion chamber-9', which exhibited minimum OP when IPCT is applied. Table 5.5 gives those with combination 'ion chamber-3, ion chamber-6 and ion chamber-8', which resulted in maximum OP. The statistics given in Tables 5.4 and 5.5 are pictorially represented in Fig. 5.8 and 5.9, respectively.

In the 3-fault scenarios described above, it can be observed from Tables 5.4 and 5.5 that for a bias of 8.5% and more, the fault is successfully detected by all the FDI techniques independently coupled with the IPCA-based DR scheme. This is evident from the 100% ODR for a bias of 8.5% and more. However, at 8.5% bias, the OP statistics, which are indicative of faulty-detector identification rate, are not significant for GLR method and IMT, while the IPCT performed well. Since the errors in measurements are because of random errors and faults, their magnitudes are expected to be reduced, when the faults are successfully identified after their detection and the subsequent fault-free data is efficiently reconciled for random errors. The AER statistics, which are measures for the efficacy of the FDI schemes, are also found to be better with IPCT. The same conclusions, as obtained with Table 5.4 (for smallest OP combination), can be drawn from Fig. 5.8 in which the DR and FDI statistics are plotted with respect to the bias magnitude. Similarly, Fig. 5.9 depict the DR and FDI statistics given in Table 5.5 for the major OP combination. In Tables 5.4 and 5.5 and Fig. 5.8 and 5.9, the superiority of the IPCT is also seen in terms of its better ability to detect subtle faults. However, the effectiveness of the DR-based FDI can be observed with all the FDI techniques. In the applications requiring online correction of the faults, the GLR method suits better as it can estimate the magnitude of the faults. When this requirement is not there, any other FDI technique exhibiting superior DR and FDI statistics can be used. Hence, the IPCT is chosen as the FDI strategy from hereinafter, as the DR problem formulation using $Q - R$ factorization automatically corrects the faults in the variables.

Table 5.4: DR and FDI statistics for the ion chamber combination with minimum OP (Note: Highlighted rows under ODR, OP and AER represent a substantial change at a particular bias magnitude.)

Bias (%)	ODR (%)			OP (%)			AER (%)			
	GLR	IMT	IPCT	GLR	IMT	IPCT	GLR-C	GLR-E	IMT	IPCT
0	0	12.90	35.48	0	0	0	22.32	22.32	20.95	23.21
0.5	3.22	9.67	35.48	0	0	0	23.01	23.38	21.41	24.94
1	6.45	12.90	35.48	0	0	0	24.68	25.43	23.90	27.16
1.5	9.67	16.12	38.70	0	0	0	25.62	25.43	25.30	30.11
2	12.90	19.35	41.93	0	0	0	25.82	27.75	26.60	31.61
2.5	16.12	25.80	48.38	0	0	0	25.14	28.16	29.93	31.37
3	22.58	29.03	51.61	0	0	3.22	23.16	28.79	31.67	30.77
3.5	38.70	35.48	64.51	3.22	0	9.67	20.00	30.90	32.01	32.95
4	51.61	41.93	64.51	6.45	0	19.35	16.05	31.73	31.77	29.88
4.5	61.29	64.51	70.96	9.67	0	19.35	13.21	32.44	36.02	29.24
5	61.29	70.96	83.87	16.12	3.22	41.93	11.64	32.86	33.23	35.22
5.5	67.74	74.19	87.09	19.35	9.67	45.16	8.49	34.12	34.37	40.15
6	77.41	80.64	93.54	29.03	12.90	54.83	5.95	36.51	35.57	43.19
6.5	83.87	80.64	96.77	35.48	22.58	61.29	6.00	43.04	36.54	49.77
7	87.09	83.87	100	41.93	32.25	70.96	5.96	44.68	38.72	49.90
7.5	96.77	87.09	100	45.16	41.93	83.87	5.43	53.25	40.68	52.44
8	100	96.77	100	54.83	54.83	87.09	3.85	54.40	43.30	53.70
8.5	100	100	100	58.06	54.83	90.32	3.66	55.57	47.49	55.74
9	100	100	100	61.29	74.19	90.32	3.53	57.35	53.14	57.21
9.5	100	100	100	64.51	80.64	93.54	3.39	58.87	54.88	56.96
10	100	100	100	64.51	90.32	93.54	3.25	60.13	55.93	58.19
10.5	100	100	100	64.51	96.77	90.32	3.18	61.15	59.19	58.11
11	100	100	100	67.74	100	87.09	3.27	62.75	60.77	59.44
11.5	100	100	100	67.74	100	87.09	3.15	63.75	61.75	60.34
12	100	100	100	67.74	100	87.09	3.02	63.79	62.68	61.45
12.5	100	100	100	70.96	100	90.32	3.06	63.31	63.55	61.00
13	100	100	100	74.19	100	90.32	5.06	65.15	64.38	61.78
13.5	100	100	100	70.96	100	90.32	6.00	65.96	65.17	62.51
14	100	100	100	61.29	100	90.32	8.00	67.18	65.91	63.20
14.5	100	100	100	58.06	100	90.32	8.77	66.86	66.62	63.86
15	100	100	100	54.83	100	90.32	10.52	66.64	67.30	64.49
15.5	100	100	100	45.16	100	90.32	12.72	67.15	67.94	65.09
16	100	100	100	35.48	100	87.09	14.10	66.86	68.56	65.14
16.5	100	100	100	19.35	100	83.87	14.15	63.45	69.14	64.76
17	100	100	100	16.12	100	83.87	13.83	61.74	69.71	66.09
17.5	100	100	100	12.90	100	83.87	14.56	61.49	70.25	66.55
18	100	100	100	6.45	100	87.09	13.76	57.66	70.76	67.94
18.5	100	100	100	0	100	90.32	13.36	54.59	71.26	67.95
19	100	100	100	0	100	90.32	13.43	54.12	71.74	68.41
19.5	100	100	100	0	100	90.32	13.10	53.50	72.20	68.85
20	100	100	100	0	100	90.32	11.90	48.66	72.64	69.27

Table 5.5: DR and FDI statistics for the ion chamber combination with largest OP (Note: Highlighted rows under ODR, OP and AER represent a substantial change at a particular bias magnitude.)

Bias (%)	**ODR (%)**			**OP (%)**			**AER (%)**			
	GLR	**IMT**	**IPCT**	**GLR**	**IMT**	**IPCT**	**GLR-C**	**GLR-E**	**IMT**	**IPCT**
0	0	12.90	35.48	0	0	0	22.32	22.32	20.95	23.22
0.5	0	12.90	32.26	0	0	0	23.47	23.47	23.06	24.00
1	3.23	19.35	38.71	0	0	0	25.66	26.03	24.54	24.61
1.5	6.45	22.58	51.61	0	0	0	26.91	26.33	27.10	27.86
2	9.68	29.03	58.06	0	0	0	29.10	28.40	29.46	32.79
2.5	29.03	29.03	74.19	0	0	3.23	28.41	35.22	31.88	35.35
3	35.48	38.71	77.42	0	0	9.68	27.72	41.09	34.06	33.65
3.5	45.16	45.16	83.87	6.45	0	16.13	24.31	39.77	34.96	33.21
4	54.84	54.84	87.10	9.68	0	19.35	22.16	41.37	36.16	34.66
4.5	67.74	74.19	90.32	12.90	3.23	29.03	16.54	40.07	41.53	35.66
5	83.87	80.65	93.55	22.58	3.23	29.03	7.66	36.36	41.70	38.65
5.5	87.10	83.87	96.77	25.81	12.90	45.16	8.30	44.19	37.25	37.44
6	90.32	83.87	100	38.71	19.35	58.06	7.94	45.97	39.32	40.91
6.5	96.77	83.87	100	41.94	25.81	70.97	6.58	48.20	41.43	46.69
7	96.77	87.10	100	48.39	38.71	77.42	6.36	50.35	45.24	50.11
7.5	100	93.55	100	54.84	58.06	80.65	5.31	52.59	48.65	50.62
8	100	96.77	100	58.06	64.52	83.87	4.94	57.38	51.68	56.20
8.5	100	100	100	58.06	74.19	90.32	3.74	57.69	54.68	57.43
9	100	100	100	58.06	83.87	93.55	3.87	60.16	58.09	57.43
9.5	100	100	100	64.52	93.55	93.55	3.69	60.62	58.17	58.64
10	100	100	100	67.74	96.77	100	3.58	61.36	59.69	60.13
10.5	100	100	100	67.74	96.77	100	3.45	62.51	60.75	61.21
11	100	100	100	64.52	96.77	96.77	3.32	63.23	62.01	61.23
11.5	100	100	100	70.97	100	96.77	3.57	64.27	62.90	62.16
12	100	100	100	77.42	100	96.77	3.73	65.45	63.80	63.04
12.5	100	100	100	80.65	100	96.77	3.68	66.39	64.65	63.87
13	100	100	100	70.97	100	96.77	5.98	67.27	65.45	64.66
13.5	100	100	100	67.74	100	96.77	7.12	66.82	66.21	65.40
14	100	100	100	54.84	100	96.77	8.57	66.06	66.94	66.11
14.5	100	100	100	48.39	100	93.55	9.91	65.47	67.63	66.16
15	100	100	100	35.48	100	96.77	10.81	63.71	68.28	67.42
15.5	100	100	100	25.81	100	96.77	13.47	65.03	68.91	68.03
16	100	100	100	12.90	100	96.77	14.86	63.36	69.50	68.61
16.5	100	100	100	9.68	100	96.77	14.97	61.63	70.07	69.17
17	100	100	100	9.68	100	96.77	14.26	60.03	70.62	69.70
17.5	100	100	100	6.45	100	96.77	13.69	57.48	71.14	70.21
18	100	100	100	0	100	100	14.54	55.28	71.64	71.90
18.5	100	100	100	0	100	100	13.84	51.99	72.12	72.38
19	100	100	100	0	100	100	13.62	51.22	72.58	72.84
19.5	100	100	100	0	100	100	12.89	47.47	73.03	73.28
20	100	100	100	0	100	100	12.27	43.23	73.45	73.70

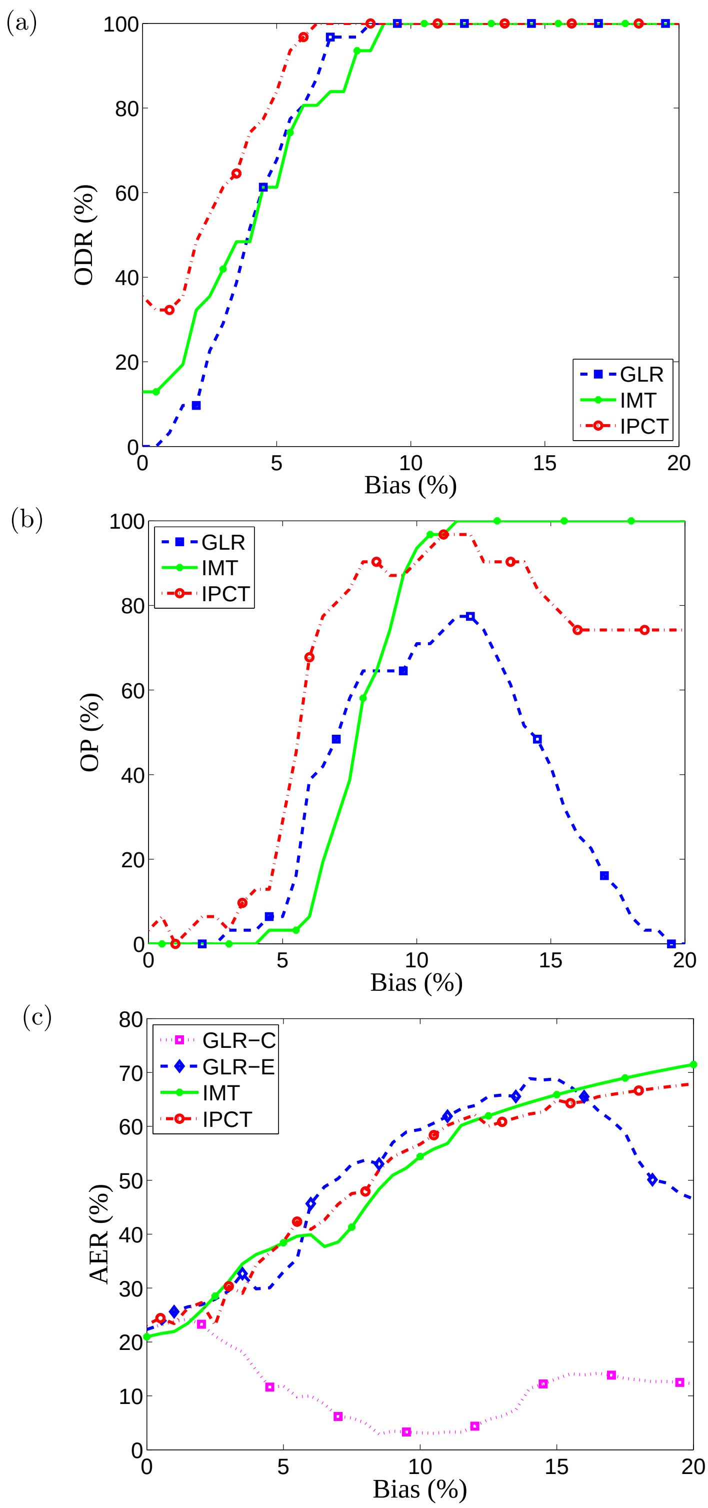

Figure 5.8: DR and FDI statistics for additive biases in smallest OP combination during open-loop transient, *i.e.*, ion chamber-2, ion chamber-4 and ion chamber-9 signals (a) ODR (b) OP (c) AER. (Note: ODR at 0% bias refers to detection of faults at healthy condition of ion chambers. It refers to Type-I error as explained in Section 3.3.)

(a)

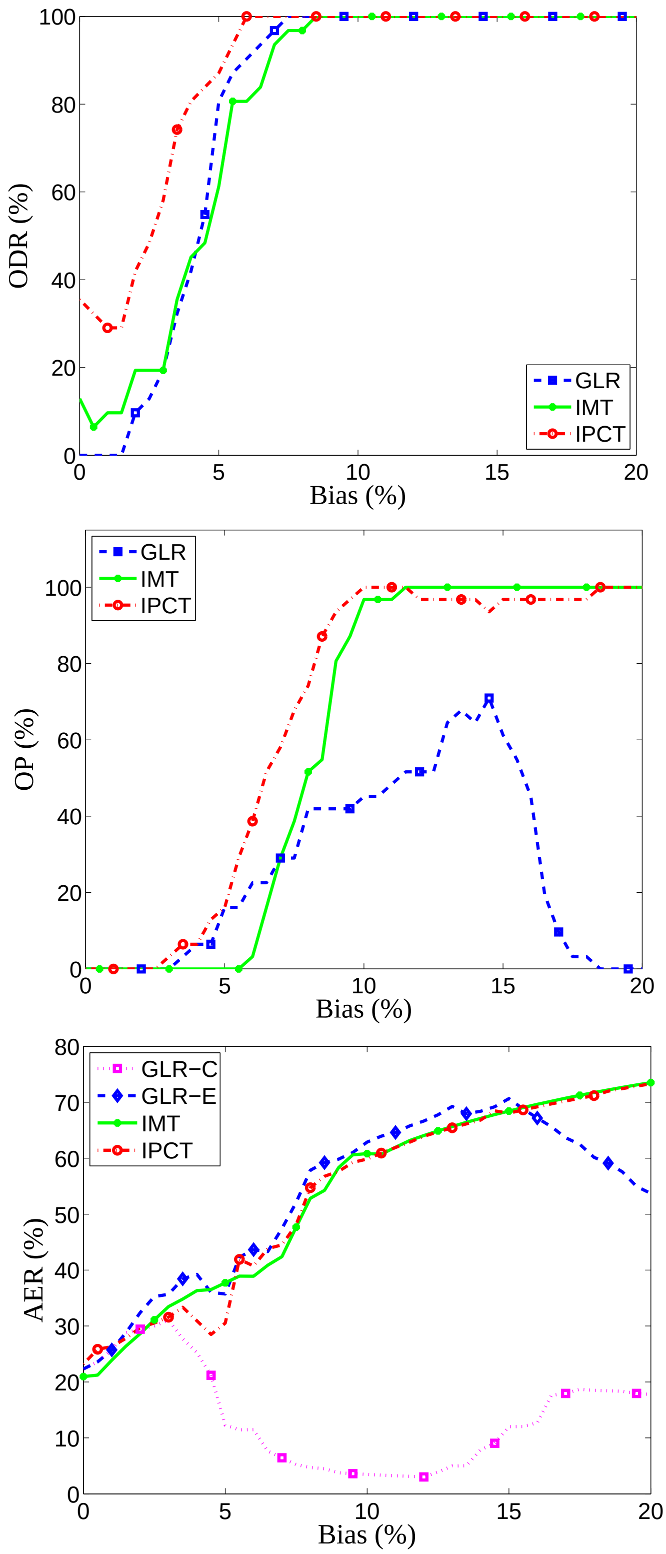

(b)

(c)

Figure 5.9: DR and FDI statistics for additive biases in largest OP combination during open-loop transient, *i.e.*, ion chamber-3, ion chamber-6 and ion chamber-8 signals (a) ODR (b) OP (c) AER.

In the above simulation, the systematic bias percentages help in easy interpretation, however, they do not represent a realistic situation. Hence, another simulation was conducted, in which the bias percentages were chosen at random, drawn from a normal distribution, which is more realistic. Faults with a standard deviation of 10% of the nominal values of the signals are first simulated at random. For the ion chamber combination {1,4,7}, 100 realizations of randomly generated bias combinations as shown in Fig. 5.10 are considered for the presentation of results. For each realization, ion chamber-1, ion chamber-4 and ion chamber-7 are corrupted by the faults of the corresponding bias combination, from the inception of second, third and forth quarters of data, respectively. For this case, the DR and FDI statistics for all 100 random bias combinations for 1-fault scenario in ion chamber-1 (during the fist quarter) are shown Fig. 5.11. Fig. 5.11(a) shows the indices, *viz.*, ODR and OP as a function of bias magnitude, for a single fault in ion chamber-1. The inverted-bell shaped curves in Fig. 5.11(a) indicate that the positive and negative faults are equally likely to get detected and identified. AER also increases as a function of bias (for positive and negative, both) as shown in Fig. 5.11(b). From AA characteristics of Fig. 5.11(c), one fact can be observed: for a bias of -20% in ion chamber-1, the adjustments made to the data of ion chamber-1 are -2.9 mA, which is equal to about -20% of the nominal signal value of 14.67 mA. This means, DR coupled with IPCT scheme is able to remove the effects of faults from the data. It can also be observed that the data of all other ion chambers are not affected as a function of bias in the signal of ion chamber-1, since their AA characteristics are close to zero. In the 2-fault case (simultaneous faults in ion chambers 1 and 4 during the third quarter) and the 3-fault case (simultaneous faults in ion chambers {1,4,7} during the fourth quarter), DR and FDI statistics are as shown in Figs. 5.12 and 5.13, respectively. In these cases, the random biases in a realization are not the same, thus, the characteristics, *viz.*, ODR, OP and AER, being dependent upon the random bias magnitudes in each of the signals, are generally high as there is a high probability

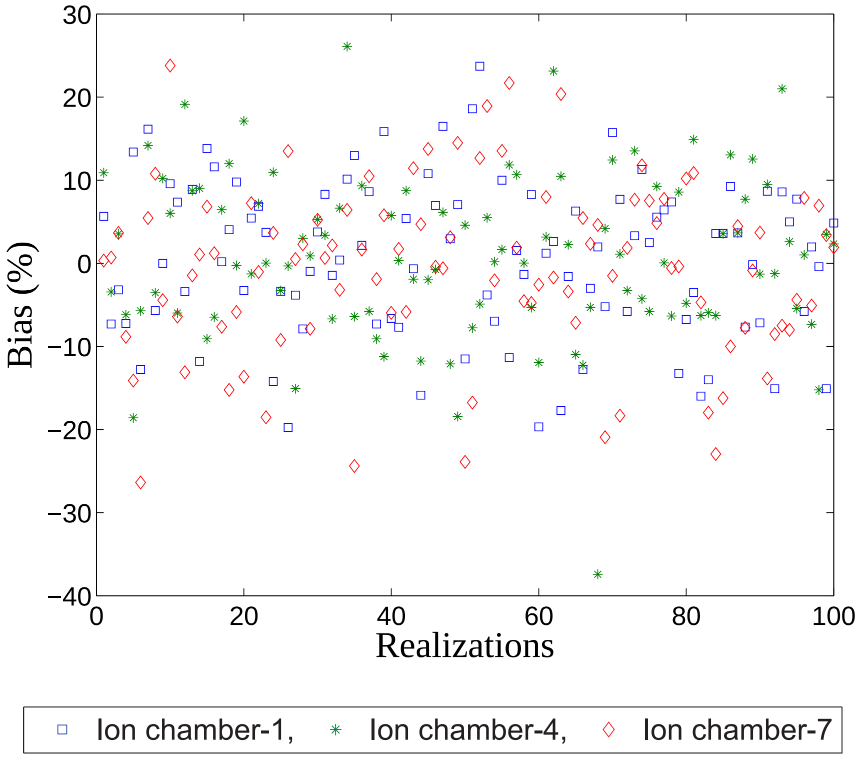

Figure 5.10: Randomly chosen bias magnitudes for open-loop transient.

that one of the fault magnitudes being of large magnitudes. AA characteristics in Figs. 5.12 and 5.13 are seen to be sorted based on the magnitude of faults in one of the ion chambers. The AA characteristics of the faulty ion chambers are seen to be non-zero (with respect to the fault magnitudes), while the others are zero. It can be observed that the ODR, OP and AER characteristics obtained in this case of bias magnitudes chosen at random are identical to those with systematic bias. Hence, in the subsequent sections, results with only systematic biases are presented.

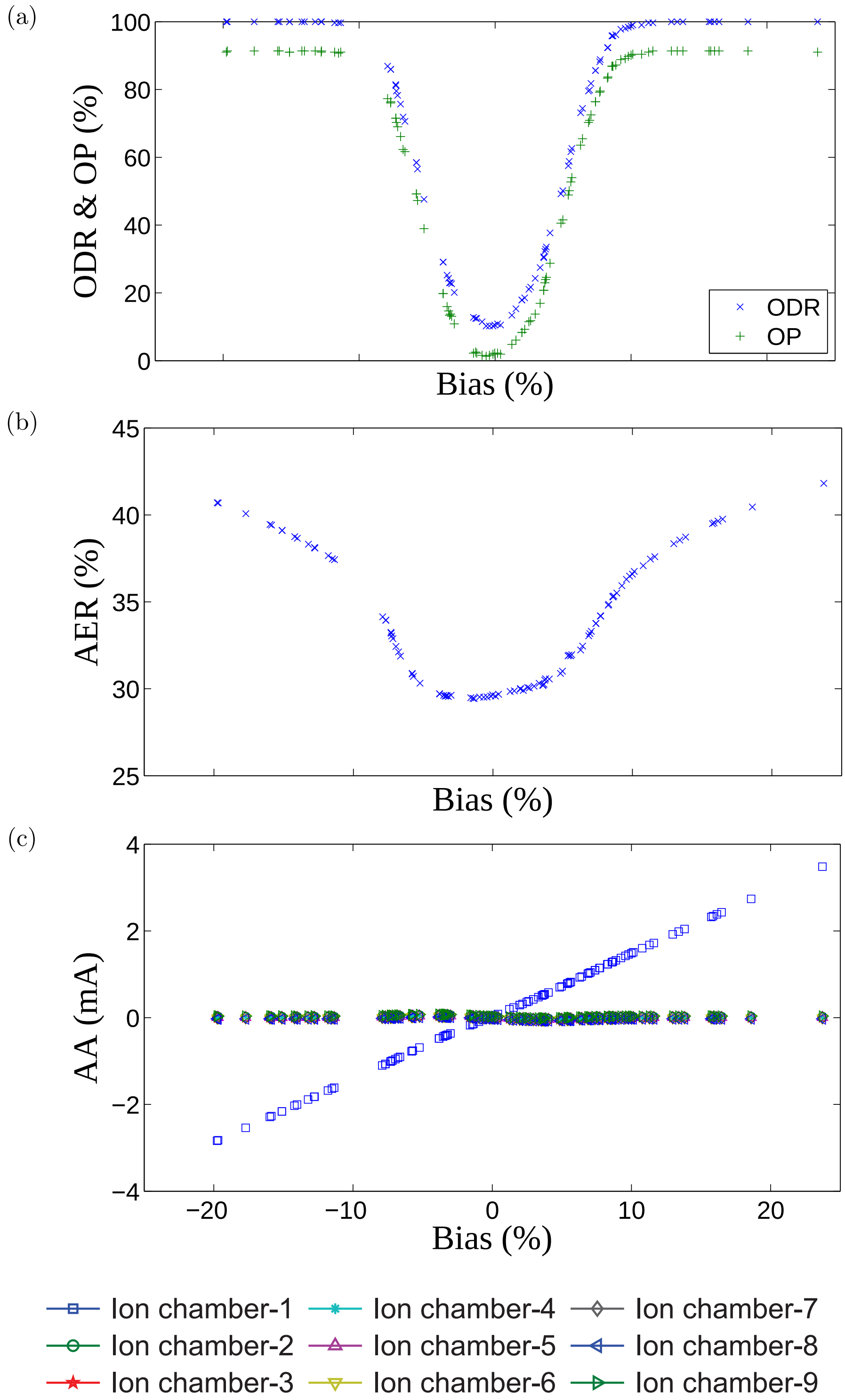

Figure 5.11: DR and FDI statistics in 1-fault scenario during the open-loop transient (fault in ion chamber-1 only) (a) ODR and OP (b) AER (c) AA.

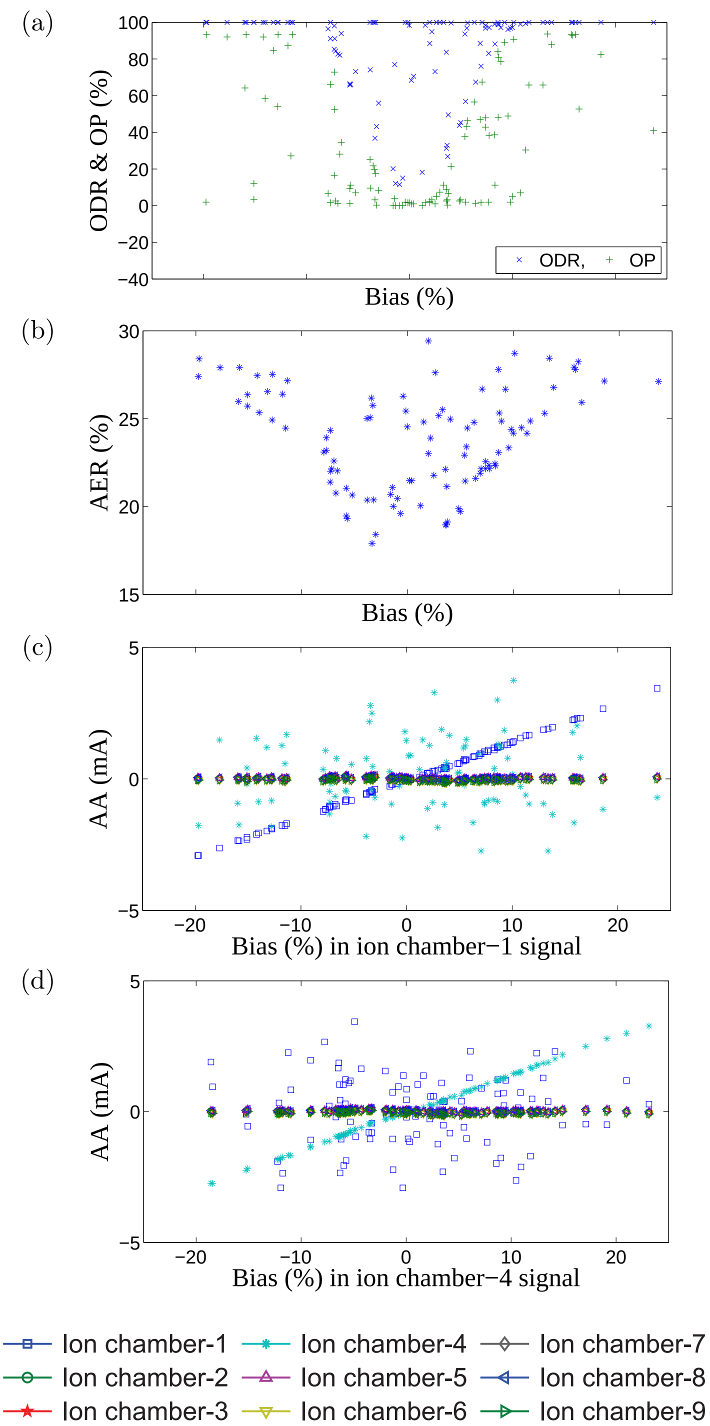

Figure 5.12: DR and FDI statistics in 2-fault scenario during the open-loop transient (faults in ion chamber-1 and ion chamber-4, both) (a) ODR and OP (b) AER (c) AA when bias (%) in ion chamber-1 signal is taken as reference (d) AA when bias (%) in ion chamber-4 signal is taken as reference.

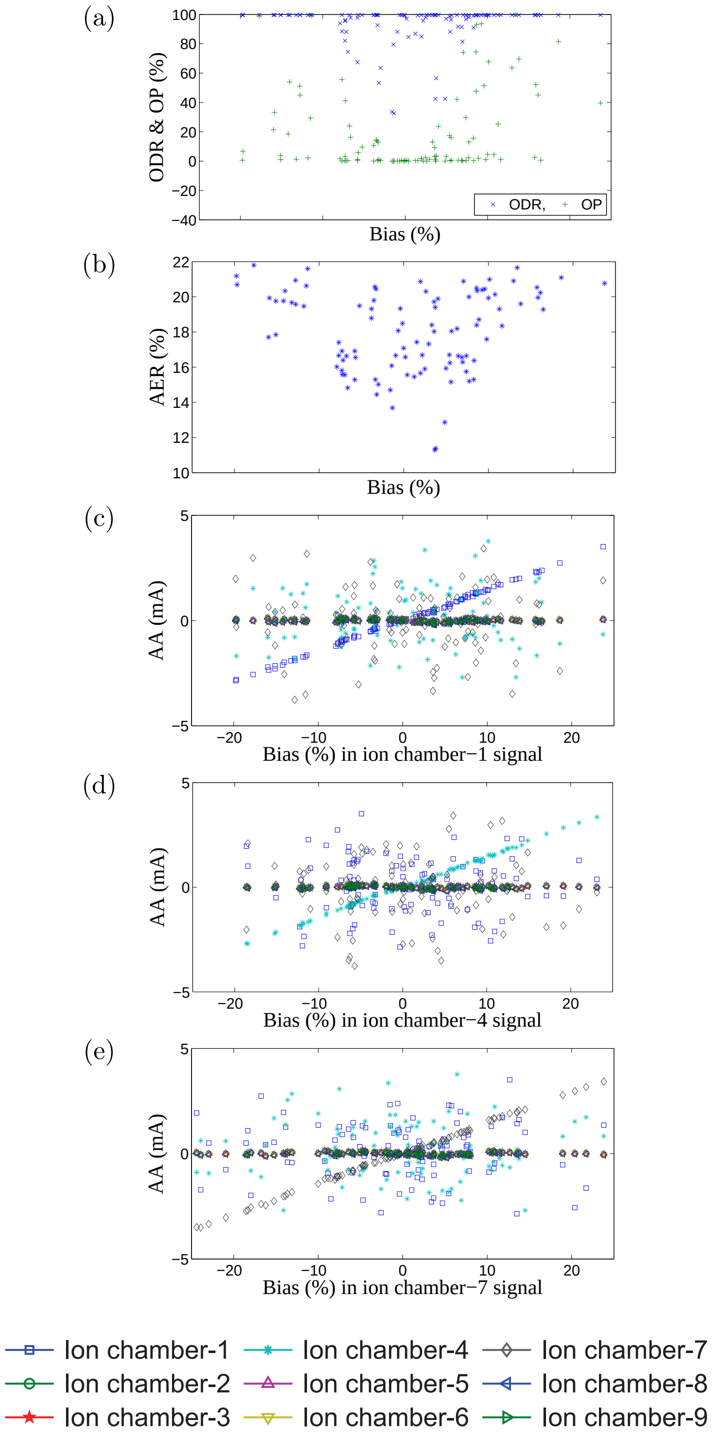

Figure 5.13: DR and FDI statistics in 3-fault scenario during the open-loop transient (faults in all the ion chambers{1,4,7}) (a) ODR and OP (b) AER (c) AA when bias (%) in ion chamber-1 signal is taken as reference (d) AA when bias (%) in ion chamber-4 signal is taken as reference (e) AA when bias (%) in ion chamber-7 signal is taken as reference.

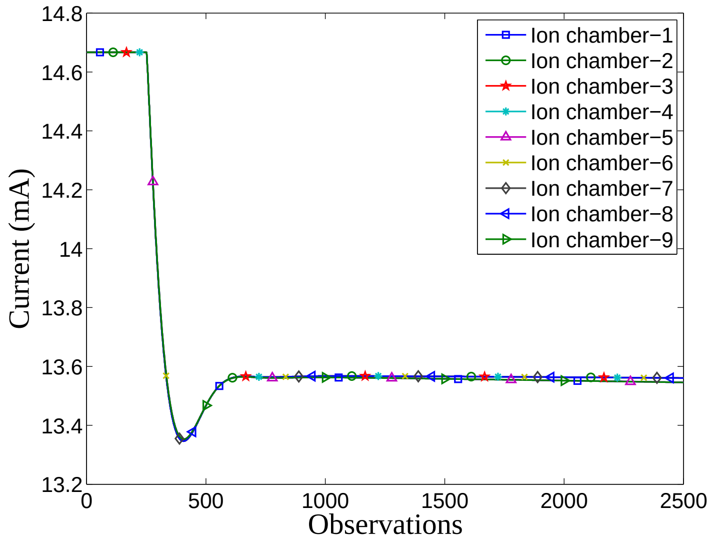

Figure 5.14: Ion chamber signals during the transient corresponding to demand power change.

5.1.2 Data of Ion Chambers during Closed-loop Response of the Reactor for a Demand Power Change

A transient is considered in which the demand power changes from 1.0 pu to 0.9 pu. Positions of all the 4 RRs meant for automatic regulation undergo variations and the new steady-state corresponding to the new demand power is reached. Fig. 5.14 depicts the resulting variations of ion chamber signals, sampled at 0.2 s for a simulation time of 500 s.

DR analysis is conducted on this data, which includes only the process variability and not sensor faults, to test the validity of the constraint model given by (5.1), which was obtained in Section 5.1.1. The analysis presented in Section 5.1.1 is conducted in this case also. The measurement adjustments $\boldsymbol{a}$ (obtained from (3.6)) corresponding to the constraint model in (5.1) and the covariance of the measurement errors obtained from the standard deviation corresponding to $m = 8$ in Table 5.2(b) are shown in Fig. 5.15. Since all the WT violation indices given in Table 5.6 are less than 5%, it can be concluded that the adjustments are white. This implies that the IPCA outcomes obtained in Section 5.1.1 can be used for the cases of demand power change as well.

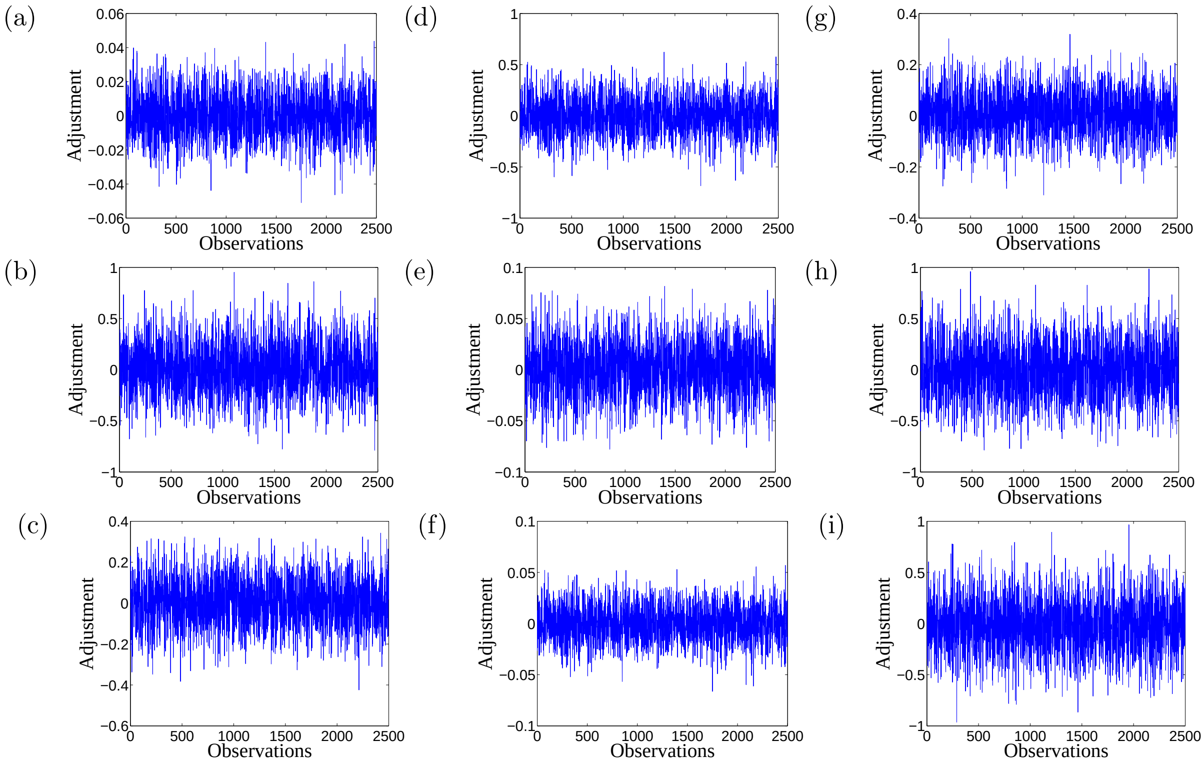

Figure 5.15: Demand power change transient: Adjustments for (a) ion chamber-1 (b) ion chamber-2 (c) ion chamber-3 (d) ion chamber-4 (e) ion chamber-5 (f) ion chamber-6 (g) ion chamber-7 (h) ion chamber-8 (i) ion chamber-9.

Table 5.6: Violation index of measurement adjustments of ion chamber data in WT for demand power change transient

Measurement adjustments	a_1	a_2	a_3	a_4	a_5	a_6	a_7	a_8	a_9
Violation index (%)	1.39	1.55	1.47	1.79	1.67	1.11	1.19	1.47	1.63

This conclusion can also be drawn from the algebraic relations among the ion chamber signals as evident from Fig. 5.3(a) and 5.14.

Bias is applied to simulate 1, 2 and 3-fault scenarios, such that different combinations with 3 ion chambers of control and protection systems are covered. This pattern is repeated for all biases from 0% to 20% of the nominal steady-state signals separated by 0.5%. The constraint model given by (5.1) and the error variance matrix, which was obtained in Section 6.1, are used for DR and FDI analyses in this case also. In the 3-fault scenarios, for bias magnitudes of 10% of the nominal steady-state signals, OP values are

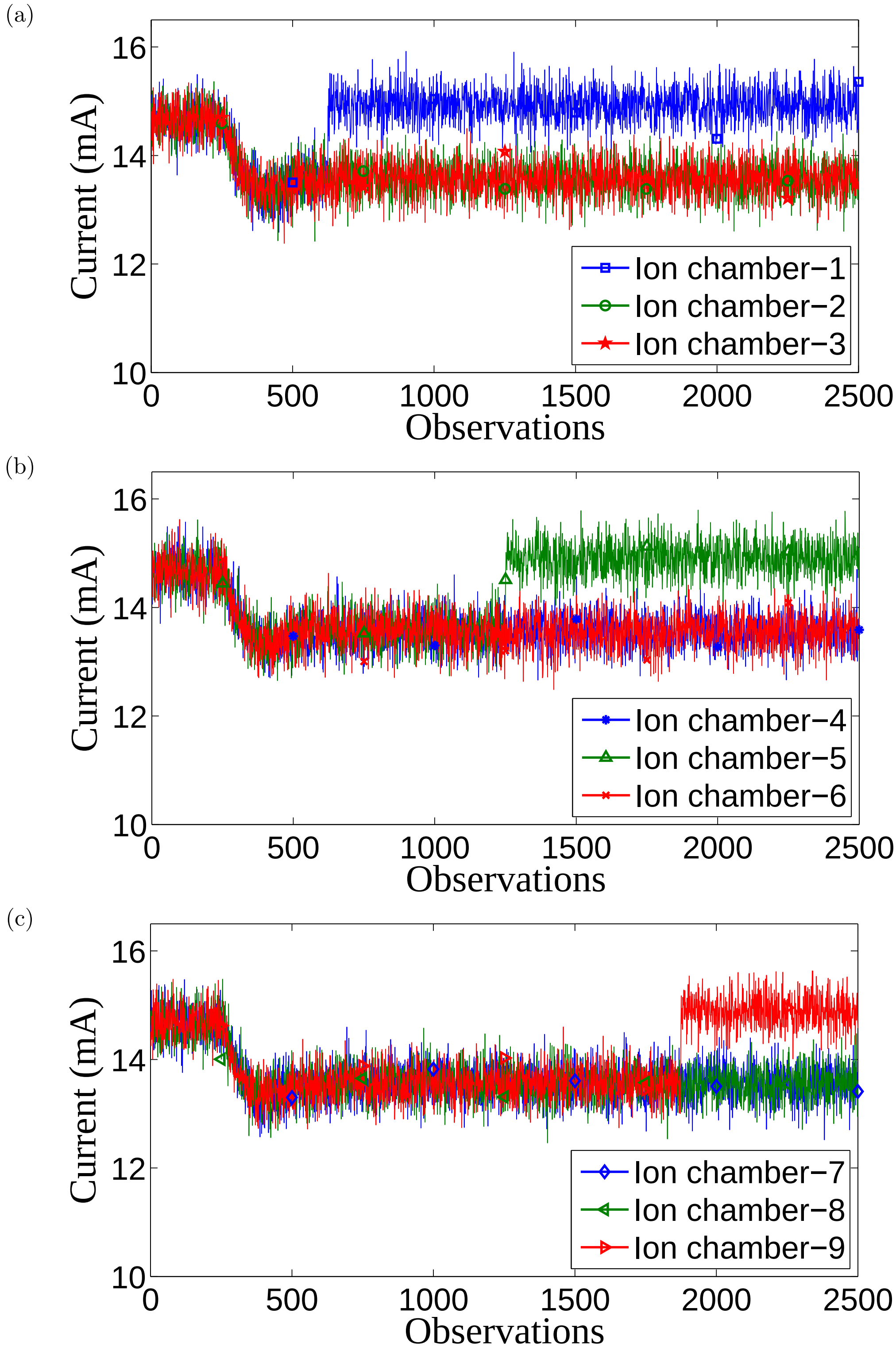

Figure 5.16: Demand power change transient: data of ion chambers with smallest OP in the 3-fault scenarios (a) Data to RRS (ion chamber-1 is faulty) (b) Data to SDS-1 (ion chamber-5 is faulty) (c) Data to SDS-2 (ion chamber-9 is faulty).

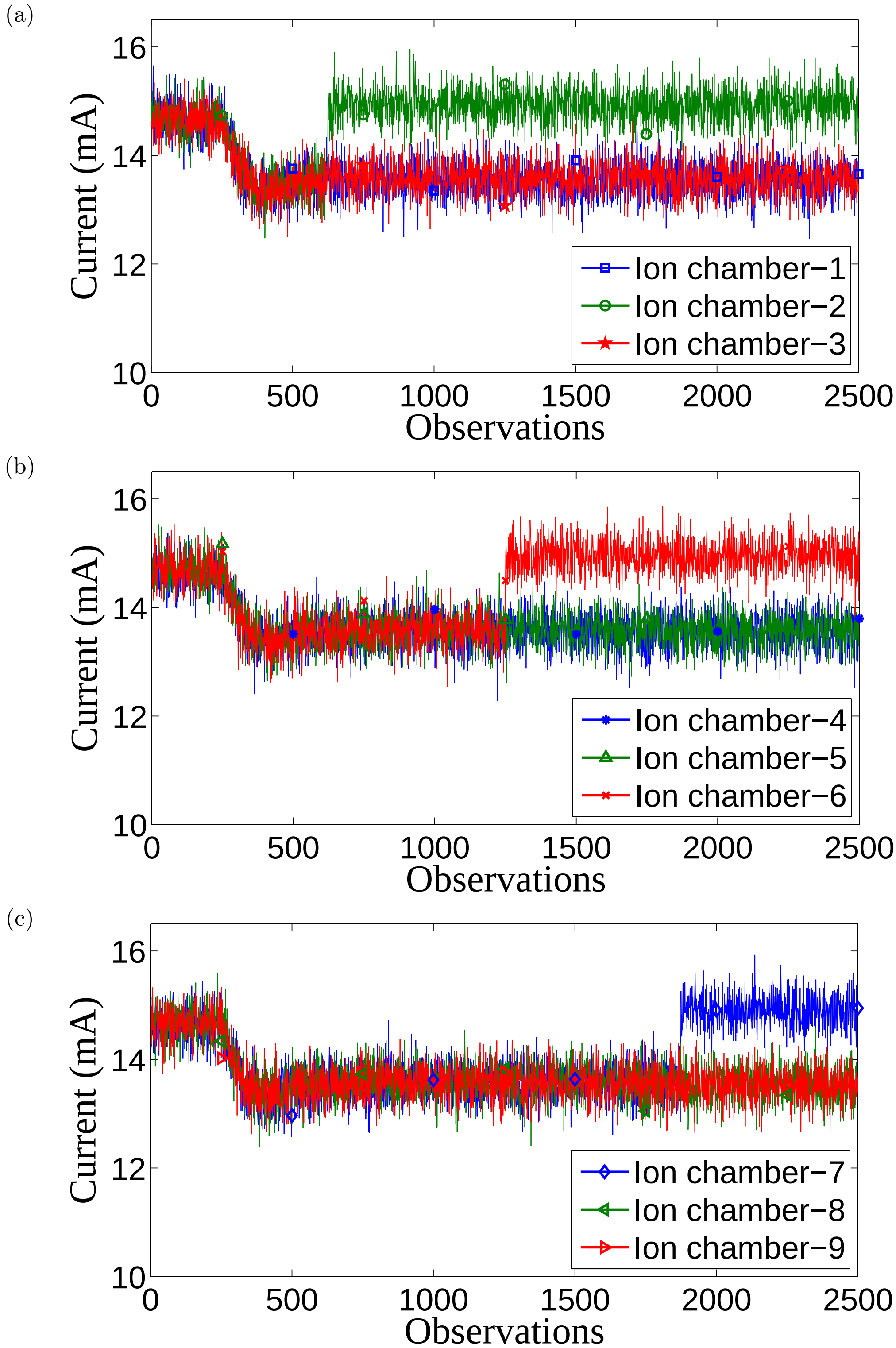

Figure 5.17: Demand power change transient: data of ion chambers with largest OP in the 3-fault scenarios (a) Data to RRS (ion chamber-2 is faulty) (b) Data to SDS-1 (ion chamber-6 is faulty) (c) Data to SDS-2 (ion chamber-7 is faulty).

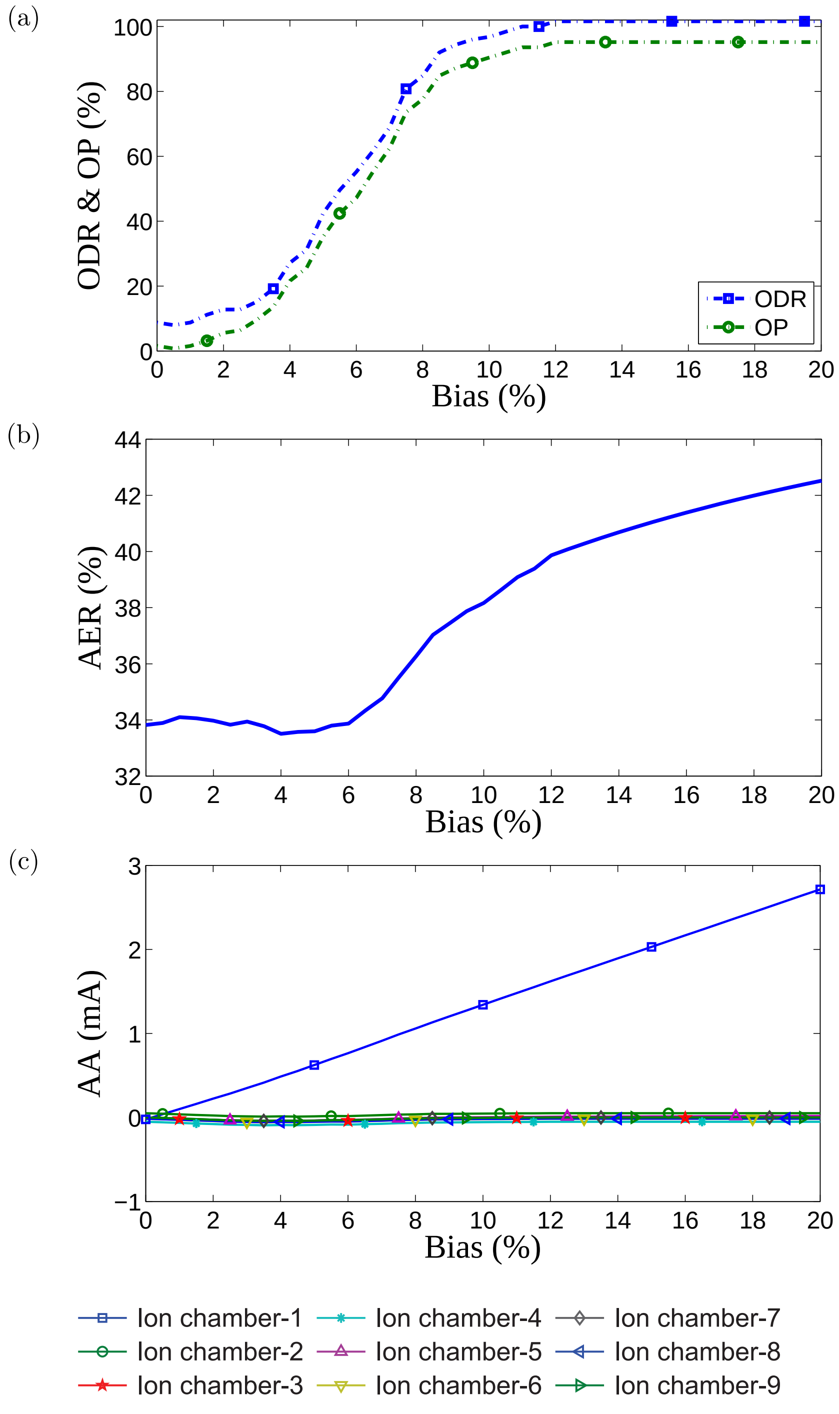

Figure 5.18: DR and FDI statistics in 1-fault scenario with smallest OP during the transient involving change of demand power (fault in ion chamber-1 only) (a) ODR and OP (b) AER (c) AA. (Note: ODR, OP and AER can be seen to increase with bias. AA refers to the adjustment made to ion chamber-1 signal to nullify the fault magnitude in it.)

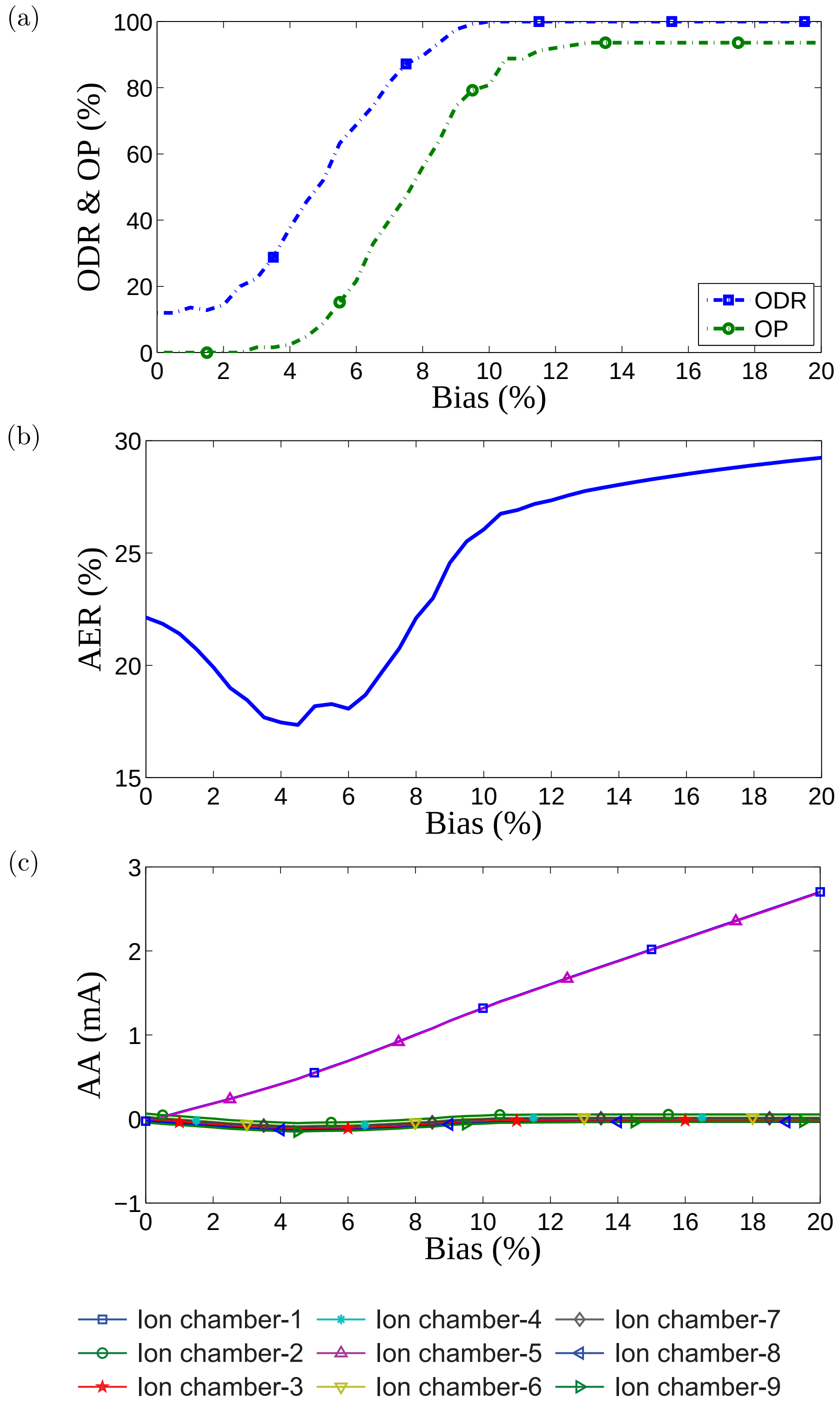

Figure 5.19: DR and FDI statistics in 2-fault scenario with smallest OP during the transient involving change of demand power (faults in ion chamber-1 and ion chamber-5, both) (a) ODR and OP (b) AER (c) AA. (Note: The signals of ion chamber-1 and ion chamber-5 are seen to be corrected from the AA characteristics.)

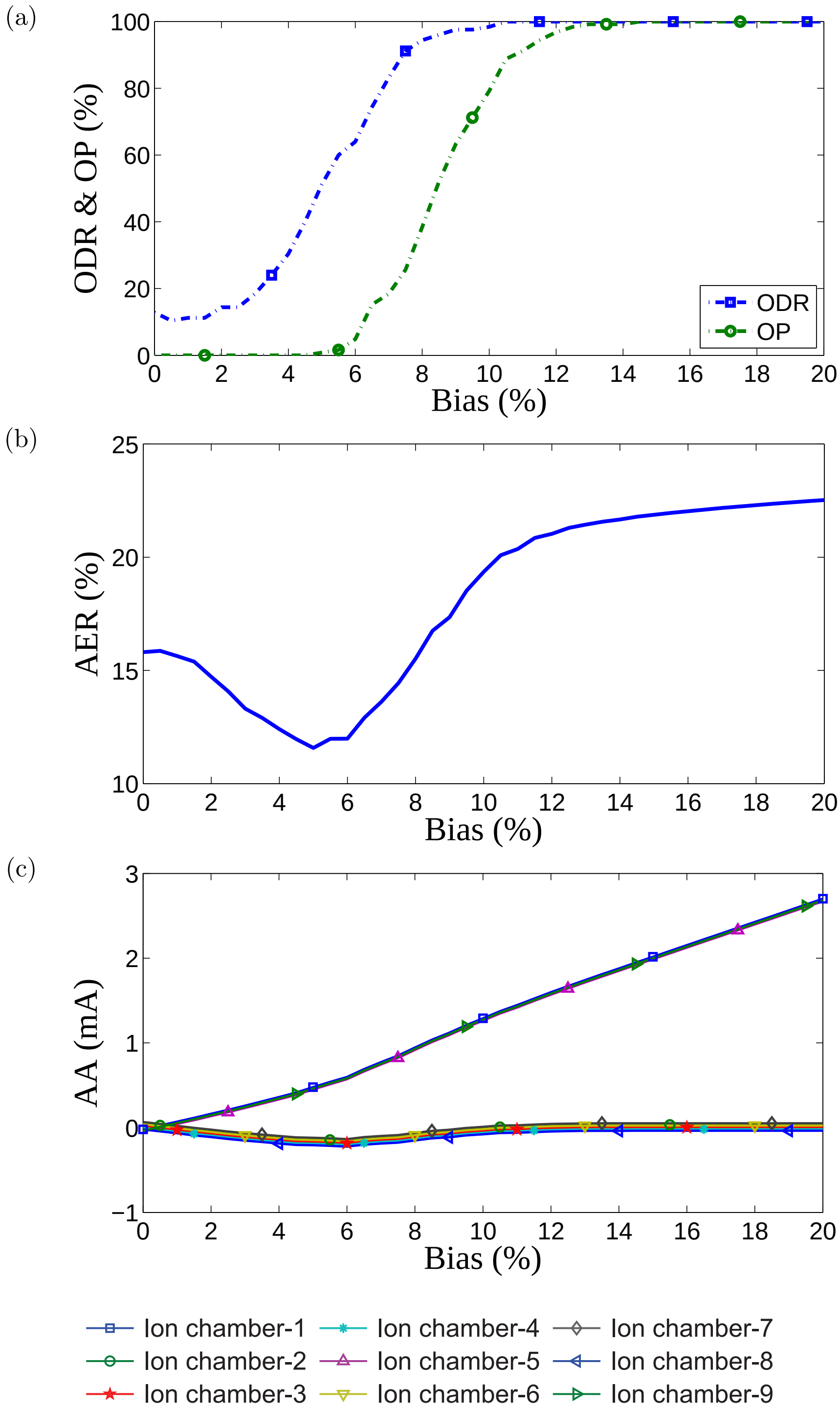

Figure 5.20: DR and FDI statistics in 3-fault scenario with smallest OP during the transient involving change of demand power (faults in ion chamber-1, ion chamber-5 and ion chamber-9) (a) ODR and OP (b) AER (c) AA.

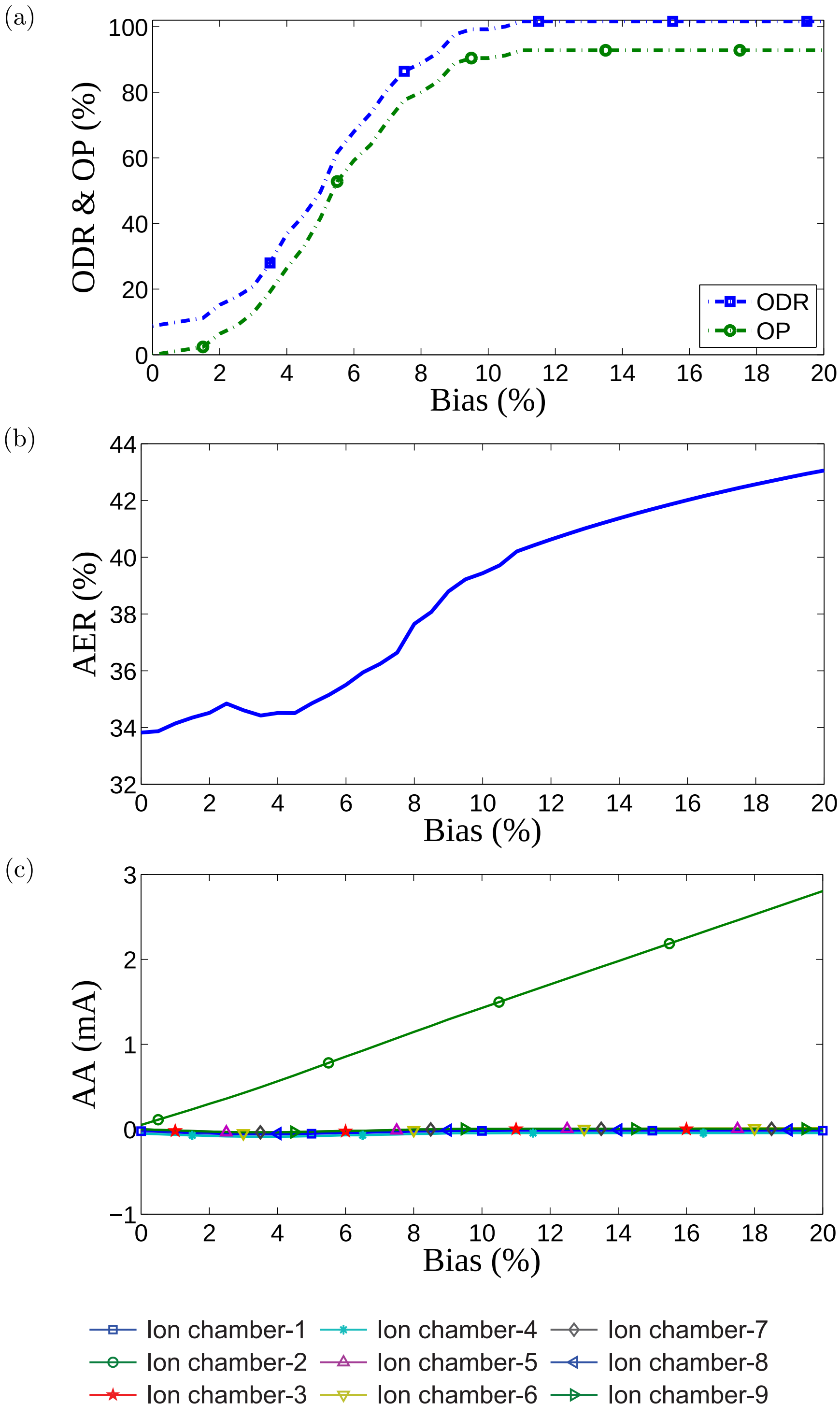

Figure 5.21: DR and FDI statistics in 1-fault scenario with largest OP during the transient involving change of demand power (fault in ion chamber-2 only) (a) ODR and OP (b) AER (c) AA.

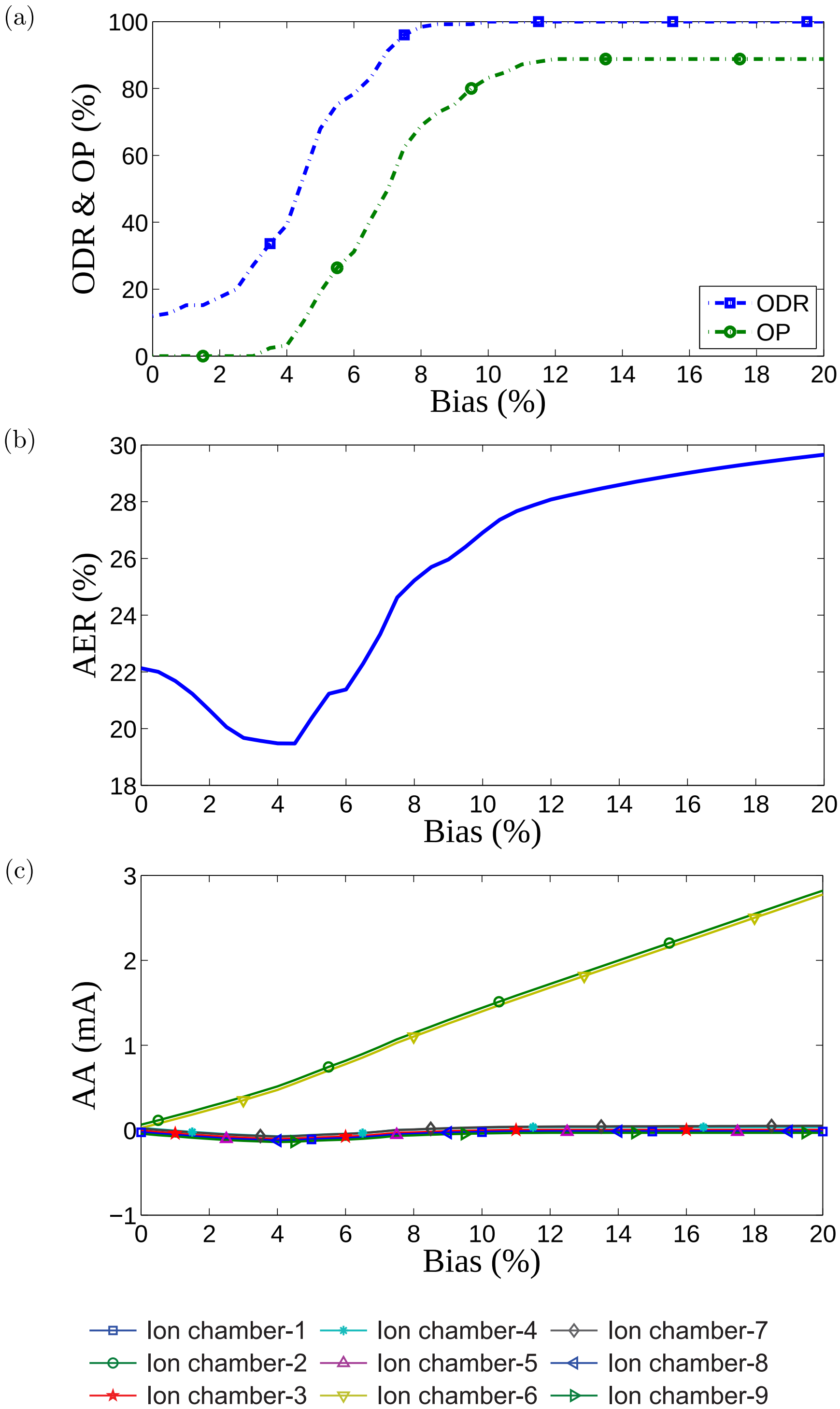

Figure 5.22: DR and FDI statistics in 2-fault scenario with largest OP during the transient involving change of demand power (faults in ion chamber-2 and ion chamber-6, both) (a) ODR and OP (b) AER (c) AA.

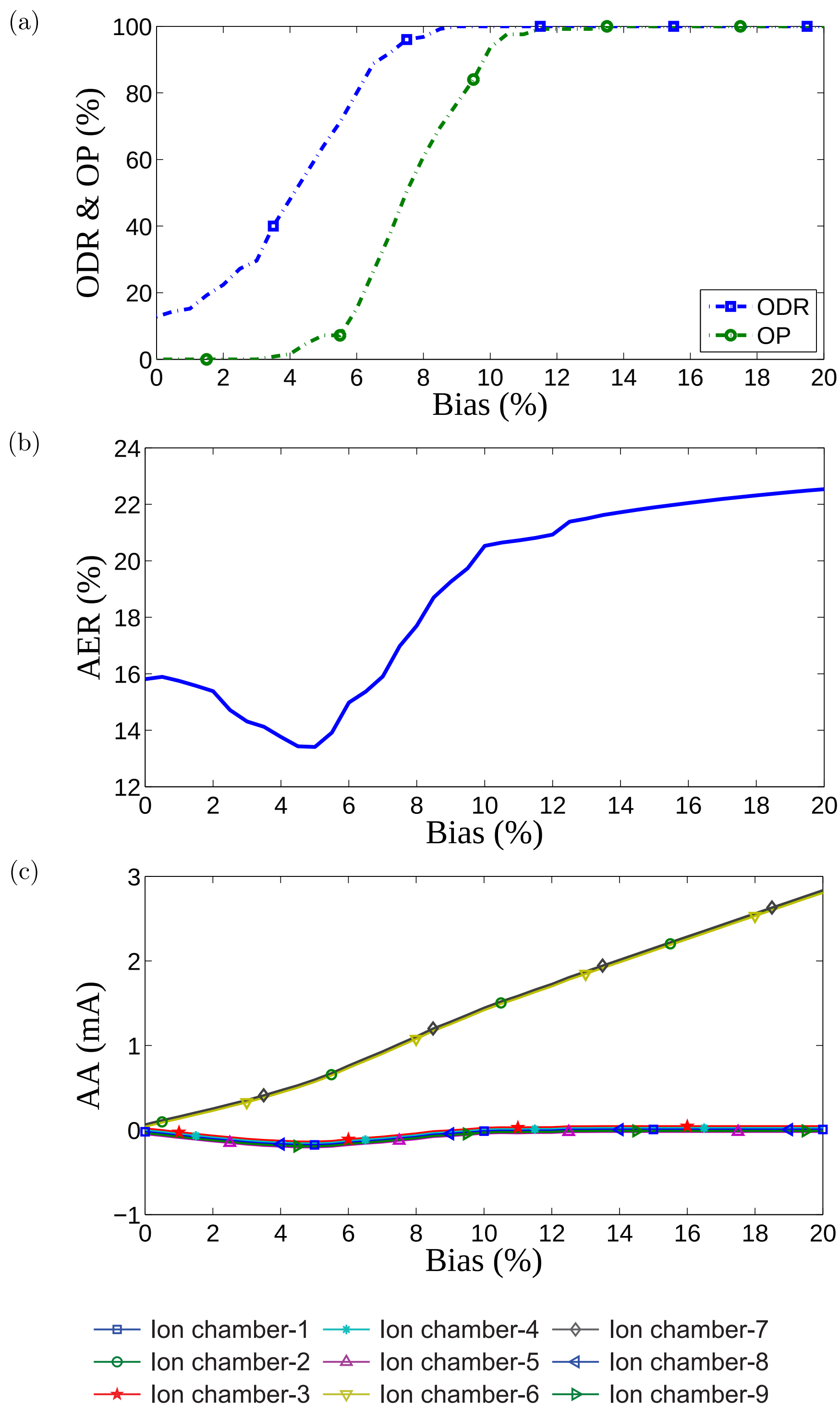

Figure 5.23: DR and FDI statistics in 3-fault scenario with largest OP during the transient involving change of demand power (faults in ion chamber-2, ion chamber-6 and ion chamber-7) (a) ODR and OP (b) AER (c) AA.

found to occur between 79.20% and 93.60%. The minimum OP of 79.20% is noticed with ion chamber-1, ion chamber-5 and ion chamber-9 being the faulty ion chambers; while the maximum OP of 93.60% is observed with ion chamber-2, ion chamber-6 and ion chamber-7 being the faulty ion chambers. The data of ion chambers contaminated by both random errors and faults in the ion chamber combinations that exhibited the minimum and the maximum OPs are shown in Fig. 5.16 and 5.17 respectively. Again, the data of three different systems, *viz.*, RRS, SDS-1 and SDS-2, are shown separately.

For minor OP combination, *i.e.*, ion chamber-1, ion chamber-5 and ion chamber-9, DR and FDI statistics are shown in Fig. 5.18 for 1-fault scenario (fault in ion chamber-1 only), Fig. 5.19 for 2-fault scenario (faults in ion chamber-1 and ion chamber-5, both), and Fig. 5.20 for 3-fault scenario (faults in ion chamber-1, ion chamber-5 and ion chamber-9). Similarly, for major OP combination, *i.e.*, ion chamber-2, ion chamber-6 and ion chamber-7, DR and FDI statistics are shown in Fig. 5.21 for 1-fault scenario (fault in ion chamber-2 only), Fig. 5.22 for 2-fault scenario (faults in ion chamber-2 and ion chamber-6, both), and Fig. 5.23 for 3-fault scenario (faults in ion chamber-2, ion chamber-6 and ion chamber-7). It can be observed that for a bias of approximately 11% and more, the fault is successfully detected and OP is more than 80%. For different bias magnitudes, AER is observed to be proportional to the bias magnitude with non-zero values of OP. Also, the adjustment in the data of faulty ion chambers is accompanied with non-zero OP. From AA characteristics of Fig. 5.18(c), it can be observed that for a bias of 20% in ion chamber-3, the adjustments made to the data of ion chamber-3 are 2.9 mA, which is equal to about 20% of the nominal signal value of 14.67 mA. This implies that DR coupled with IPCT is able to remove the effects of faults from the data. It can also be observed that the data of all other ion chambers are not affected as a function of bias in ion chamber-3, since their AA characteristics are close to zero. Similar conclusions can be drawn from the AA characteristics in other fault scenarios as well.

5.1.3 Data of Ion Chambers during Closed-loop Response of the Reactor for a Refuelling Operation

A refuelling transient is considered as follows. Fuel is removed from one of the channels and a fresh fuel is inserted; the removal of exhausted fuel at a uniform rate typically leads to introduction of a negative reactivity of -0.5×10^{-3} in 1800 s, while a positive reactivity of 0.7×10^{-3} is introduced into the zone when it is gradually fuelled with a fresh fuel in 1800 s. The resulting reactivity variation by the refuelling operation might occur as shown in Fig. 5.24. Here, fuel removal is assumed to commence at $t = 500$ s and end at $t = 2300$ s. Insertion of fresh fuel is assumed to begin at $t = 2900$ s and end at $t = 4700$ s. During the transient in zone-2 (see Fig. 4.10), the linear amplifier currents (mA) of the ion chambers sampled at every 0.2 s for 7200 s, vary as shown in Fig. 5.25. In this case, there is hardly any deviation in the ion chamber signals due to the RRs in all 4 zones manoeuvred in such a way that all the zones produce equal power.

When the WT is conducted on the data corresponding to fault-free case, no serial correlations have been observed in the measurement adjustments obtained with the IPCA outcomes of Section 5.1.1. WT violation index is given in Table 5.7. Since no measurement adjustment violated the 5% upper limit, the IPCA outcomes obtained in Section 5.1.1 are used in this case as well.

The faulty ion chamber combinations {1, 4, 9} and {2, 5, 9} respectively yielded a minimum OP of 81.33% and a maximum OP of 87.11%, for bias magnitudes of 10% in 3-fault scenarios with IPCA algorithm corresponding to open loop data (that of Fig. 5.3(a)). The DR and FDI statistics obtained are shown in Fig. 5.27, 5.28, and 5.29 for ion chamber combination {1, 4, 9}; and in Fig. 5.30, 5.31, and 5.32 for combination {2, 5, 9}. For different bias magnitudes, AER is found to be increasing with non-zero values of OP. The data of faulty ion chambers are adjusted properly as seen from AA characteristics.

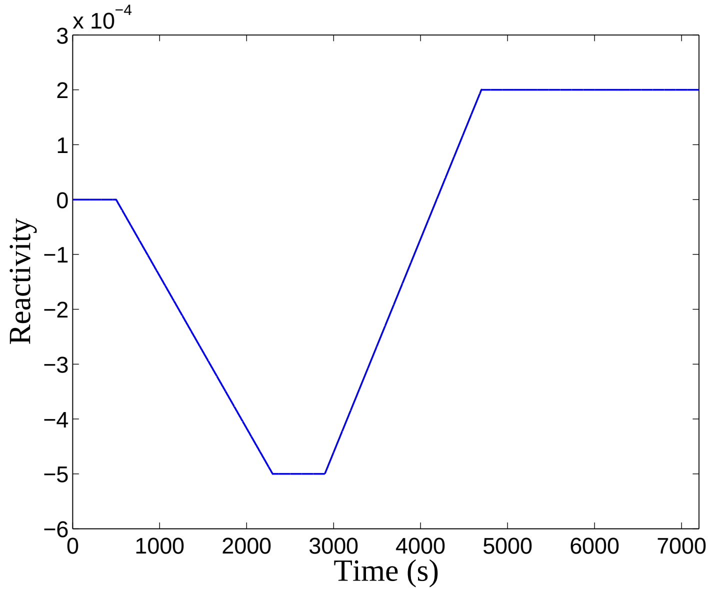

Figure 5.24: Refuelling transient.

Table 5.7: Violation index of measurement adjustments of ion chamber data in WT for refuelling transient

Measurement adjustments	a_1	a_2	a_3	a_4	a_5	a_6	a_7	a_8	a_9
Violation index (%)	1.38	1.32	1.23	1.36	1.24	1.36	1.31	1.21	1.39

5.1.4 Data of Ion Chambers during Xenon-induced Spatial Oscillations

Large reactors like the AHWR are provided with control systems consisting of total power control as well as spatial control, with the overall objective of maintaining the total power constant and at the same time, flux distribution close to the desired profile. If spatial control is assumed to be ineffective, xenon-induced oscillations may be observed. In such a situation, power in different regions of the core might oscillate while the total power remains constant at its nominal value [98, 110]. During these oscillations, the signals of the ion chambers vary as shown in Fig. 5.33. These ion chamber signals are sampled for every 30 seconds in 45 hours of simulation, leading to the generation of 5400 observations.

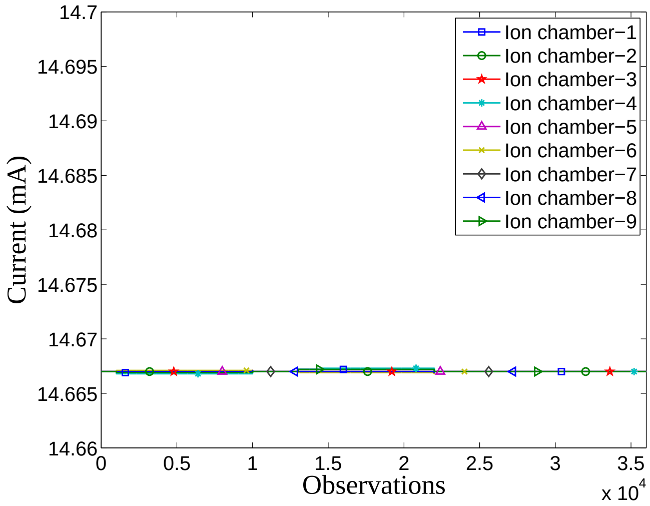

Figure 5.25: Ion chamber signals during refuelling transient in zone-2.

Table 5.8: Violation index of measurement adjustments of ion chamber data in WT for Xenon oscillations

Measurement adjustments	a_1	a_2	a_3	a_4	a_5	a_6	a_7	a_8	a_9
Violation index (%)	26.68	34.64	42.10	22.08	40.38	28.38	35.38	44.32	31.30

The measurement adjustments and the WT statistic corresponding to the fault-free case are shown respectively in Fig. 5.34 and 5.35. It can be observed that the measurement adjustments are serially correlated, after about 1500 samples after the commencement of the simulation. From Table. 5.8 it is clear that the measurement adjustments do not represent a promising situation for the FDI, as the violation index in WT is greater than 5% for the measurement adjustments of all the 9 ion chambers.

When the variation in the data from the respective steady-state is significant, it might not be directly utilized, as the basic assumption for static DR and FDI analysis is not satisfied. One way of dealing with such situations is to separate the data into many windows, and to apply static DR to the aggregated data of all consequent windows, where the sign of correlation of the variables is preserved. For the transient shown in Fig. 5.33, the sign of correlation of variables is consistent for the first 1500 observations. This is also supported by the fact that thre is no serial correlation in the fault-free measurement adjustments in Fig. 5.34. When WT is conducted on the measurement

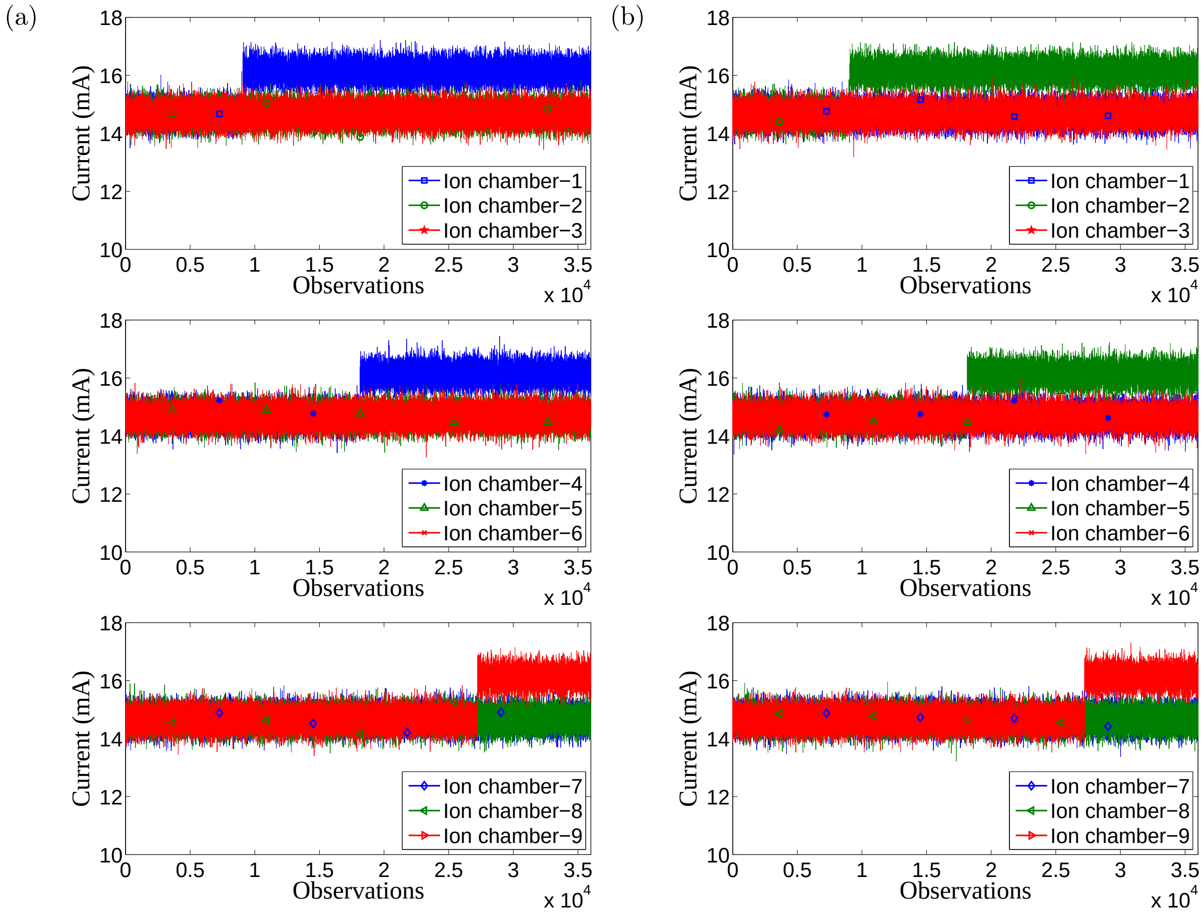

Figure 5.26: Data of ion chambers in the 3-fault scenarios during the refuelling transient (a) with minor OP (b) with major OP.

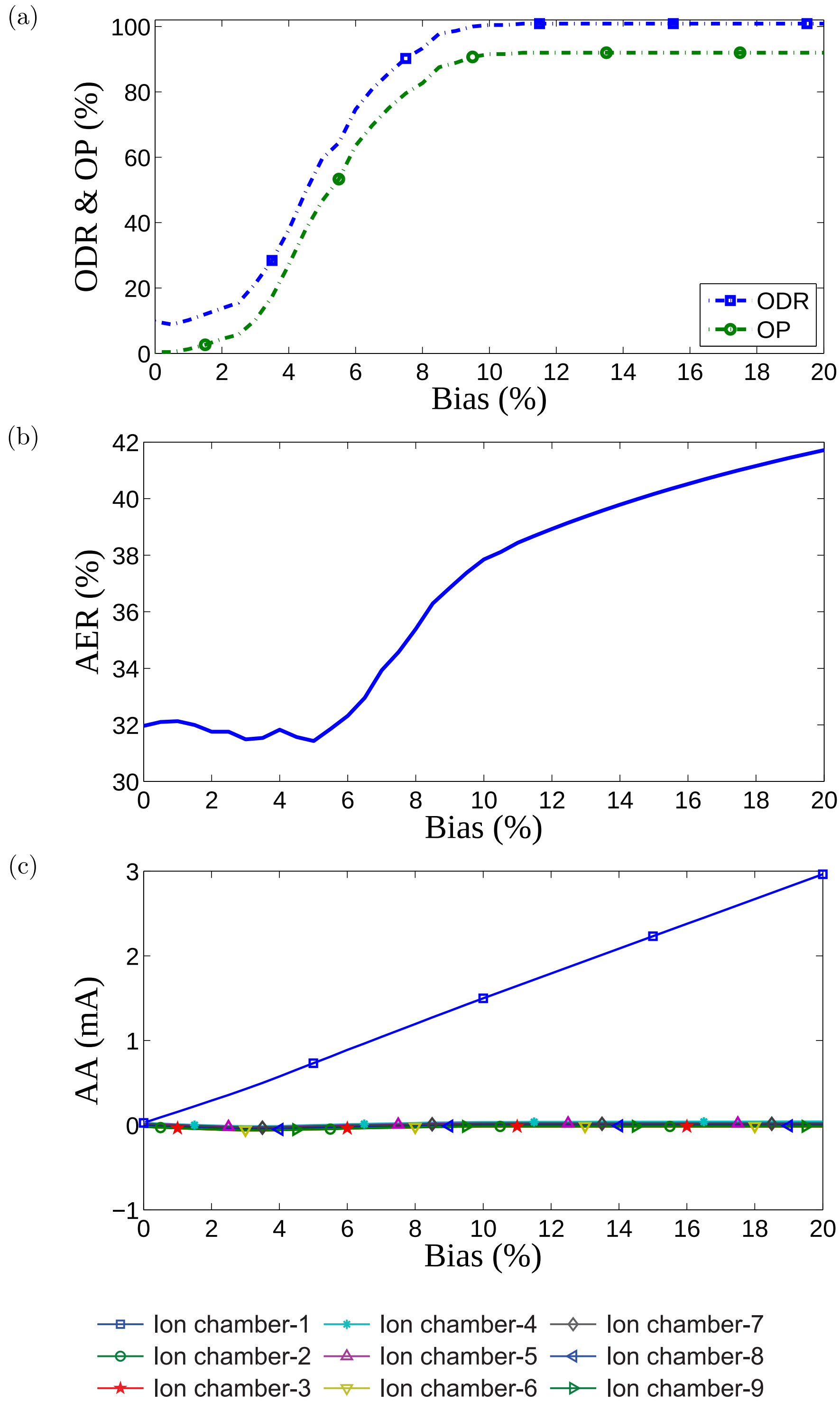

Figure 5.27: DR and FDI statistics in refuelling transient: 1-fault scenario with smallest OP (fault in ion chamber-1 only) (a) ODR and OP (b) AER (c) AA.

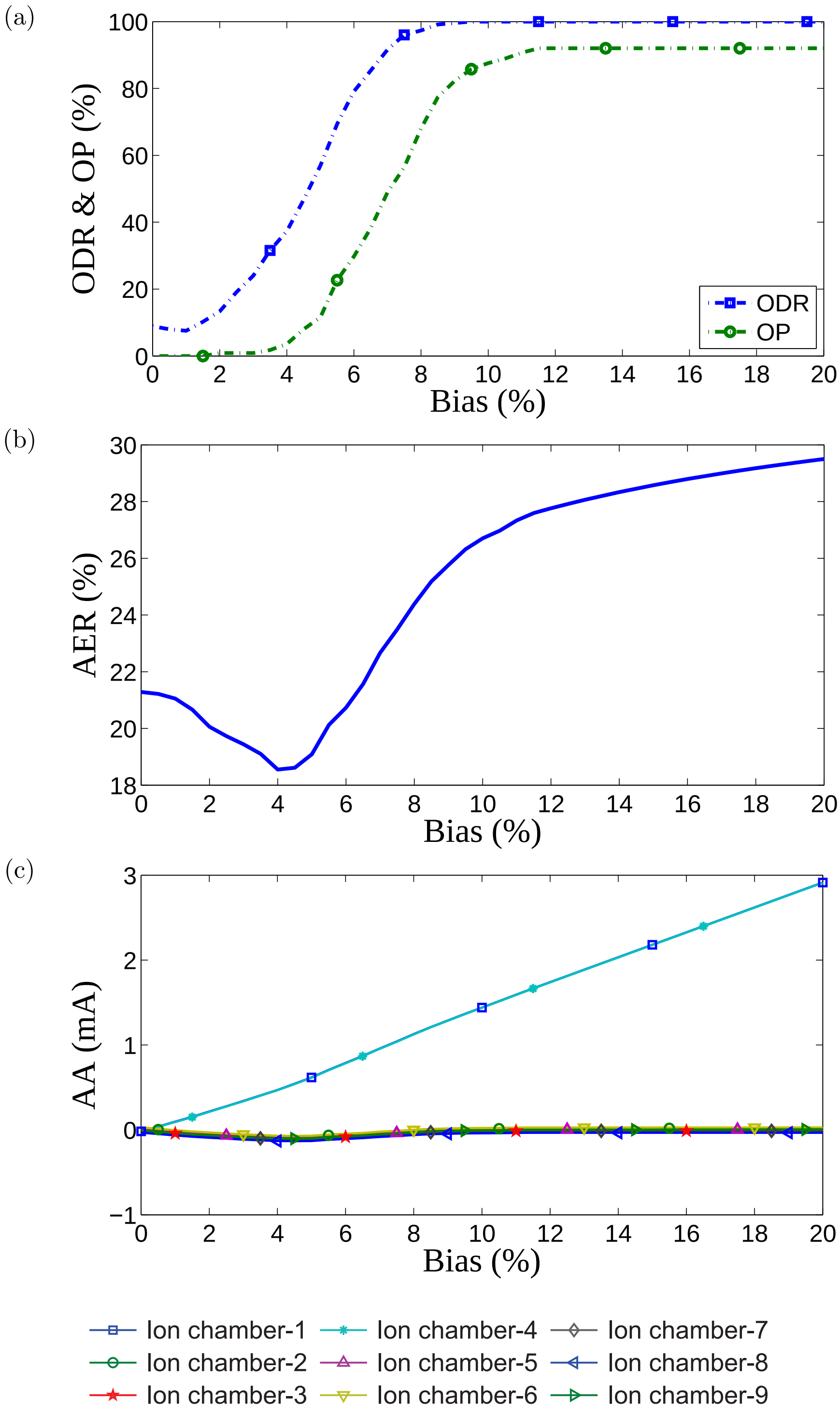

Figure 5.28: DR and FDI statistics in refuelling transient: 2-fault scenario with smallest OP (faults in ion chamber-1 and ion chamber-4, both) (a) ODR and OP (b) AER (c) AA.

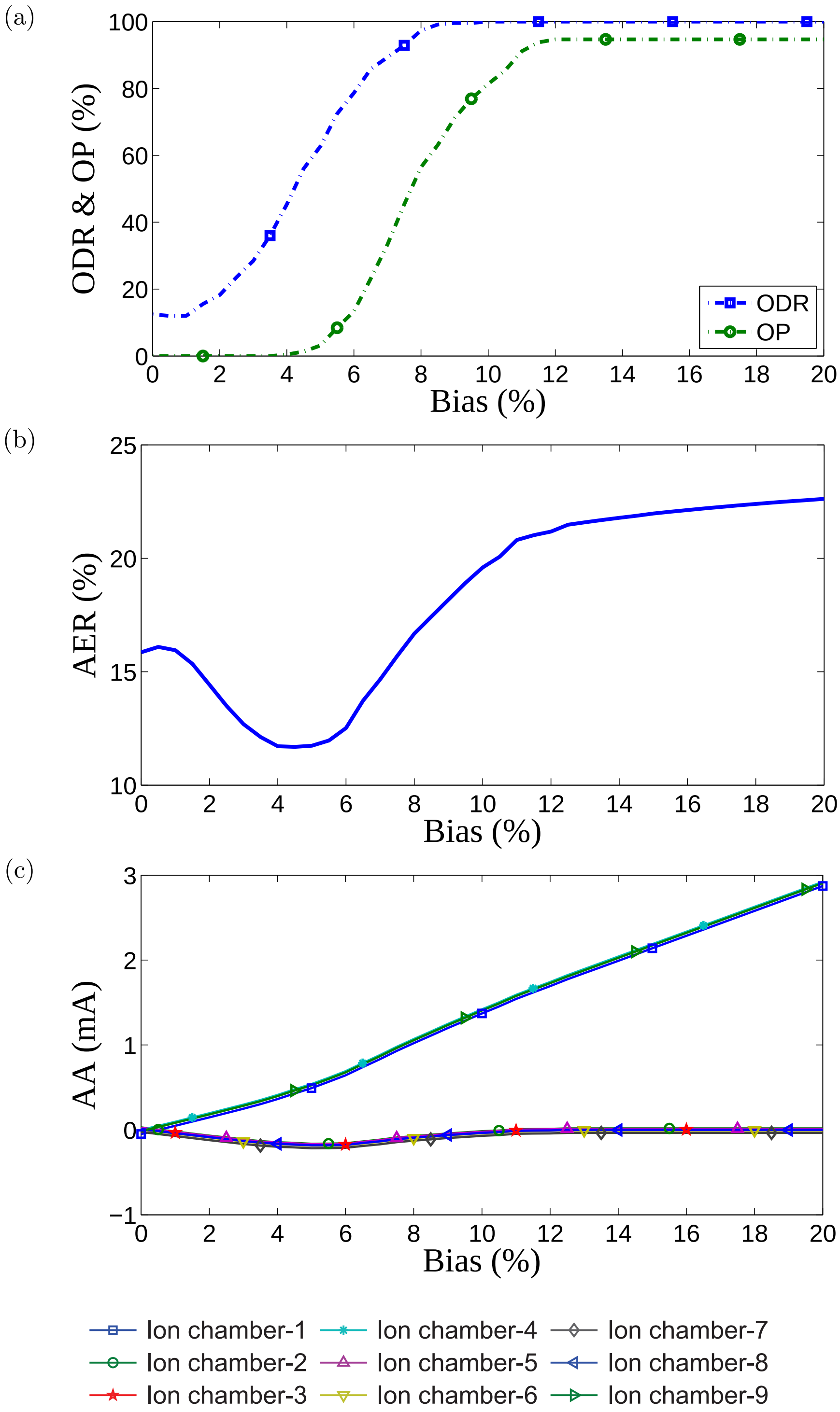

Figure 5.29: DR and FDI statistics in refuelling transient: 3-fault scenario with smallest OP (faults in ion chamber-1, ion chamber-4 and ion chamber-9) (a) ODR and OP (b) AER (c) AA.

(a)

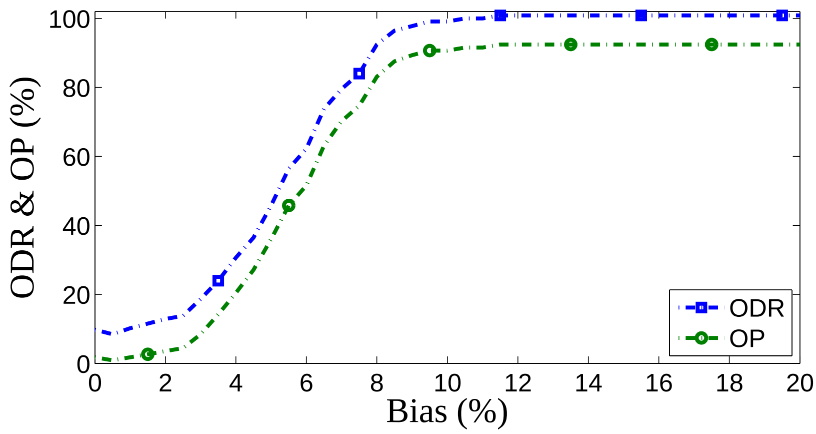

(b)

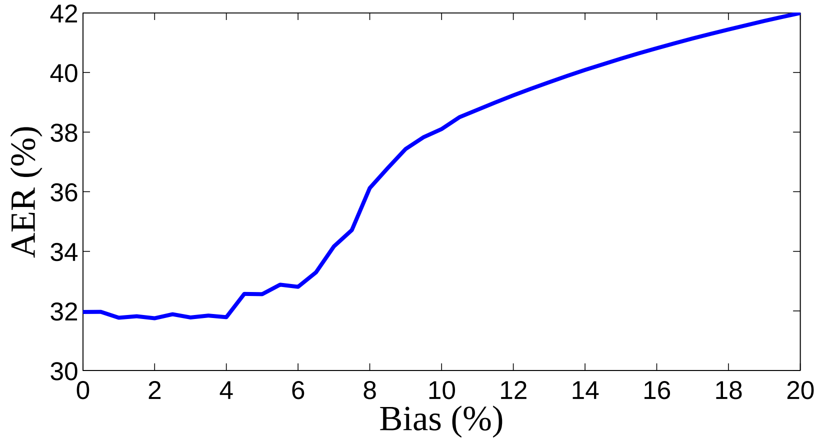

(c)

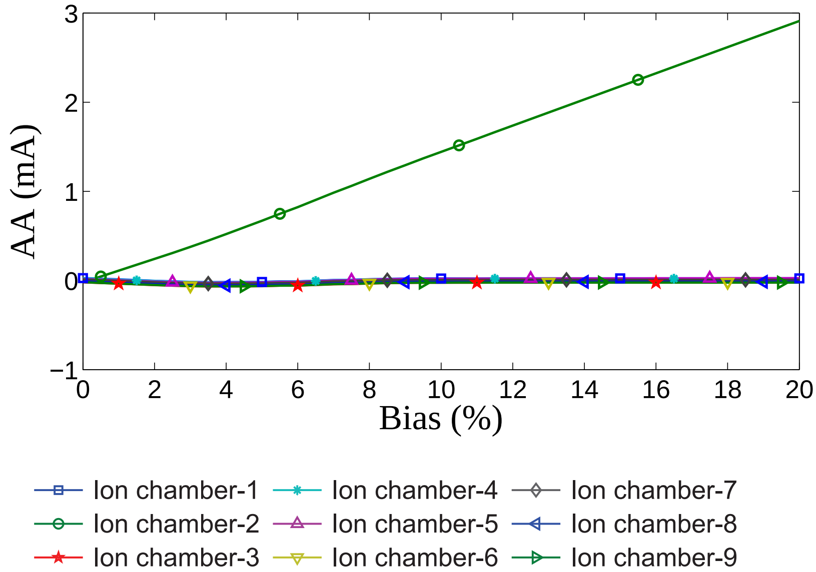

Figure 5.30: DR and FDI statistics in refuelling transient: 1-fault scenario with largest OP (fault in ion chamber-2 only) (a) ODR and OP (b) AER (c) AA.

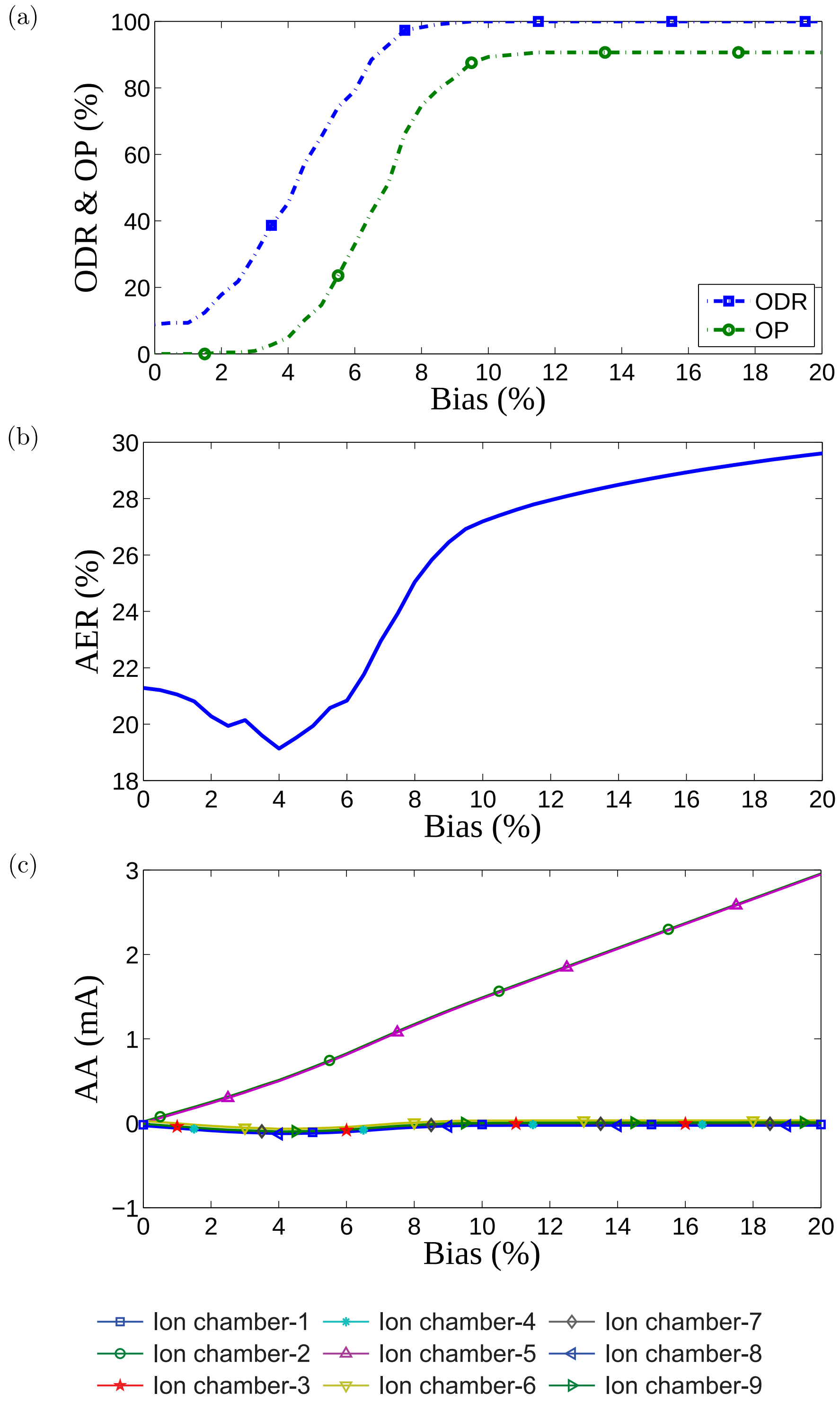

Figure 5.31: DR and FDI statistics in refuelling transient: 2-fault scenario with largest OP (faults in ion chamber-2 and ion chamber-5, both) (a) ODR and OP (b) AER (c) AA.

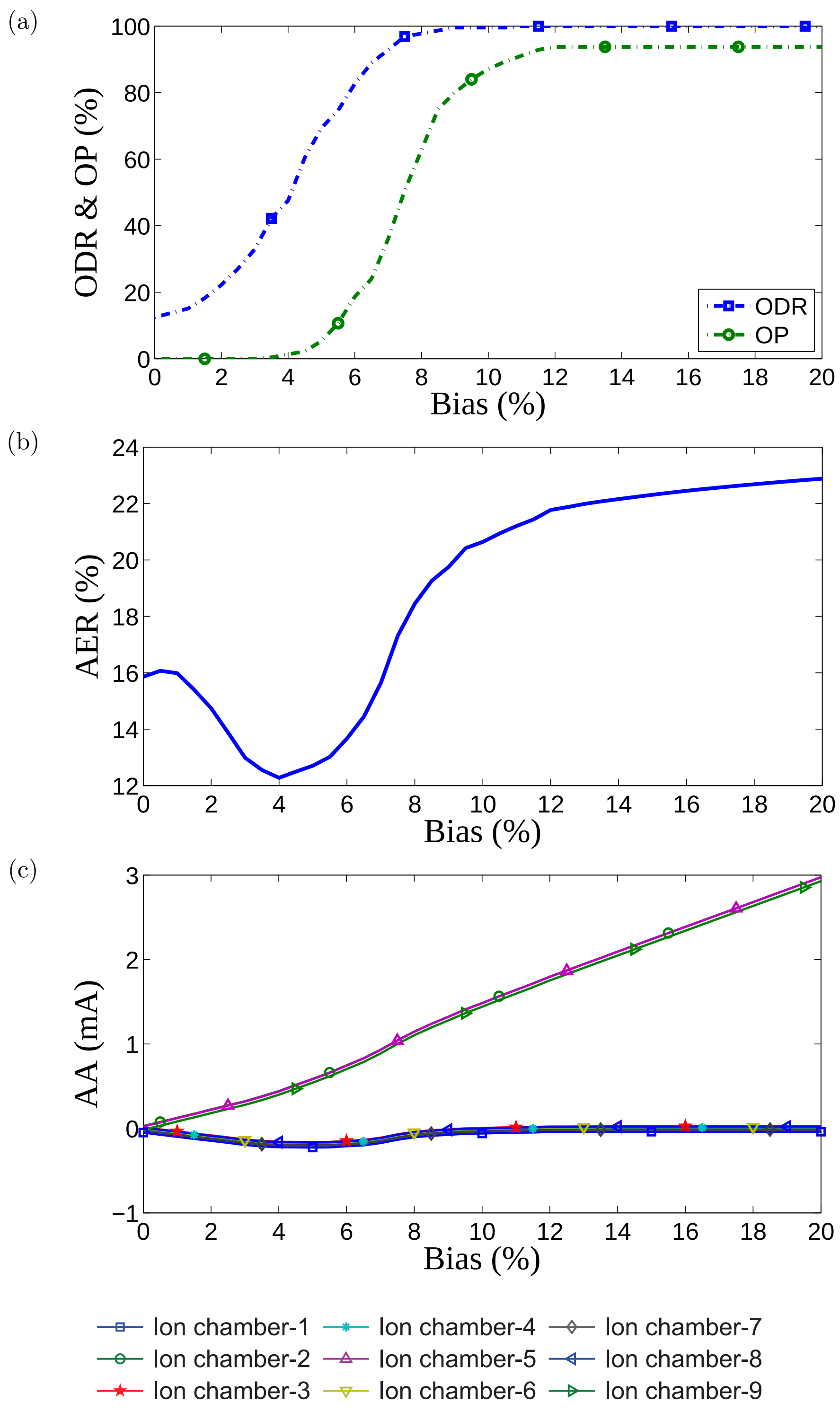

Figure 5.32: DR and FDI statistics in refuelling transient: 3-fault scenario with largest OP (faults in ion chamber-2, ion chamber-5 and ion chamber-9) (a) ODR and OP (b) AER (c) AA.

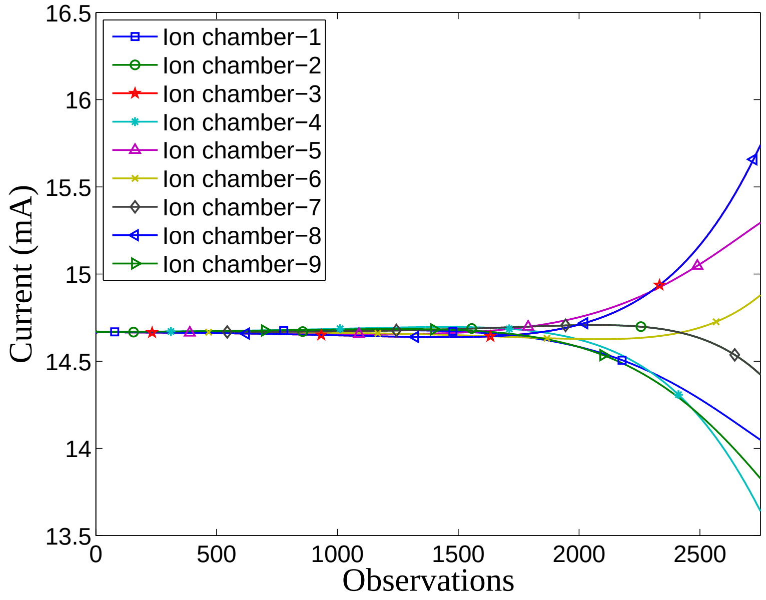

Figure 5.33: Ion chamber signals during xenon-induced oscillations.

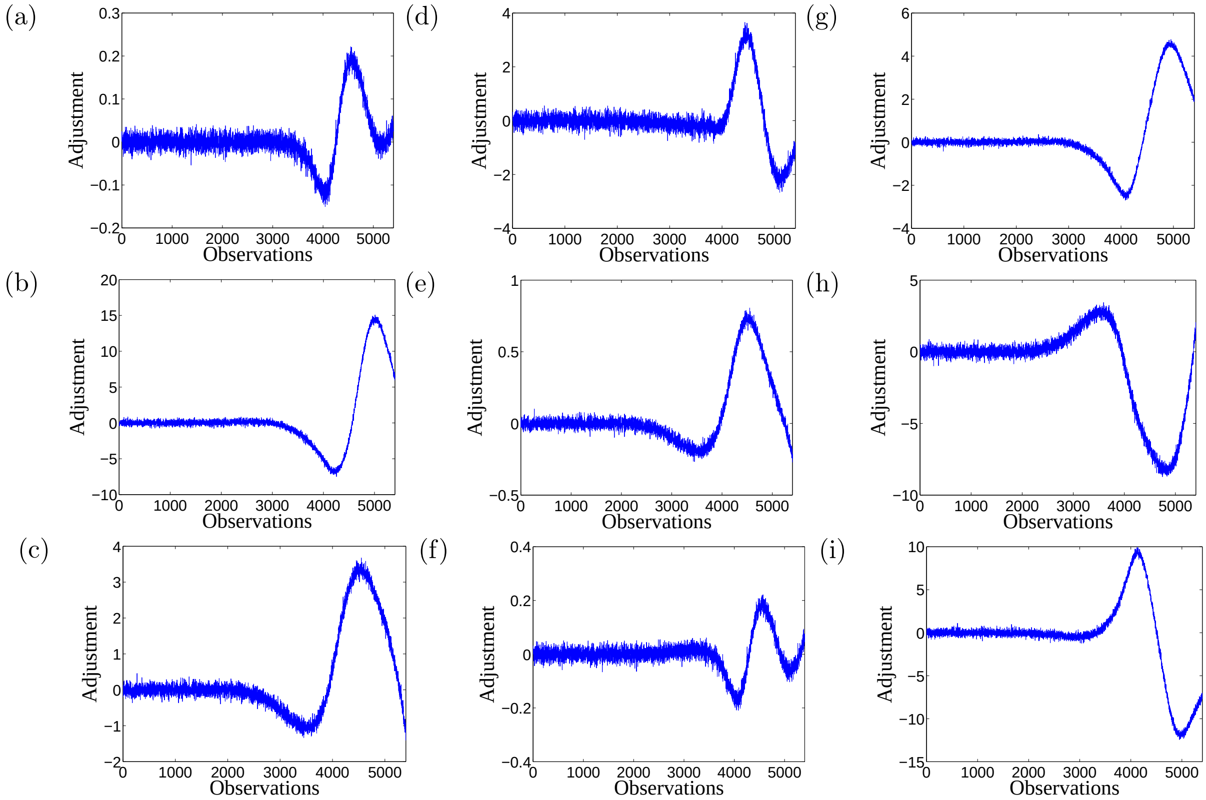

Figure 5.34: Xenon oscillations: Adjustments for (a) ion chamber-1 (b) ion chamber-2 (c) ion chamber-3 (d) ion chamber-4 (e) ion chamber-5 (f) ion chamber-6 (g) ion chamber-7 (h) ion chamber-8 (i) ion chamber-9.

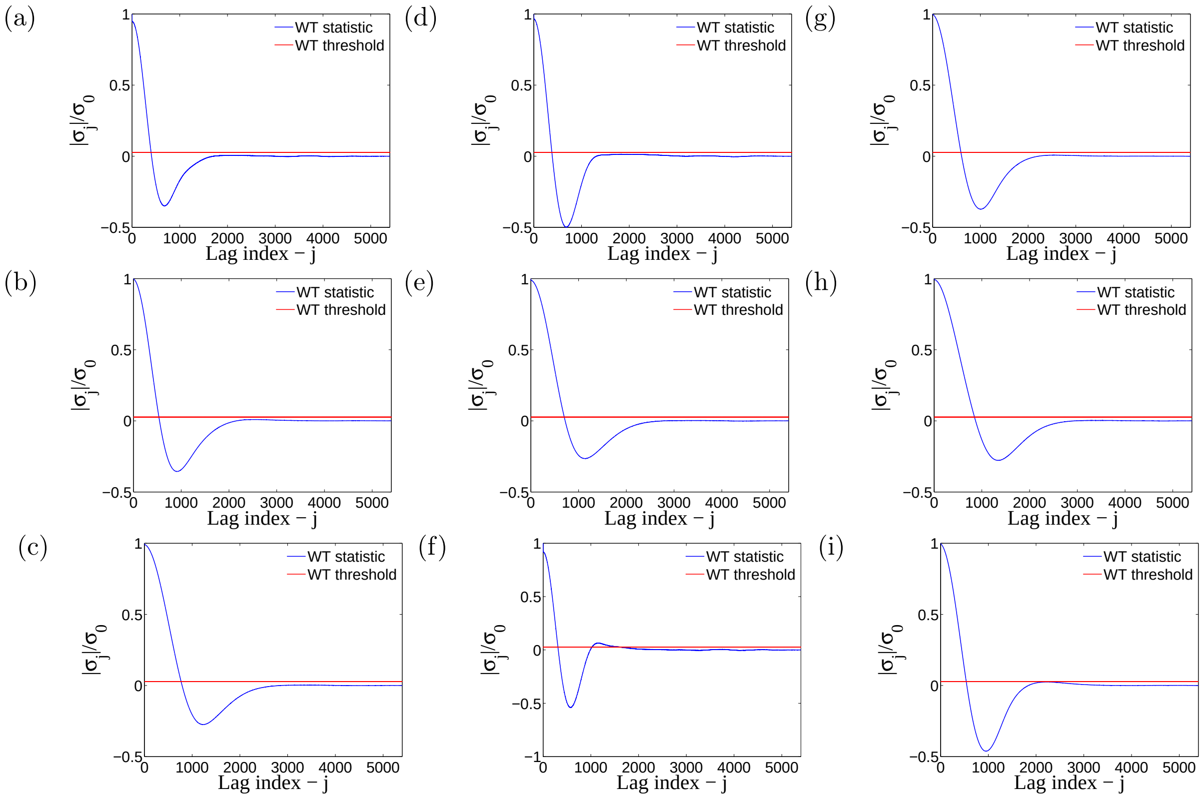

Figure 5.35: Xenon oscillations: Whiteness test statistics for (a) ion chamber-1 (b) ion chamber-2 (c) ion chamber-3 (d) ion chamber-4 (e) ion chamber-5 (f) ion chamber-6 (g) ion chamber-7 (h) ion chamber-8 (i) ion chamber-9.

Table 5.9: Violation index of truncated measurement adjustments of ion chamber data in WT for Xenon oscillations

Measurement adjustments	a_1	a_2	a_3	a_4	a_5	a_6	a_7	a_8	a_9
Violation index (%)	1.49	1.22	1.11	1.55	1.33	1.27	0.99	0.94	1.27

adjustments obtained for the first 1500 samples, violation indices are obtained as given in Table 5.9. Since the violation indices support the claim of whiteness, the static DR and FDI can be performed from the operating data obtained in the first 1500 observations. Hence, again the IPCA model given by (5.1) is used for DR and FDI.

In the 3-fault scenarios, for bias magnitudes of 10% of the nominal steady-state signals, a minimum OP of 68.42% is found with ion chamber-3, ion chamber-6 and ion chamber-8 being the faulty ion chambers; while a maximum OP of 92.10% is observed with ion chamber-2, ion chamber-6 and ion chamber-7 being the faulty ion chambers.

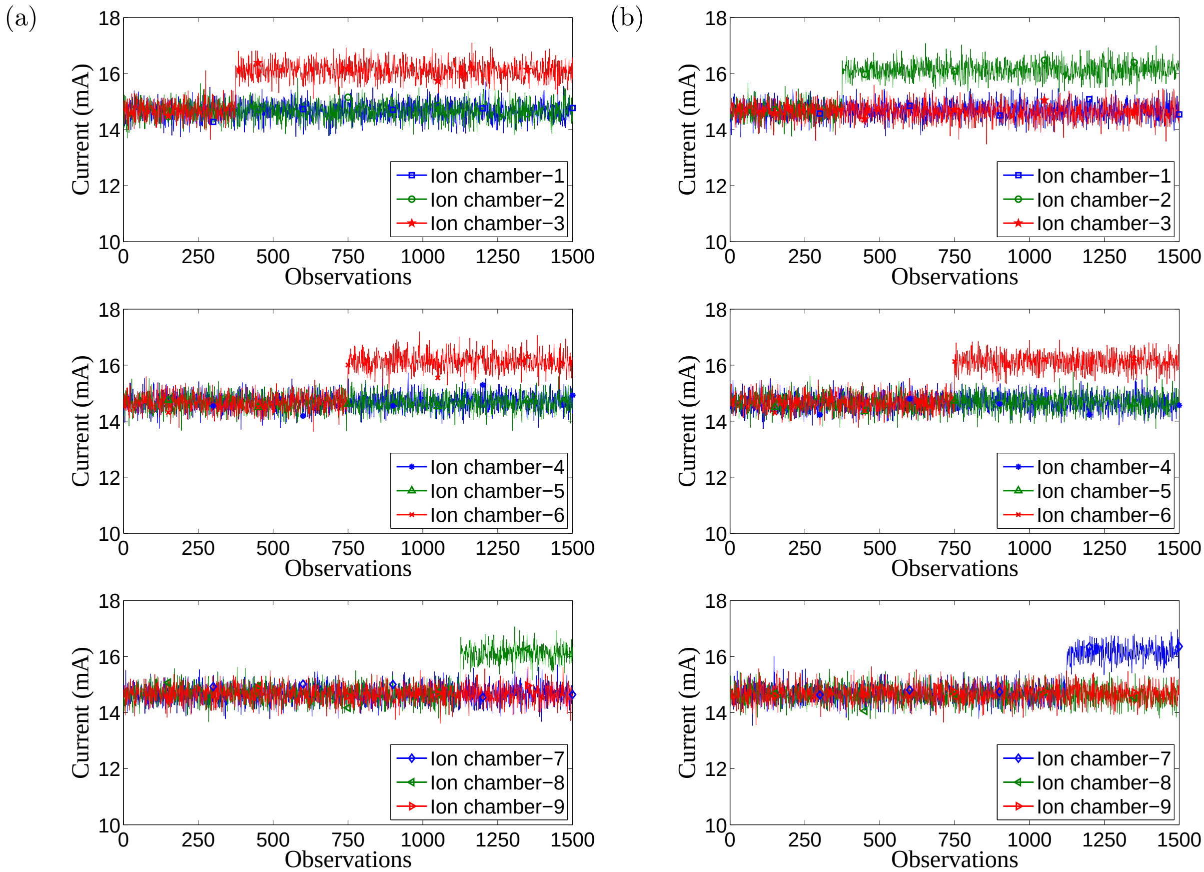

Figure 5.36: Data of ion chambers in the 3-fault scenarios during Xenon-induced oscillations (a) with smallest OP (b) with largest OP.

Fig. 5.36 shows the data of ion chambers contaminated by both random errors and faults in the ion chamber combinations exhibiting the smallest and the largest OPs. DR and FDI statistics during 1, 2 and 3-fault scenarios for these ion chamber combinations are shown in Fig. 5.37 to 5.42. Under all fault scenarios, it can be observed that for a bias of approximately 10% and more, the fault is successfully detected and OP is more than 80%. For different bias magnitudes, AER can be seen increasing with non-zero values of OP. The data of faulty ion chambers are adjusted properly as seen from AA characteristics and this effect is more pronounced with non-zero values of OP.

Hence the static DR coupled with IPCT is found to have worked well for the first 1500 observations. However, beyond these 1500 observations, the application of the technique leads to false detections and infeasible adjustments. This is because the correlation

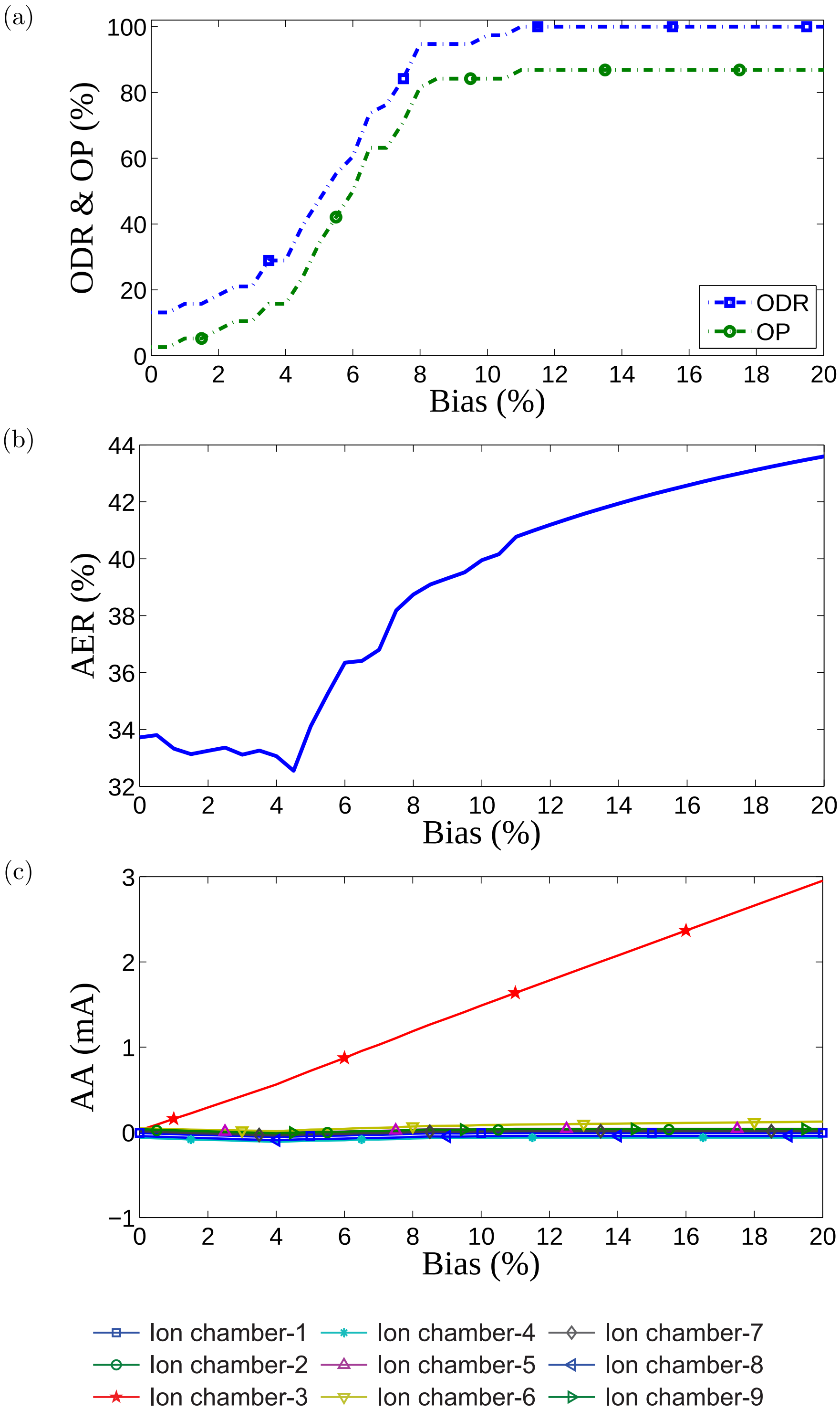

Figure 5.37: DR and FDI statistics during Xenon-induced oscillations: 1-fault scenario with smallest OP (fault in ion chamber-3 only) (a) ODR and OP (b) AER (c) AA.

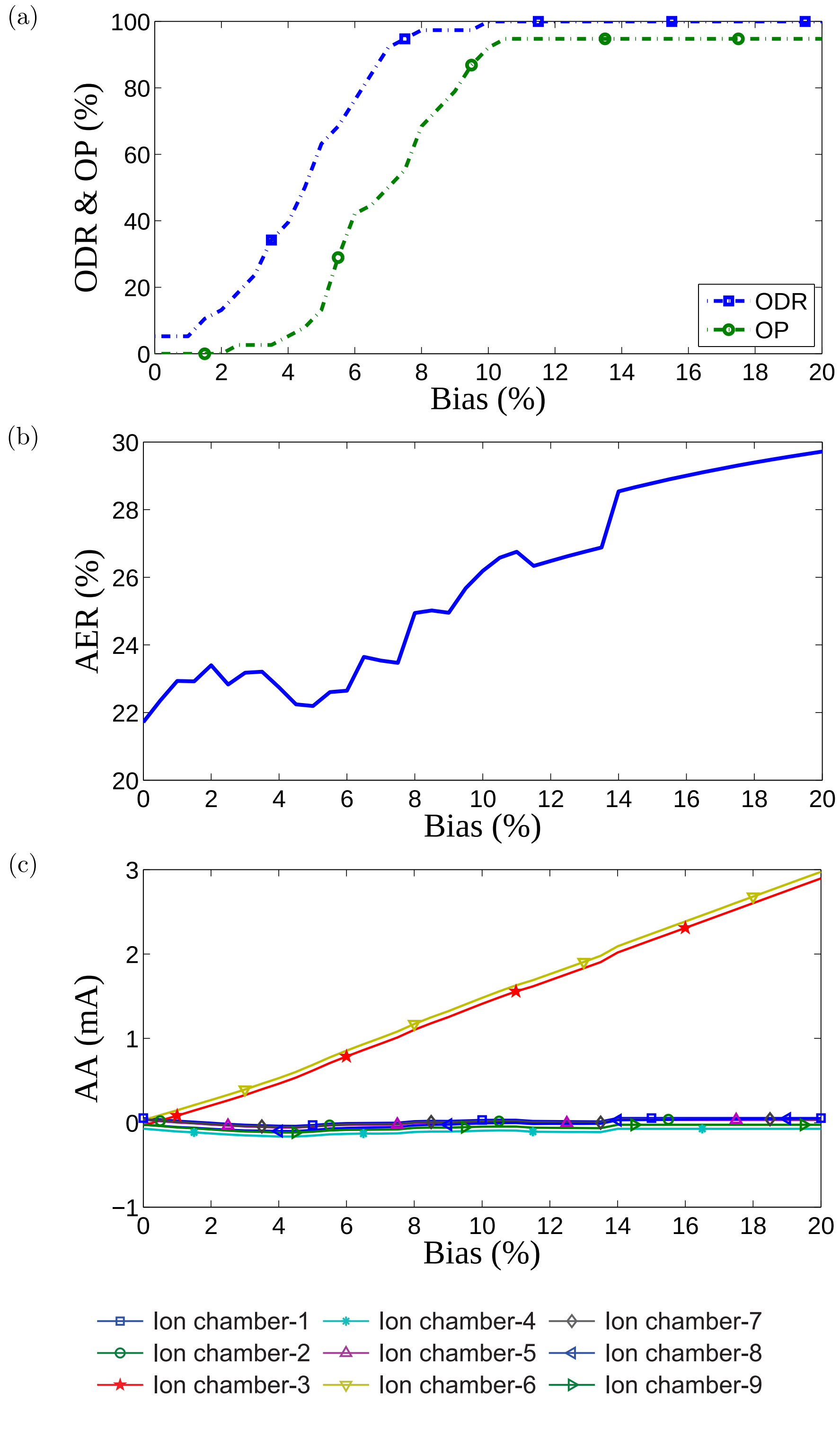

Figure 5.38: DR and FDI statistics during Xenon-induced oscillations: 2-fault scenario with smallest OP (faults in ion chamber-3 and ion chamber-6, both) (a) ODR and OP (b) AER (c) AA.

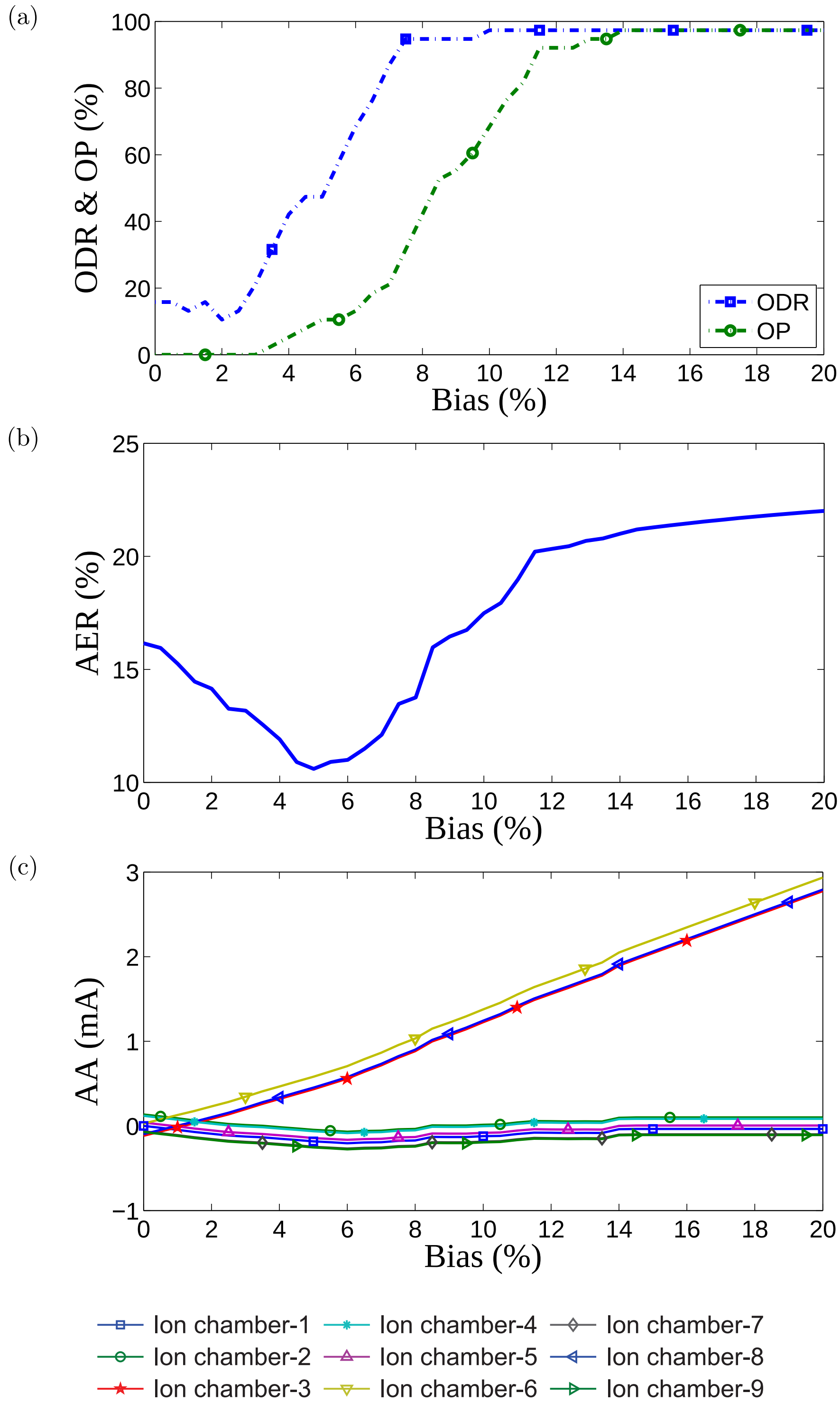

Figure 5.39: DR and FDI statistics during Xenon-induced oscillations: 3-fault scenario with smallest OP (faults in ion chamber-3, ion chamber-6 and ion chamber-8) (a) ODR and OP (b) AER (c) AA.

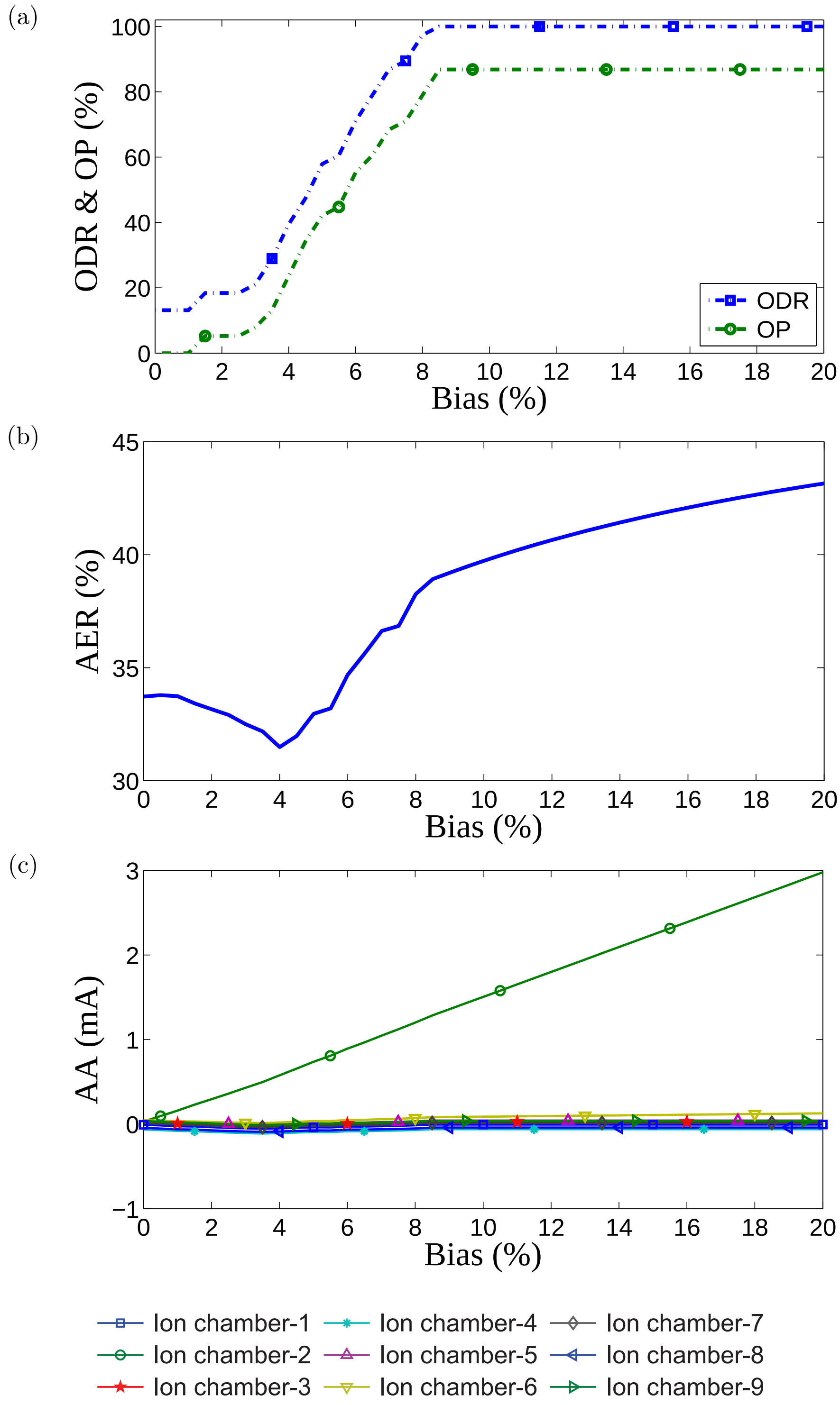

Figure 5.40: DR and FDI statistics during Xenon-induced oscillations: 1-fault scenario with largest OP (fault in ion chamber-2 only) (a) ODR and OP (b) AER (c) AA.

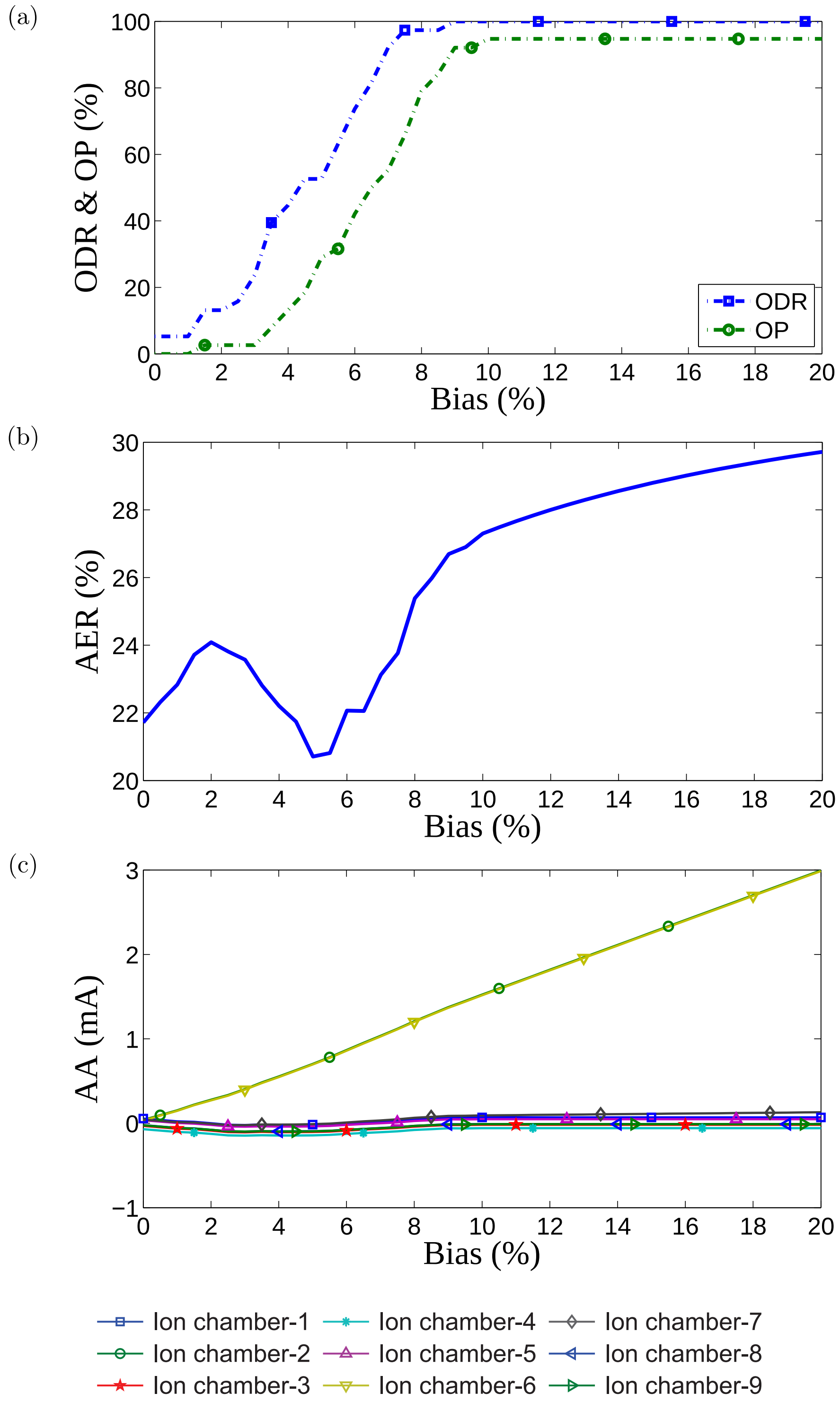

Figure 5.41: DR and FDI statistics during Xenon-induced oscillations: 2-fault scenario with largest OP (faults in ion chamber-2 and ion chamber-6, both) (a) ODR and OP (b) AER (c) AA.

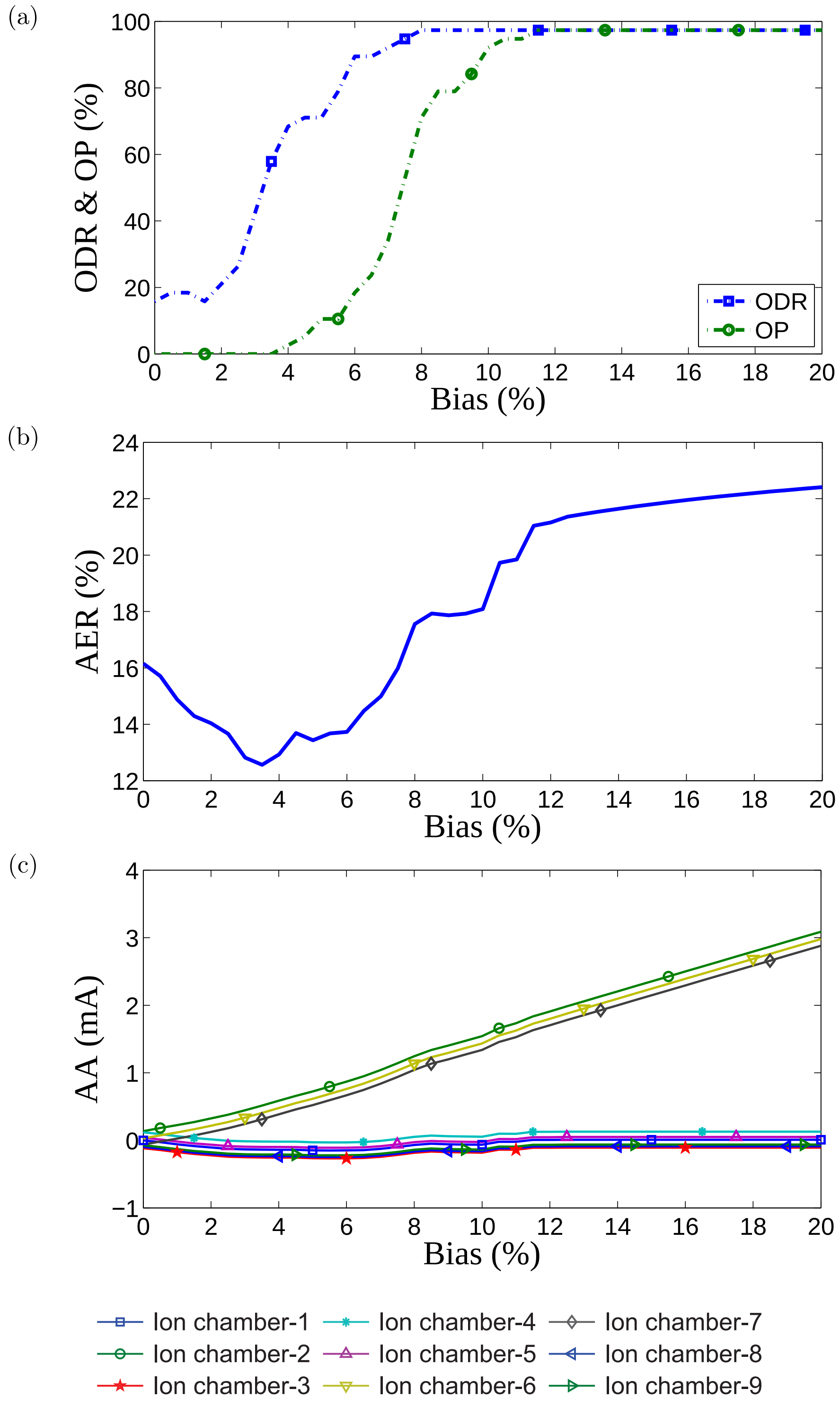

Figure 5.42: DR and FDI statistics during Xenon-induced oscillations: 3-fault scenario with largest OP (faults in ion chamber-2, ion chamber-6 and ion chamber-7) (a) ODR and OP (b) AER (c) AA.

patterns among the variables beyond the first 1500 observations is different from the correlation pattern near the steady-state. However, since xenon spatial oscillations are controlled by the RRS, the variations in flux distributions in the core are not expected to be so large as to affect the correlation pattern adversely. Hence, it can be expected that the IPCA model alongwith the DR and FDI algorithms based on IPCT would work in scenarios involving transient variations in flux distribution caused due to xenon-induced spatial oscillations.

5.2 Steady-state DR and FDI of VSPNDs

In this section, results of DR and FDI analyses carried out on VSPNDs are presented. As previously mentioned, the data of VSPNDs need to be clustered before attempting DR and FDI and the $k-$means algorithm explained in Section 3.4 is used for this. In this case, the measurement matrix $\boldsymbol{Y}$ is $200 \times N$ dimensional, *i.e.*, $\in \mathbb{R}^{200\times N}$, since n, the number of detector signals, is equal to 200. Out of 200, closely situated VSPNDs are expected to be subjected to similar variations in the neutron flux and their measurement data have good correlation. They show a strong tendency to fall in a single cluster unless k, number of clusters, is large. A large k may lead to the allotment of only 1 or 2 VSPNDs in a cluster, thereby reduces the degree of analytical redundancy required for the identification of a fault in the VSPNDs of that cluster. A reasonable OP (identification rate) in case of a single fault suggests that the number of VSPNDs in each cluster should be more than 3, hence, there should be a limit for the value of k. It means that for a fair distribution of 3 VSPNDs in a cluster, k should not be greater than one-third of the total number of VSPNDs, *i.e.*, 200. Hence, number of clusters has been chosen to range from 1 to 66. However, the distribution of equal number of VSPNDs in each cluster is generally not achieved, since highly correlated detectors show a strong tendency to be in a single cluster. In the subsequent analysis, the averaged maximum spread, as discussed in Section 3.4, is plotted against the number of clusters, and the number of clusters near the knee point of the curve are taken as the final k.

5.2.1 Data of VSPNDs during the Demand Power Change

The same demand power transient explained in Section 5.1.2 is considered for the generation of VSPND data. Since the spatial control is active, the correlations among the VSPND signals do not change as a function of time. The sampling duration of 0.2 s led to the generation of 2500 observations from VSPNDs. The same noise levels of ion chamber data are assumed in this case also.

The averaged maximum spread can be seen in Fig. 5.43 in which a knee position near k, number of clusters, is equal to 10 can be observed. 25-cluster configuration of data of 200 VSPNDs is chosen from the outcomes of the k-means algorithm. This selection of the 25 clusters was because of convergence achieved by the IPCA algorithm (refer to Fig. 3.1) while being close to the knee point of the curve in Fig. 5.43. For this 25-cluster configuration, the VSPNDs and the clusters to which they belong to, can be seen in the Table 5.10. It can be observed from Fig. 4.5, Tables 4.1 and 5.10, that the closely situated VSPNDs, are more likely to fall into a single cluster. The results of DR and FDI analyses on the data of VSPNDs in cluster-1 (see Table 5.10) are presented. Fig. 5.44 shows the data of VSPNDs corresponding to cluster-1.

Cluster-1 has 8 number of VSPNDs as given in Table 5.10. Hence, model order m can range from 1 to 7, since minimum and maximum model orders respectively are 1 and $n-1$, where recall that n is the number of measurements. When the IPCA algorithm is applied to the data shown in Fig. 5.44, the singular values of scaled data matrix $\boldsymbol{Y}_s$ and standard deviations of errors for different model orders are obtained as given in Table 5.11.

It can be observed that with an m, the model order, of 7 as well as 6, the standard deviations of the measurement errors are accurately estimated and the last 7 singular values are converged close to 1. As a higher model order is preferred for FDI, $m = 7$ is taken as model order for the residual subspace. The constraint model obtained by

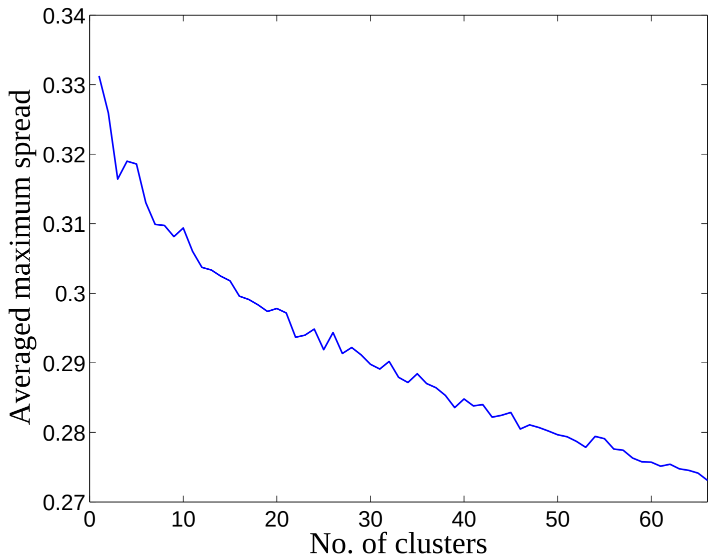

Figure 5.43: Averaged maximum spread with number of clusters.

IPCA for $m = 7$ is given by

$$\boldsymbol{A} \triangleq \boldsymbol{A}_I = \begin{bmatrix} 0.4904 & 0.2224 & -0.3309 & -0.3262 & 0.0259 & 0.5305 & -0.4183 & -0.1924 \\ -0.0829 & 0.0693 & -0.2888 & 0.4710 & -0.5765 & 0.1611 & -0.2602 & 0.5070 \\ 0.3968 & -0.6765 & 0.2834 & 0.0642 & -0.3898 & 0.2634 & 0.2272 & -0.1658 \\ 0.2340 & -0.2110 & -0.5059 & -0.3782 & 0.0772 & -0.1775 & 0.4607 & 0.5020 \\ 0.2316 & 0.4678 & -0.2141 & 0.1597 & -0.3961 & -0.2450 & 0.4675 & -0.4699 \\ 0.0174 & -0.3339 & -0.4929 & 0.5947 & 0.4520 & 0.0454 & 0.0099 & -0.2918 \\ -0.5921 & 0.0248 & -0.1454 & -0.1545 & -0.0702 & 0.6334 & 0.4272 & -0.1229 \end{bmatrix}. \quad (5.6)$$

Its reduced row echelon form [107] is given by

$$\boldsymbol{A} \triangleq \boldsymbol{A}_I = \begin{bmatrix} 1.0000 & 0 & 0 & 0 & 0 & 0 & 0 & -0.9966 \\ 0 & 1.0000 & 0 & 0 & 0 & 0 & 0 & -1.0004 \\ 0 & 0 & 1.0000 & 0 & 0 & 0 & 0 & -1.0001 \\ 0 & 0 & 0 & 1.0000 & 0 & 0 & 0 & -0.9990 \\ 0 & 0 & 0 & 0 & 1.0000 & 0 & 0 & -1.0002 \\ 0 & 0 & 0 & 0 & 0 & 1.0000 & 0 & -0.9978 \\ 0 & 0 & 0 & 0 & 0 & 0 & 1.0000 & -0.9975 \end{bmatrix}, \quad (5.7)$$

which indicates that all the VSPND signals are almost equal for this cluster. Hence, these outcomes can be used for any other transient for which the same correlation pattern persists. Since the DR and FDI analyses on a data set, performed with the

Table 5.10: VSPNDs in 25 clusters

Cluster No.	No. of VSPNDs	VSPNDs
1	8	V_{13}, V_{18}, V_{28}, V_{49}, V_{82}, V_{108}, V_{113}, V_{180}
2	6	V_{16}, V_{17}, V_{58}, V_{60}, V_{127}, V_{186}
3	6	V_{46}, V_{93}, V_{100}, V_{101}, V_{178}, V_{179}
4	8	V_{12}, V_{36}, V_{74}, V_{83}, V_{112}, V_{147}, V_{160}, V_{188}
5	8	V_{14}, V_{15}, V_{21}, V_{29}, V_{64}, V_{88}, V_{111}, V_{125}
6	6	V_{63}, V_{69}, V_{76}, V_{81}, V_{139}, V_{146}
7	10	V_{78}, V_{99}, V_{115}, V_{122}, V_{137}, V_{152}, V_{172}, V_{177}, V_{184}, V_{196}
8	7	V_{3}, V_{27}, V_{30}, V_{114}, V_{129}, V_{140}, V_{169}
9	9	V_{20}, V_{67}, V_{155}, V_{158}, V_{171}, V_{183}, V_{192}, V_{194}, V_{200}
10	7	V_{23}, V_{24}, V_{53}, V_{85}, V_{97}, V_{106}, V_{156}
11	9	V_{43}, V_{59}, V_{94}, V_{105}, V_{131}, V_{138}, V_{143}, V_{149}, V_{150}
12	7	V_{1}, V_{44}, V_{52}, V_{98}, V_{136}, V_{187}, V_{190}
13	8	V_{7}, V_{8}, V_{19}, V_{25}, V_{51}, V_{57}, V_{134}, V_{142}
14	15	V_{2}, V_{9}, V_{22}, V_{26}, V_{33}, V_{45}, V_{47}, V_{65}, V_{86}, V_{120}, V_{128}, V_{144}, V_{148}, V_{151}, V_{199}
15	10	V_{32}, V_{35}, V_{70}, V_{92}, V_{102}, V_{117}, V_{123}, V_{167}, V_{181}, V_{198}
16	8	V_{5}, V_{54}, V_{103}, V_{104}, V_{110}, V_{162}, V_{175}, V_{193}
17	7	V_{11}, V_{56}, V_{80}, V_{84}, V_{87}, V_{157}, V_{185}
18	9	V_{48}, V_{61}, V_{72}, V_{77}, V_{79}, V_{91}, V_{145}, V_{168}, V_{195}
19	9	V_{4}, V_{62}, V_{73}, V_{95}, V_{118}, V_{130}, V_{135}, V_{173}, V_{174}
20	6	V_{34}, V_{39}, V_{42}, V_{50}, V_{66}, V_{109}
21	9	V_{10}, V_{37}, V_{107}, V_{113}, V_{124}, V_{132}, V_{159}, V_{182}, V_{189}
22	6	V_{55}, V_{68}, V_{75}, V_{90}, V_{116}, V_{166}
23	10	V_{31}, V_{41}, V_{89}, V_{96}, V_{119}, V_{121}, V_{126}, V_{170}, V_{176}, V_{191}
24	7	V_{6}, V_{71}, V_{141}, V_{153}, V_{154}, V_{163}, V_{197}
25	5	V_{38}, V_{40}, V_{161}, V_{164}, V_{165}

IPCA outcomes of the same data, are effective as evidenced by the case in Section 5.1.1, the WT is not conducted in this case. However, it needs to be conducted, when these outcomes are used for the DR and FDI of other data.

Additive biases are introduced into the data corresponding to three different VSPNDs, in a sequential manner as explained in Sections 5.1.1 to 5.1.4. Initial one-fourth length of data corresponds to the case of no fault. Bias is added to signal of a VSPND V_a from the instant corresponding to one-fourth of the length of data. Again bias is added to V_b, $b \neq a$, signal from half of the data, and finally in V_c, $c \notin \{a, b\}$, for the last one-fourth length of data. Here, the VSPND indices $a,\ b,\ c \in \{13,\ 18,\ 28,\ 49,\ 82,\ 108,\ 133,\ 180\}$. As described, the data is contaminated by a single fault, 2 faults and 3 faults during second, third and fourth quarters length of data respectively, leading to fault scenarios with up to 3 faulty VSPNDs. The DR and FDI indices (when IPCT in Fig. 3.4 is applied) are computed for each fault scenario for different additive biases from 0% to 20% of the nominal values of the VSPND signals, separated by 0.5%.

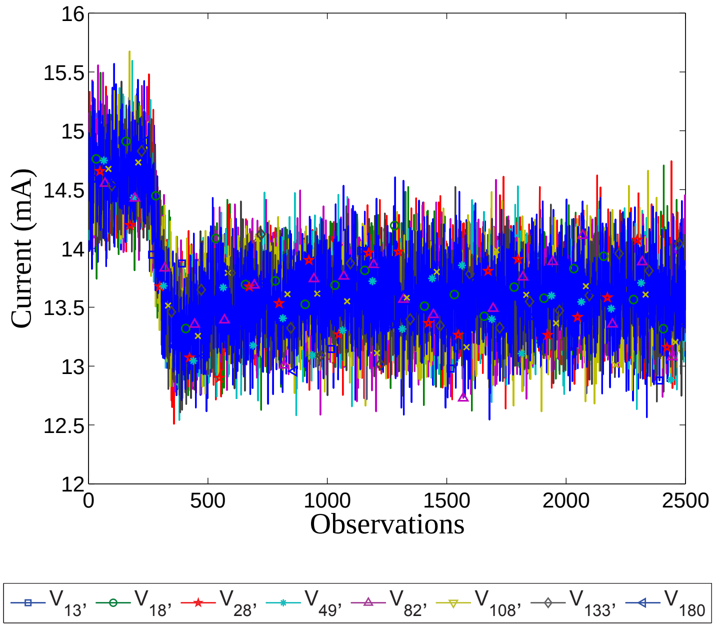

Figure 5.44: Signals of VSPNDs in cluster-1 during the transient corresponding to demand power change.

In the 3-fault scenarios, for a bias magnitude of 10% of the nominal steady-state signals, the smallest OP of 81.02% is found with V_{13}, V_{49} and V_{82} being the faulty VSPNDs; while the largest OP of 88.35% is observed with V_{18}, V_{82} and V_{180} being faulty. In other combinations of 3 faults, the OP was found to be between these smallest and largest values. DR and FDI statistics for the VSPND combination yielding the smallest OP are shown in Fig. 5.45, 5.46, and 5.47, respectively for 1, 2 and 3-fault scenarios. Those during 1, 2 and 3-fault scenarios for the VSPND combinations yielding the largest OP are shown in Fig. 5.48, 5.49, and 5.50.

In all fault scenarios, it can be observed that for a bias of approximately 10% and more, the fault is successfully detected and OP is more than 80%. For different bias magnitudes, AER can be seen increasing with non-zero values of OP. Positive AER at 0% of the bias is error reduction in the data corresponding to random errors, since there is no presence of faults at this bias. The adjustment in the data of faulty VSPNDs is accompanied with non-zero OP. The data of faulty VSPNDs are seen to be adjusted to represent the healthy values, as evident from the AA characteristics.

Table 5.11: IPCA results for different model orders for the data corresponding to DP Change

(a) Singular values of $\boldsymbol{Y}_s$

S. No.	$m=7$	$m=6$
1	138.33	137.63
2	1.07	1.08
3	1.04	1.03
4	1.03	1.02
5	1.02	1.02
6	1.01	1.02
7	1.01	1.00
8	1.00	1.00

(b) Standard deviation vector ($\boldsymbol{\sigma}_\varepsilon$)

VSPND	**True $\boldsymbol{\sigma}_\varepsilon$**	**Estimated $\boldsymbol{\sigma}_\varepsilon$**	
		$m=7$	$m=6$
V_{13}	0.2933	0.2909	0.2870
V_{18}	0.2933	0.2861	0.2864
V_{28}	0.2933	0.2965	0.2947
V_{49}	0.2933	0.2892	0.2881
V_{82}	0.2933	0.2928	0.2931
V_{108}	0.2933	0.2894	0.2781
V_{113}	0.2933	0.2822	0.2781
V_{180}	0.2933	0.2849	0.2847

5.2.2 Data of VSPNDs during the Refuelling Operation

In this section, the results of DR and FDI analyses are presented for the case of VSPND signal data obtained during the refuelling transient explained in Section 5.1.3, when the outcomes of the demand power change of Section 5.2.1 are utilized. In other words, constraint model and error variances obtained from IPCA and the cluster configuration of Section 5.2.1 are retained in this case also. DR and FDI analyses are carried out on the data of cluster-1 (refer to Table 5.10) during the refuelling transient and IPCA model in (5.6) (or (5.7)) is used for DR powered by the IPCT for FDI. The same bias profile explained in Section 5.2.1 is used also in this case to simulate 1, 2 and 3-fault scenarios.

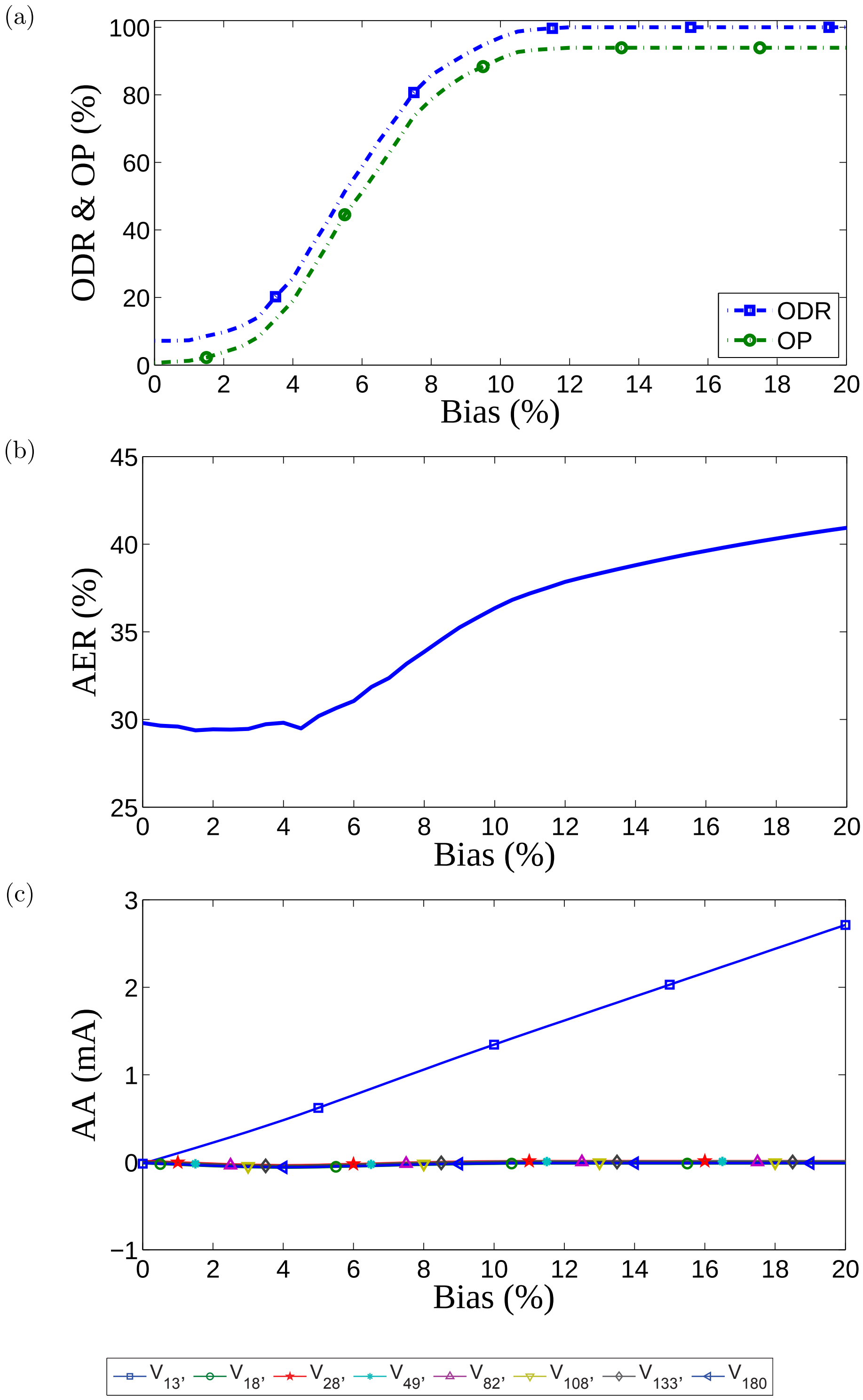

Figure 5.45: DR and FDI statistics in transient involving demand power change: 1-fault scenario with smallest OP (fault in V_{13} only) (a) ODR and OP (b) AER (c) AA.

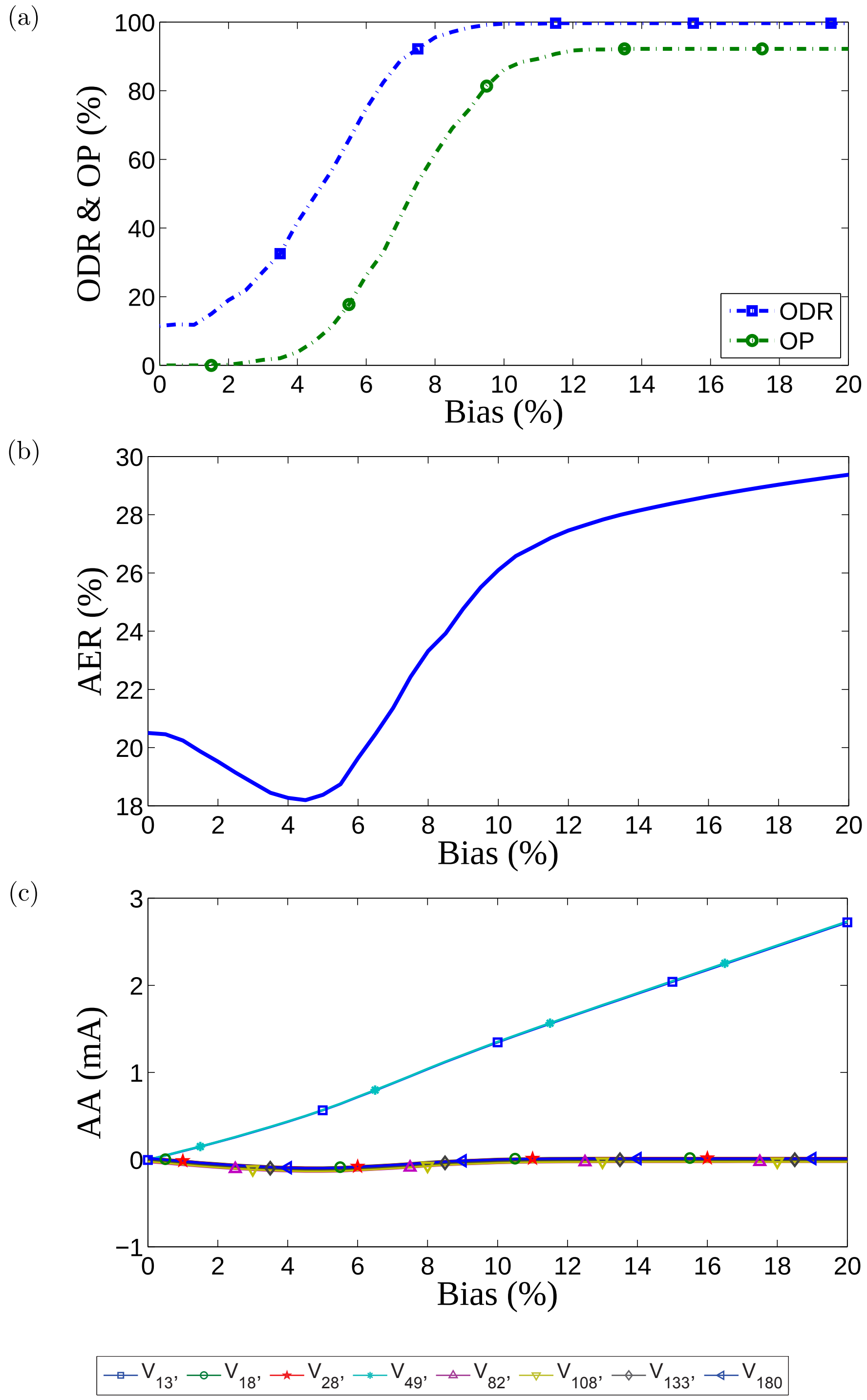

Figure 5.46: DR and FDI statistics of VSPNDs in transient involving demand power change: 2-fault scenario with smallest OP (faults in V_{13} and V_{49}, both) (a) ODR and OP (b) AER (c) AA.

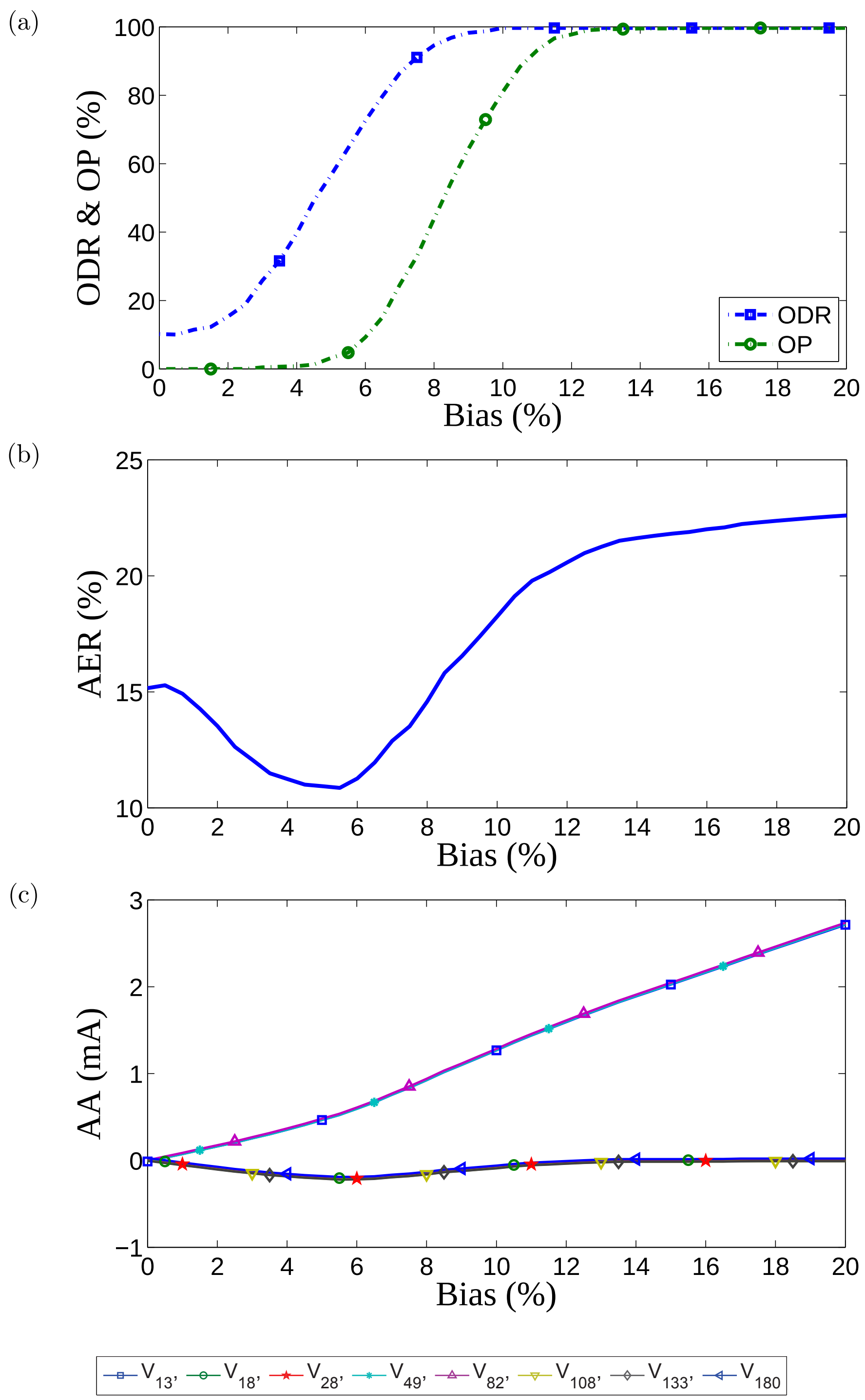

Figure 5.47: DR and FDI statistics in transient involving demand power change: 3-fault scenario with smallest OP (faults in V_{13}, V_{49} and V_{82}) (a) ODR and OP (b) AER (c) AA.

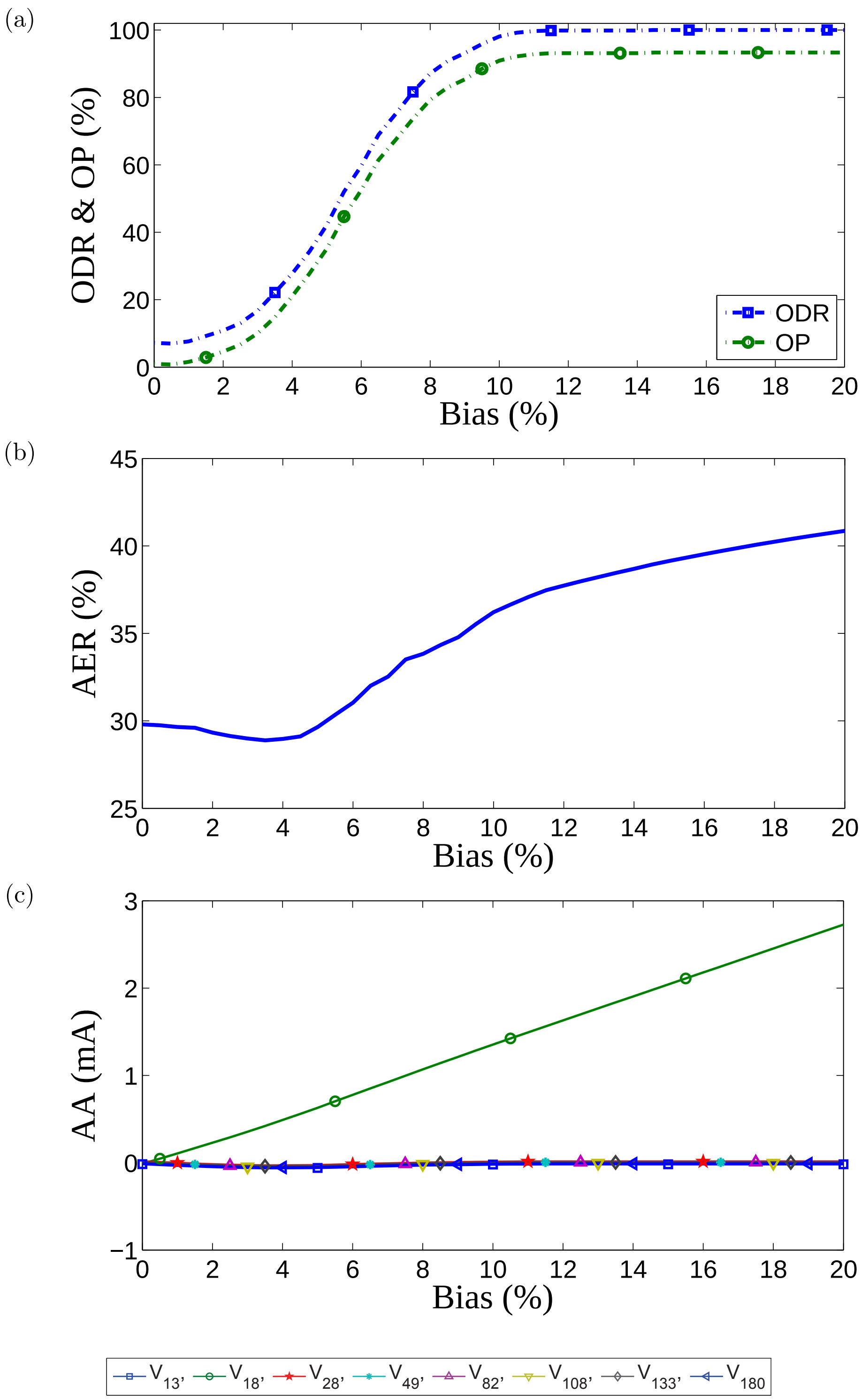

Figure 5.48: DR and FDI statistics in transient involving demand power change: 1-fault scenario with largest OP (fault in V_{18} only) (a) ODR and OP (b) AER (c) AA.

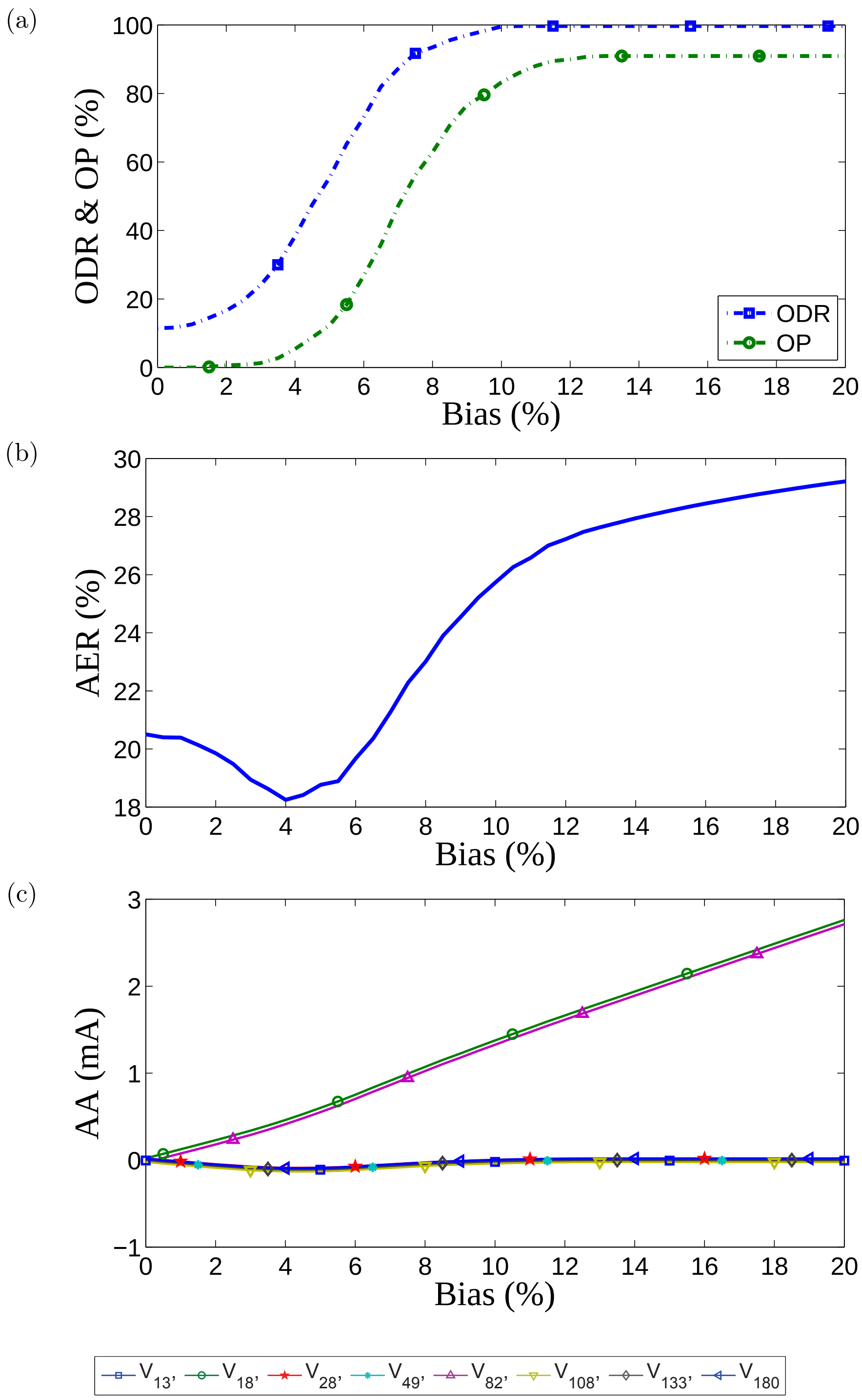

Figure 5.49: DR and FDI statistics in transient involving demand power change: 2-fault scenario with largest OP (faults in V_{18} and V_{82}, both) (a) ODR and OP (b) AER (c) AA.

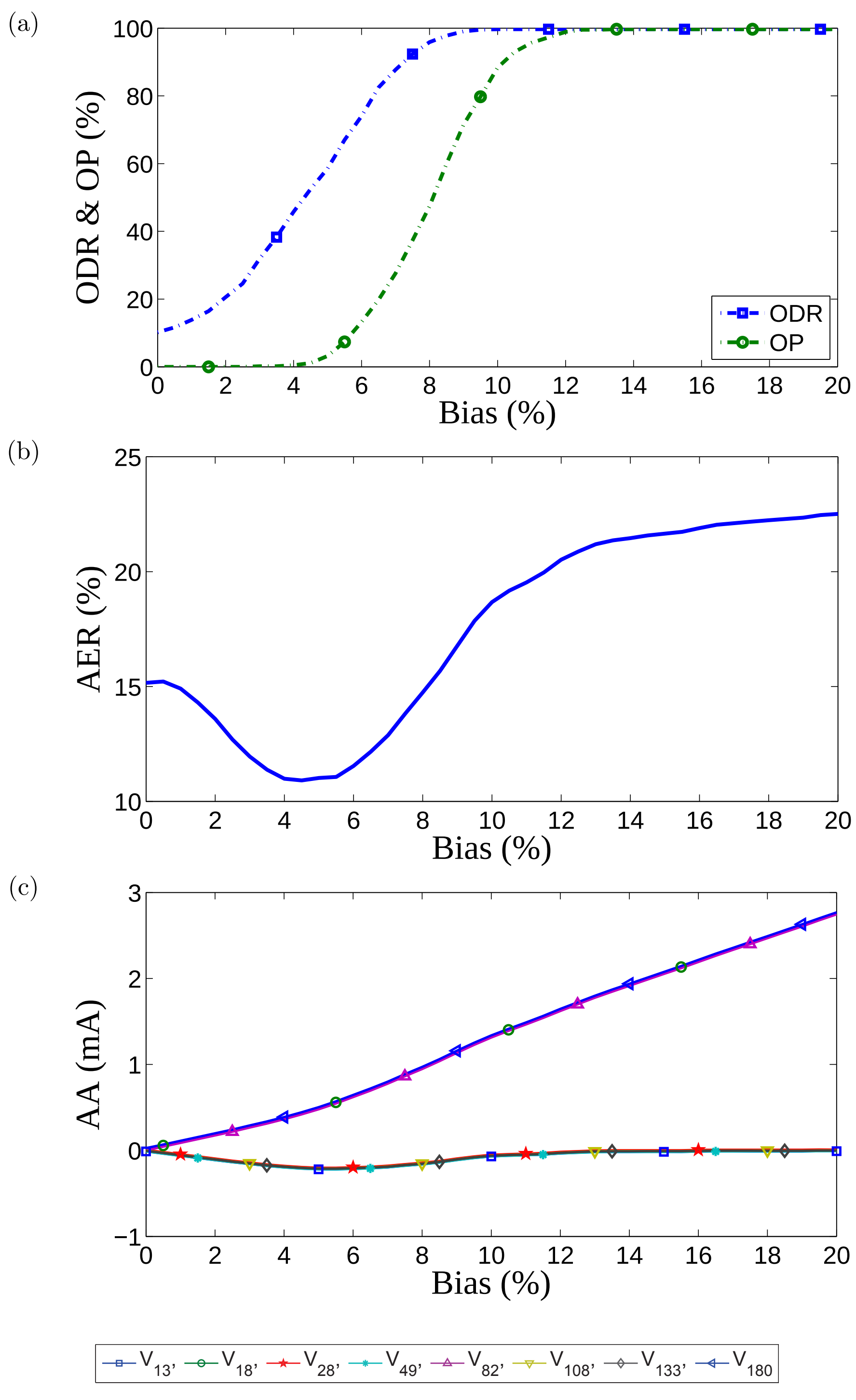

Figure 5.50: DR and FDI statistics in transient involving demand power change: 3-fault scenario with largest OP (faults in V_{18}, V_{82} and V_{180}) (a) ODR and OP (b) AER (c) AA.

In the case when the zonal power control is not implemented, the constraint relationships of the VSPNDs are no longer the same as those obtained during the model development. They vary as a function of time. The VSPND signals of cluster-1, which are supposed to be equal with respect to time (from (5.7) and Fig. 5.44), are different from each other as shown in Fig. 5.51(a). The VSPND combinations that exhibited minor and major OP at 10% bias (during 3-fault scenarios) are V_{13}, V_{28} and V_{82}; and V_{18}, V_{49} and V_{180} respectively. As is evident from Fig. 5.52 to 5.57 (corresponding to no zonal power control case), it can be said that the outcomes of the DR and FDI analyses are not up to the mark. This is due to the higher misclassification of faults (from ODR and OP statistics), negative error reduction (from AER characteristics) and infeasible adjustments made to the healthy signals as a result of faults (from AA characteristics). Hence, the scenario does not represent the effective DR-based FDI.

However, when zonal power control is successfully implemented, the VSPND signals are consistent with the constraint relations obtained during the model development. The same refuelling transient is simulated again with zonal power control to generate the VSPND signals. In this case, the VSPND signals of cluster-1 are as shown in Fig. 5.51(b). When this data employed the same model and the error covariance matrix obtained for the case of Section 5.2.1, the VSPND combinations that exhibited minor and major OP at 10% bias (during 3-fault scenarios) are V_{18}, V_{28} and V_{49}; and V_{13}, V_{18} and V_{82} respectively. The DR and FDI statistics are obtained as shown in Fig. 5.52 to 5.57 (corresponding to zonal power control case). It can be inferred from Fig. 5.52 to 5.57 that DR-based FDI scheme is promising for efficient detection, identification and elimination of faults, while the random errors are successfully reconciled.

The non-suitability of the constraint model of Section 5.2.1 for the case of VSPND data with no spatial control is also understood from the whiteness properties. The violation indices in WT by the measurement adjustments of individual VSPNDs of cluster-1 are given in Table 5.12 for the case of no spatial power control; and in Table 5.13 for the case in which the spatial power control is adopted. From the violation indices

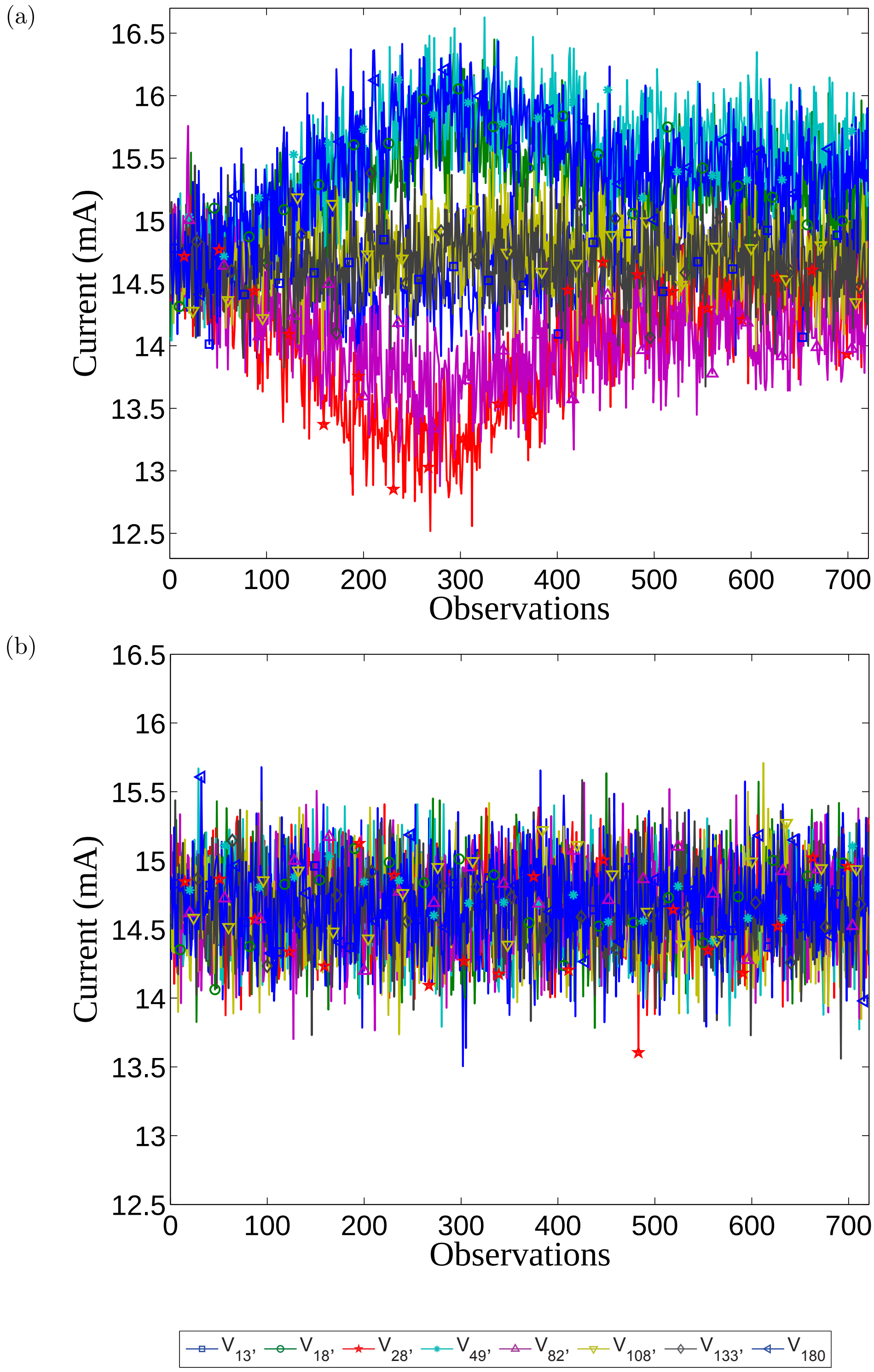

Figure 5.51: Signals of VSPNDs in cluster-1 during the transient corresponding to refuelling operation (a) with no zonal power control (b) with zonal power control.

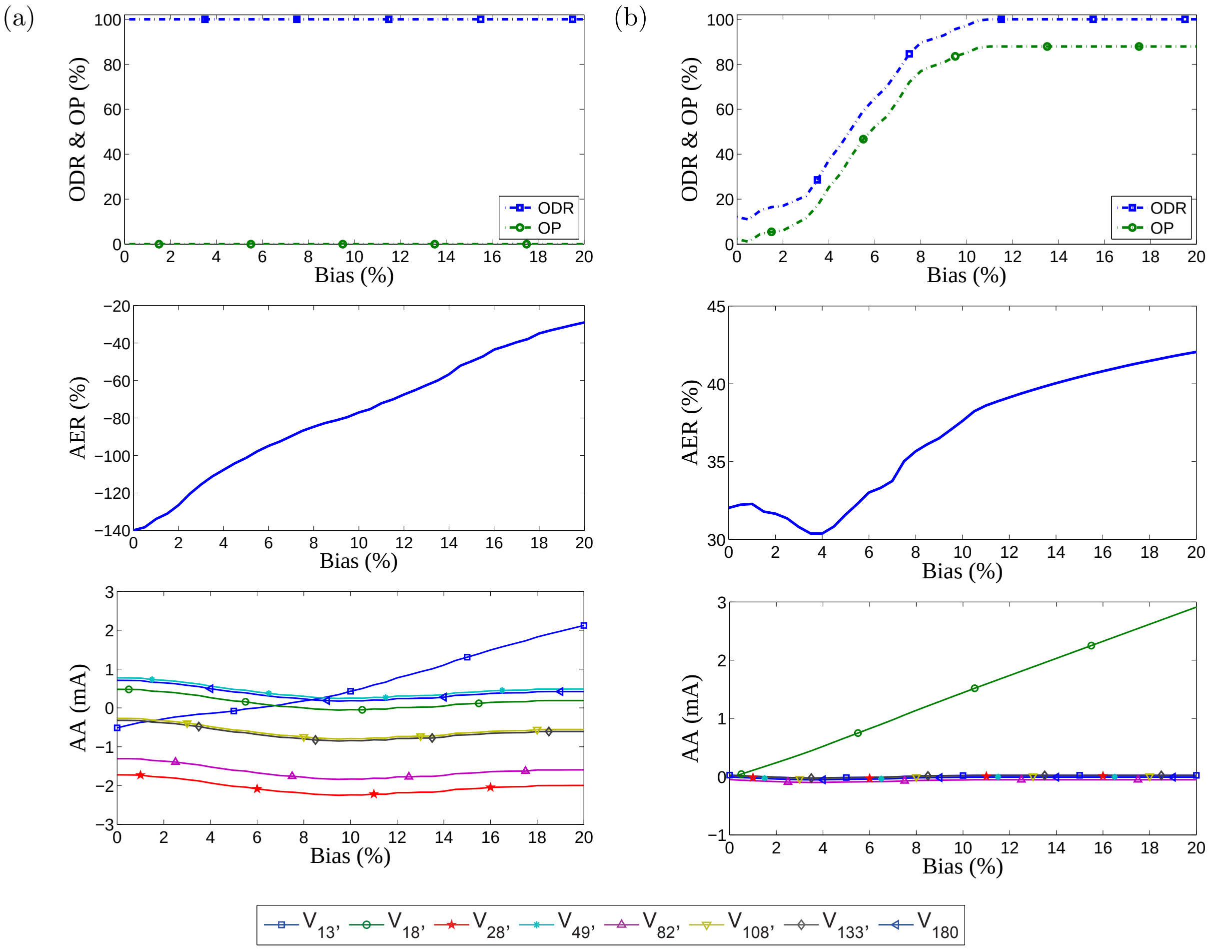

Figure 5.52: Refuelling operation: DR and FDI statistics for minor OP combinations in 1-fault scenarios with (a) no zonal power control (fault in V_{13} only) (b) zonal power control (fault in V_{18} only).

in both the cases, it can be concluded that spatial control is an important requirement for the steady-state DR and FDI. However, spatial control is very commonly employed for large reactors, hence, the steady-state DR and FDI is hassle-free.

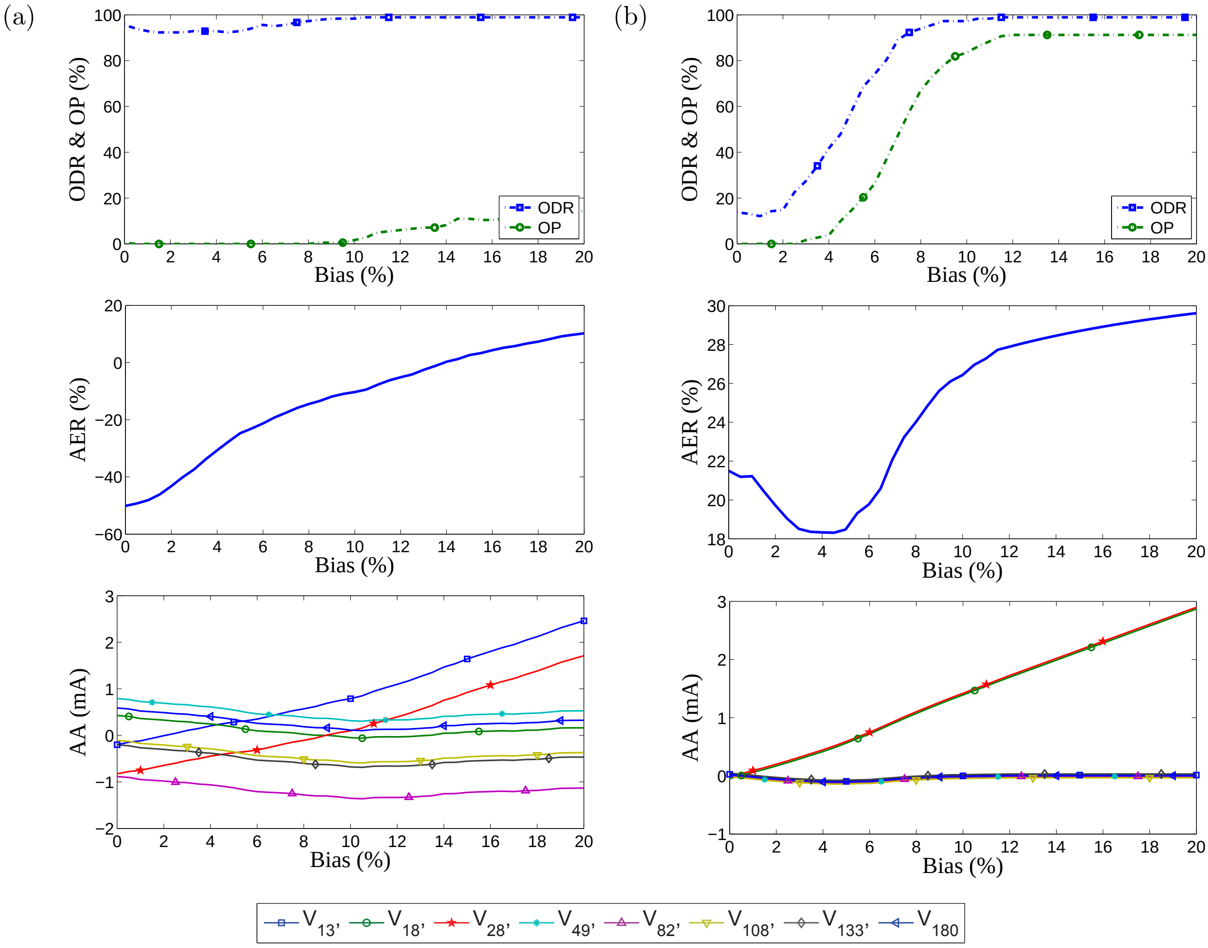

Figure 5.53: Refuelling operation: DR and FDI statistics for minor OP combinations in 2-fault scenarios with (a) no zonal power control (faults in V_{13} and V_{28}, both) (b) zonal power control (faults in V_{18} and V_{28}, both).

Table 5.12: Violation index of measurement adjustments of VSPND data in WT for refuelling operation with no spatial power control

Measurement adjustments	a_1	a_2	a_3	a_4	a_5	a_6	a_7	a_8
Violation index (%)	70.36	70.36	70.36	70.36	70.36	70.36	70.36	70.36

Table 5.13: Violation index of measurement adjustments of VSPND data in WT for refuelling operation with spatial power control

Measurement adjustments	a_1	a_2	a_3	a_4	a_5	a_6	a_7	a_8
Violation index (%)	1.10	1.10	1.10	1.10	1.10	1.10	1.10	1.10

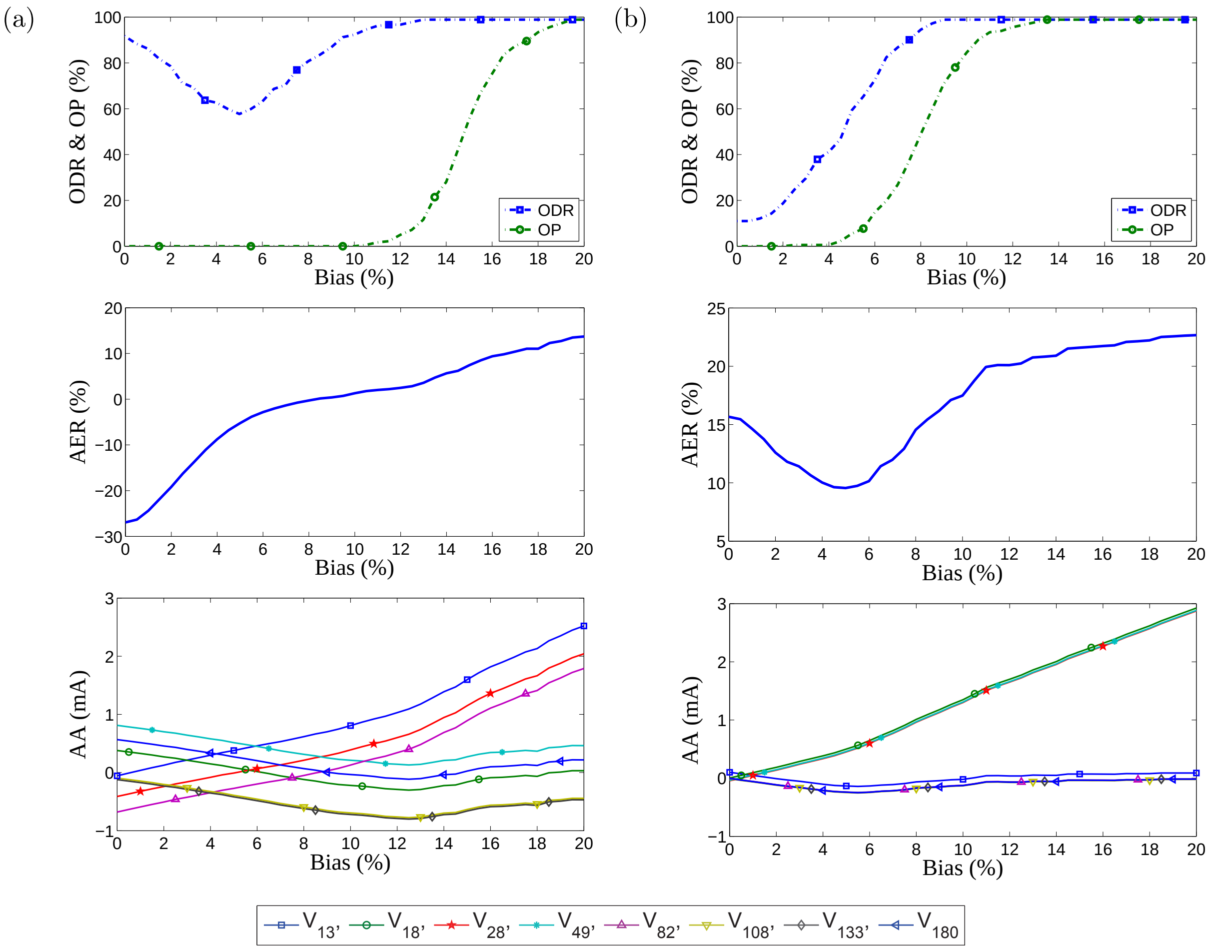

Figure 5.54: Refuelling operation: DR and FDI statistics for minor OP combinations in 3-fault scenarios with (a) no zonal power control (faults in V_{13}, V_{28} and V_{82}) (b) zonal power control (faults in V_{18}, V_{28} and V_{49}).

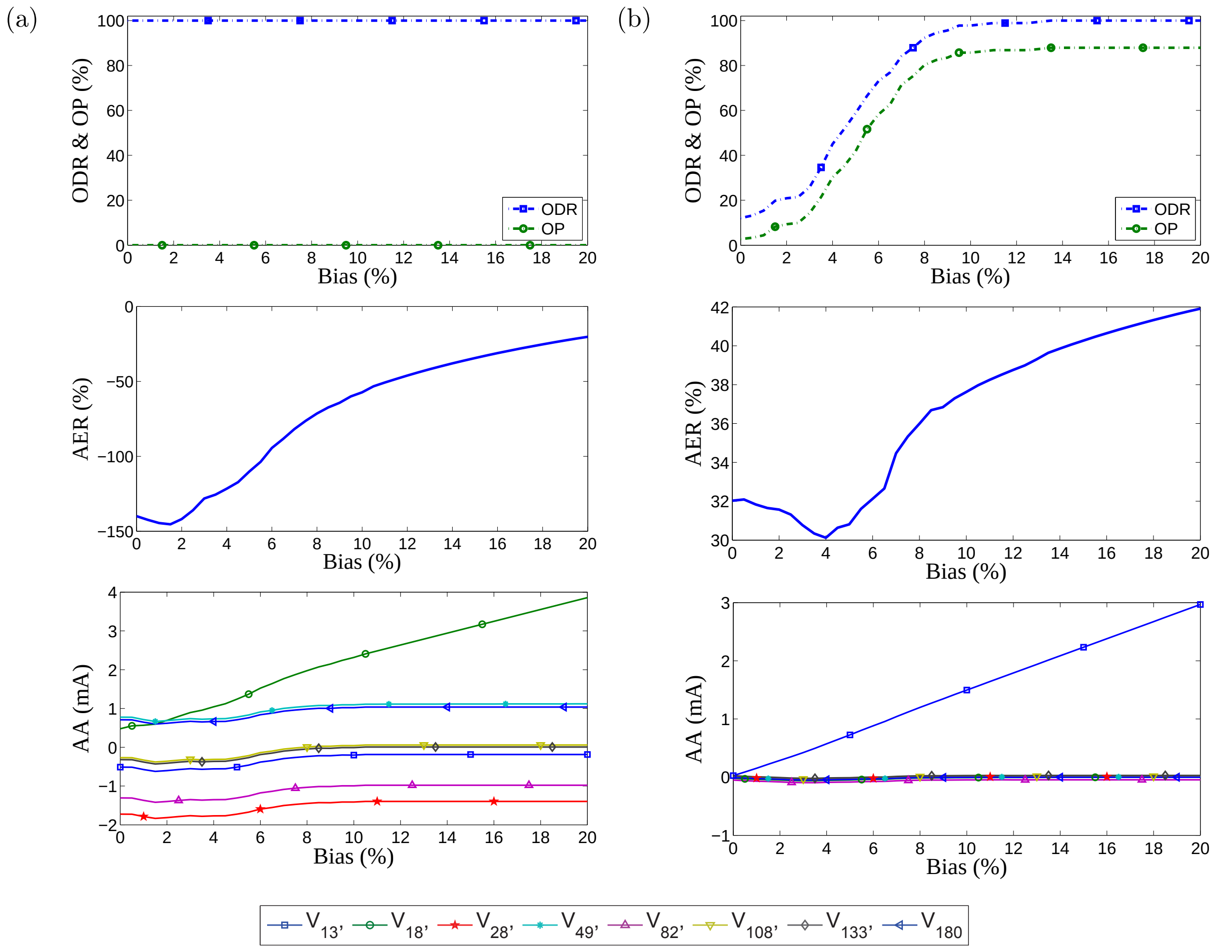

Figure 5.55: Refuelling operation: DR and FDI statistics for major OP combinations in 1-fault scenarios with (a) no zonal power control (fault in V_{18} only) (b) zonal power control (fault in V_{13} only).

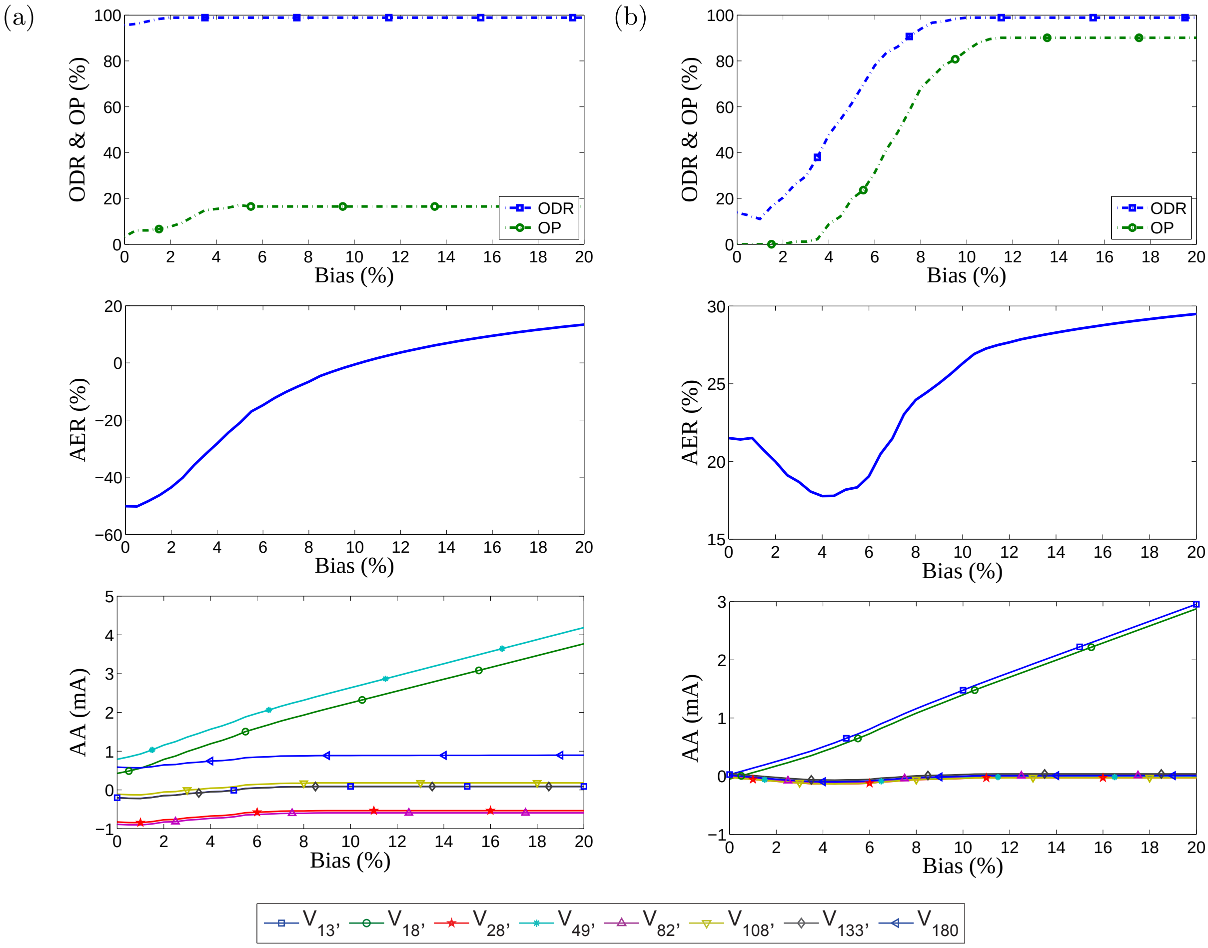

Figure 5.56: Refuelling operation: DR and FDI statistics for major OP combinations in 2-fault scenarios with (a) no zonal power control (faults in V_{18} and V_{49}, both) (b) zonal power control (faults in V_{13} and V_{18}, both).

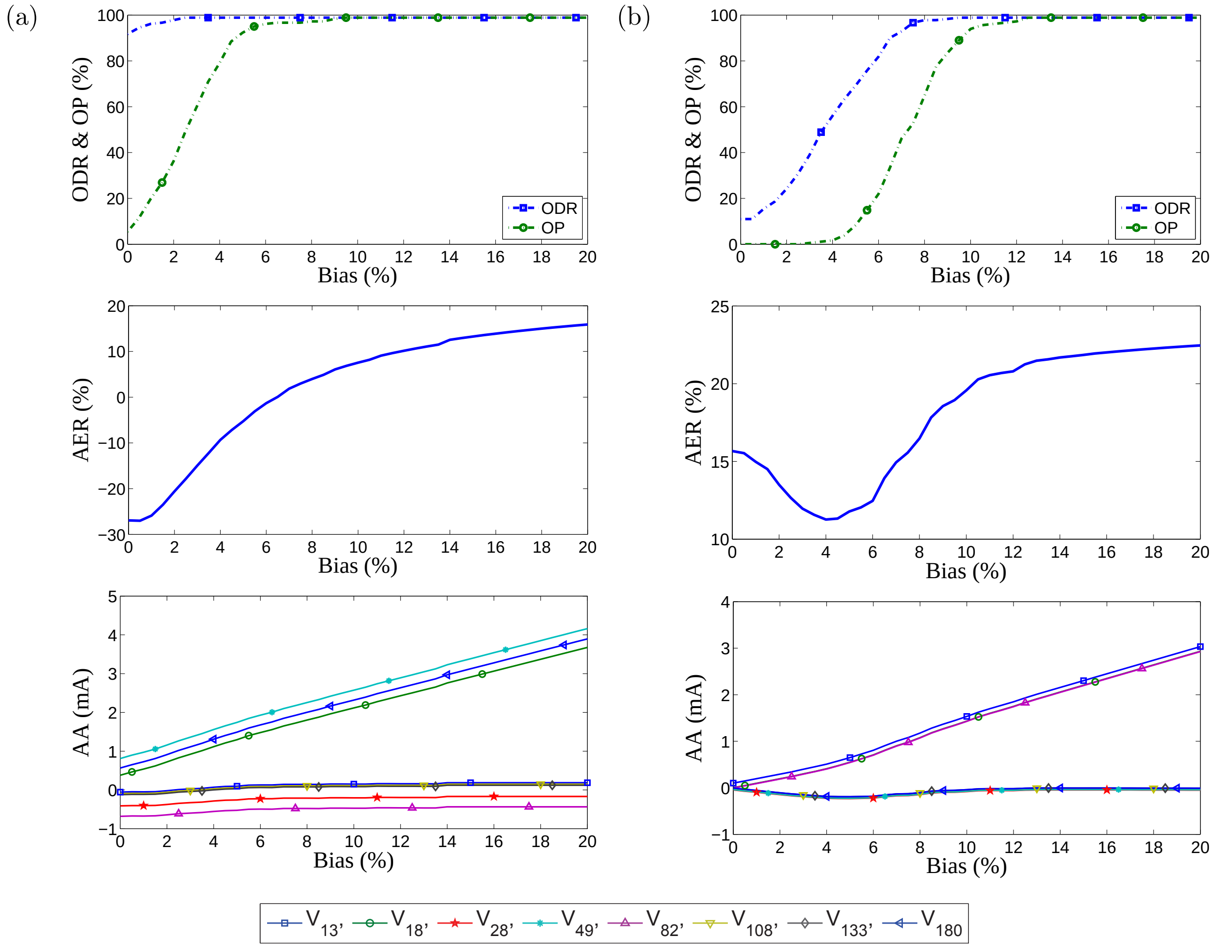

Figure 5.57: Refuelling operation: DR and FDI statistics for major OP combinations in 3-fault scenarios with (a) no zonal power control (faults in V_{18}, V_{49} and V_{180}) (b) zonal power control (faults in V_{13}, V_{18} and V_{82}).

Remarks:

The following remarks about the above simulations are worth mentioning:

1. The steady-state FDI based on DR is concerned about the measurement vector only at a single time instant and hence time dependent behaviour of the faults does not affect the performance of FDI. Any type of faults, *i.e.*, whether abrupt or incipient, including those mentioned in Sections 4.1.1 and 4.1.2 can be detected and isolated when they make test statistic exceed the threshold. Hence, in the simulations, some degradations in the form of only additive biases are introduced in the signals and FDI is performed. Since the multiple-fault detection and isolation techniques such as IPCT (refer to Section 3.3) are used, the faults are detected even if they occur in series with very little or no delay. However, to get enough observations in the 1-fault, 2-fault and 3-fault scenarios for the calculation of DR indices, *viz.*, AER and AA; and FDI indices, *viz.*, ODR and OP, sufficient gap between their occurrence is assumed in the simulations.

2. The algorithms and steps involved in statistical model building are given in Chapter 3. The online implementation of the scheme is depicted in Fig. 5.1 for the case of ion chamber data. In this chapter, only the application is presented.

3. Online monitoring in this chapter does not need any moving window. This is due to the fact that all the multiple-fault detection and isolation techniques, which are explained in Section 3.3 and used in Chapter 5, work only on a measurement vector at a single time-step. The fixed number of observations in each fault scenario (1-fault, 2-fault and 3-fault) are assumed only for the calculation of DR and FDI indices.

4. In the simulations, the performance of GLR method is seen to deteriorate in terms of fault identification or OP. This is due to some columns of the constraint model being proportional.

5.3 Discussions

Simulations are carried out on the simulated measurement data of the ion chambers and VSPNDs of the AHWR. Summarizing the results obtained in different simulations, it is possible to state that faults in detector (both ion chambers and VSPNDs) readings are detected with good overall success rate and the data of faulty detectors are seen to be estimated properly from the developed IPCA-based model, when powered by the IPCT. It was observed that the scheme requires the reactor to be near steady-state for maintaining the consistent constraint relationships among the detector signals. However, with successful spatial control [110], the models developed from the data of transients of Sections 5.1.1 and 5.2.1 alone are sufficient to perform satisfactory DR and FDI analyses under all transients. In summary, the DR-based FDI scheme can be said to be successful in detecting the faults; identifying the faults; reducing the effects of random errors from the data; and adjusting the measurement signals such that effects of faults are compensated.

In the next chapter, a model-based scheme for FDI is proposed. This scheme is based on the dynamic model of the VSPND.

Chapter 6

Kalman Filter-Based FDI of VSPNDs

Kalman filter is a linear optimal state estimator. It utilizes both the process model and the measurements, with uncertainty to obtain the best estimate for the states. It is best suitable for online applications as it recursively processes the data.

In this chapter, the Kalman filter framework, when it is extended to perform FDI of VSPNDs using GLR method, is explained. The estimates of faults are used for online correction of VSPND measurements. The model of VSPNDs developed in [60] is used here. A hybrid scheme is presented which dynamically compensates the VSPND signal for promptness; minimizes the random errors through Kalman filter; performs FDI with GLR method; and does online correction. The theoretical concepts are introduced one by one and the effectiveness of the scheme is explained with the help of simulations performed on the measurement data of VSPNDs.

6.1 General framework of GLR-based FDI

GLR method [127] is designed to detect abrupt changes either in the state variables or in the measurements. It quantifies the type and magnitude of faults alongwith the time of occurrence. This section describes the formulation of the GLR-based FDI scheme in LTI systems in a stochastic framework, with a Kalman filter used for state estimation. Since

A part of this chapter was published in *IEEE Transactions on Nuclear Science,* Vol. 62 (6).

FDI in recent times is performed using digital computers, discrete-time formulation is required for the Kalman filter.

The equations characterizing the dynamics of an LTI system are given as

$$\bar{\boldsymbol{x}}(k+1) = \boldsymbol{\Phi}\boldsymbol{x}(k) + \boldsymbol{\Gamma}\bar{\boldsymbol{u}}(k) + \boldsymbol{w}(k), \tag{6.1}$$

$$\boldsymbol{y}(k) = \boldsymbol{C}\bar{\boldsymbol{x}}(k) + \boldsymbol{\varepsilon}(k) + b\boldsymbol{e}_i s(k-\theta), \tag{6.2}$$

where $\bar{\boldsymbol{x}} \in \mathbb{R}^{\bar{m}\times 1}$ is the state vector, $\bar{\boldsymbol{u}} \in \mathbb{R}^{\bar{p}\times 1}$ is the input vector, $\boldsymbol{y} \in \mathbb{R}^{n\times 1}$ is the output vector, $\boldsymbol{\Phi} \in \mathbb{R}^{\bar{m}\times\bar{m}}$ is the state transition matrix, $\boldsymbol{\Gamma} \in \mathbb{R}^{\bar{m}\times\bar{p}}$ is the input matrix; $\boldsymbol{C} \in \mathbb{R}^{n\times\bar{m}}$ is the output matrix, $\boldsymbol{w} \in \mathbb{R}^{\bar{m}\times 1}$ represents the uncertainty involved in process model on addition of which the modelled state reaches the true one, and $\boldsymbol{\varepsilon} \in \mathbb{R}^{n\times 1}$ is the measurement noise, which accounts for the uncertainty in measurement. The last term in (6.2) constitutes the measurement bias model or fault model, where b is the magnitude of bias which occurs at a hypothesized time instant θ and persists thereafter, $\boldsymbol{e}_i \in \mathbb{R}^{n\times 1}$ is a vector with zeros in all positions except for a 1 corresponding to the corrupted measurement i. $s(k-\theta)$ represents a step change, to account for the fact that the bias occurs at the time instant θ, with the properties

$$s(k-\theta) = \begin{cases} 0 \text{ if } k < \theta \\ 1 \text{ if } k \geq \theta. \end{cases}$$

The uncertainty vectors $\boldsymbol{w}$ and $\boldsymbol{\varepsilon}$ are assumed to be normally distributed with the following properties:

$$\left.\begin{aligned} \mathrm{E}[\boldsymbol{w}] = \mathbf{0}, \mathrm{E}[\boldsymbol{\varepsilon}] = \mathbf{0}, \mathrm{E}[\boldsymbol{w}\boldsymbol{\varepsilon}^T] = \mathbf{0}, \\ \mathrm{E}[\boldsymbol{w}(k)\boldsymbol{w}(l)^T] = \boldsymbol{\Sigma}_{\boldsymbol{w}}\delta(k,l), \mathrm{E}[\boldsymbol{\varepsilon}(k)\boldsymbol{\varepsilon}(l)^T] = \boldsymbol{\Sigma}_{\boldsymbol{\varepsilon}}\delta(k,l), \end{aligned}\right\} \tag{6.3}$$

where $\boldsymbol{\Sigma}_{\boldsymbol{w}}$ and $\boldsymbol{\Sigma}_{\boldsymbol{\varepsilon}}$ are respectively the process and measurement uncertainties, and $\delta(k,l)$ is Kronecker delta.

Based on the above model, a Kalman filter can be designed for the estimation of the states. The following recursive equations represent the Kalman filter [58]:

$$\hat{\boldsymbol{x}}(k|k-1) = \boldsymbol{\Phi}\hat{\boldsymbol{x}}(k-1|k-1) + \boldsymbol{\Gamma}\bar{\boldsymbol{u}}(k), \tag{6.4}$$

$$\boldsymbol{\Sigma_p}(k|k-1) = \boldsymbol{\Phi}\boldsymbol{\Sigma_p}(k-1|k-1)\boldsymbol{\Phi}^T + \boldsymbol{\Sigma_w}, \tag{6.5}$$

$$\boldsymbol{\xi}(k) = \boldsymbol{y}(k) - \boldsymbol{C}\hat{\boldsymbol{x}}(k|k-1), \tag{6.6}$$

$$\boldsymbol{\Sigma_\xi}(k) = \boldsymbol{C}\boldsymbol{\Sigma_p}(k|k-1)\boldsymbol{C}^T + \boldsymbol{\Sigma_\varepsilon}, \tag{6.7}$$

$$\boldsymbol{K}(k) = \boldsymbol{\Sigma_p}(k|k-1)\boldsymbol{C}^T\boldsymbol{\Sigma_\xi}^{-1}(k), \tag{6.8}$$

$$\hat{\boldsymbol{x}}(k|k) = \hat{\boldsymbol{x}}(k|k-1) + \boldsymbol{K}(k)\boldsymbol{\xi}(k), \tag{6.9}$$

$$\boldsymbol{\Sigma_p}(k|k) = (\boldsymbol{I} - \boldsymbol{K}(k)\boldsymbol{C})\boldsymbol{\Sigma_p}(k|k-1), \tag{6.10}$$

where $\hat{\boldsymbol{x}}$ is the estimated state, and $\boldsymbol{\Sigma_p}$ is the covariance of the error in the estimated state. $\boldsymbol{\xi}(k)$ is the innovation, which reflects the discrepancy between actual measurement $\boldsymbol{y}(k)$ and predicted measurement $\boldsymbol{C}\hat{\boldsymbol{x}}(k|k-1)$, with covariance matrix $\boldsymbol{\Sigma_\xi}(k)$ and represents additional information available to the filter as a consequence of the new observation $\boldsymbol{y}(k)$. When the model of the system under consideration is accurate and the VSPND, whose signal is used to update the estimates, is working properly, the innovation sequence is expected to be a zero mean normal white noise process with covariance given by (6.7) [61]. In (6.8), $\boldsymbol{K}(k)$ is the Kalman gain, which blends the innovation with the predicted state as indicated in (6.9). In the set of equations (6.4)-(6.10), indices $k|k$ and $k|k-1$ indicate the conditional estimates at instant k when measurements are available up to instants k and $k-1$ respectively.

Innovations from the Kalman filter can be used for detection of anomalies in the system. When a fault is present, the whiteness property of innovations is lost. This feature of innovations can be exploited for FDI. A GLR method utilizing this phenomenon [64, 127, 128] is developed, with which sudden jumps in the measurements and states can be detected and estimated.

6.1.1 Effect of a Step Change in the Measurements on Innovations

A dual hypothesis method is adopted for fault detection, as per which the null hypothesis H_0 stands for no fault condition and H_1 stands for existence of fault.

By utilizing the linearity property of the system under consideration, conditional state estimates, measurements and innovations can be expressed respectively as

$$\hat{\bar{\boldsymbol{x}}}(k|k) = \hat{\bar{\boldsymbol{x}}}^{(h)}(k|k) + \hat{\bar{\boldsymbol{x}}}^{(f)}(k|k), \tag{6.11}$$

$$\boldsymbol{y}(k) = \boldsymbol{y}^{(h)}(k) + \boldsymbol{y}^{(f)}(k), \tag{6.12}$$

$$\text{and} \quad \boldsymbol{\xi}(k) = \boldsymbol{\xi}^{(h)}(k) + \boldsymbol{\xi}^{(f)}(k), \tag{6.13}$$

where $\hat{\bar{\boldsymbol{x}}}^{(h)}(k|k)$, $\boldsymbol{y}^{(h)}(k)$ and $\boldsymbol{\xi}^{(h)}(k)$ denote the respective variables corresponding to the healthy condition while $\hat{\bar{\boldsymbol{x}}}^{(f)}(k|k)$, $\boldsymbol{y}^{(f)}(k)$ and $\boldsymbol{\xi}^{(f)}(k)$ denote the effects of step change in the measurement. In the following, a lemma on the effect of a bias on innovations is given for which an alternate proof different from that in literature is presented.

Lemma I: Let b represent the measurement bias occurring in one sensor at a time instant θ, then the components $\boldsymbol{\xi}^{(f)}(k)$ and $\hat{\bar{\boldsymbol{x}}}^{(f)}(k|k)$ are given by

$$\boldsymbol{\xi}^{(f)}(k) = b\boldsymbol{G}(k,\theta)\boldsymbol{e}_i, \tag{6.14}$$

$$\text{and} \quad \hat{\bar{\boldsymbol{x}}}^{(f)}(k|k) = b\boldsymbol{J}(k,\theta)\boldsymbol{e}_i, \tag{6.15}$$

where $\boldsymbol{G}(k,\theta) \in \mathbb{R}^{n\times n}$ and $\boldsymbol{J}(k,\theta) \in \mathbb{R}^{\bar{m}\times n}$ are fault signature matrices obtained by the recursive solution of

$$\boldsymbol{G}(k,\theta) = (\boldsymbol{I} - \boldsymbol{C}\boldsymbol{\Phi}\boldsymbol{J}(k-1,\theta));\ \boldsymbol{G}(\theta,\theta) = \boldsymbol{I} \tag{6.16}$$

$$\boldsymbol{J}(k,\theta) = \boldsymbol{\Phi}\boldsymbol{J}(k-1,\theta) + \boldsymbol{K}(k)\boldsymbol{G}(k,\theta);\ \boldsymbol{J}(\theta,\theta) = \boldsymbol{K}(\theta), \tag{6.17}$$

where $\boldsymbol{I}$ is the identity matrix of appropriate dimension.

Proof. From (6.6) and (6.13), just before and at the instant of occurrence of step change,

$$\boldsymbol{\xi}^{(f)}(\theta) = b\boldsymbol{e}_i - \boldsymbol{C}\hat{\bar{\boldsymbol{x}}}^{(f)}(\theta|\theta-1) = b\boldsymbol{e}_i - \boldsymbol{C}(\boldsymbol{\Phi}\hat{\bar{\boldsymbol{x}}}^{(f)}(\theta-1|\theta-1)) = b\boldsymbol{e}_i, \tag{6.18}$$

as the term $\hat{\bar{\boldsymbol{x}}}^{(f)}(\theta-1|\theta-1)$ is equal to zero, since it is the component of fault before its occurrence. At θ, we can also compute $\hat{\bar{\boldsymbol{x}}}^{(f)}(\theta|\theta)$ which helps obtaining the innovation as a function of bias, at immediately next sampling instant $\theta+1$. From (6.9) and (6.11), we have

$$\hat{\bar{\boldsymbol{x}}}^{(f)}(\theta|\theta) = \hat{\bar{\boldsymbol{x}}}^{(f)}(\theta|\theta-1) + \boldsymbol{K}(\theta)\boldsymbol{\xi}^{(f)}(\theta). \tag{6.19}$$

Substituting $\boldsymbol{\xi}^{(f)}(\theta)$ from (6.18) in (6.19) yields

$$\begin{aligned}\hat{\bar{\boldsymbol{x}}}^{(f)}(\theta|\theta) &= \boldsymbol{\Phi}\hat{\bar{\boldsymbol{x}}}^{(f)}(\theta-1|\theta-1) + b\boldsymbol{K}(\theta)\boldsymbol{e}_i \\ &= b\boldsymbol{K}(\theta)\boldsymbol{e}_i \end{aligned} \tag{6.20}$$

as $\hat{\bar{\boldsymbol{x}}}^{(f)}(\theta-1|\theta-1) = \mathbf{0}$.

Hence, by comparing (6.18) and (6.20) respectively with (6.14) and (6.15),

$$\boldsymbol{G}(\theta,\theta) = \boldsymbol{I} \tag{6.21a}$$

$$\boldsymbol{J}(\theta,\theta) = \boldsymbol{K}(\theta) \tag{6.21b}$$

The component of innovation for bias subsequent to the instant of occurrence of step change is given by

$$\begin{aligned}\boldsymbol{\xi}^{(f)}(\theta+1) &= b\boldsymbol{e}_i - \boldsymbol{C}\hat{\bar{\boldsymbol{x}}}^{(f)}(\theta+1|\theta) \\ &= b\boldsymbol{e}_i - \boldsymbol{C}(\boldsymbol{\Phi}\hat{\bar{\boldsymbol{x}}}^{(f)}(\theta|\theta)). \end{aligned} \tag{6.22}$$

Substituting $\hat{\hat{\boldsymbol{x}}}^{(f)}(\theta|\theta)$ from (6.20) yields

$$\boldsymbol{\xi}^{(f)}(\theta+1) = b\boldsymbol{e}_i - b\boldsymbol{C}\boldsymbol{\Phi}\boldsymbol{K}(\theta)\boldsymbol{e}_i = b(\boldsymbol{I} - \boldsymbol{C}\boldsymbol{\Phi}\boldsymbol{K}(\theta))\boldsymbol{e}_i. \tag{6.23}$$

Conditional state estimate after correction through Kalman filter, when measurements up to instant $\theta+1$ are available, is as follows:

$$\begin{aligned}
\hat{\hat{\boldsymbol{x}}}^{(f)}(\theta+1|\theta+1) &= \hat{\hat{\boldsymbol{x}}}^{(f)}(\theta+1|\theta) + \boldsymbol{K}(\theta+1)\boldsymbol{\xi}^{(f)}(\theta+1) \\
&= \boldsymbol{\Phi}\hat{\hat{\boldsymbol{x}}}^{(f)}(\theta|\theta) + \boldsymbol{K}(\theta+1)\boldsymbol{\xi}^{(f)}(\theta+1), \\
&= b\boldsymbol{\Phi}\boldsymbol{K}(\theta)\boldsymbol{e}_i + b\boldsymbol{K}(\theta+1)(\boldsymbol{I} - \boldsymbol{C}\boldsymbol{\Phi}\boldsymbol{K}(\theta))\boldsymbol{e}_i.
\end{aligned} \tag{6.24}$$

So,

$$\boldsymbol{G}(\theta+1,\theta) = (\boldsymbol{I} - \boldsymbol{C}\boldsymbol{\Phi}\boldsymbol{K}(\theta)) \tag{6.25a}$$

$$\boldsymbol{J}(\theta+1,\theta) = \boldsymbol{\Phi}\boldsymbol{K}(\theta) + \boldsymbol{K}(\theta+1)(\boldsymbol{I} - \boldsymbol{C}\boldsymbol{\Phi}\boldsymbol{K}(\theta)) \tag{6.25b}$$

From (6.23), (6.24) and (6.25), it can be written that

$$\boldsymbol{\xi}^{(f)}(\theta+2) = b\boldsymbol{e}_i - \boldsymbol{C}\hat{\hat{\boldsymbol{x}}}^{(f)}(\theta+2|\theta+1) = b\boldsymbol{e}_i - \boldsymbol{C}\boldsymbol{\Phi}\hat{\hat{\boldsymbol{x}}}^{(f)}(\theta+1|\theta+1),$$

or,

$$\boldsymbol{\xi}^{(f)}(\theta+2) = b(\boldsymbol{I} - \boldsymbol{C}\boldsymbol{\Phi}\boldsymbol{J}(\theta+1,\theta))\boldsymbol{e}_i = b\boldsymbol{G}(\theta+2,\theta)\boldsymbol{e}_i. \tag{6.26}$$

And from (6.26),

$$\begin{aligned}
\hat{\hat{\boldsymbol{x}}}^{(f)}(\theta+2|\theta+2) &= \hat{\hat{\boldsymbol{x}}}^{(f)}(\theta+2|\theta+1) + \boldsymbol{K}(\theta+2)\boldsymbol{\xi}^{(f)}(\theta+2) \\
&= \boldsymbol{\Phi}\hat{\hat{\boldsymbol{x}}}^{(f)}(\theta+1|\theta+1) + \boldsymbol{K}(\theta+2)\boldsymbol{\xi}^{(f)}(\theta+1), \\
&= b(\boldsymbol{\Phi}\boldsymbol{J}(\theta+1,\theta) + \boldsymbol{K}(\theta+2)\boldsymbol{G}(\theta+2,\theta))\boldsymbol{e}_i.
\end{aligned} \tag{6.27}$$

Table 6.1: Statistical properties of innovations at time k

Property	H_0	H_1
Mean	0	$b\boldsymbol{G}(k,\theta)\boldsymbol{e}_i$
Covariance	$\boldsymbol{\Sigma_{\xi}}(k)$	$\boldsymbol{\Sigma_{\xi}}(k)$

Hence, the variation of fault signature matrices $\boldsymbol{G}(k,\theta)$ and $\boldsymbol{J}(k,\theta)$ at any other time $k > \theta$, are expressed by the set of recursive equations

$$\boldsymbol{G}(k,\theta) = (\boldsymbol{I} - \boldsymbol{C}\boldsymbol{\Phi}\boldsymbol{J}(k-1,\theta)) \tag{6.28a}$$

$$\boldsymbol{J}(k,\theta) = \boldsymbol{\Phi}\boldsymbol{J}(k-1,\theta) + \boldsymbol{K}(k)\boldsymbol{G}(k,\theta). \tag{6.28b}$$

For a hypothesized bias occurrence time $\hat{\theta} \simeq \theta$ (with reference to Section 6.1.2), the above fault signature matrix is calculated for any instant k after $\hat{\theta}$, as follows:

$$\boldsymbol{G}(k,\hat{\theta}) = (\boldsymbol{I} - \boldsymbol{C}\boldsymbol{\Phi}\boldsymbol{J}(k-1,\hat{\theta})) \tag{6.29}$$

The GLR test explained in Section 6.1.3 is applied to obtain the maximum likelihood estimate for the magnitude of bias over all choices for faulty VSPND i. □

Now the statistical properties of the innovations, as shown in Table 6.1, are obvious from (6.14) for the hypotheses H_0 and H_1. Thus the magnitude of bias is obtained from $\boldsymbol{G}(k,\theta)$ but the time instant θ needs to be specified.

6.1.2 Estimation of Time of Occurrence of Bias

During a fault, the innovation experiences a change in its mean value, which may exceed certain threshold value. A Fault Detection Test (FDT) can be conducted based on the test statistic defined as [64]

$$\varphi(k) = \boldsymbol{\xi}^T(k)\boldsymbol{\Sigma_{\xi}}^{-1}(k)\boldsymbol{\xi}(k). \tag{6.30}$$

In the above, $\mathbf{\Sigma}_{\boldsymbol{\xi}}(k)$ given by (6.7) is invertible as the measurement errors are assumed to be independent of each other. Note that $\varphi(k)$ is a quadratic term of innovations normalized by their covariance $\mathbf{\Sigma}_{\boldsymbol{\xi}}(k)$ at k^{th} instant amounting to the sum of the squares of n independent standard normal random variables. Hence, $\varphi(k)$ follows a central χ^2 distribution of n degrees of freedom [36, 64]. It can be inferred that $\hat{k}$ is the possible instant of bias occurrence if $\varphi(\hat{k}) > \chi^2_{n,1-\alpha}$. Here, $\chi^2_{n,1-\alpha}$ represents the value of the statistic at which χ^2 distribution curve spans $1-\alpha$ portion of the total area under the curve, where α is a measure for false detection. Since the decision process is based on the distribution known under healthy condition, it is natural that the α fraction of the curve that represents the abnormalities also erroneously declares the faults if the statistics under healthy condition exceed the threshold because of random errors. Hence α is known as false detection rate and is generally chosen as 0.05 [64, 65]. Apart from random errors, some occasional outliers (not step changes) also make the FDT statistic exceed the threshold. One way for reliable detection of bias is to conduct a Fault Confirmation Test (FCT) on the FDT statistics in a time window of certain number of samples. According to this, $\hat{k}$ is declared as the estimate of θ, the time of occurrence of step change, if

$$\psi(\hat{k}) > \chi^2_{n\times N_f,1-\alpha},$$

where $\psi(\hat{k})$, FCT statistic, is defined as

$$\psi(\hat{k}) = \sum_{i=\hat{k}}^{\hat{k}+N_f-1} \varphi(i), \tag{6.31}$$

where N_f is the number of sampling instants in the time window. FCT statistic follows a central χ^2 distribution of $n \times N_f$ degrees of freedom. Thus the computation of fault signature matrices can be initiated from $\hat{k} = \hat{\theta}$, where $\hat{\theta}$ is the estimate of θ. This procedure is followed for each and every sampling instant.

6.1.3 GLR Test for Fault Identification

Isolation of faulty VSPND and identification (estimation) of magnitude of bias needs to be accomplished subsequent to the FDI. If $f(\bar{\boldsymbol{\xi}})$ denotes the joint probability density function of the n-variate innovations from time $\hat{\theta}$ to $\hat{\theta} + N_f - 1$, then the GLR can be written as

$$\lambda(\bar{\boldsymbol{\xi}}) = \sup \frac{f(\bar{\boldsymbol{\xi}}|H_1)}{f(\bar{\boldsymbol{\xi}}|H_0)}. \tag{6.32}$$

Using the expression for the multivariate normal probability density function given in [58] and from Table 6.1, we have

$$\lambda(\bar{\boldsymbol{\xi}}) = \sup_{\boldsymbol{e}_i, b} \frac{\exp\left\{-\frac{1}{2} \sum_{k=\hat{\theta}}^{\hat{\theta}+N_f-1} \boldsymbol{\varrho}(k,\hat{\theta},i)^T \boldsymbol{\Sigma_\xi}^{-1}(k) \boldsymbol{\varrho}(k,\hat{\theta},i)\right\}}{\exp\left\{-\frac{1}{2} \sum_{k=\hat{\theta}}^{\hat{\theta}+N_f-1} \boldsymbol{\xi}^T(k) \boldsymbol{\Sigma_\xi}^{-1}(k) \boldsymbol{\xi}(k)\right\}}, \tag{6.33}$$

where

$$\boldsymbol{\varrho}(k,\hat{\theta},i) = \boldsymbol{\xi}(k) - b\boldsymbol{G}(k,\hat{\theta})\boldsymbol{e}_i. \tag{6.34}$$

For simplicity, define

$$T = 2\ln \lambda(\bar{\boldsymbol{\xi}}) = \sup_{\boldsymbol{e}_i} T_i, \tag{6.35}$$

where

$$\begin{aligned} T_i = & \sum_{k=\hat{\theta}}^{\hat{\theta}+N_f-1} \boldsymbol{\xi}^T(k) \boldsymbol{\Sigma_\xi}^{-1}(k) \boldsymbol{\xi}(k) \\ & - \sup_b \sum_{k=\hat{\theta}}^{\hat{\theta}+N_f-1} \boldsymbol{\varrho}(k,\hat{\theta},i)^T \boldsymbol{\Sigma_\xi}^{-1}(k) \boldsymbol{\varrho}(k,\hat{\theta},i), \; i = 1, 2, \ldots, n. \end{aligned} \tag{6.36}$$

The maximum likelihood estimate $\hat{b}$ is obtained by equating the first derivative of (6.36) with respect to b to zero. Thus

$$\hat{b} = \frac{\boldsymbol{e}_i^T \sum_{k=\hat{\theta}}^{\hat{\theta}+N_f-1} \boldsymbol{G}^T(k,\hat{\theta})\boldsymbol{\Sigma_\xi}^{-1}(k)\boldsymbol{\xi}(k)}{\boldsymbol{e}_i^T \left(\sum_{k=\hat{\theta}}^{\hat{\theta}+N_f-1} \boldsymbol{G}^T(k,\hat{\theta})\boldsymbol{\Sigma_\xi}^{-1}(k)\boldsymbol{G}(k,\hat{\theta}) \right) \boldsymbol{e}_i}. \tag{6.37}$$

Substituting the value of $\hat{b}$ in (6.34) and manipulating (6.33), (6.34) and (6.36), we get

$$T_i = \frac{\left(\boldsymbol{e}_i^T \sum_{k=\hat{\theta}}^{\hat{\theta}+N_f-1} \boldsymbol{G}^T(k,\hat{\theta})\boldsymbol{\Sigma_\xi}^{-1}(k)\boldsymbol{\xi}(k) \right)^2}{\boldsymbol{e}_i^T \left(\sum_{k=\hat{\theta}}^{\hat{\theta}+N_f-1} \boldsymbol{G}^T(k,\hat{\theta})\boldsymbol{\Sigma_\xi}^{-1}(k)\boldsymbol{G}(k,\hat{\theta}) \right) \boldsymbol{e}_i}. \tag{6.38}$$

Note that T_i is computed for all $\boldsymbol{e}_i,\ i = 1, ..., n$. If a bias is detected by FCT, the VSPND i that generated maximum T_i is declared as the faulty VSPND $\hat{i}$. The estimate computed from (6.37) corresponding to the faulty VSPND $\hat{i}$ is declared as the fault magnitude $\hat{b}$.

However, incorrect isolation of the VSPNDs is still possible because of occasional rejections by fault detection and fault confirmation tests, due to the measurement noise content in the healthy VSPND readings. Nevertheless, these erroneous rejections are associated with a non-zero bias estimate close to zero. Such isolations and identifications have negligible impact on the overall performance because of very small bias estimates.

6.1.4 On-line Correction for Bias

Step faults in the measurement data not only corrupt the quality of the data but also make the innovations non-white, which might hinder the detection of subsequent faults, if any. An on-line scheme for correction of the bias in the measurements is of utmost importance. The FDI outcomes such as isolation and estimation of bias can be used for on-line correction for the bias in the measurement data. For an isolated VSPND $\hat{\imath}$, the corrected measurement vector is given by

$$\boldsymbol{y}^{(c)}(k) = \boldsymbol{y}(k) - \hat{b}\boldsymbol{e}_{\hat{\imath}}. \tag{6.39}$$

Note that the correction is delayed by N_f samples after the fault occurrence. Too large a value for N_f makes the detection procedure delayed by the same number of samples, while too small a value makes the bias estimate erroneous. So a trade-off is required in the selection of N_f, and a reasonable value for it is known only by simulations with different choices of N_f and looking for the best accurate bias estimate.

Flow chart of GLR method is shown in Fig. 6.1. At every instant, the Kalman Filter generates the innovation vector from (6.6). This vector is used for conducting FDT based on the statistic given by (6.30). FDT statistic φ_k is computed and FDT is carried out. If H_1 is false, the computations are continued over the new cycle. If H_1 is found true by FDT at an instant k, the instant is declared as the FDT rejection instant $\hat{k}$. N_f number of fault signature matrices are computed recursively from (6.16) and (6.17), where $\theta = \hat{k}$, FCT statistic $\psi_{\hat{k}}$ is computed using (6.31) and FCT is conducted. Note that a rejection of null hypothesis H_0 in FDT doesn't guarantee the same in FCT, which means that FCT rejection instants are a subset of FDT rejection instants which in turn are a subset of entire set of observations. If FCT also declares the fault at $\hat{k}$, the instant is denoted as $\hat{\theta}$. The outcomes of the GLR test such as $\hat{\imath}$ and $\hat{b}$ (refer to Section 6.1.3) are used for the on-line correction of the faults using (6.39).

6.2 Application of GLR-based FDI Scheme to VSPNDs

The method discussed in Section 6.1 is used for detection and diagnosis of step changes in VSPND signals. Its application necessitates a mathematical model of VSPNDs. Modeling of VSPNDs is well explained in [60, 61], according to which the standard LTI state-space formulation for a VSPND V_i, $\forall\ i = 1, 2, \ldots, 200$, in continuous time domain is given by

$$\dot{\bar{\boldsymbol{x}}}^{(i)}(t) = \boldsymbol{A}^{(i)}\bar{\boldsymbol{x}}^{(i)}(t) + \boldsymbol{w}(t), \tag{6.40}$$

$$y^{(i)}(t) = \boldsymbol{c}^{(i)}\bar{\boldsymbol{x}}^{(i)}(t) + \varepsilon(t), \tag{6.41}$$

where

$$\bar{\boldsymbol{x}}^{(i)}(t) = [\zeta^{(i)}(t)\ \phi^{(i)}(t)\ \eta^{(i)}(t)]^T \tag{6.42}$$

represents the state vector, $y^{(i)}(t)$ represents the output, which is identical to the current generated by the VSPND. $\boldsymbol{A}^{(i)}$ and $\boldsymbol{c}^{(i)}$ respectively denote the system and output matrices, given as

$$\boldsymbol{A}^{(i)} = \begin{bmatrix} \frac{-1}{\tau_v} & \frac{S_v f_q}{\tau_v} & 0 \\ 0 & 0 & 1 \\ 0 & 0 & 0 \end{bmatrix}, \tag{6.43}$$

and

$$\boldsymbol{c}^{(i)} = \begin{bmatrix} 1 & S_v f_p & 0 \end{bmatrix}, \tag{6.44}$$

where τ_v is the time-constant of ${}^{52}_{23}V$; S_v is the sensitivity of VSPND; f_p and f_q are respectively the prompt and delayed fractions of the output signal of VSPND.

In (6.42), we have

$$\zeta^{(i)}(t) = y^{(i)}(t) - S_v f_p \phi^{(i)}(t) \tag{6.45}$$

and the remaining two states correspond to the state-space representation of first order power-series approximation for unknown input flux, given by

$$\phi^{(i)}(t) = \eta_0^{(i)} + \eta^{(i)} t, \tag{6.46}$$

where $\eta_0^{(i)}$ and $\eta^{(i)}$ are arbitrary constants.

The above continuous time model is discretized to obtain the following state and measurement equations for the i^{th} VSPND:

$$\bar{\boldsymbol{x}}^{(i)}(k+1) = \boldsymbol{\Phi}^{(i)} \bar{\boldsymbol{x}}^{(i)}(k) + \boldsymbol{w}^{(i)}(k), \tag{6.47}$$

$$y^{(i)}(k) = \boldsymbol{c}^{(i)} \bar{\boldsymbol{x}}^{(i)}(k) + \varepsilon^{(i)}(k), \tag{6.48}$$

where $\boldsymbol{\Phi}^{(i)} \in \mathbb{R}^{3\times 3}$ is the state transition matrix. The models given by (6.47) and (6.48) for all the 200 VSPNDs can be arranged as

$$\bar{\boldsymbol{x}}(k+1) = \boldsymbol{\Phi} \bar{\boldsymbol{x}}(k) + \boldsymbol{w}(k), \tag{6.49}$$

$$\boldsymbol{y}(k) = \boldsymbol{C} \bar{\boldsymbol{x}}(k) + \boldsymbol{\varepsilon}(k), \tag{6.50}$$

where

$$\bar{\boldsymbol{x}}(k) = \begin{bmatrix} \bar{\boldsymbol{x}}^{(1)}(k) \\ \bar{\boldsymbol{x}}^{(2)}(k) \\ \vdots \\ \bar{\boldsymbol{x}}^{(200)}(k) \end{bmatrix}, \quad \boldsymbol{w}(k) = \begin{bmatrix} \boldsymbol{w}^{(1)}(k) \\ \boldsymbol{w}^{(2)}(k) \\ \vdots \\ \boldsymbol{w}^{(200)}(k) \end{bmatrix},$$

$$\boldsymbol{\Phi} = \text{diag.}[\boldsymbol{\Phi}^{(1)}\ \boldsymbol{\Phi}^{(2)} \cdots \boldsymbol{\Phi}^{(200)}],$$

$$\boldsymbol{y}(k) = [y^{(1)}(k)\ y^{(2)}(k) \ldots y^{(200)}(k)]^T,$$

$$\boldsymbol{\varepsilon}(k) = [\varepsilon^{(1)}(k)\ \varepsilon^{(2)}(k) \ldots \varepsilon^{(200)}(k)]^T,$$

$$\text{and } \boldsymbol{C} = \text{diag.}[\boldsymbol{c}^{(1)}\ \boldsymbol{c}^{(2)} \cdots \boldsymbol{c}^{(200)}].$$

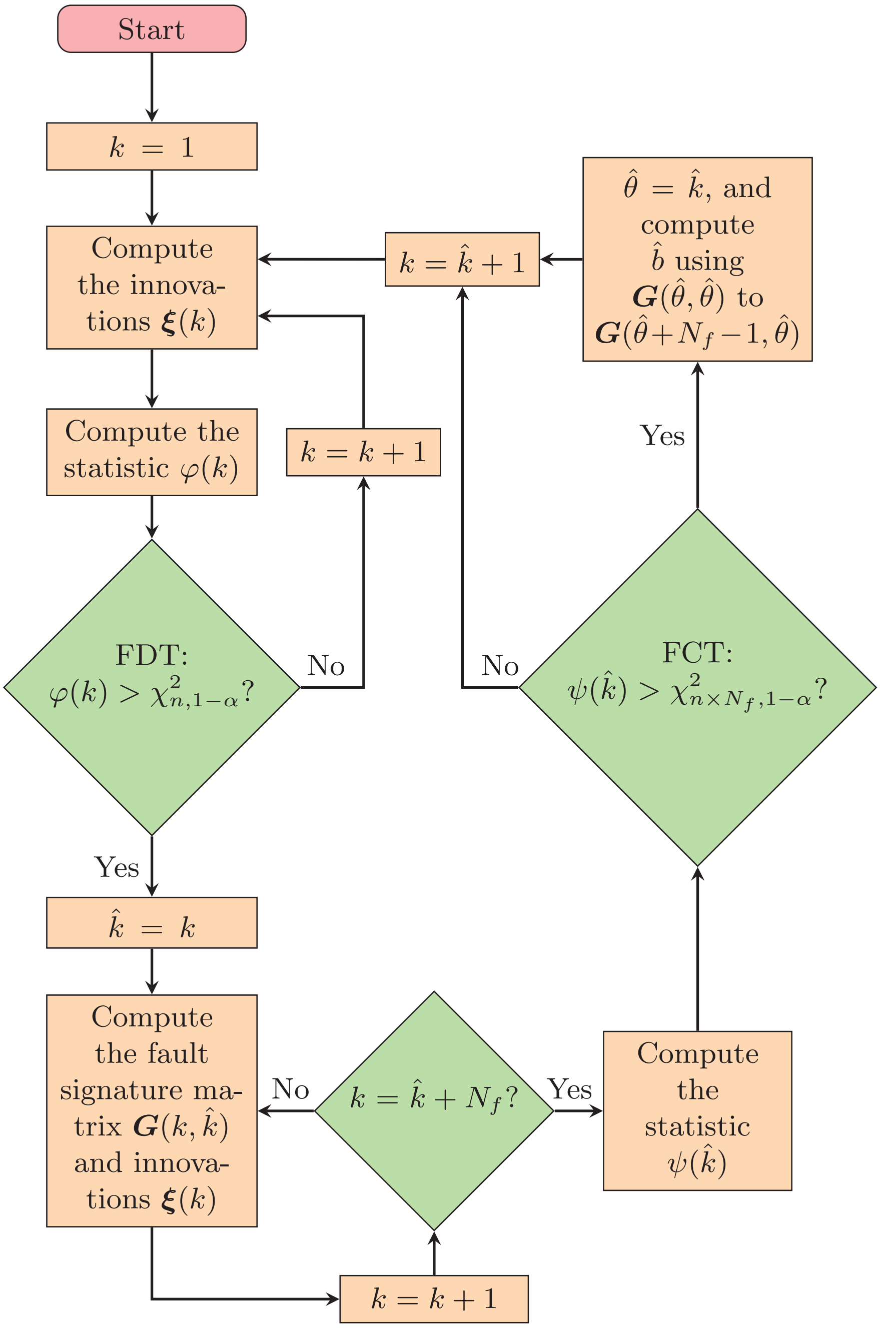

Figure 6.1: Flow chart of GLR method for dynamic systems

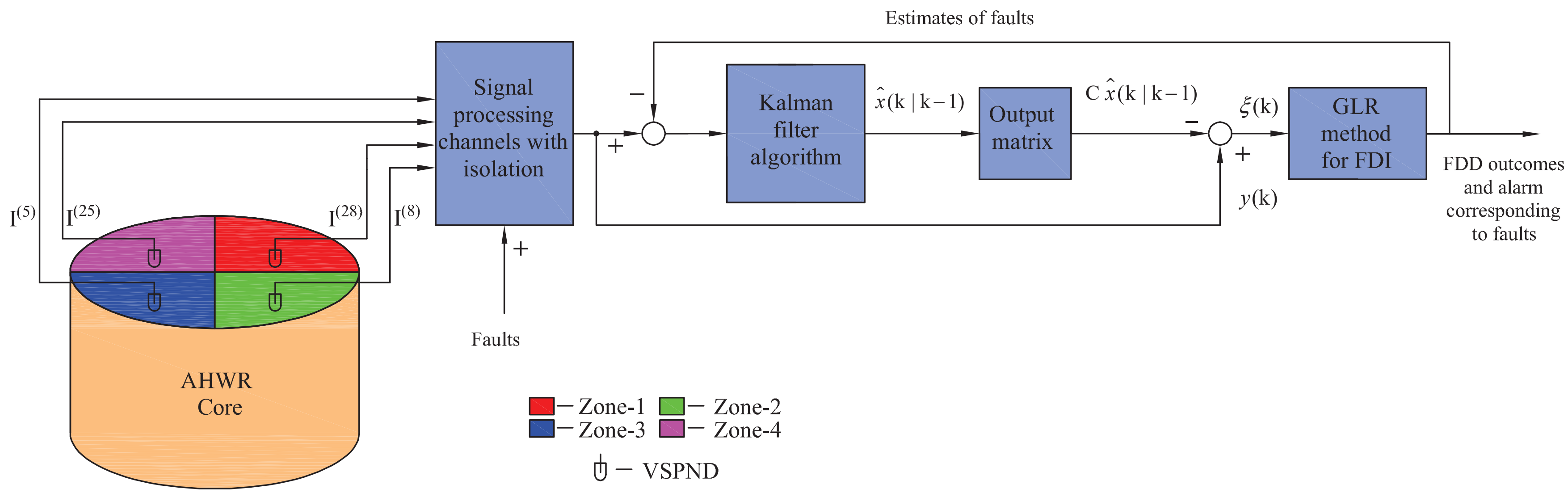

Figure 6.2: Overall scheme of the Kalman filter-based FDI using GLR for 4 VSPNDs in different zones.

For simulating a realistic behaviour, a white noise having standard deviation of the order of 2% of the nominal signal around the full power steady-state is superimposed on the VSPND output signal. Since the reactor is assumed to be operating at the power level of 1.0 pu, the measurement noise variance obtained from the simulated data is about 0.04 for each VSPND.

The process noise covariance matrix ${\mathbf{\Sigma}_{\boldsymbol{w}}}^{(i)}$ for the i^{th} VSPND is considered as [61]:

$$
{\mathbf{\Sigma}_{\boldsymbol{w}}}^{(i)} = 4 \times 10^{-7} \times \begin{bmatrix} 0 & 0 & 0 \\ 0 & 0.01 & 0 \\ 0 & 0 & 1 \end{bmatrix}.
$$

In the above, the first diagonal element of ${\mathbf{\Sigma}_{\boldsymbol{w}}}^{(i)}$ is considered zero, which corresponds to the fact that the VSPND model is known with reasonably high accuracy as evident from the validation results given in [60]. Remaining two diagonal elements of the process covariance matrix are large because of poor confidence in approximation of neutron flux near the VSPND by a first order power-series [61]. Now, the covariance matrices for the process noise and measurement noise for the composite Kalman filter are

$$
\mathbf{\Sigma}_{\boldsymbol{w}} = \text{diag.}[{\mathbf{\Sigma}_{\boldsymbol{w}}}^{(1)} \ {\mathbf{\Sigma}_{\boldsymbol{w}}}^{(2)} \cdots {\mathbf{\Sigma}_{\boldsymbol{w}}}^{(200)}]
$$

and

$$
\mathbf{\Sigma}_{\boldsymbol{\varepsilon}} = 0.04\boldsymbol{I}.
$$

Optimality of the Kalman filter with these $\mathbf{\Sigma}_{\boldsymbol{w}}$ and $\mathbf{\Sigma}_{\boldsymbol{\varepsilon}}$ matrices is addressed in the following.

Whiteness of innovations of one of the VSPNDs V_i is tested [106] for the different values for the tuning matrices. WT similar to that explained in Section 5.1.1 is conducted on the innovation sequence of one of the VSPND signals. Fig. 6.3 shows the auto-correlation characteristic as a function of the lag index j, when maximum value for it,

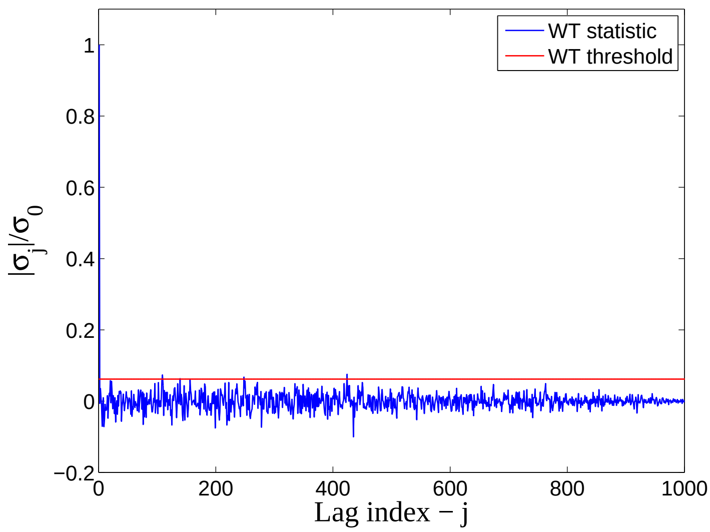

Figure 6.3: Whiteness statistic

k, is taken as 1000 for $N_w = 10000$. Violation of the WT threshold by this characteristic is calculated to be 0.16%. Since this is less than the 5% tolerance, innovation sequence can be declared white. Hence, the Kalman filter is found to be optimal and no more tuning is required [61].

6.3 Results

Methods described in the preceding sections can be generalized for FDI of all the 200 VSPNDs of the AHWR. However, for the purpose of illustration while retaining simplicity, four different VSPNDs from the four quadrants are considered, which are on the same layer. Specifically, VSPNDs V_5, V_8, V_{25} and V_{28} in layer Z_1, are considered. Individual VSPND signals are passed through the dynamic compensations. In this case, since number of measurements $n = 4$, the fault signature matrix is a diagonal matrix of size 4×4. Innovations from the Kalman filter combined with this fault signature matrix are used for the identification of faulty VSPND and estimation of bias magnitude, using the GLR method as already described in Sec. 6.1. The overall schematic of the proposed method for this case is shown in Fig. 6.2, in which the block named 'GLR method for FDI' works on the basis of the algorithm given in Fig. 6.1. N_f is taken as 50 and level of significance (α) is taken as 0.05 for all tests.

Table 6.2: GLR outcomes for the open-loop transient

S. No.	VSPND	Actual values		Estimated values	
		b (%)	θ	$\hat{b}$ (%)	$\hat{\theta}$
1	V_5	5	2500	5.20	2507
2	V_8	-10	3500	-10.11	3500
3	V_{25}	15	4500	14.14	4500
4	V_{28}	-20	5500	-20.89	5501
5	V_5	1.5	6500	-	-
6	V_8	2	7500	-	-
7	V_{25}	2.5	8500	2.45	8501
8	V_{28}	3	9500	3.40	9503

In this section, results are presented for two different simulated operating conditions of the AHWR. In the first transient, biases are introduced in the VSPND measurement data during the open-loop operation, and in the second one, biases are introduced while the reactor is maintained under closed loop control. Simulations are done for 300 s and 200 s respectively in first and second cases, with a sampling duration of 0.02 s. VSPND signals are generated with the help of their dynamic models. Results are explained in the following.

6.3.1 Open-loop RR Transient

When the reactor is critical, all the RRs are at 66.66 % -in position. Starting from this configuration, simultaneous movement of the RRs in nodes 2, 4, 6 and 8 was simulated. At time $t = 150$ s or at the sampling instant $k = 7500$, control signals to the drives of these RRs are chosen such that the rods move linearly into the reactor core and take 100%-in position in 120 s, *i.e.*, at $t = 270$ s or $k = 13500$. Then the RRs are held at this position till $t = 300$ s or $k = 15000$. Fig. 5.2 shows the position of the RRs during the transient.

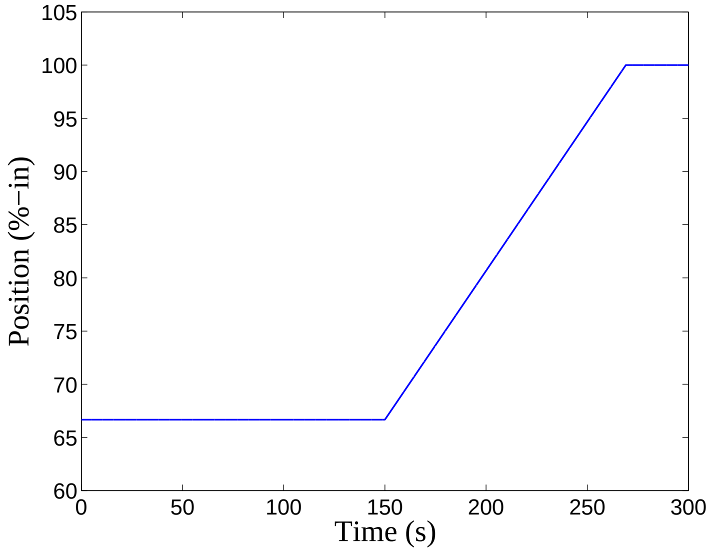

Figure 6.4: Position of RRs during open-loop transient.

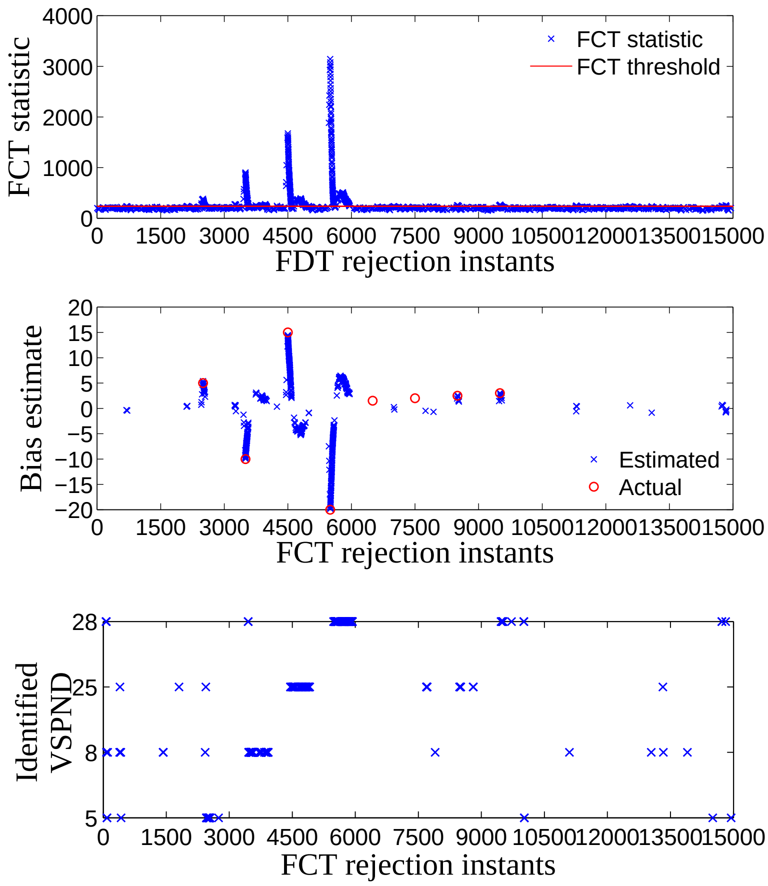

Figure 6.5: Different GLR outcomes during open-loop transient: FCT statistic on FDT rejections, bias estimate and identified faulty VSPNDs at FCT rejection instants.

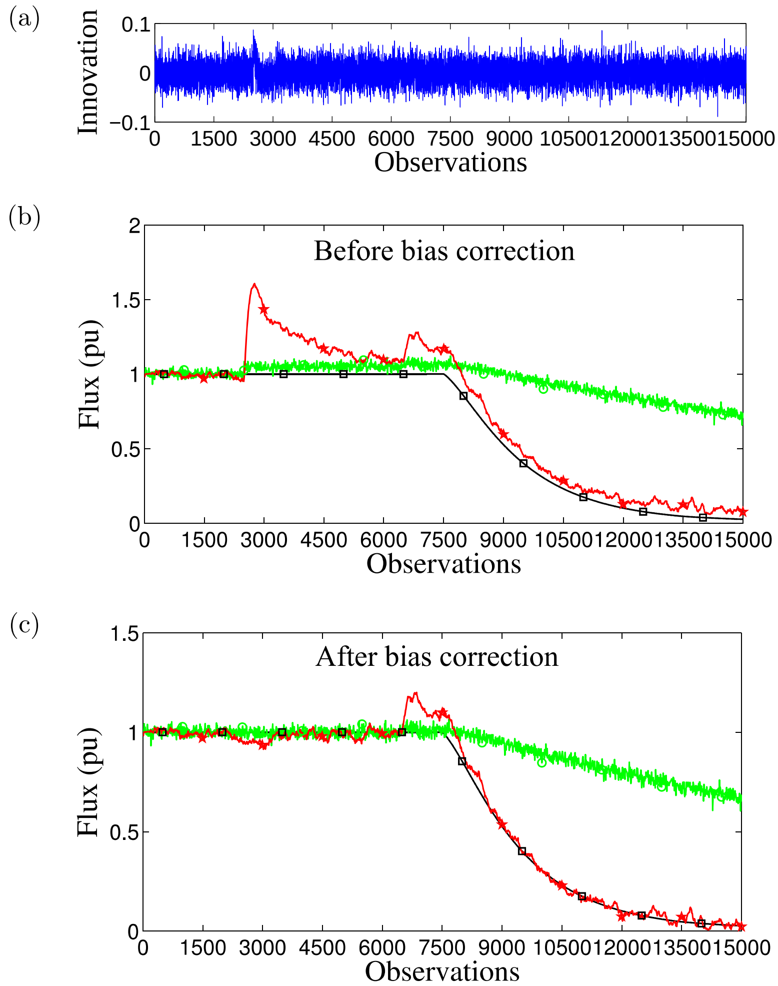

Figure 6.6: Open-loop RR transient: Different plots for V_5 (a) Innovation sequence, (b) Actual, delayed and estimated signals before bias correction, and (c) Actual, delayed and estimated signals after bias correction. (Note: Additive biases are introduced at $k = 2500$ and at $k = 6500$ corresponding to which there can be seen some changes in the innovation sequence. However, the bias at $k = 6500$, being lesser in magnitude, is not detected by the algorithm. Hence, the estimated signal of V_5 has been corrected for the bias at $k = 2500$ and not corrected for the bias at $k = 6500$.)

Additive biases are introduced into the VSPND data, in a sequential manner. Initial $\frac{1}{6}^{\text{th}}$ length of data corresponds to the case of no fault. Bias equivalent to 5% of the steady-state value, is added to signal of V_5, from the 2500^{th} sampling instant ($t = 50$ s). Similarly biases of different magnitudes are added in the simulated measurement data of V_8, V_{25} and V_{28} at the observation indices θ, as given in Table 6.2, in which the GLR statistics (estimates of the bias magnitude ($\hat{b}$) and bias occurrence instant

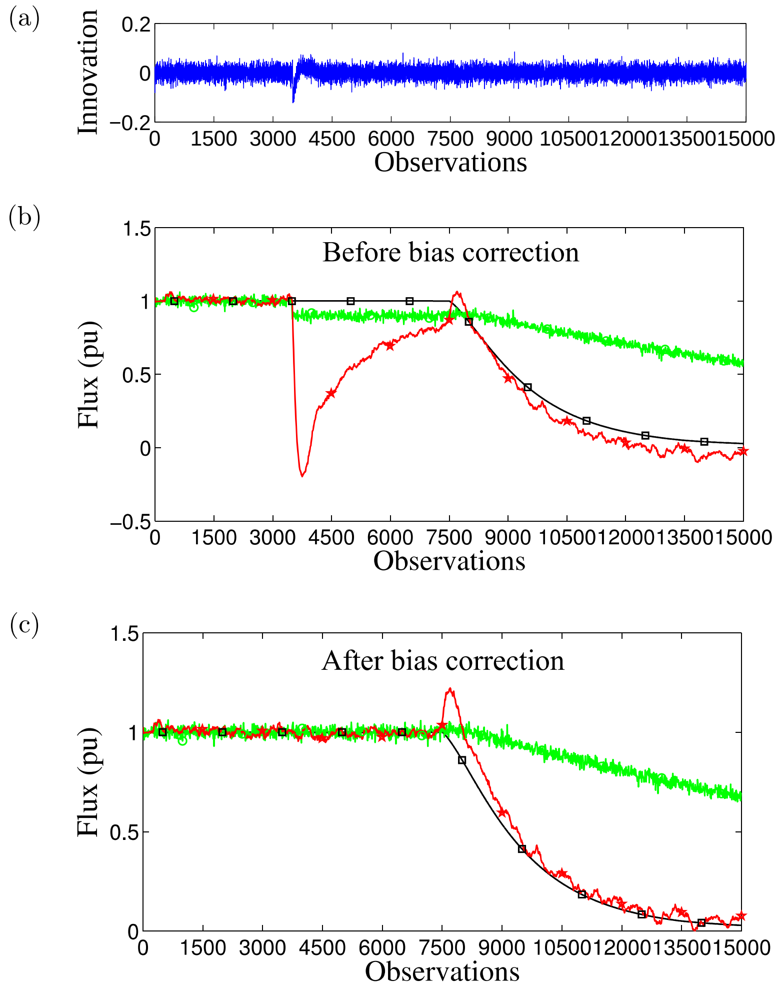

Figure 6.7: Open-loop RR transient: Different plots for V_8 (a) Innovation sequence, (b) Actual, delayed and estimated signals before bias correction, and (c) Actual, delayed and estimated signals after bias correction. (Note: The magnitudes of bias and the time of bias injection can be seen from Table 6.2.)

$(\hat{\theta})$) are also given. From 6500$^{\text{th}}$ sampling instant, biases of magnitude 1.5, 2, 2.5 and 3% are introduced in the simulated measurement data of V_5, V_8, V_{25} and V_{28} for every 1000 sampling instants (20 s) till $\theta = 9500$ ($t = 190$ s), as given alongwith the GLR statistics in Table 6.2. FCT statistic is computed on the rejection of FDT, and on every FCT rejection faulty VSPNDs are identified and the bias magnitude is estimated. From Table 6.2, it is clear that for a bias magnitude greater than the standard deviation of measurement errors, *i.e.*, 2% (refer to Section 6.2), $\hat{\theta}$ and $\hat{b}$ are close to their actual values.

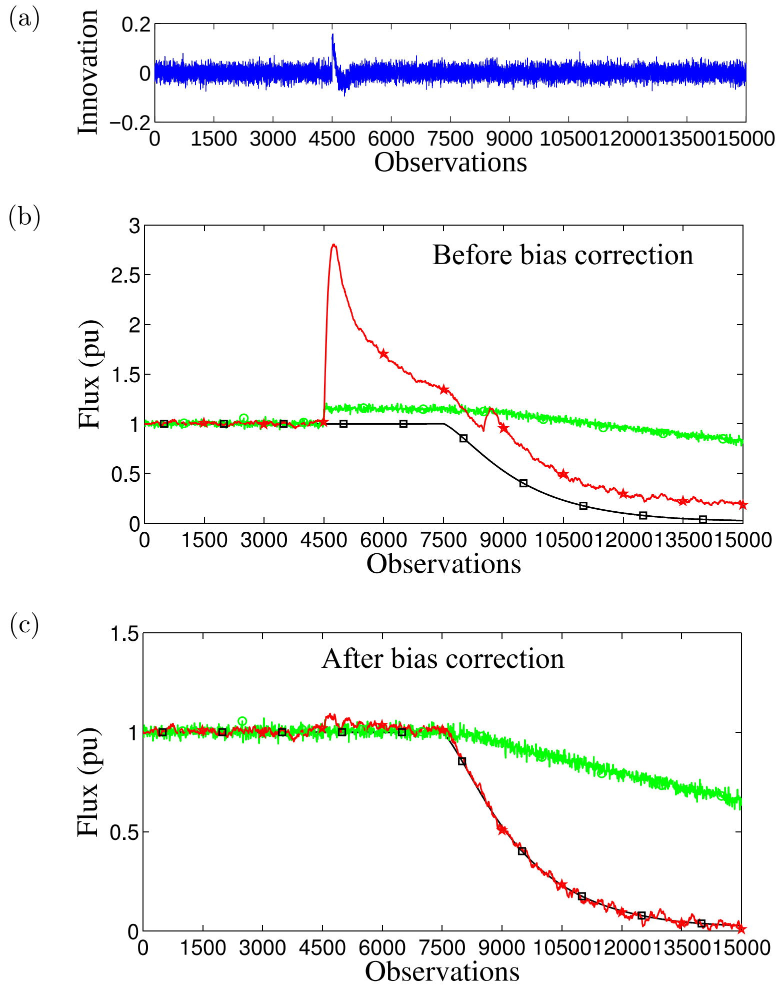

Figure 6.8: Open-loop RR transient: Different plots for V_{25} (a) Innovation sequence, (b) Actual, delayed and estimated signals before bias correction, and (c) Actual, delayed and estimated signals after bias correction.

Fig. 6.5 shows the plot of FCT statistic computed from (6.31) for all the instants for which H_0 is rejected in FDT, estimate of bias, $\hat{b}$ and the identified faulty VSPND $\hat{i}$. The sudden jumps in FCT statistic, at the observations 2500, 3500, 4500 and 5500, are in response to the injected additive biases in the signals of VSPNDs V_5, V_8, V_{25} and V_{28}, respectively. The bias correction equivalent to $\hat{b}$, is made in the VSPND signal using (6.39) from the instant $\hat{\theta}$. The innovation sequence, VSPND output and the estimated output for the 4 VSPNDs are shown in Fig. 6.6-6.9, for both before bias correction and after bias correction, obtained using (6.2) and (6.39) respectively. The true reactor flux

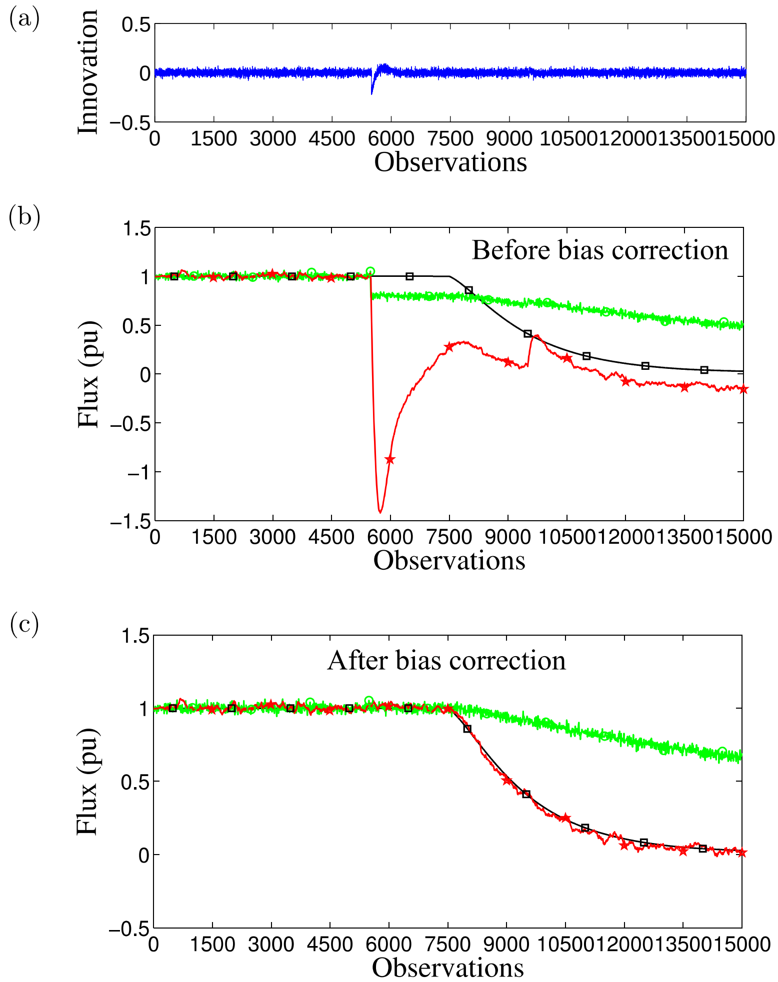

Figure 6.9: Open-loop RR transient: Different plots for V_{28} (a) Innovation sequence, (b) Actual, delayed and estimated signals before bias correction, and (c) Actual, delayed and estimated signals after bias correction.

variation is also shown. In these plots, it can be observed that the sudden jumps as a result of faults in VSPND outputs before bias correction are eliminated after bias correction. The plot of innovation sequences shown in Fig. 6.6-6.9 have abrupt jumps that can be related to the sign and magnitude of the bias in the corresponding VSPND. The actual and estimated outputs of the VSPNDs also experience a similar jump following the introduction of fault if bias correction is not incorporated. However, with correction of bias the jump is appreciably reduced, establishing the effectiveness of the proposed method.

6.3.2 Demand Power Change

In this transient, the demand power changes from 1.0 pu to 0.9 pu, and all the 4 RRs meant for automatic regulation act to reach the new steady-state corresponding to the new demand power. The variation of total power of the reactor, in response to the change in demand is depicted in Fig. 6.10.

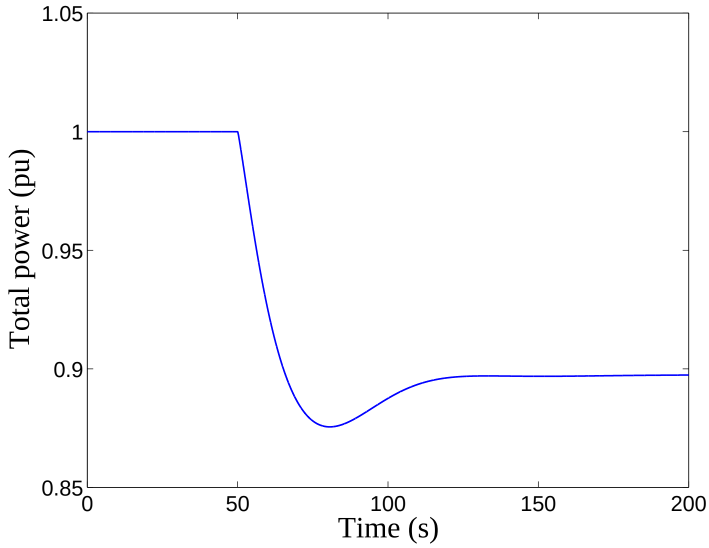

Figure 6.10: Variation of total power during demand power change.

In this case, additive biases are introduced in the signals of VSPNDs V_5, V_8, V_{25} and V_{28} according to the magnitudes of biases and time instants at which they are introduced as given in Table 6.3. It should be noted that when a bias is introduced in a VSPND at a particular time instant, it is persistent thereafter. Table 6.3 gives the corresponding statistics and Fig. 6.11 shows the characteristics such as FCT statistic, bias estimate, and the identified faulty VSPND. Fig. 6.12(a)-6.12(d) show the innovation sequences, reactor flux, and delayed and estimated values of all four VSPND signals. In this case also, it can be observed that the fault-driven jumps in VSPND delayed outputs are not present after bias correction obtained using (6.39). On overall basis, Table 6.3 and Fig. 6.12 make it clear that the proposed hybrid strategy for dynamic compensation and FDI, performed well even for faults during the transient condition.

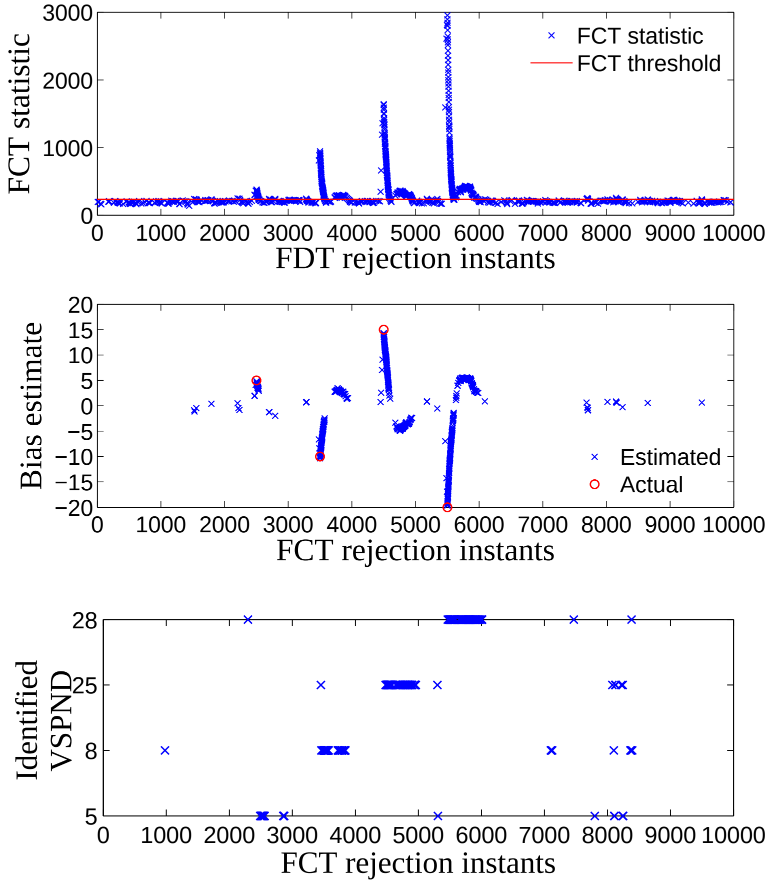

Figure 6.11: Different GLR outcomes during demand power change: FCT statistic on FDT rejections, bias estimate and identified faulty VSPNDs at FCT rejection instants.

Table 6.3: GLR outcomes for change in the demand power

S. No.	SPND	Actual values		Estimated values	
		b (%)	θ	$\hat{b}$ (%)	$\hat{\theta}$
1	V_5	5	2500	4.80	2500
2	V_8	-10	3500	-9.56	3500
3	V_{25}	15	4500	15.02	4500
4	V_{28}	-20	5500	-19.73	5501

Summarizing the results obtained in these cases, it is possible to say that the developed strategy with bias correction shows significant improvement in the performance in terms of successful detection and diagnosis of step changes in the measurement signals, satisfactory tracking and the dynamic compensation as compared to the case in which no FDI scheme is employed.

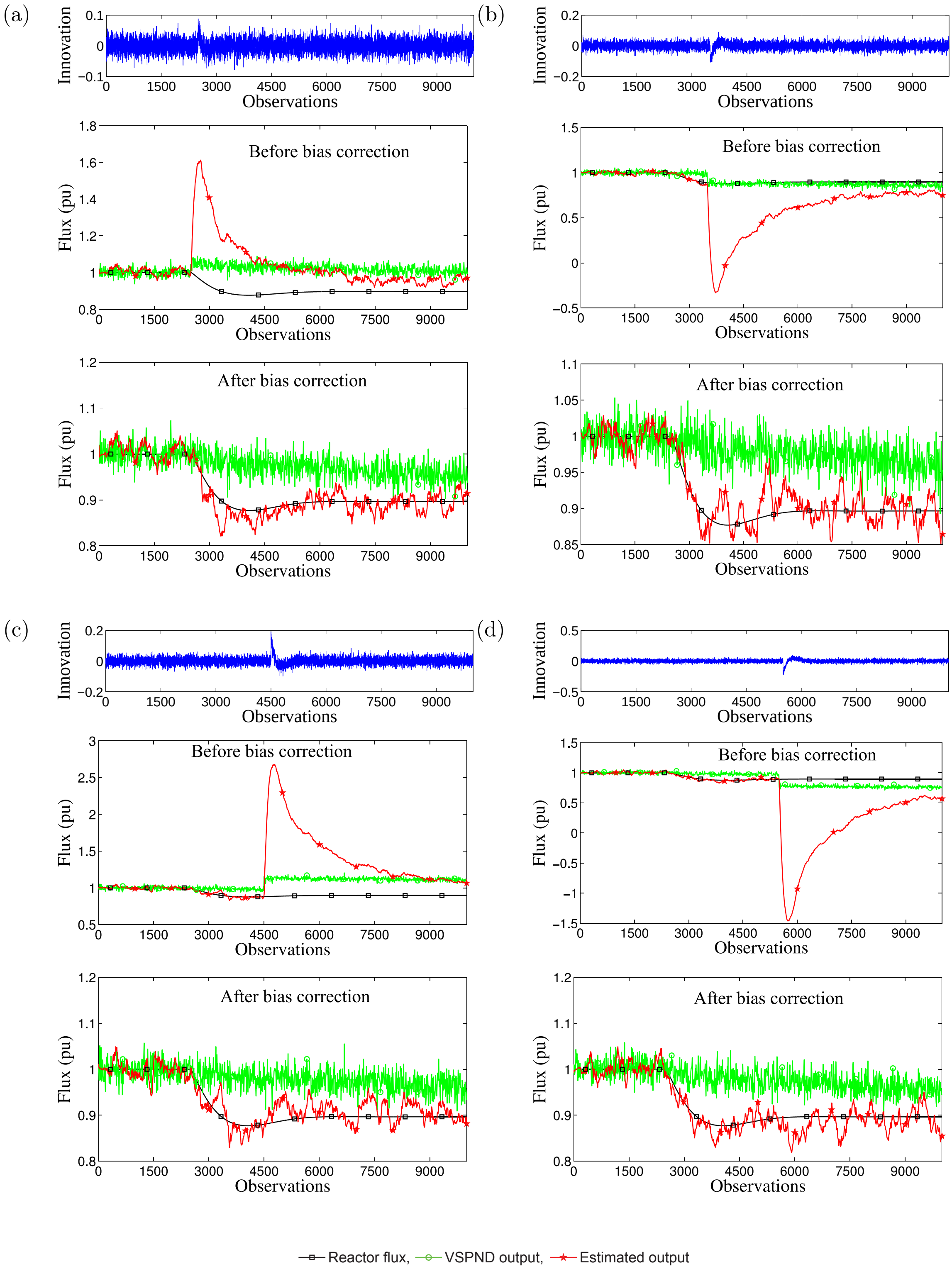

Figure 6.12: Demand power change transient: Innovation sequence and actual, delayed and estimated signals before and after bias correction for (a) V_5, (b) V_8, (c) V_{25}, and (d) V_{28}.

6.4 Discussions

When Vanadium or Rhodium SPNDs are used for in-core neutron flux monitoring and control, a system that can compensate for the delayed response of the SPNDs could be deployed. If such a system is based on a very accurate model of the SPNDs, it can also be exploited for detection and diagnosis of faults, if any, in the SPNDs. In this chapter, the Kalman filter-based dynamic compensator is coupled with GLR method for dynamic systems. Apart from dynamic compensation, the method performs simultaneous detection and correction of step changes in the signals of the SPND or the associated circuit as a result of faults, which might be experienced during their operation. The fault correction is facilitated by the GLR method by virtue of its ability to quantify the fault magnitude. As established through simulation of realistic transients in AHWR, the hybrid method is effective in obtaining prompt neutron flux variations from the delayed signal of the VSPND as well as in estimation of magnitude of step change in the signal alongwith the time of its occurrence. Moreover, when correction of step change is incorporated, the estimated output matches closely with the true neutron flux variation. The proposed technique would be useful to other instruments like Resistance Temperature Detectors, which are used extensively in nuclear reactors. If the fault correction is deployed alongwith closed loop control, overall accuracy and availability will improve.

Chapter 7

Conclusions and Future Scope

The measurement signals from the sensors or detectors should accurately represent the plant behaviour and should be free from errors, for the realization of the benefits from the control, monitoring and protection systems. Faults and random errors add uncertainty in the measurement data. Some filtering techniques, which are capable of eliminating the random errors, were of use at the early stages. A fault detection and isolation scheme should also be implemented alongwith the random error filtering to avoid erroneous inferences about the plant operation and erroneous counteractions by the control and protection systems. A fault detection and isolation scheme utilizing analytical redundancy is particularly important, as it exploits spatial redundancy to simultaneously reduce the effects of both random errors and faults. Among different fault detection and isolation schemes, the model-based schemes turn out to be not only complex but also erroneous for the case of large processes in which large number of variables are involved. Hence, data-based (process history-based) fault detection schemes are more suitable. The data reconciliation scheme is particularly suitable for sensor fault detection and isolation, as it involves only checking the detector signals for consistency represented by a constraint model. However, this scheme requires the constraint model and a fault detection and isolation scheme. In addition, a check also needs to be performed for the validity of the constraint model under different operational transients of the plant.

Development of a mathematical model of the plant may be required for the generation of training data to the constraint model development as well as checking the validity of the constraint model.

Nuclear reactors, besides being complex systems, also require large number of variables to be monitored. Detection of faults in the neutron flux detectors is very important task, as the primary functions of monitoring, control and protection of the reactor are achieved based on the signals from these detectors. These detectors are situated in harsh environment either within or out of the core. Along with occasional faults, random errors are also present in the detector signals.

In advanced heavy water reactor, a large reactor, 9 ion chambers are used in ex-core locations for core flux measurement and 200 Vanadium self-powered neutron detectors are placed at in-core locations for local flux monitoring. In this thesis, a detailed non-linear dynamic model developed for advanced heavy water reactor has been augmented with detector equations to obtain a simulation model for validation of the data based schemes for fault detection and isolation of ion chambers and Vanadium self-powered neutron detectors. Data-driven modeling techniques, *viz.*, principal component analysis and iterative principal component analysis have been used for the development of constraint model from the ion chamber and Vanadium self-powered neutron detectors signal data of advanced heavy water reactor. The development of constraint model is straight forward for the signals of ion chambers, which are relatively smaller in number than Vanadium self-powered neutron detectors. Vanadium self-powered neutron detectors, being large in number, necessitated the development of individual constraint models for different highly correlated groups or clusters in them, which were obtained through k-means clustering technique. Constraint models developed from time-series data of the detectors during an operating mode of the reactor have been used for other operating modes involving similar correlation pattern among the signals. The data reconciliation and fault detection and isolation scheme exhibited desired performances in all cases, when the constraint relations among the signals do not vary. This was possible because of spatial or zonal control, which is commonly employed by large reactors like advanced heavy water reactor. As a part of fault detection and isolation, different multiple-fault detection tests such as generalized likelihood ratio method, iterative measurement test and iterative principal component test, which is the outcome of this research work, are used alongwith data reconciliation. Out of these tests iterative principal component test has been found to be efficient. As a part of data reconciliation, alongwith the reconciled estimates of fault-free signals, estimates of faulty signals also are obtained using the projection matrix. Results of data reconciliation-based fault detection and isolation are presented when iterative principal component test is employed.

Apart from data reconciliation-based fault detection and isolation, model-based fault detection and isolation with the use of dynamic model of the Vanadium self-powered neutron detectors is also attempted in this thesis. This scheme using Kalman filter for generation of the innovation also performed well, when coupled with generalized likelihood ratio method for the information regarding the fault, *i.e.*, fault occurrence time, fault location, and magnitude of the fault. This hybrid scheme dynamically compensates the Vanadium self-powered neutron detector signals for promptness; minimizes the random errors through Kalman filter; performs detection and diagnosis of the faults with generalized likelihood ratio method; and corrects the faulty measurements online. This scheme may be implemented in the reactor regulating system of advanced heavy water reactor. However, it can detect only the abrupt faults because of the unknown-input framework.

The work carried out for this thesis provides some directions for future scope in the applications to nuclear reactors for sensor fault detection and isolation. In particular, the following topics merit consideration:

- Adaptive modeling approach can be considered as in the case of recursive principal component analysis for updating the constraint model recursively in response to the operating modes.
- Structured residuals approach and fault sub-space analysis can also be considered.
- The principal component analysis or iterative principal component analysis constraint model among the Vanadium self-powered neutron detector signals may be combined with the state-space formulation based on the Vanadium self-powered neutron detector model to facilitate incipient fault detection. This technique refers to the augmented state Kalman filter.
- A dynamic data reconciliation scheme, which utilizes the dynamic model of advanced heavy water reactor, can also be implemented.

Aspects such as online implementation of the algorithms, assessment of real time behaviour, *etc.* may also be investigated.

References

[1] S. N. Ahmed. *Physics and Engineering of Radiation Detection.* Elsevier, Netherlands, second edition, 2015.

[2] G. Allaire and S. M. Kaber. *Numerical Linear Algebra.* Springer, 2008.

[3] G. A. Almacy and T. Sztano. Checking and correction of measurements on the basis of linear system model. *Prob. Contr. Inform. Theory*, 4:57–69, 1975.

[4] M. R. Anderberg. *Cluster analysis for applications.* Probability and mathematical statistics. Academic Press, 1973.

[5] B. R. Bakshi. Multiscale PCA with application to multivariate statistical process monitoring. *AIChE J.*, 44(7):1596–1610, 1998.

[6] L. A. Banda. Operational experience in rhodium self-powered detectors. *IEEE Trans. Nucl. Sci.*, 26(1):910–915, Feb 1979.

[7] M. Basseville and I. V. Nikiforov. *Detection of Abrupt Changes: Theory and Application.* Prentice-Hall, Inc., NJ, USA, 1993.

[8] E. Chow and A. S. Willsky. Analytical redundancy and the design of robust failure detection systems. *IEEE Trans. Automatic Control*, 29(7):603–614, Jul 1984.

[9] D. A. Cooper, R. J. Ledoux, K. Kamieniecki, S. E. Korbly, J. Thompson, M. Ryan, N. Roza, L. Perry, D. Hwang, J. Costales, and M. Kuznetsova. Intelligent Radiation

Sensor System (IRSS) Advanced Technology Demonstration (ATD). In *2010 IEEE Int. Conf. Tech. for Homeland Security (HST)*, pages 414–420, Nov 2010.

[10] D. A. Cooper, R. J. Ledoux, K. Kamieniecki, S. E. Korbly, J. Thompson, J. Batcheler, S. Chowdhury, N. Roza, J. Costales, and V. Aiyawar. Intelligent Radiation Sensor System (IRSS) advanced technology demonstrator (ATD). In *2012 IEEE Int. Conf. Tech. for Homeland Security (HST)*, pages 511–516, Nov 2012.

[11] D. A. Cooper, R. J. Ledoux, K. Kamieniecki, S. E. Korbly, J. Thompson, J. Batcheler, and J. Costales. Integration of inertial measurement data for improved localization and tracking of radiation sources. In *2013 IEEE Int. Conf. Tech. for Homeland Security (HST)*, pages 613–617, Nov 2013.

[12] C. M. Crowe, Y. A. G. Campos, and A. Hrymak. Reconciliation of process flow rates by matrix projection. part I: Linear case. *AIChE J.*, 29(6):881–888, 1983.

[13] C. M. Crowe. Formulation of linear data reconciliation using information theory. *Chemical Eng. Sci.*, 51(12):3359–3366, 1996.

[14] C. M. Crowe. Data reconciliation-progress and challenges. *J. Process Control*, 6 (2-3):89–98, 1996.

[15] R. Davis. Diagnostic reasoning based on structure and behavior. *Artificial Intelligence*, 24(1-3):347–410, 1984.

[16] B. Deb, J. A. F. Ross, A. Ivan, and M. J. Hartman. Radioactive source estimation using a system of directional and non-directional detectors. *IEEE Trans. Nucl. Sci.,*, 58(6):3281–3290, Dec 2011.

[17] B. Deb. Iterative estimation of location and trajectory of radioactive sources with a networked system of detectors. *IEEE Trans. Nucl. Sci.,*, 60(2):1315–1326, April 2013.

[18] D. Dong and T. J. McAvoy. Batch tracking via nonlinear principal component analysis. *AIChE J.*, 42(8):2199–2208, 1996.

[19] J. J. Duderstadt and L. J. Hamilton. *Nuclear Reactor Analysis.* John Wiley & Sons, New York, 1976.

[20] R. Dunia, S. J. Qin, T. F. Edgar, and T. J. McAvoy. Identification of faulty sensors using principal component analysis. *AIChE J.*, 42(10):2797–2812, 1996.

[21] R. Dunia and S. J. Qin. Subspace approach to multidimensional fault identification and reconstruction. *AIChE J.*, 44(8):1813–1831, 1998.

[22] B. S. Everitt, S. Landau, M. Leese, and D. Stahl. *Cluster Analysis.* Wiley Series in Probability and Statistics. Wiley, 2011.

[23] H. Ezure. Estimation of most probable power distribution in BWRs by least squares method using in-core measurements. *J. of Nucl. Sci. and Tech.*, pages 731–740, 1988.

[24] Y. M. Farawila. Application of modal neutron kinetics to boiling water reactor oscillation problems. *Nucl. Sci. and Eng.*, 129(3):261–272, 1998.

[25] J. B. Fussell, G. J. Powers, and R. G. Bennetts. Fault trees: A state of the art discussion. *IEEE Trans. Reliability*, R-23(1):51–55, April 1974.

[26] S. Glasstone and A. Sesonske. *Nuclear Reactor Engineering: Reactor Design Basics/Reactor Systems Engineering.* Number v. 1. Chapman & Hall, USA, 1994.

[27] B. M. Golchert. *Error Analysis, Improvement, and New Applications of Nodal Flux Reconstruction Methods.* University of Illinois at Urbana-Champaign, 1997.

[28] L. M. Grossman and J. P. Hennart. Nodal diffusion methods for space-time neutron kinetics. *Prog. Nucl. Energy*, 49(3):181 – 216, 2007.

[29] J. A. Hartigan. *Clustering Algorithms.* John Wiley & Sons, Inc., New York, USA, 99th edition, 1975.

[30] I. Hideaki and T. Toshikazu. Development and verification of an efficient spatial neutron kinetics method for reactivity-initiated event analyses. *Nucl. Sci. and Tech.*, 38(7):492–502, 2001.

[31] D. Hodouin and M. D. Everell. A hierarchical procedure for adjustment and material balancing of mineral processes data. *Int. J. Mineral Processing*, 7(2):91–116, 1980.

[32] H. Hotelling. Multivariable quality control-illustrated by the air testing of sample bombsights. In *Techniques of Statistical Analysis*, pages 111–184. McGraw Hill, New York, 1947.

[33] C. Iordache, R. S. H. Mah, and A. C. Tamhane. Performance studies of the measurement test for detection of gross errors in process data. *AIChE J.*, 31(7):1187–1201, 1985.

[34] R. Isermann. *Fault-Diagnosis Systems: An Introduction from Fault Detection to Fault Tolerance*. Springer, Darmstadt, 2006.

[35] Y. Iwasaki and H. A. Simon. Causality in device behavior. *Artificial Intelligence*, 29(1):3–32, 1986.

[36] R. A. Johnson and D. W. Wichern. *Applied multivariate statistical analysis*. Number 1. Prentice Hall, USA, 2002.

[37] L. P. M. Johnston and M. A. Kramer. Maximum likelihood data rectification: Steady-state systems. *AIChE J.*, 41(11):2415–2426, 1995.

[38] H. L. D. Jr. Accuracy of the quasistatic method for two-dimensional thermal reactor transients with feedback. *Nucl. Sci. and Eng.*, 59(3):271–281, 1976.

[39] S. J. Julier and J. K. Uhlmann. Unscented filtering and nonlinear estimation. *Proceedings of the IEEE*, 92(3):401–422, 2004.

[40] N. Kaistha and B. R. Upadhyaya. Incipient fault detection and isolation of field devices in nuclear power systems using principal component analysis. *Nucl. Tech.*, 136:221–230, 2001.

[41] R. E. Kalman. A New Approach to Linear Filtering And Prediction Problems. *J. Basic Eng.*, 82:35-45, 1960.

[42] J. D. Kleer and J. S. Brown. A qualitative physics based on confluences. *Artificial Intelligence*, 24(1):7–83, 1984.

[43] J. C. Knepper and J. W. Gorman. Statistical analysis of constrained data sets. *AIChE J.*, 26(2):260–264, 1980.

[44] G. F. Knoll. *Radiation Detection and Measurement.* John Wiley & Sons, 2010.

[45] D. R. Kuehn and H. Davidson. Computer control II. mathematics of control. *Chem. Eng. Progress*, 57:44–47, 1961.

[46] W. E. Larimore. Canonical variate analysis in identification, filtering and adaptive control. In *Conf. Decision and Control*, 29, 596–604, 1990.

[47] F. Li, B. R. Upadhyaya, and S. R. P. Perillo. Fault diagnosis of helical coil steam generator systems of an integral pressurized water reactor using optimal sensor selection. *IEEE Trans. Nucl. Sci.*, 59(2):403–410, April 2012.

[48] W. Li, H. H. Yue, S. V. Cervantes, and S. J. Qin. Recursive PCA for adaptive process monitoring. *J. Process Control*, 10(5):471–486, 2000.

[49] B. Lu and B. R. Upadhyaya. Monitoring and fault diagnosis of the steam generator system of a nuclear power plant using data-driven modeling and residual space analysis. *Ann. Nucl. Energy*, 32:897–912, 2005.

[50] J. Ma and J. Jiang. Applications of fault detection and diagnosis methods in nuclear power plants: A review. *Prog. Nucl. Energy*, 53(3):255 – 266, 2011.

[51] J. F. MacGregor and T. Kourti. Statistical process control of multivariate processes. *Control Eng. Practice*, 3(3):403–414, 1995.

[52] J. F. MacGregor, C. Jaeckle, C. Kiparissides, and M. Koutoudi. Process monitoring and diagnosis by multiblock PLS methods. *AIChE J.*, 40(5):826–838, 1994.

[53] J. MacQueen. Some methods for classification and analysis of multivariate observations. In *Proceedings of the Fifth Berkeley Symposium on Mathematical Statistics and Probability, Volume 1: Statistics*, pages 281–297, Berkeley, Calif., 1967. University of California Press.

[54] F. Madron. A new approach to the identification of gross errors in chemical engineering measurements. *Chemical Eng. Sci.*, 40(10):1855–1860, 1985.

[55] R. S. H. Mah, G. M. Stanley, and D. M. Downing. Reconcillation and rectification of process flow and inventory data. *Ind. Eng. Chem. Proc. Des. Dev.*, 15(1):175–183, 1976.

[56] R. S. H. Mah and A. C. Tamhane. Detection of gross errors in process data. *AIChE J.*, 28(5):828–830, 1982.

[57] F. D. Maio, P. Baraldi, E. Zio, and R. Seraoui. Fault detection in nuclear power plants components by a combination of statistical methods. *IEEE Trans. Reliability*, 62(4):833–845, Dec 2013.

[58] P. S. Maybeck. *Stochastic Models, Estimation and Control*, volume 1. Academic Press, New York, 1982.

[59] R. Milne. Strategies for diagnosis. *IEEE Trans. on Systems, Man and Cybernetics,*, 17(3):333–339, 1987. ISSN 0018-9472.

[60] A. K. Mishra, S. R. Shimjith, T. U. Bhatt, and A. P. Tiwari. Dynamic compensation

of vanadium self powered neutron detectors for use in reactor control. *IEEE Trans. Nucl. Sci.*, 60(1):310–318, Feb 2013.

[61] A. K. Mishra, S. R. Shimjith, T. U. Bhatt, and A. P. Tiwari. Kalman filter-based dynamic compensator for vanadium self powered neutron detectors. *IEEE Trans. Nucl. Sci.*, 61(3):1360–1368, June 2014.

[62] J. L. Munoz-Cobo, S. Chiva, and A. Sekhri. A reduced order model of BWR dynamics with subcooled boiling and modal kinetics: application to out of phase oscillations. *Ann. Nucl. Energy*, 31(10):1135–1162, 2004.

[63] S. Narasimhan and R. S. H. Mah. Generalized likelihood ratio method for gross error identification. *AIChE J.*, 33(9):1514–1521, 1987.

[64] S. Narasimhan and R. S. H. Mah. Generalized likelihood ratios for gross error identification in dynamic processes. *AIChE J.*, 34(8):1321–1331, 1988.

[65] S. Narasimhan and C. Jordache. *Data Reconciliation & Gross Error Detection: An Intelligent Use of Process Data.* Gulf Publishing, Houston, 2000.

[66] S. Narasimhan and S. L. Shah. Model identification and error covariance matrix estimation from noisy data using PCA. *Cont. Eng. Prac.*, 16:146–155, 2008.

[67] M. Naskar, A. P. Tiwari, S. V. G. Menon, and V. Kumar. Finite difference approximation for computation of neutron flux distribution in large PHWR. *Proceedings of International Conference on Quality, Reliability and Control (ICQRC), Le Royal Meridien, Mumbai, India*, 2001.

[68] J. N. Ning and H. P. Chou. Construction and evaluation of fault detection network for signal validation. *IEEE Trans. Nucl. Sci.*, 39(4):943–947, Aug 1992.

[69] B. Noble and J. W. Daniel. *Applied Linear Algebra.* Englewood Cliffs, N.J., Prentice-Hall Inc., 1977.

[70] P. Nomikos and J. F. MacGregor. Monitoring batch processes using multiway principal component analysis. *AIChE J.*, 40(8):1361–1375, 1994.

[71] K. O. Ott and D. A. Meneley. Accuracy of the quasistatic treatment of spatial reactor kinetics. *Nucl. Sci. and Eng.*, 36(3):402–411, 1969.

[72] E. S. Page. Continuous inspection schemes. *Biometrika*, 41(1/2):100–115, 1954.

[73] C. C. D. Pai and G. D. Fisher. Application of broyden's method to reconciliation of nonlinearly constrained data. *AIChE J.*, 34(5):873–876, 1988.

[74] K. Pearson. *On Lines and Planes of Closest Fit to Systems of Points in Space.* University College, London, 1901.

[75] X. Peng, Q. Li, and K. Wang. Fault detection and isolation for self powered neutron detectors based on principal component analysis. *Ann. Nucl. Energy*, 85:213 – 219, 2015.

[76] S. J. Qin and T. J. McAvoy. Nonlinear PLS modeling using neural networks. *Comp. & Chem. Eng.*, 16(4):379–391, 1992.

[77] S. J. Qin. Recursive PLS algorithms for adaptive data modeling. *Comp. & Chem. Eng.*, 22(4-5):503–514, 1998.

[78] S. J. Qin and W. Li. Detection, identification, and reconstruction of faulty sensors with maximized sensitivity. *AIChE J.*, 45(9):1963–1976, 1999.

[79] S. J. Qin. Survey on data-driven industrial process monitoring and diagnosis. *Annual Reviews in Control*, 36(2):220–234, 2012.

[80] R. A. Razak, M. Bhushan, M. N. Belur, A. P. Tiwari, M. G. Kelkar, and M. Pramanik. Data reconciliation and gross error analysis of self powered neutron detectors: comparison of PCA and IPCA based models. *Int. J. Adv. Eng. Sci. Appl. Math.*, 4: 91–115, 2012.

[81] R. A. Razak, M. Bhushan, M. N. Belur, A. P. Tiwari, M. G. Kelkar, and M. Pramanik. Clustering of self powered neutron detectors: Combining prompt and slow dynamics. *IEEE Trans. Nucl. Sci.*, 61(6):3635–3643, Dec 2014.

[82] P. M. Reilly and R. E. Carpani. Application of statistical theory of adjustment to material balances. In *13th Canadian Chem. Eng. Conf.*, 1963.

[83] S. H. Rich and V. Venkatasubramanian. Model-based reasoning in diagnostic expert systems for chemical process plants. *Comp. & Chem. Eng.*, 11(2):111–122, 1987.

[84] S. H. Rich and V. Venkatasubramanian. Causality-based failure-driven learning in diagnostic expert systems. *AIChE J.*, 35(6):943–950, 1989.

[85] D. L. Ripps. Adjustment of experimental data. In *Chem. Eng. Prog. Symp.*, pages 8–13, 1965.

[86] S. W. Roberts. Control chart tests based on geometric moving averages. *Technometrics*, 1:239–250, 1959.

[87] D. K. Rollins and J. F. Davis. Unbiased estimation of gross errors in process measurements. *AIChE J.*, 38(4):563–572, 1992.

[88] J. A. Romagnoli and G. Stephanopoulos. Rectification of process measurement data in the presence of gross errors. *Chemical Eng. Sci.*, 36(11):1849–1863, 1981.

[89] J. Rosenberg, R. S. H. Mah, and C. Iordache. Evaluation of schemes for detecting and identifying gross errors in process data. *Industrial & Eng. Chemistry Research*, 26(3):555–564, 1987.

[90] K. Roy, R. N. Banavar, and S. Thangasamy. Application of fault detection and identification (FDI) techniques in power regulating systems of nuclear reactors. *IEEE Trans. Nucl. Sci.*, 45(6):3184–3201, Dec 1998.

[91] K. Roy, R. N. Banavar, and S. Thangasamy. Temporal redundancy methods using risk-sensitive filtering and parameter estimation to detect failures in neutronic sensors during reactor start-up and steady-state operation. *IEEE Trans. Nucl. Sci.*, 47 (6):2706–2714, Dec 2000.

[92] M. Sanchez and J. Romagnoli. Use of orthogonal transformations in data classification-reconciliation. *Comp. & Chem. Eng.*, 20(5):483–493, 1996.

[93] C. D. Schaper, W. E. Larimore, D. E. Seborg and D. A. Mellichamp. Identification of Chemical Processes using Canonical Variate Analysis. *Comp. & Chem. Eng.*, 18: 55–69, 1994.

[94] S. Schmidt. Application of state-space methods to navigation problems. *Advances in Control Systems*, 293–340, 1966.

[95] R. W. Serth and W. A. Heenan. Gross error detection and data reconciliation in steam-metering systems. *AIChE J.*, 32(5):733–742, 1986.

[96] W. A. Shewhart. *Economic Control of Quality of Manufactures Product.* Number v. 509. ASQ Press, New York, 1931.

[97] S. R. Shimjith, A. P. Tiwari, M. Naskar, and B. Bandyopadhyay. Space-time kinetics modeling of advanced heavy water reactor for control studies. *Ann. Nucl. Energy*, 37(3):310–324, 2010.

[98] S. R. Shimjith, A. P. Tiwari, B. Bandyopadhyay, and R. K. Patil. Spatial stabilization of advanced heavy water reactor. *Ann. Nucl. Energy*, 38(7):1545–1558, 2011.

[99] S. R. Shimjith, A. P. Tiwari, and B. Bandyopadhyay. *Modeling and Control of a Large Nuclear Reactor: A Three-Time-Scale Approach.* Lecture Notes in Control and Information Sciences. Springer, 2012.

[100] D. Simon. Kalman filtering with state constraints: a survey of linear and nonlinear algorithms. *Control Theory Applications, IET*, 4(8):1303–1318, August 2010.

[101] H. A. Simon. *Models of Discovery.* Springer, Netherlands, 1 edition, 1977.

[102] D. E. Simpson, V. R. Voller, and M. G. Everett. An efficient algorithm for mineral processing data adjustment. *Int. J. Mineral Processing*, 31(1-2):73–96, 1991.

[103] R. K. Sinha and A. Kakodkar. Design and development of the AHWR - the indian thorium fuelled innovative nuclear reactor. *Nucl. Eng. and Design*, 236(7-8):683–700, 2006.

[104] W. M. Stacey. *Space-time nuclear reactor kinetics.* Academic Press, New York, 1969.

[105] G. M. Stanley and R. S. H. Mah. Estimation of flows and temperatures in process networks. *AIChE J.*, 23(5):642–650, 1977.

[106] P. Stoica. A test for whiteness. *IEEE Trans. Automatic Control*, 22(6):992–993, Dec 1977.

[107] G. Strang. *Linear Algebra and Its Applications.* Thomson, Brooks/Cole, 2006.

[108] T. M. Sutton and B. N. Aviles. Diffusion theory methods for spatial kinetics calculations. *Prog. Nucl. Energy*, 30(2):119–182, 1996.

[109] A. C. Tamhane. A note on the use of residuals for detecting an outlier in linear regression. *Biometrika*, 69(2):488–489, 1982.

[110] A. P. Tiwari, B. Bandyopadhyay, and G. Govindarajan. Spatial control of a large pressurized heavy water reactor. *IEEE Trans. Nucl. Sci.*, 43(4):2440–2453, 1996.

[111] A. P. Tiwari. *Modeling and Control of a Large Pressurized Heavy Water Reactor.* PhD Thesis, IIT Bombay, 1999.

[112] I. B. Tjoa and L. T. Biegler. Simultaneous strategies for data reconciliation and gross error detection of nonlinear systems. *Comp. & Chem. Eng.*, 15(10):679–690, 1991.

[113] H. Tong and C. M. Crowe. Detection of gross erros in data reconciliation by principal component analysis. *AIChE J.*, 41(7):1712–1722, 1995.

[114] R. C. Tryon and D. E. Bailey. *Cluster analysis.* McGraw-Hill, 1970.

[115] N. Tsoulfanidis and S. Landsberger. *Measurement and Detection of Radiation, Third Edition.* Taylor & Francis, 2010.

[116] B. R. Upadhyaya and M. Skorska. Fault analysis of in-core detectors in a PWR using time-series models. In *The 22nd IEEE Conference on Decision and Control, 1983*, volume 22, pages 758–763, Dec 1983.

[117] B. R. Upadhyaya, K. Zhao, and B. Lu. Fault monitoring of nuclear power plant sensors and field devices. *Prog. Nucl. Energy*, 43:337–342, 2003.

[118] V. Vaclavek. Studies on system engineering. II. on the application of the calculus of observations in calculations of chemical engineering balances. *Collect. Czech. Chem. Commun.*, 34(2):364–372, 1969.

[119] V. Vaclavek and M. Loucka. Selection of measurements necessary to achieve multicomponent mass balances in chemical plant. *Chemical Engineering Science*, 31(12): 1199–1205, 1976.

[120] V. Venkatasubramanian and S. H. Rich. An object-oriented two-tier architecture for integrating compiled and deep-level knowledge for process diagnosis. *Comp. & Chem. Eng.*, 12(9-10):903–921, 1988.

[121] V. Venkatasubramanian, R. Rengaswamy, K. Yin, and S. N. Kavuri. A review

of process fault detection and diagnosis: Part I: Quantitative model-based methods. *Comp. & Chem. Eng.*, 27(3):293–311, 2003.

[122] V. Venkatasubramanian, R. Rengaswamy, and S. N. Kavuri. A review of process fault detection and diagnosis: Part II: Qualitative models and search strategies. *Comp. & Chem. Eng.*, 27(3):313–326, 2003.

[123] V. Venkatasubramanian, R. Rengaswamy, S. N. Kavuri, and K. Yin. A review of process fault detection and diagnosis: Part III: Process history based methods. *Comp. & Chem. Eng.*, 27(3):327–346, 2003.

[124] M. Viberg. Subspace-based method for the identification of linear time-invariant systems. *Automatica*, 31(12):1835–1851, 1995.

[125] P. D. Wentzell, D. T. Andrews, D. C. Hamilton, K. Faber, and B. R. Kowalski. Maximum likelihood principal component analysis. *J. of Chemometrics*, 11:339–366, 1997.

[126] R. L. Wiegel. Advances in mineral processing material balances. *Canadian Metallurgical Quarterly*, 11(2):413–424, 1972.

[127] A. S. Willsky and H. L. Jones. A generalized likelihood ratio approach to the detection and estimation of jumps in linear systems. *IEEE Trans. Automatic Control*, 21(1):108–112, 1976.

[128] A. S. Willsky. A survey of design methods for failure detection in dynamic systems. *Automatica*, 12(6):601–611, 1976.

[129] H. Wold. Soft modeling : the basic design and some extensions, 1982.

[130] K. Zhao and B. R. Upadhyaya. Model based approach for fault detection and isolation of helical coil steam generator systems using principal component analysis. *IEEE Trans. Nucl. Sci.*, 53(4):2343–2352, 2006.